Contract No:

This document was prepared in conjunction with work accomplished under Contract No. DE-AC09-08SR22470 with the U.S. Department of Energy (DOE) Office of Environmental Management (EM).

Disclaimer:

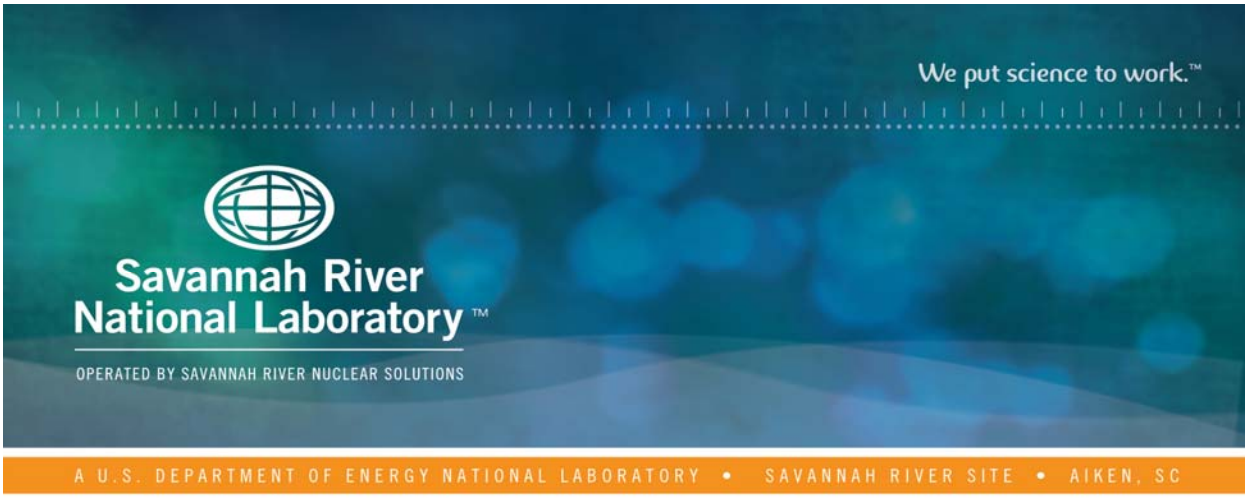

Defense Waste Processing Facility (DWPF) Liquidus Model: Revisions for Processing Higher TiO_2 Containing Glasses

C.M. Jantzen

T.B. Edwards

C.L. Trivelpiece

May 2017

SRNL-STI-2017-00016, Revision 0

DISCLAIMER

Printed in the United States of America

Prepared for
U.S. Department of Energy

Keywords: *DWPF, process control, glass, liquidus, Salt Waste Processing Facility, Monosodium Titanate*

Retention: *Permanent*

Defense Waste Processing Facility (DWPF) Liquidus Model: Revisions for Processing Higher TiO_2 Containing Glasses

C.M. Jantzen
T.B. Edwards
C.L. Trivelpiece

May 2017

Prepared for the U.S. Department of Energy under contract number DE-AC09-08SR22470.

Savannah River National Laboratory™
OPERATED BY SAVANNAH RIVER NUCLEAR SOLUTIONS

REVIEWS AND APPROVALS

AUTHORS:

C.M. Jantzen, Waste Form Processing Technologies Date

T.B. Edwards, Immobilization Technology Date

C.L. Trivelpiece, Immobilization Technology Date

TECHNICAL REVIEW:

D.L. McClane, Immobilization Technology Date

K.M. Fox, Waste Form Processing Technologies, Reviewed per E7 2.60 Date

APPROVAL:

S.D. Fink, Manager
Chemical Processing Technologies Date

D.E. Dooley, Director Date
Chemical Processing Technologies

E.J. Freed, Manager Date
Defense Waste Processing and Saltstone Facility Engineering

ACKNOWLEDGEMENTS

The research presented in this document was sponsored by the Savannah River Defense Waste Processing Facility (DWPF) in connection with work done under Contract No. DE-AC09-96SR18500 with the U.S. Department of Energy. The development of the 2001 liquidus model, the new data presented in this study, and the associated validation data were accumulated from 1988 to present under DOE Contracts No. DE-AC09-89SR18035 with E.I. DuPont deNemours & Co., Contract No. DE-AC09-96SR18500 with Westinghouse Savannah River Co. (WSRC) and Washington Group Inc. (WGI), and Contract No. DE-AC09-08SR22470 with Savannah River Nuclear Solutions (SRNS).

EXECUTIVE SUMMARY

Radioactive high level waste (HLW) at the Savannah River Site (SRS) has successfully been vitrified into borosilicate glass in the Defense Waste Processing Facility (DWPF) since 1996. Vitrification requires stringent product/process (P/P) constraints since the glass cannot be reworked once it is poured into ten foot tall by two foot diameter canisters. A unique "feed forward" statistical *process* control (SPC) was developed for this control rather than statistical *quality* control (SQC). In SPC, the feed composition to the DWPF melter is controlled *prior* to vitrification. In SQC, the glass product would be sampled *after* it is vitrified. Individual glass property-composition models form the basis for the "feed forward" SPC. The models transform constraints on the melt and glass properties into constraints on the feed composition going to the melter in order to guarantee, at the 95% confidence level, that the feed will be processable and that the durability of the resulting waste form will be acceptable to a geologic repository.

The DWPF SPC system is known as the Product Composition Control System (PCCS). One of the process models within the PCCS is the liquidus model, which was first developed in 1991 as a simple equilibrium between spinel and nepheline. The liquidus model was revised in 2001 to be more accurate. Additional documentation of the quasicrystalline basis for the 2001 model was provided in 2006. The 2001 model will be referred to as the "historic" PCCS liquidus model throughout this document.

The DWPF PCCS modeling approach for each property model is parsimonious in that the oxide terms in each model are only those that are necessary and sufficient to describe the glass property of interest. This approach excludes composition terms that are unnecessary to the implementation of the DWPF flowsheets and helps to minimize the sources of error in the PCCS models. These parsimonious models have successfully operated the DWPF vitrification process over the last 20 years. The DWPF "historic" 2001 liquidus model is based on quasicrystalline melt species interactions including glass bonding and octahedral site preference energies (OSPE).

The liquidus temperature (T_L) for a glass is the *maximum* temperature at which the molten glass and primary crystalline phase (e.g., spinel for DWPF) are at thermodynamic equilibrium. The constraint on liquidus temperature in the DWPF melter prevents melt pool crystallization, i.e., volume crystallization from nucleation sites, during routine operation. This type of crystallization can involve almost simultaneous nucleation of the entire melt pool volume. Furthermore, once formed in the DWPF melter, spinel crystals are refractory and cannot be re-melted due to the melter temperature limitations. When a significant amount of volume crystallization has occurred and the material has settled to the floor of the melter, the pour spout may become partially or completely blocked. In addition, the melt pool may no longer be able to sustain Joule heating, which would cause the melt pool to solidify. A liquidus limit for the DWPF was set at 1050°C (100°C lower than the nominal DWPF melt temperature), and the liquidus limit allows for no melt crystallization. The Measurement Acceptability Region (MAR) and Property Acceptability Region (PAR) get added to the 1050°C limit which further minimizes the tendency for volume crystallization. It is of note that the MAR and PAR of the current DWPF liquidus model and the new model are comparable but are compositionally dependent. Finally, minimizing the tendency for volume crystallization to form by being further from the liquidus temperature simultaneously minimizes subsequent devitrification of the glass once it is poured into a canister. Thus, prevention of volume crystallization is of primary concern for DWPF process control.

The DWPF will soon be receiving wastes from the Salt Waste Processing Facility (SWPF) containing increased concentrations of TiO_2, Na_2O, and Cs_2O. The SWPF is being built to pretreat the high-curie fraction of the salt waste to be removed from the HLW tanks in the F- and H-Area Tank Farms at the SRS. The SWPF contains unit operations that remove and concentrate the radioactive cesium (^{137}Cs), strontium (^{90}Sr), and actinides from the bulk salt solution feed. Separation processes to be used at SRS include

caustic side solvent extraction (CSSX) for ^{137}Cs removal and ion exchange/sorption of ^{90}Sr and alpha-emitting radionuclides with monosodium titanate (MST) which is $NaHTi_2O_5 2.8H_2O$. The predominant alpha-emitting radionuclides in the highly alkaline waste solutions include plutonium isotopes ^{238}Pu, ^{239}Pu and ^{240}Pu. The MST is the primary source of the TiO_2 and Na_2O enriched wastes, while the Cs_2O is derived from the CSSX stream that will be coming to the DWPF from the SWPF. Sodium also comes in from the neutralization of the nitric or oxalic acid washing of the filters and this is transferred along with the MST.

The SWPF process will replace the Actinide Removal Process (ARP)/Modular CSSX Unit (MCU) process currently in use. The ARP already sends MST and caustic to the DWPF for vitrification but the volume of the ARP product, including the associated MST component, is less than the volume anticipated with the SWPF actinide removal stream MST and caustic wastes. Currently, the DWPF is operating under a TiO_2 solubility constraint of 2 weight percent (wt%) in the final glass. At the 2.0 wt% solubility concentration, a TiO_2 term was not needed in the PCCS viscosity model and the existing TiO_2 terms in the PCCS durability and liquidus models had not been validated at TiO_2 concentrations greater than 2.0 wt%.

To process TiO_2 concentrations >2.0 wt% in the DWPF, new liquidus data were developed over the range of 1.90 to 5.85 wt% TiO_2 (measured compositions for glasses acceptable for modeling) and evaluated against the 2001 historic liquidus model. The compositions of the SWPF study glasses were designed to cover the anticipated concentrations of TiO_2, Na_2O, and Cs_2O based on the projected processing volumes of SWPF material. These glasses were also designed to cover any gaps in TiO_2 content above the 2.0 wt% solubility limit and the 6.0 wt% maximum TiO_2 anticipated during coupled (sludge + SWPF product) processing at DWPF. At the same time, the adequacy of the Na_2O and Cs_2O liquidus model terms were evaluated over the SWPF targeted range, i.e. 8 to 18 wt% Na_2O and 0.3 to 1.0 wt% Cs_2O since the historic DWPF liquidus model only covers 5.8-15.8 wt% Na_2O and 0-0.33 wt% Cs_2O.

As part of the PCCS durability model and Reduction of Constraints (ROC) TiO_2 assessment, a 4.0 wt% Al_2O_3 restriction had to be placed on the ROC for SWPF high TiO_2 containing glasses. The durability and ROC assessment, documented in a separate study, removed several glasses from liquidus modeling, which altered the ranges for TiO_2 in the glasses used for modeling to 1.9-5.85 wt%. Within measurement error, the 5.85 wt% TiO_2 limit can be rounded up to 6.0 wt% TiO_2, the projected upper limit for the SWPF study, so that the mechanistic TiO_2 liquidus model will adequately predict to 6.0 wt% although it was validated up to 6.52 wt% TiO_2. The analyzed high TiO_2 glasses were higher in Na_2O and Cs_2O than the targeted concentrations; giving a range of 8.03-18.14 wt% Na_2O and 0.48-1.62 wt% Cs_2O. It was determined that the TiO_2 term in the historic 2001 liquidus model, along with the Li_2O, Fe_2O_3, and Na_2O terms in the 2001 historic model, needed to be refit to adequately describe the impact of higher TiO_2 concentrations on liquidus. The higher Cs_2O content of the SWPF glasses had no impact on the liquidus model as there is no Cs_2O term in the model. This is due to the fact that the cesium cation does not participate in the pyroxene melt structure, which is the precursor to spinel crystallization, i.e. pyroxene melts incongruently to spinel. The new liquidus model will be called the SWPF liquidus model throughout this document.

This report documents the development of revised TiO_2, Na_2O, Li_2O and Fe_2O_3 coefficients in the SWPF liquidus model and revised coefficients (a, b, c, and d) from the model equation shown below. The form of the new model developed in this study to predict spinel liquidus temperature, T_L, from composition is defined as:

$$T_L(^\circ C) = \{a\ln(M_2) + b\ln(M_1) + c\ln(M_T) + d\}^{-1} - 273$$

where

$$\Sigma_{MT} \equiv \phi_{MT,SiO_2} z_{SiO_2} + \phi_{MT,Al_2O_3} z_{Al_2O_3} + \phi_{MT,Fe_2O_3} z_{Fe_2O_3}$$

$$\Sigma_{M1} \equiv \phi_{M1,Al_2O_3} z_{Al_2O_3} + \phi_{M1,Fe_2O_3} z_{Fe_2O_3} + \phi_{M1,TiO_2} z_{TiO_2} + \phi_{M1,Cr_2O_3} z_{Cr_2O_3} + \phi_{M1,ZrO_2} z_{ZrO_2} + \phi_{M1,NiO} z_{NiO} + \phi_{M1,MgO} z_{MgO} + \phi_{M1,MnO} z_{MnO}$$

$$\Sigma_{M2} \equiv \phi_{M2,NiO} z_{NiO} + \phi_{M2,MgO} z_{MgO} + \phi_{M2,MnO} z_{MnO} + \phi_{M2,CaO} z_{CaO} + \phi_{M2,K_2O} z_{K_2O} + \phi_{M2,Li_2O} z_{Li_2O} + \phi_{M2,Na_2O} z_{Na_2O}$$

$$\Sigma_{T1} \equiv \phi_{T1,SiO_2} z_{SiO_2} + \phi_{T1,Al_2O_3} z_{Al_2O_3} + \phi_{T1,Fe_2O_3} z_{Fe_2O_3} + \phi_{T1,TiO_2} z_{TiO_2}$$

$$\Sigma_{N1} \equiv \phi_{N1,K_2O} z_{K_2O} + \phi_{N1,Li_2O} z_{Li_2O} + \phi_{N1,Na_2O} z_{Na_2O}$$

and

$$M_2 \equiv \frac{\Sigma_{M2}}{\Sigma}, M_1 \equiv \frac{\Sigma_{M1}}{\Sigma}, M_T \equiv \frac{\Sigma_{MT}}{\Sigma}, \text{and } \Sigma \equiv \Sigma_{M2} + \Sigma_{M1} + \Sigma_{MT} + \Sigma_{T1} + \Sigma_{N1}.$$

Assuming that pyroxene-like melt phase complexes or precursors control crystallization in expected DWPF glasses, the new ϕ coefficients representing the distribution of the various species in the pyroxene-like precursors are provided in the body of the report. The least-squares results for the $(1/T_L)$ versus the above expression for 142 model data representing DWPF compositions were used to estimate the parameters in the above model; these were a = –0.000353617, b = –0.000691213, c = –0.000389016, and d = –0.002023544 for the model data. The summary statistics for the least-squares fit obtained were R^2 = 0.856 and the root mean square error (RMSE) $s_r = 2.417 \times 10^{-5} K^{-1}$. The results indicated no significant lack-of-fit. (The RMSE value may be re-expressed as 40.6°C.)

Two additional SRNL/PNNL (Savannah River National Laboratory/Pacific Northwest National Laboratory) liquidus studies were used as validation data and included glasses with TiO_2 concentrations up to 6.52 wt%. The SWPF liquidus model was also shown to be valid up to 4.286 wt% CaO (in the validation data) and 2.65 wt% MgO (in the historical and high TiO_2 data). This means that CaO and/or MgO can be added to frit compositions up to these concentrations since CaO is known to suppress nepheline crystallization and MgO is known to improve glass durability and reduce DWPF refractory corrosion and wear. While the SWPF liquidus model has been modeled up to of 5.85 wt% TiO_2 and validated up to 6.52 wt% TiO_2 with two glasses >5.85 wt%, the role of TiO_2 on viscosity switches from being a network modifier to being a network former somewhere between 6.62 and 8.38 wt% TiO_2. The exact region at which this switch occurs has not been investigated so the usage of the SWPF liquidus model and other models will be limited to ~6.0 wt% TiO_2, which has been the range investigated in all the SWPF modeling studies.

The ultimate limit on the amount of TiO_2 that can be accommodated from SWPF will be determined by the three PCCS models, the waste composition of a given sludge batch, the waste loading of the sludge batch, and the frit used for vitrification. Once a component like TiO_2 is present at larger concentrations than 2 wt%, the interactions of that component with other components in the melter feed must be considered simultaneously, i.e. an individual solubility limit cannot be defined to globally account for the interactions with all the remaining sludge/frit composition variables.

Only the ϕ parameters for TiO_2, Fe_2O_3, Li_2O, and Na_2O were refit along with the equation coefficients for M_2, M_1, M_T and the intercept. It is known that TiO_4 or TiO_5 melt species can compete with Al^{3+} for alkali bonding, and it is known that TiO_4 or TiO_5 melt species have a coupled impact with Fe^{3+} on their joint solubility in a melt or glass which is why the TiO_2, Fe_2O_3, Na_2O and Li_2O coefficients were refit in the liquidus model. The Al_2O_3 term was not refit as Al remains tetrahedrally coordinated as AlO_4 in both the melt and in the crystalline state.

TABLE OF CONTENTS

LIST OF TABLES xi
LIST OF EXHIBITS xii
LIST OF ABBREVIATIONS xiii
1.0 Introduction 1
1.1 Anticipated Changes to DWPF's Flowsheet 1
1.2 Liquidus Temperature 2
1.3 Current PCCS Liquidus Temperature-Composition Model 3
1.4 Crystal Chemical Basis for Current Liquidus Model 4
1.4.1 Definition of Liquidus, Medium Range Order and Quasicrystalline Theory 4
1.4.2 Identification of Quasicrystals in Nuclear Waste Glasses for Historic Liquidus Model 7
1.4.3 Identification and Analyses of Primary Liquidus Phases 9
1.4.4 Quasicrystalline Confirmation Experiments Performed for Historic Liquidus Model 13
1.5 Objectives of this Report 17
1.6 Quality Assurance 17
2.0 DWPF Process/Product (P/P) Modeling Constraints 18
2.1 Modeling Constraints Common to PCCS Models 18
2.2 Modeling Constraints Unique to the PCCS Liquidus Model 19
3.0 Experimental 20
3.1 Historic Liquidus Model 20
3.2 SWPF Liquidus Model Database 21
3.3 Liquidus Temperature Determinations 22
3.4 SWPF (TiO_2-only) Liquidus Validation Database 25
3.5 Quasicrystalline Glass Experiments 25
4.0 T_L Model Evaluation and Development 27
4.1 Evaluation of the 2001 Historic Model with the SWPF Data 27
4.2 Trials Re-fitting of the Parameters a, b, c, and d of the 2001 Historic Model 28
4.3 Trials Exploring the Use of Different Speciation Values 29
4.3.1 Quasicrystalline Rational for Re-speciation of TiO_2 Only 31
4.3.2 Trials Re-Speciating for TiO_2 Only 32
4.3.3 Quasicrystalline Rationale for Re-speciation of Al_2O_3, Fe_2O_3, Li_2O, Na_2O, and TiO_2 33
4.3.4 Trials Re-Speciating for Al_2O_3, Fe_2O_3, Li_2O, Na_2O, and TiO_2 36
4.3.5 Quasicrystalline Rationale for Re-speciation of Fe_2O_3, Li_2O, Na_2O, and TiO_2 Only 36

4.3.6 Final Model Re-speciating for Fe_2O_3, Li_2O, Na_2O, and TiO_2 38
5.0 T_L Model Recommendation and Evaluations 40
5.1 Model Evaluations Against 2001 Historic and SWPF Data Sets 40
5.2 Model Evaluations Against Validation Data 41
5.3 Recommended SWPF T_L Model 42
5.4 Evaluation of the Impact on PCCS 43
6.0 Conclusions 43
Appendix A. Supporting Tables and Exhibits 45
Appendix B. Property Acceptance Region (PAR) Determination 78
Appendix C. Measurement Acceptance Region (MAR) Determination 79
7.0 References 88

LIST OF TABLES

Table 1-1. Values of the ϕ Coefficients for Current T_L-Composition Model.* 4

Table 1-2. Proposed Cation Substitutions for Waste Glass Quasicrystalline Complexes..... 11

Table 1-3. Spinel Solid Solutions Formed in Limited Component Waste Glasses Melted at 1050°C and 1150°C. 14

Table 1-4. Quasi-Chemical Glass Composition Tests for Historic Liquidus Model (wt% as-batched). ... 15

Table 3-1. T_L Determinations and Primary Crystalline Phases..... 24

Table 3-2. Quasi-Chemical Glass Compositions for the SWPF Liquidus Model (wt% as-batched)..... 26

Table 4-1. Modified Values of the ϕ Coefficients for TiO_2 Only 32

Table 4-2. Spinel Solid Solutions Formed in Limited Component Waste Glasses Melted at 1050°C and 1150°C with 4 wt% TiO_2. 35

Table 4-3. Aggressively Modified Values of the ϕ Coefficients 36

Table 4-4. Modified Values of the ϕ Coefficients in Red with those for Al_2O_3 Fixed 39

LIST OF FIGURES

Figure 1-1. Perspective view of the structure of spinel. Large spheres (white) represent oxygen, small black spheres represent four-fold coordination positions ($^{[4]}$A) and cross-hatched spheres represent six-fold coordination positions ($^{[6]}$B).[] 7

Figure 2-1. Graphical Representation of the Constraints Applied to the Choice of Model and Validation Data for the Durability, Viscosity, and Liquidus P/P Models for glasses with 0-2.00 wt% TiO_2. The Al_2O_3 term in the inhomogeneous by visible crystallization is 2.99 wt% to accommodate the Waste Compliance Plan (WCP) Purex glass which contains 2.99 wt% Al_2O_3..... 19

Figure 2-2. Graphical Representation of the Constraints Applied to the Choice of Model and Validation Data for the Durability, Viscosity, and Liquidus P/P Models for glasses with 0-2.00 wt% TiO_2 and glasses with ≥ 2.00 wt% TiO_2. The Al_2O_3 term in the "inhomogeneous by visible crystallization" box is 2.99 wt% to accommodate the WCP Purex glass. 19

Figure 4-1. Large Region of Solid Solutions is Exhibited between FeO, Fe_2O_3, and TiO_2.[95] 32

LIST OF EXHIBITS

Exhibit 4-1. Measured T_L Values for Higher TiO_2 Glasses versus 2001 Historic Model Predictions..... 28

Exhibit 4-2. Re-fitting of the a, b, c, and d Parameters of the Current T_L Model 29

Exhibit 4-3. Modifying the TiO_2 Speciation Values and Re-fitting of the a, b, c, and d Parameters of the T_L Model..... 33

Exhibit 4-4. Aggressively Modifying Speciation Values and Re-fitting of the a, b, c, and d Parameters of the T_L Model. 38

Exhibit 4-5. Modifying Speciation Values with Those for Al_2O_3 Fixed and Re-fitting of the a, b, c, and d Parameters of the T_L Model. 40

Exhibit 5-1. Predictability of Model Data (2001 Historic and SWPF Data Sets). 41

Exhibit 5-2. Predictability of Validation Data. 42

LIST OF ABBREVIATIONS

AA	Atomic Absorption Spectroscopy
ADD	Analytic Development Directorate
ARP	Actinide Removal Process
ASTM	American Society for Testing and Materials
CELS	Corning Engineering Laboratory Services
CFSE	Crystal Field Stabilization Energy
CSSX	Caustic-Side Solvent Extraction
CUA	Catholic University of America
DCP	Direct Current Plasma Emission Spectrometry
DOE	Department of Energy
DWPF	Defense Waste Processing Facility
EA	Environmental Assessment
EDAX	Energy Dispersive Analysis by X-ray
EM	Environmental Management
EPAR	Expected Property Acceptable Region
HLW	High Level Waste
IC	Ion Chromatography
ICP-ES	Inductively Coupled Plasma-Emission Spectroscopy
L95	Lower 95% confidence interval
LHS	Left Hand Side
MAR	Measurement Acceptability Region
MCU	Modular CSSX Unit
MRO	Medium Range Order
MST	MonoSodium Titanate
NBO	Non-Bridging Oxygen
OSPE	Octahedral Site Preference Energy
P/P	Product/Process
PAR	Property Acceptability Region
PCCS	Product Composition Control System
PNNL	Pacific Northwest National Laboratory
PSAL	Process Science Analytic Laboratory
REDOX	REDuction/OXidation
RHS	Right Hand Side
ROC	Reduction of Constraints
RMSE	Root Mean Square Error
SEM	Scanning Electron Microscopy
SGM	Scale Glass Melter
SME	Slurry Mix Evaporator
SPC	Statistical Process Control
SQC	Statistical Quality Control
SRNL	Savannah River National Laboratory
SRNS	Savannah River Nuclear Solutions
SRO	Short Range Order
SRS	Savannah River Site
SWPF	Salt Waste Processing Facility
TEM	Transmission Electron Microscopy
THERMO™	Thermodynamic Hydration Energy Reaction MOdel
T_L	Liquidus Temperature
TTQAP	Task Technical and Quality Assurance Plan
TTR	Task Technical Request
TTT	Time-Temperature-Transformation
U95	Upper 95% confidence interval
VSL	Vitreous State Laboratory

wt%	Weight percent
WCP	Waste Compliance Plan
WGI	Washington Group Inc.
WSRC	Westinghouse Savannah River Co.
WVDP	West Valley Demonstration Project
XAFS	X-ray Absorption Fine Structure
XRD	X-ray Diffraction
XRF	X-ray Fluorescence

1.0 Introduction

Radioactive high level waste (HLW) has successfully been vitrified into borosilicate glass at the Defense Waste Processing Facility (DWPF) since 1996. The DWPF must measure melt/glass acceptability a priori to the melter, since no remediation of the glass composition to ensure durability and processability is possible except in the vessel (i.e., in the Slurry Mix Evaporator (SME) vessel) in which frit and waste are blended. Therefore, the acceptability decision is made on the upstream process (specifically, at the SME), rather than on the downstream melt or glass product. That is, it is based on "feed forward" statistical process control† (SPC) rather than statistical quality control (SQC).†† The DWPF SPC control system is known as the Product Composition Control System (PCCS). Individual property-composition models enable the monitoring and process control strategies embedded in the DWPF PCCS [1]. These models transform constraints on the melt and glass properties such as viscosity, liquidus, and durability into constraints on feed composition.

The DWPF property-composition models that are currently being used by PCCS have been under development and validation since the late 1980s. The property models that have been developed are mechanistic[t] in nature and depend on known relationships between glass structure/bonding (viscosity) [2,3], thermodynamics of melt structures and components (durability) [4, 5], and quasicrystalline melt species (liquidus) [6, 7, 8]. The process/product (P/P) models group terms with very similar effects so that each model only contains the terms that are necessary and sufficient (parsimonious) to model the P/P property of interest.

1.1 Anticipated Changes to DWPF's Flowsheet

The DWPF will soon be receiving waste enriched in TiO_2, Na_2O, and Cs_2O from the Salt Waste Processing Facility (SWPF). The SWPF has been built to pretreat the high-curie fraction of the salt waste to be removed from the HLW tanks in the F- and H-Area Tank Farms at the Savannah River Site (SRS). The SWPF contains unit operations that remove and concentrate the radioactive cesium (^{137}Cs), strontium (^{90}Sr), and actinides from the bulk salt solution. Separation processes planned at SWPF include caustic side solvent extraction (CSSX) for ^{137}Cs removal, and ion exchange/sorption of ^{90}Sr and alpha-emitting radionuclides with monosodium titanate (MST) which is $NaHTi_2O_5 \bullet 2.8H_2O$ also known as an MST strike. The predominant alpha-emitting radionuclides in the highly alkaline waste solutions include uranium and plutonium isotopes. The MST and filter washes are the source of the TiO_2 and Na_2O enriched wastes, while the Cs_2O is derived from the CSSX stream that will be coming to the DWPF from the SWPF.

The SWPF process will replace the Actinide Removal Process (ARP)/Modular CSSX Unit (MCU) process currently in use. The ARP already sends MST and associated filter wash solutions containing the actinides and Sr to the DWPF for vitrification, but the volume of the ARP product, including the associated MST component, is less than the volume anticipated with the SWPF wastes. While the current liquidus model includes a TiO_2 term, the DWPF has been operating under a TiO_2 solubility constraint of 2 wt% in the final glass [9]. However, when SWPF does become operational, it is likely that higher TiO_2 concentrations in the actinide removal stream will occur because of the higher activity of the salt to be processed in the SWPF.

---

† This controls the slurry feed to the melter *prior* to vitrification.

†† Which would adjudicate product release by sampling the glass *after* it's been made.

t Mechanistic models can be applied to composition regions outside of the regions for which they were developed. The DWPF mechanistic models allow more flexibility for process control than empirical models which are (1) restricted to the compositional region over which they were developed and (2) require glass formulations near the center of a pre-qualified glass composition region instead of in regions where waste loading can be maximized.

A glass study was conducted to provide an opportunity to investigate the performance of the current property-composition models over the glass region anticipated for the SWPF/DWPF coupled flowsheet [10]. A test matrix consisting of 50 glasses was developed [11]. These glasses were batched and fabricated, and measurements of the composition, viscosity, durability, and liquidus temperature of these glasses were conducted by the Vitreous State Laboratory (VSL) of The Catholic University of America (CUA) [12, 13, 14]. The purpose of this report is to investigate the liquidus temperature (T_L) measurements for these glasses, to evaluate the performance of the current T_L-composition model for these new data, and to add the new data to those already available to modify the current liquidus temperature model as necessary, so that it may be used once SWPF becomes operational.

1.2 Liquidus Temperature

T_L for a glass is the maximum temperature at which the molten glass and primary crystalline phase (e.g., spinel for DWPF) are at equilibrium. The constraint on liquidus temperature in the DWPF melter prevents melt pool crystallization, i.e., volume crystallization from nucleation sites, during routine operation. This type of crystallization can involve almost simultaneous crystallization of the entire melt pool volume. A liquidus limit for the DWPF was set at 1050°C (100°C lower than the nominal DWPF melt temperature) and the liquidus limit allows for no melt crystallization [15]. The Measurement Acceptability Region (MAR) and Property Acceptability Region (PAR) get added to the 1050°C limit which further minimizes the tendency for volume crystallization.

Moreover, once formed in the DWPF melter, spinel crystals are refractory and cannot easily be re-melted due to melter temperature limits. The presence of crystals may cause the melt viscosity and resistivity to increase [16, 17], which may cause difficulty in discharging glass from the melter as well as difficulty in melting via Joule heating. When a significant amount of volume crystallization has occurred and the material has settled to the floor of the melter, the pour spout may become partially or completely blocked. In addition, the melt pool may no longer be able to sustain Joule heating which would cause the melt pool to solidify [16, 17]. Finally, minimizing the tendency for volume crystallization to form by being further from the liquidus temperature. Thus, prevention of volume crystallization is an important concern for DWPF process control.

In fact, liquidus temperature concerns have historically been focused on volume rather than other types of crystallization because volume crystallization has the greatest potential impact on glass processing. The DWPF melt volume (2.5 m^3) is much larger than the volume of glass that can crystallize along the refractory walls and floor [18]. The melter walls normally crystallize 0.025-0.05 m (1-2") of spinel [19, 20].[ξ] Furthermore, spinel precursors such as $NaFe_2O_4$ rather than insoluble spinels such as $NiFe_2O_4$ (trevorite) have been found to form in the cold cap [16], and the melt appears to form a protective layer along the refractory walls, which minimizes spinel formation from the refractory surfaces [19, 20]. Therefore, the melt volume is the most likely location of a crystallization event that could lead to a melter failure.

The original DWPF liquidus model was developed on only 22 data points [21]. The liquidus model was revised between 1997 and 2001 [6] as additional data became available. A "spinel only" liquidus model was developed assuming that spinel was the solute and nepheline and the remaining glass constituents

[ξ] The melter refractory surfaces that induce crystallization can be approximated by a cylinder with a circular bottom but open at the top. The radius r of the floor is 0.9 m (see reference 18) so the area of the floor is $\pi(r^2)$ which is an area of 2.54 m^2. The cylindrical walls have a surface area of $2\pi(r)h$ where h is the height of the glass on the sidewall which is 0.86 m (see reference 18). So the area of the walls exposed to glass where crystallization can occur is 4.86 m^2. The combined surface area of the floor and cylindrical walls is 7.4 m^2. Using a depth of crystallization of 0.05 m (2") gives a volume of crystallization of 0.37 m^3 which is much smaller than if the entire DWPF melt pool crystallized simultaneously, i.e. 2.5 m^3.

were the solvent. Because spinel was the primary liquidus phase expected in most DWPF glasses (and for a given composition the predicted spinel liquidus temperature will be higher than that for the other phases), the modeling efforts in 2001 were concentrated on predicting a "spinel only" liquidus model for DWPF glasses. Modeling the tendency of DWPF glass to undergo volume crystallization was pursued using a mechanistic crystal chemical approach. That is, the derived model adheres as closely as possible to accepted fundamental laws governing the behavior of spinel crystallization.

1.3 Current PCCS Liquidus Temperature-Composition Model

The model developed in 2001 to predict spinel liquidus temperature, T_L, from composition was defined as [6]:

Equation 1

$$T_L(^oC) = \{a\ln(M_2) + b\ln(M_1) + c\ln(M_T) + d\}^{-1} - 273$$

where

$$\Sigma_{MT} \equiv \phi_{MT,SiO_2} z_{SiO_2} + \phi_{MT,Al_2O_3} z_{Al_2O_3} + \phi_{MT,Fe_2O_3} z_{Fe_2O_3}$$

$$\Sigma_{M1} \equiv \phi_{M1,Al_2O_3} z_{Al_2O_3} + \phi_{M1,Fe_2O_3} z_{Fe_2O_3} + \phi_{M1,TiO_2} z_{TiO_2} + \phi_{M1,Cr_2O_3} z_{Cr_2O_3} + \phi_{M1,ZrO_2} z_{ZrO_2} + \phi_{M1,NiO} z_{NiO} + \phi_{M1,MgO} z_{MgO} + \phi_{M1,MnO} z_{MnO}$$

$$\Sigma_{M2} \equiv \phi_{M2,NiO} z_{NiO} + \phi_{M2,MgO} z_{MgO} + \phi_{M2,MnO} z_{MnO} + \phi_{M2,CaO} z_{CaO} + \phi_{M2,K_2O} z_{K_2O} + \phi_{M2,Li_2O} z_{Li_2O} + \phi_{M2,Na_2O} z_{Na_2O}$$

$$\Sigma_{T1} \equiv \phi_{T1,SiO_2} z_{SiO_2} + \phi_{T1,Al_2O_3} z_{Al_2O_3} + \phi_{T1,Fe_2O_3} z_{Fe_2O_3} + \phi_{T1,TiO_2} z_{TiO_2}$$

$$\Sigma_{N1} \equiv \phi_{N1,K_2O} z_{K_2O} + \phi_{N1,Li_2O} z_{Li_2O} + \phi_{N1,Na_2O} z_{Na_2O}$$

$$M_2 \equiv \frac{\Sigma_{M2}}{\Sigma}, M_1 \equiv \frac{\Sigma_{M1}}{\Sigma}, M_T \equiv \frac{\Sigma_{MT}}{\Sigma}, \text{and } \Sigma \equiv \Sigma_{M2} + \Sigma_{M1} + \Sigma_{MT} + \Sigma_{T1} + \Sigma_{N1}, \text{ and}$$

$\phi_{i,j}$ is the fraction of the moles of j associated with the i^{th} site and z_j represents the total moles of oxide j per 100 grams of glass.

Because pyroxene melts incongruently to Fe_2O_3 (hematite) or spinel depending on the availability of Fe^{2+} or other divalent cations [22, 23, 24], it was assumed that pyroxene-like melt phase complexes or precursors control crystallization in expected DWPF glasses where acmite (aka aegerine; $NaFeSi_2O_6$) and augite ($(Ca,Na)(Mg,Fe,Al,Ti)(Si,Al)_2O_6$) are pyroxene solid solutions observed at sub-liquidus temperatures during time-temperature-transformation (TTT) investigations of DWPF glass. The 2001 liquidus ϕ coefficients representing the distribution of the various species in the pyroxene-like precursors are provided in Table 1-1. The least-squares results from fitting $1/T_L$ for the 105 model data available in 2001 were used to estimate the parameters in the above model; these were a = –0.000260, b = –0.000566, c = –0.000153, and d = –0.00144 for the model data [6]. The summary statistics for the least-squares fit obtained were $R^2 = 0.891$ and root mean square error (RMSE) = 2.28×10^{-5} K^{-1}. The results indicated no significant lack-of-fit. (The RMSE value may be re-expressed as 38.1°C.)

Table 1-1. Values of the ϕ Coefficients for Current T_L-Composition Model.*

	Pyroxene-like Precursors [6]			Nepheline-like Precursors [6]		
	M2	**M1**	**MT**	**N1**	**T1**	**SUM**
Al_2O_3	0	0.0607	0.9393	0	0	1.0000
B_2O_3	0	0	0	0	0	0.0000
CaO	0.029	0	0	0	0	0.0290
Cr_2O_3	0	0.9202	0	0	0	0.9202
Fe_2O_3	0	0.1079	0.0193	0	0.6094	0.7366
K_2O	0.3041	0	0	0.1049	0	0.4090
Li_2O	0.1745	0	0	0.1068	0	0.2813
MgO	0.0167	0.0223	0	0	0	0.0390
MnO	0.994	0.006	0	0	0	1.0000
Na_2O	0.1671	0	0	0.2518	0	0.4189
NiO	0	0.1079	0	0	0	0.1079
SiO_2	0	0	0.0193	0	0.0133	0.0326
TiO_2	0	0.0568	0	0	0.5667	0.6235
U_3O_8	0	0	0	0	0	0.0000
ZrO_2	0	0.0458	0	0	0	0.0458

*Where the M1, M2 and MT are crystallographic sites in pyroxene solutes and N1 and T1 are crystallographic sites in nepheline solutes. SUM=1-crystallographic site populations and represents the solvent, i.e. the glass.

1.4 Crystal Chemical Basis for Current Liquidus Model

1.4.1 *Definition of Liquidus, Medium Range Order and Quasicrystalline Theory*

Thermodynamically, liquidus boundaries represent boundaries between phases of contrasting degrees of polymerization in the melt and are, therefore, systematic functions of the type and amount of specific oxide components in the system, e.g. activity-composition relationships [25, 26, 27]. In 1981, Burnham pioneered the concept of pseudocrystalline structure of silicate melts [28], which is now commonly known as the quasicrystalline approach or model. The quasicrystalline model is based on the following three premises:

1. At near-liquidus temperatures, the melt phase contains structural units that resemble the structure and stoichiometry of the liquidus crystalline phase(s)

2. In a congruently melting compound, there is a correspondence between liquidus phase crystal structure and that of the melt on the liquidus: in incongruently melting compounds the melt contains units or species that mimic the phase(s) formed upon incongruent melting

3. Melts formed from multiphase mineral assemblages are presumed to contain the species or units that resemble those minerals that crystallize from these melts.

For example, the work of Ryerson [27] in 1985 demonstrated that for simple binary systems the activity coefficients of SiO_2 in silica-aluminate melts are a systematic function of the Z/r^2 of the charge-balancing metal cations. Ryerson [27] also demonstrated that simple relationships between the mole fraction of the SiO_2 in an MgO-SiO_2 melt plotted against the ratio of the mole fraction of various metal cations partially substituting for MgO, defined the liquidus boundaries between phases of contrasting degree of polymerization in the MgO-MO-SiO_2 systems being modeled.

Borosilicate waste glasses and melts, like natural silicate glasses and melts, possess short-range order (SRO; radius of influence ~1.6-3Å) around a central atom, e.g. polyhedra such as tetrahedral and octahedral structural units [29]. Glasses also possess medium range order (MRO) [29], which encompasses second- and third-neighbor environments around a central atom (radius of influence ~3-6 Å). The more highly ordered regions, referred to as clusters or quasicrystals, often have atomic arrangements that approach those of crystals [28, 29]. Thus, the PCCS liquidus model represents the glass-crystal equilibrium and links the macroscopic phases crystallizing at the liquidus to their MRO state in the melt. The historic liquidus model addressed the following: (1) how do the network modifying cations apportion between anionic structural groups such as $(SiO_4)^{-4}$, $(AlO_4)^{-5}$, $(FeO_4)^{-5}$, $(BO_4)^{-5}$and $(BO_3)^{-3}$, (2) what is the role of the melt polymerization expressed as Q^x distributions[f], and (3) what is the role of the octahedral site preference energies (OSPE) in crystalline phase formation. Because the pertinent thermodynamic data does not exist for these complex systems, a coupled quasicrystalline and mathematical approach is used to apportion cations with anionic groups and to model the liquidus (crystal-liquid) equilibrium based on these quasicrystalline species.

When the MRO in a glass or melt becomes enough like that of a crystalline phase, nucleation and crystal growth may occur given a sufficient energy drive such as undercooling.[29] Williams [30] was the first (1959) to suggest that the partitioning of a cation from melt to crystal, e.g. at the liquidus, usually involves an increase in the average coordination number or a decrease in the average atomic distance of a cation as given in

Equation 2 $$\text{melt}_{\text{cation}} \xrightarrow{\text{increased coordination or decreased M–O distance}} \text{crystalline}_{\text{cation}}$$

In particular, transition metal ions, which have large polarization energies, will gain energy on transfer from the liquid to the solid phase due to the shortening of the interatomic distances, e.g. by leaving sites of irregular coordination in the melt for regular octahedrally coordinated sites in a crystalline structure. This has been confirmed by recent experiments that cations occupy fewer octahedral sites in the melt than in the coexisting crystal [31]. This OSPE tendency can be calculated and/or measured for simple systems [32]. For example, measurements of glass and melt structures have demonstrated that the coordination of Ni is octahedral ($^{[6]}$Ni) in crystalline silicates, pentahedral ($^{[5]}$Ni) in silicate glasses, and tetrahedral ($^{[4]}$Ni) in silicate melts, e.g. the assumption that the structure of a glass is the same as that of its melt or the crystalline species from which it was derived is not always true [29]. Specifically, the simple concept of using bond lengths and bond strength from SRO parameters for crystalline species is not always appropriate to the domain for MRO or quasicrystals in glass because the bond lengths expand and the coordination of the cation changes as a function of temperature. This may be a short-coming of the recently developed SRO ion potential model for modeling liquidus temperature in waste glasses [33].

MRO in glasses and melts has been measured for many single component mineral melts and glasses, e.g. SiO_2 glass [29] and nepheline glass [34], as well as in complex natural silicate melts [29]. For example, the formation of nuclei (clusters or quasicrystals) of Ni-diopside, $(Ca,Mg,Ni)_2Si_4O_{12}$, were observed in situ near 1100K in a diopside composition glass containing 2 wt% Ni [29]. Thus, both structurally and thermodynamically, the liquidus represents a boundary between phases of contrasting degrees of polymerization in a melt [26].

Examples of MRO are repetitive arrangements of corner-linked polyhedra, such as silicate tetrahedra with four bridging oxygens attached to neighboring silica tetrahedra (Q^4 units), or six or eight membered rings or sheets of corner-linked silicate tetrahedra. Here, the polymerization notation from ^{29}Si NMR spectroscopy is used to designate the number of bridging oxygens for a given silica tetrahedra as a

[f] Definitions for 'Q^x ' terminology: '*x*' is the number of bridging oxygens around a silica or alumina tetrahedron in glass or crystals.

superscript. The polymerization or extent of MRO of a melt can thus be expressed by calculating [35] or measuring [36] a Q distribution, e.g. the number of Q^4, Q^3, Q^2, Q^1, and Q^0 species in the melt. For example, Smart and Glasser [36] measured Q^1 (SiO_4), Q^2 (Si_2O_7), Q^3 (Si_3O_9 cyclic trimers and Si_3O_{10} chains), Q^4 (Si_4O_{12} four membered rings and Si_6O_{18} six membered rings or clusters) species in PbO-SiO_2 glasses containing between 55-90 mol% PbO.

The number of Q^4 units in a melt, e.g. silica tetrahedra that have not reacted with a metal cation to form a non-bridging oxygen, can be correlated to the thermodynamic activity of SiO_2 in the melt [37]. The Q distribution in a glass has been shown to also influence freezing point depression of a glass, i.e. the liquidus, as well as crystallization rate and phase separation [37]. In particular, a bimodal Q distribution will promote phase separation while systems which have larger concentrations of Q^0 and Q^1 species (more modifier rich) will crystallize more rapidly than melts with oxides which produce primarily Q^3. Systems with lower temperature liquidus curves have been shown to have lower concentrations of low Q species and, hence, crystallize more slowly [37].

Studies have shown that the solution properties of cations in multicomponent silicate melts not only depend upon Q distribution or the Si:O ratio, but also on the identities and concentrations of the other cations in the melt, particularly the highly charged cations of high field strengths [38]. One approach has been to model the microstate of a melt as a homogeneous equilibrium between polyhedral complexes formed between silicate anionic groups and their network-modifying cations [38]. Thermodynamic data from glasses and melts have been used to establish a hierarchy of the relative stability of aluminum-bearing silicate clusters or quasicrystals in melts. The stability of the aluminate groups are $KAlO_2$ >$NaAlO_2$>$LiAlO_2$ > $Ca_{0.5}AlO_2$>$Fe_{0.5}AlO_2$>$Mg_{0.5}AlO_2$ [26]. Qualitatively, the behavior of tetrahedrally coordinated Fe^{3+} resembles that of Al^{3+} in that it requires electrical charge-balance with alkali metals, alkaline earths or ferrous iron [26]. The hierarchy for Fe^{3+} complexes suggested by Mysen [26] is similar to that of the aluminate complexes, e.g. $KFeO_2$ > $NaFeO_2$>$LiFeO_2$>$Ca_{0.5}FeO_2$ >$Fe_{0.5}AlO_2$ >$Mg_{0.5}FeO_2$. Since both Al^{3+} and Fe^{3+} in tetrahedral coordination need to be charge balanced, and the relative stability of the Al^{3+} and Fe^{3+} complexes is considered to be the same, the convention is to first assign cations to the ferric iron complexes [26].

Notation such as $^{[6]}$B and $^{[4]}$A will be used throughout this study to designate the coordination of the lattice sites. Octahedral ([6]) coordination defines a cation that has 6 nearest oxygen neighbors and the lattice site is octahedral in shape. Tetrahedral ([4]) coordination defines a cation that has 4 nearest oxygen neighbors that form a tetrahedral shaped lattice site.

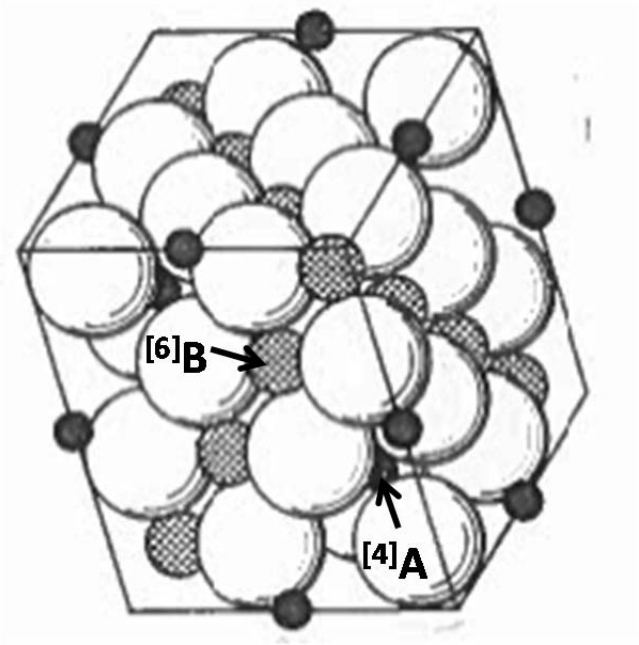

Figure 1-1. Perspective view of the structure of spinel. Large spheres (white) represent oxygen, small black spheres represent four-fold coordination positions ($^{[4]}$A) and cross-hatched spheres represent six-fold coordination positions ($^{[6]}$B).[39]

1.4.2 *Identification of Quasicrystals in Nuclear Waste Glasses for Historic Liquidus Model*

In 1990, Ellison and Navrotsky [40] studied the thermochemistry (enthalpies of solution) and structure of a DWPF average composition glass representative of the first radioactive waste glass to be processed in the DWPF (Blend 1). Based on studies in natural analog systems, the authors concluded that this waste glass should be composed of the following polymerized tetrahedral groups: ~5.2 mole% (K,Na,Li)AlO_2, ~5.8 mole% (K,Na,Li)FeO_2, ~15.3 mole% (K,Na,Li)BO_2, and ~55.4 mole% SiO_2. The approximately 10 mole% minor components such as NiO, FeO, MnO, MgO, CaO, TiO_2 and excess $(K,Na,Li)_2O$ over that needed to stabilize the B^{3+}, Al^{3+}, and Fe^{3+} tetrahedral units were ignored. The excess $(K,Na,Li)_2O$ in this waste glass suggests that network-modifier-rich polymerization dominates over silica-rich polymerization [40]. This is an important distinction relative to possible quasicrystalline reactions governing liquidus crystallization.

Ellison and Navrotsky [40] hypothesized that the hierarchy for polymerization for Na^+ tetrahedral groups in DWPF type glasses would be $NaBO_2$>$NaFeO_2$>$NaAlO_2$. The following was also noted regarding DWPF type glasses:

- some fraction of the tetrahedral $^{[4]}T^{3+}$ cations (Al^{3+}, Fe^{3+}, B^{3+}) must be charge-balanced by divalent cations, setting up an equilibrium represented by Equation 3

$$M^+TO_2 + M^+_{0.5} - O - Si \leftrightarrow M^+_{0.5}TO_2 + M^+ - O - Si$$

- divalent cations were predicted to compete more effectively with Al^{3+} for available oxygen than monovalent cations: this reduces the stability of potential $M^{+}_{0.5}TO_2$ complexes
- the hierarchy governing the formation of $M^{+}AlO_2$ and $M^{2+}_{0.5}TO_2$ complexes suggested was

$$CsAlO_2 = RbAlO_2 = KAlO_2 > NaAlO_2 > LiAlO_2 > Ba_{0.5}AlO_2 > Pb_{0.5}AlO_2 = Sr_{0.5}AlO_2 > Ca_{0.5}AlO_2 > Mg_{0.5}AlO_2$$

, and

- highly charged +4, +5, and +6 cations in the excess modifier waste glasses were hypothesized to allow oxide species such as TiO_2, ZrO_2, and SnO_2 to form local alkali-titanate, alkali-zirconate, or alkali-stannate polymerized groups with nearly stoichiometric compositions, e.g. Na_2TiO_3 or $CaTiO_3$.

Experimental evidence for the existence of alkali ferric iron clusters ($NaFeO_2$ and $LiFeO_2$ complexes) in nuclear waste glasses is supported by the x-ray identification of $NaFe_2O_4$ and $LiFe_2O_4$ spinel structured crystallites during the melter feed to glass conversion. The alkali ferric iron clusters have been observed in both pilot scale melter tests [16] and crucible tests [41]. These alkali ferric iron clusters appear to contain no Ni or Cr and are transient in the melt, later converting to $Ni(Fe,Cr)_2O_4$ spinels [16, 41, 42].

Experimental evidence for $(Na,K,Li)BO_2$ structural groups in the melt is supported by mass spectrometric analyses of $(Na,Li)BO_2$ vapors [43, 44] present above simulated waste glass melts at temperatures between 800-1150°C, e.g. $(Na,Li)BO_2$ in the melt must be in equilibrium with $(Na,Li)BO_2$ in the vapor [45].

The existence of $NaAlO_2$ clusters or quasicrystals has been studied in simulated nuclear waste glasses by Li et.al. [46, 47]. This Raman spectroscopy study of nuclear waste glasses prone to form nepheline as the primary liquidus phase demonstrated that these quenched glasses contained discrete clusters of $[NaAlSiO_4]$ units. Indeed, the 850 cm^{-1} vibration in the spectra, characteristic of the $[NaAlSiO_4]$ clusters was shown to correlate to the measured liquidus temperature of these glasses yielding a correlation with an R^2 value of 0.98. Li's findings were similar to the results [34] obtained by X-ray radial distribution function (RDF) analysis on pure nepheline glass and the results of molecular dynamics simulations of glasses in the $NaAlSiO_4$-SiO_2 system [48]. Pure nepheline glass was shown to have a stuffed tridymite-like structure (six-membered rings of silica tetrahedra) similar to that of crystalline nepheline. Li's conclusions about nepheline rich nuclear waste glasses are:

- increasing the concentration of Na_2O in a high Al_2O_3 containing waste glasses increases the concentration of $NaAlO_2$ nepheline forming groups
- increasing the SiO_2 content decreases the tendency of $[NaAlSiO_4]$ formation by diluting the number of available $NaAlO_2$ nepheline forming groups
- increasing the B_2O_3 content of the glass allows the Na_2O to preferentially bond to the B_2O_3 forming $NaBO_2$ groups decreasing the number of available $NaAlO_2$ nepheline forming groups, and
- the effect of increasing B_2O_3 was stronger than increasing SiO_2 on inhibiting the formation of nepheline forming groups.

Experimental evidence for transition metal-silicate structures is supported by the Raman spectroscopy and optical absorption spectroscopy of Nelson, Furukawa and White [49].

1.4.3 *Identification and Analyses of Primary Liquidus Phases*

Spinel is the primary liquidus phase in almost all of the waste glasses examined at SRS.[6, 7, 8, 50, 51, 52, 53] Occasionally nepheline forms at the liquidus along with spinel [51, 54] or alone. [47, 54] There is evidence that the primary liquidus phase spinel may persist metastably and/or nucleate nepheline crystallization, since the two phases are often found together as primary liquidus phases as discussed above. Furthermore, microscopy has shown that primary phase nepheline has inclusions of spinel [47]. The presence of TiO_2 in a glass is known to preferentially cause nucleation of spinel [55] and nepheline in glass [56]. The Ti in nepheline is primarily tetrahedral [57].

Clinopyroxenes of the acmite ($NaFe_2Si_2O_6$)-augite ($Ca,Na,Mg,Fe^{2+},Mn,Fe^{3+},Al,Ti)_2[(Si,Al)_2O_6]$)[‡] and hedenbergite ($CaFe^{2+}[Si_2O_6]$)-diopside ($CaMg[Si_2O_6]$)[f] type sometimes appear as liquidus phases [7,8], but this is rare as the clinopyroxenes melt incongruently to spinel. Therefore, clinopyroxenes are usually found as sub-liquidus phases as are lithium silicates.[6, 7, 8, 50, 51, 52] For Hanford type borosilicate glasses, which cover a wider composition range than the DWPF glasses, the clinopyroxene primary phases, hedenbergite ($CaFe^{2+}[Si_2O_6]$) and diopside ($CaMg[Si_2O_6]$), have been associated with the absence of transition metal species such as Ni^{2+} and higher concentrations of Mg^{2+} and Ca^{2+} [58, 59].

The spinel liquidus phase that crystallizes from HLW waste glass melts is nominally $NiFe_2O_4$, an inverse $^{[4]}B^{+3[6]}(A^{+2}B^{+3})O_4$ spinel structure [39], where all the divalent elements ($^{[6]}A=Mg^{2+}$, Zn^{2+}, Fe^{2+}, Ni^{2+}) are in octahedral coordination and half of the Fe^{3+} are in octahedral coordination at the $^{[6]}B$ site, while the remaining Fe^{3+} are tetrahedrally coordinated in the $^{[4]}B$ lattice site. In ferrite spinels, the divalent ion goes preferably into an octahedral site and they are all inverse spinels [39]. Thus magnetite and trevorite are inverse spinels. Small amounts of Cr^{3+} and Al^{3+} substitution, and occasionally substitution of Ti^{4+}or Ti^{3+} [60], can occur in these inverse spinels. However, the remaining aluminate and chromite spinels as well as $MnFe_2O_4$ spinels have a normal[ff] spinel structure in which all of the +3 species prefer the octahedral sites and the Mn^{2+} occupies the $^{[4]}A$ lattice site. This structure results because the excess octahedral site preference energy (OSPE), which is a measure of the preference of any ion for the octahedral (6 coordinated) site or the difference between the octahedral and tetrahedral crystal field stabilization energy (CFSE)[fff], diminishes in the following order for spinels [39]:

$$Cr^{3+} > Ni^{2+} > Ti^{3+} > Fe^{2+} > Fe^{3+} > Mn^{2+}$$

which means that Cr has a highest preference energy for an octahedral site.

The ordering of diminishing OSPE in kcal was experimentally determined for a wide variety of spinels by Navrotsky and Kleppa [61] and shown to be:

$$Cr^{3+} > Mn^{3+} > Ni^{2+} > Al^{3+} > Cu^{2+} > Fe^{2+} > Mg^{2+} > Co^{2+} > Ga^{3+} > Fe^{3+} > Mn^{2+} > Zn^{2+}$$

‡ a solid solution series exists between the Na (acmite) and Ca (augite) rich end members of this clinopyroxene series.

f a solid solution series exists between the Fe^{2+} (hedenbergite) and Mg (diopside) rich end members of this clinopyroxene series

ff Normal spinels have $^{[4]}A^{+2[6]}B^{+3}{}_2O_4$

fff the OSPE = $CFSE_{(oct)}$-$CFSE_{(tet)}$

Conversely, the elements from Mg^{2+} to Zn^{2+} show an increasing tendency for tetrahedral site preference in the order Zn^{2+}> Mn^{2+}> Fe^{3+}> Ga^{3+}>Co^{2+}>Mg^{2+}.

Indeed, Reynolds has been able to correlate the OSPE of various spinel forming oxides in empirical liquidus models to the OSPE of that cation in the spinel structure [62].

The spinels observed in high iron containing waste glasses [50] were analyzed by electron microprobe and found to be 85-95 mol% $NiFe_2O_4$ as tabulated in References 7 and 8. Subsequent studies confirmed that the spinel composition was predominately $NiFe_2O_4$ spinel containing only 3 mol% Mn and 0.9 mol% Mg, ~25 mol% Cr^{3+}, 2 mol% Al , and 2 mol% Si [7, 8]. For borosilicate waste glass compositions relevant to the disposal of Hanford wastes [53], the primary phase was also a $NiFe_2O_4$ type spinel but the Ni was determined to vary between 53-74 mol%, Mn between 5-7 mol%, Fe^{2+} between 0.21-0.42 mol%, Fe^{3+} between 31-91 mol%, and Cr between 9-69 mol% depending on the SiO_2 content of the glass matrix.

Since clinopyroxenes (disilicates) melt incongruently to spinel, the crystal chemistry of the incongruently melting minerals must be understood in order to understand liquidus melt-crystal equilibrium per Burnham's [28] second premise given above. Clinopyroxenes have the general formula $M_2M_1[T_2O_6]$, where the distorted 6 to 8 coordinated $^{[6-8]}M_2$ sites can be occupied by Ni, Mg, Mn, Ca, K, Li, or Na, while the regular 6 coordinated $^{[6]}M_1$ sites can be occupied by Mn, Mg, Ni, Zr, Cr, Ti, Fe or Al, and the tetrahedral $^{[4]}$T sites by Si, Al or Fe^{3+} [63]. The $^{[6-8]}M_2$ sites can accommodate larger cations, such as Na and Ca, versus the $^{[6]}M_1$ sites. Acmite, nominally $NaFeSi_2O_6$, is frequently found in DWPF glasses but it is not a primary liquidus phase. The acmite typically takes on one of two melt structures, appearing to grow from nickel iron spinel or from RuO_2 insoluble phases during cooling [50]. An analysis of the Ni rich acmite typically found in DWPF type waste glasses contained ~1 wt% NiO [7, 8]. Excess B_2O_3 in waste glasses (>12 wt%) was found to suppress the formation of clinopyroxene crystals [58], ratios of (Na+K)/Al > 1 were found to stabilize acmite over augite, and the presence of TiO_2 was found to stabilize augite over acmite [64].

It should be noted that no radioactive species have been observed as primary liquidus phases in over 400 waste glasses studied [7, 8]. Spinel appears as the primary liquidus phase in West Valley Demonstration Project (WVDP) glasses even though these glasses contain approximately 3.6 wt% ThO_2. Solid solutions of ThO_2-CeO_2 crystallize ~150ºC below the liquidus temperature [65]. There is microscopy and electron microprobe evidence that the ThO_2 and ThO_2-CeO_2 solid solutions nucleate on the spinel primary phase [65, 66]. Cerium oxide as CeO_2 was found to precipitate from certain waste glasses when present in excess of 3 wt% [67]. There is no experimental evidence that UO_2 or any other uranium containing phase forms as a primary liquidus phase[†] in glasses containing up to 4.2 wt% UO_2 [68].

Thus Table 1-2 of cation substitutions in quasicrystalline complexes was used to define the appropriate molar concentrations to allow liquidus temperature to be predicted from the melt composition.[6, 7, 8] Table 1-2 indicates that various cations (e.g., Fe^{3+}, Al^{3+}, Mg^{2+}, etc.) may occupy multiple sites in pyroxene and it is assumed that the same substitutions can occur in the quasicrystalline melt phase precursor. However, the definition of a reasonable composition basis for liquidus temperature prediction is complicated by the fact that many of these same cations are present in the substituted nepheline precursor or disilicate melt phase complex. It is further assumed that this will be the case in the hypothesized melt phase complexes or precursors representing (substituted) nepheline and general disilicate. This is not to say that the melt phase complexes or precursors have exactly the same structure as their corresponding crystalline analogs (as they likely will not) nor that the cations in the melt phase precursors have the same coordination numbers as in the corresponding crystalline structures; this is merely one way to represent the complicated melt phase complexes. Further, it is assumed that if a cation

[†] UO_2 has been observed as a crystallization product that forms at annealing times of >40 hours at temperatures ≤700°C.

is associated with a site in one quasicrystalline melt phase complex, it will not be available to another complex or precursor. However, this does not mean that there is not some degree of interchange of cations as crystalline material begins to form at the liquidus temperature (i.e., the system establishes a new equilibrium at the given temperature). The resulting assumed cation distribution information is provided in Table 1-2.

Table 1-2. Proposed Cation Substitutions for Waste Glass Quasicrystalline Complexes

Pyroxene-like Precursor [6,7,8]*			**Nepheline-like Precursor** [6,7,8]		**Metasilicate or Disilicate Precursor** [6,7,8]	
MT [4] CN^{f}	**M1 [6] CN**	**M2 [6-8] CN**	**T1 [4] CN**	**N1 [8-9] CN**	**T2 [4] CN**	**N2 [6-8] CN**
Si^{4+}			Si^{4+}		Si^{4+}	
Al^{3+}	Al^{3+}		Al^{3+}			Al^{3+}
Fe^{3+}	Fe^{3+}		Fe^{3+}			Fe^{3+}
	Ti^{4+}		Ti^{4+}			Ti^{4+}
	Cr^{3+}					Cr^{3+}
	Zr^{4+}					Zr^{4+}
	Ni^{2+}	Ni^{2+}				Ni^{2+}
	Mg^{2+}	Mg^{2+}				Mg^{2+}
	Mn^{2+}	Mn^{2+}				Mn^{2+}
		Ca^{2+}				Ca^{2+}
		K^{+}		K^{+}		K^{+}
		Li^{+}		Li^{+}		Li^{+}
		Na^{+}		Na^{+}		

* Zn^{2+} is not included because it is not found in significant concentrations in waste glasses. Fe^{2+} was removed as its impact on liquidus temperature (T_L) is normally indistinguishable since T_L measurements are performed in air.

f CN is coordination number of the lattice site

The availability of cations to the various melt phase complexes or precursors can be accounted for by defining the following molar site distributions based on the information in Table 1-2:

Pyroxene-like Complex or Precursor:†

$$\Sigma_{MT} \equiv \phi_{MT,SiO_2} z_{SiO_2} + \phi_{MT,Al_2O_3} z_{Al_2O_3} + \phi_{MT,Fe_2O_3} z_{Fe_2O_3}$$

$$\Sigma_{M1} \equiv \phi_{M1,Al_2O_3} z_{Al_2O_3} + \phi_{M1,Fe_2O_3} z_{Fe_2O_3} + \phi_{M1,TiO_2} z_{TiO_2} + \phi_{M1,Cr_2O_3} z_{Cr_2O_3} + \phi_{M1,ZrO_2} z_{ZrO_2} + \phi_{M1,NiO} z_{NiO} + \phi_{M1,MgO} z_{MgO} + \phi_{M1,MnO} z_{MnO}$$

$$\Sigma_{M2} \equiv \phi_{M2,NiO} z_{NiO} + \phi_{M2,MgO} z_{MgO} + \phi_{M2,MnO} z_{MnO} + \phi_{M2,CaO} z_{CaO} + \phi_{M2,K_2O} z_{K_2O} + \phi_{M2,Li_2O} z_{Li_2O} + \phi_{M2,Na_2O} z_{Na_2O}$$

Nepheline-like Complex or Precursor:

$$\Sigma_{T1} \equiv \phi_{T1,SiO_2} z_{SiO_2} + \phi_{T1,Al_2O_3} z_{Al_2O_3} + \phi_{T1,Fe_2O_3} z_{Fe_2O_3} + \phi_{T1,TiO_2} z_{TiO_2}$$

$$\Sigma_{N1} \equiv \phi_{N1,K_2O} z_{K_2O} + \phi_{N1,Li_2O} z_{Li_2O} + \phi_{N1,Na_2O} z_{Na_2O}$$

† A term representing the ZnO concentration must be added to ΣM_2 when the liquidus temperatures of glasses containing significant concentrations of this oxide are to be predicted.

where $\phi_{i,j}$ is the fraction of the moles of j associated with the i^{th} site and z_j represents the total moles of j per 100 grams of glass. The manner in which the fractions are defined is discussed in the paragraphs below.

Thus the appropriate mole fractions that represent the liquid phase activities for the components comprising the proposed melt phase complexes or precursors are [7,8]:

$$M_2 = \left[(M2)_2O_{(l)}\right] \equiv \frac{\Sigma_{M2}}{\Sigma},\quad M_1 = \left[(M1)_2O_{3(l)}\right] \equiv \frac{\Sigma_{M1}}{\Sigma}, \text{ and } \quad M_T = \left[(MT)O_{2(l)}\right] \equiv \frac{\Sigma_{MT}}{\Sigma}$$

where

$$\Sigma \equiv \Sigma_{M2} + \Sigma_{M1} + \Sigma_{MT} + \Sigma_{T1} + \Sigma_{N1}$$

because only the pyroxene-nepheline pseudobinary is of concern. The pyroxene melt phase precursor liquid phase activity can then be approximated by:

Equation 4
$$a\left(P_{(l)}\right) \approx K_P\left(M_2\right)^a\left(M_1\right)^b\left(M_T\right)^c$$

where K_p is the constant of proportionality and is represented by the equilibrium constant.

And the equation that relates the activity of a species in the liquid (or melt) phase and the reciprocal of the liquidus temperature (see footnote t), then, upon substitution, becomes:

Equation 5
$$-R\ln\left\{K_P\left(M_2\right)^a\left(M_1\right)^b\left(M_T\right)^c\right\} \approx \Delta\overline{H}_{fus,P}\left(T_P^*\right)\left(\frac{1}{T_L} - \frac{1}{T_P^*}\right).$$

Where T_L is the liquidus temperature (°K), T_P is the temperature of the related MRO species in the melt (°K), and $\Delta\overline{H}_{fus,P}$ is the enthalpy of fusion at standard pressure.

Equation 5 provides a relationship between melt concentrations and the liquidus temperature, T_L. Rearranging the above relationship provides a way to estimate the (reciprocal) liquidus temperature as a function of the molar melt constituent concentrations:

Equation 6
$$\left(\frac{1}{T_L}\right) \approx -\frac{R}{\Delta\overline{H}_{fus,P}\left(T_P^*\right)}\ln\left\{M_2{}^aM_1{}^bM_T{}^c\right\} + \left\{\left(\frac{1}{T_P^*}\right) - \frac{R\ln\left(K_P\right)}{\Delta\overline{H}_{fus,P}\left(T_P^*\right)}\right\}.$$

Equation 6 provides a parsimonious basis for predicting liquidus temperature for waste glasses assuming the presence of a pyroxene intermediate that then melts incongruently to spinel. Thus to a priori predict

---

t $-R\ln\left\{a\left(P_{(l)}\right)\right\} \approx \Delta\overline{H}_{fus,P}\left(T_P^*\right)\left(\frac{1}{T_L} - \frac{1}{T_P^*}\right)$ see references 6,7,8 for additional detail of the freezing point depression equation

the liquidus temperatures for a given set of DWPF compositions, the enthalpy of fusion, melt temperature, distribution of cations among melt phase complexes or precursors, and equilibrium constant and stoichiometry of the pertinent equilibrium reaction must be known. In the case of waste glasses, such information is not available; therefore, this information is estimated from fitting available data.

1.4.4 *Quasicrystalline Confirmation Experiments Performed for Historic Liquidus Model*

In order to understand the role of the OSPE and the relative stability of spinel forming quasicrystals $Y_{0.5}AlO_2$, $Y_{0.5}CrO_2$, and $Y_{0.5}FeO_2$ (Y= Ni^{2+}, Fe^{2+}, Mn^{2+} and Mg^{2+}) versus the stability of the Y, Al, Cr, and Fe^{3+} cations in crystalline spinels being formed, the divalent cation effects were studied one at a time in the presence and absence of the tetrahedral Al, Cr, and Fe^{3+} species (see Table 1-3 and Table 1-4). Since alkali (X =K, Na, Li) is always present in waste glasses from either the waste or the glass forming additives, these one at a time interactions were used to qualitatively determine the relative stability of the $Y_{0.5}AlO_2$, $Y_{0.5}CrO_2$, and $Y_{0.5}FeO_2$ in the melt, the $XAlO_2$, $XCrO_2$, and $XFeO_2$ in the melt, and the role of the Y and Al, Cr, and Fe^{3+} cations in the crystalline spinels with which the melt was in equilibrium at typical melt temperatures of ~1150ºC.

In the absence of Al^{3+} and Cr^{3+} in the melt, the spinels that form at melt temperatures between 1050-1150ºC, are $MgFe_2O_4$, $NiFe_2O_4$ and $FeFe_2O_4$ (Table 1-3). While $NiFe_2O_4$ and $FeFe_2O_4$ also form in the combined presence of Fe^{3+} and Al^{3+} in the melt, $MgFe_2O_4$ does not. Likewise, $MgCr_2O_4$ does not form in the combined presence of Cr^{3+} and Al^{3+} in the melt. This indicates that crystalline $MgFe_2O_4$ can only form in the absence of aluminate ($Mg_{0.5}AlO_2$ or $XAlO_2$) or chromate ($Mg_{0.5}CrO_2$ or $XCrO_2$) quasicrystals in the melt. This also indicates that magnesium or alkali $^{[4]}Fe^{3+}$ quasicrystals ($Mg_{0.5}FeO_2$ or $XFeO_2$) are more stable in the melt than $^{[6]}Mg^{2+}$, $^{[6]}Fe^{3+}$, or $^{[4]}Fe^{3+}$ in crystalline spinel when Al^{3+} and/or Cr^{3+} is present. This is confirmed by the lack of crystallization of $MgFe_2O_4$ or $MgCr_2O_4$ in the melts in which both Fe^{3+} and Al^{3+} are present or Cr^{3+} and Al^{3+} are present. In summary, $Mg_{0.5}AlO_2$(melt) is more stable in the melt than $Mg_{0.5}FeO_2$ (melt) which in turn is more stable than crystalline $MgFe_2O_4$ or mixed $Mg(Fe,Al)_2O_4$.

$NiFe_2O_4$ and $FeFe_2O_4$ spinels crystallize at melt temperatures of 1050-1150ºC in the presence or absence of Al^{3+} in the melt indicating that the high OSPE of $^{[6]}Ni^{2+}$ and $^{[6]}Fe^{3+}$ in crystalline $NiFe_2O_4$ dominates whether the melt is depleted in $^{[4]}Al^{3+}$ species such as $XAlO_2$ or not. In comparison, no chromate spinels form in a chromate rich melt when Al^{3+} was absent. This indicates that $^{[4]}Cr^{3+}$ quasicrystals (such as $XCrO_2$) are more stable in the melt than $^{[6]}Cr^{3+}$ in the crystalline species. It also indicates that despite the high OSPE of $^{[6]}Ni^{2+}$ and $^{[6]}Cr^{3+}$, $NiCr_2O_4$ spinel will not crystallize (maximize the polarization energy of Ni^{2+}) when the melt is depleted in tetrahedral $^{[4]}Al^{3+}$so Ni remains tetrahedral as $^{[4]}Ni^{2+}$ in the melt.

The crystallization of the trevorite ($NiFe_2O_4$) and magnetite ($FeFe_2O_4$) also indicates that the $^{[6]}Ni^{2+}$ $^{[6]}Fe^{3+}$ and $^{[6]}Fe^{2+}$ $^{[6]}Fe^{3+}$ of the crystalline spinels are more stable than $^{[4]}Fe^{3+}$ quasicrystals in the melt, e.g. $(K,Na,Li)FeO_2$. The absence of the formation of $MgFe_2O_4$ and $MnFe_2O_4$ in the presence of both Fe^{3+} and Al^{3+} in the melt indicates that the $Mg_{0.5}AlO_2$ and $Mn_{0.5}AlO_2$ or $XAlO_2$ and $XFeO_2$ quasicrystals in the melt are more stable than the corresponding ferrite crystalline spinels.

When Cr^{3+} and Al^{3+} are together in a melt, the normal situation in waste glasses, both $NiCr_2O_4$ and $MnCr_2O_4$ readily crystallize. This demonstrates that the Ni^{2+} and Cr^{3+} OSPE energy term dominates when sufficient $^{[4]}Al^{3+}$ is present in the melt. The crystallization of the chromate spinels also indicates that the $^{[6]}Ni^{2+}$ $^{[6]}Cr^{3+}$ and $^{[6]}Mn^{2+}$ $^{[6]}Cr^{3+}$ of the crystalline species are more stable than $^{[4]}Cr$ quasicrystals in the melt. The absence of the formation of $MgCr_2O_4$ and $FeCr_2O_4$ in the presence of both Cr^{3+} and Al^{3+} in the melt indicates that the $Mg_{0.5}AlO_2$ and $Fe_{0.5}AlO_2$ quasicrystals in the melt are more stable than the corresponding chromate crystalline spinels. Lastly, the lack of any spinel formation in Al^{3+} only melts is an indication that all of the $^{[4]}Al$ quasicrystals in the melt, e.g. $Fe_{0.5}AlO_2$, $Mg_{0.5}AlO_2$, $Mn_{0.5}AlO_2$, $Ni_{0.5}AlO_2$ and/or $XAlO_2$, are more stable than the corresponding $^{[6]}Al$ positions in crystalline aluminate spinels.

Table 1-3. **Spinel Solid Solutions Formed in Limited Component Waste Glasses Melted at 1050°C and 1150°C.**

Only Divalent Cation Present	Fe^{3+}	Fe^{3+} and Al^{3+}	Cr^{3+}	Cr^{3+} and Al^{3+}	Al^{3+}
Melt Temperature of 1150°C					
Ni^{2+}	Amorphous	$NiFe_2O_4$	Cr_2O_3 +SiO_2	$NiCr_2O_4$ + Cr_2O_3	Amorphous
Fe^{2+}	Amorphous	Fe_3O_4*	(Oxidized and reduced) Cr_2O_3 +SiO_2 Crist§	(Oxidized and reduced) Cr_2O_3§	Amorphous§§
Mn^{2+}	Amorphous	Fe_2O_3 + $SiO_{2\ (Qtz.)}$	Cr_2O_3	$MnCr_2O_4$ + Cr_2O_3	Amorphous
Mg^{2+}	$MgFe_2O_4$-Fe_3O_4 Solid solution (poorly crystallized)	Fe_2O_3	Cr_2O_3 + SiO_2 Crist.	Cr_2O_3	Amorphous
Melt Temperature of 1050°C					
Ni^{2+}	$NiFe_2O_4$	$NiFe_2O4$	Cr_2O_3 +SiO_2 (Tridy+Crist+Qtz) $LiCr(SiO_3)_2$	Cr_2O_3	SiO_2
Fe^{2+}	Fe_3O_4**	Fe_3O_4*	(oxidized) Cr_2O_3 +$LiCr(SiO_3)_2$ +SiO_2 Crist (reduced) Cr_2O_3 +$LiCr(SiO_3)_2$ +SiO_2 (Crist)§	(oxidized) Cr_2O_3 +$LiCr(SiO_3)_2$ (reduced)Cr_2O_3§	SiO_2§§
Mn^{2+}	Amorphous	Did not melt	Cr_2O_3	$Mn_{1.5}Cr_{1.5}O_4$ + Cr_2O_3	SiO_2
Mg^{2+}	Amorphous	Fe_2O_3	Cr_2O_3	Cr_2O_3	SiO_2

* forms at $Fe^{2+}/\Sigma Fe$ of 0.1-0.18; otherwise forms Fe_2O_3 at $Fe^{2+}/\Sigma Fe$ of 0.02-0.04

** forms at $Fe^{2+}/\Sigma Fe$ of 0.1-0.18; otherwise forms Fe_2O_3 at $Fe^{2+}/\Sigma Fe$ of 0.02-0.04

§ Since only 2.06-2.22 wt% FeO was theoretically present in these glasses and no Fe_2O_3, the REDOX (REDuction/OXidation) measurement is difficult to perform due to excess matrix effects; the REDOX values designated as reduced were $Fe^{2+}/\Sigma Fe$ = 0.02-0.07 so not all of the Fe^{2+} may have been in the reduced state while those designated as oxidized were $Fe^{2+}/\Sigma Fe$ = 0-0.05.

§§ Since only 2.58 wt% FeO was theoretically present in these glasses and no Fe_2O_3, the REDOX measurement is difficult to perform due to excess matrix effects; the $Fe^{2+}/\Sigma Fe$ = 0-0.03 so not all the Fe_2O_3 may have been reduced

Table 1-4. Quasi-Chemical Glass Composition Tests for Historic Liquidus Model (wt% as-batched).

Oxide Wt%	NiFe with Al	NiFe w/o Al	MnFe with Al	MnFe w/o Al	MgFe with Al	MgFe w/o Al	FeFe with Al	FeFe w/o Al	NiCr with Al	NiCr w/o Al	MnCr with Al	MnCr w/o Al	MgCr with Al	MgCr w/o Al	FeCr with Al	FeCr w/o Al	NiAl w/o Fe/Cr	MnAl w/o Fe/Cr	MgAl w/o Fe/Cr	FeAl w/o Fe/Cr
Al_2O_3	7.37	0.00	7.17	0.00	7.12	0.00	7.52	0.00	7.37	0.00	7.17	0.00	7.12	0.00	7.34	0.00	9.21	8.90	8.83	9.17
B_2O_3	7.59	8.20	7.39	7.96	7.34	7.90	7.74	8.37	7.59	8.20	7.39	7.96	7.34	7.90	7.57	8.16	9.48	9.18	9.10	9.44
Cr_2O_3	0.00	0.00	0.00	0.00	0.00	0.00	0.00	0.00	19.97	21.55	19.44	20.95	19.31	20.79	19.90	21.48	0.00	0.00	0.00	0.00
Fe_2O_3	19.97	21.55	19.44	20.95	19.31	20.79	18.02	19.49	0.00	0.00	0.00	0.00	0.00	0.00	0.00	0.00	0.00	0.00	0.00	0.00
FeO	0.00	0.00	0.00	0.00	0.00	0.00	2.11	2.28	0.00	0.00	0.00	0.00	0.00	0.00	2.06	2.22	0.00	0.00	0.00	2.58
K_2O	3.26	3.52	3.18	3.42	3.15	3.39	3.33	3.60	3.26	3.52	3.18	3.42	3.15	3.39	3.25	3.51	4.08	3.95	3.91	4.06
Li_2O	4.51	4.87	4.39	4.73	4.36	4.69	4.60	4.97	4.51	4.87	4.39	4.73	4.36	4.69	4.49	4.85	5.64	5.45	5.40	5.61
MgO	0.00	0.00	0.00	0.00	4.98	5.36	0.00	0.00	0.00	0.00	0.00	0.00	4.98	5.36	0.00	0.00	0.00	0.00	6.17	0.00
MnO	0.00	0.00	4.31	4.65	0.00	0.00	0.00	0.00	0.00	0.00	4.31	4.65	0.00	0.00	0.00	0.00	0.00	5.35	0.00	0.00
Na_2O	5.98	6.45	5.82	6.27	5.78	6.22	6.10	6.59	5.98	6.45	5.82	6.27	5.78	6.22	5.96	6.43	7.47	7.23	7.17	7.44
NiO	1.73	1.87	0.00	0.00	0.00	0.00	0.00	0.00	1.73	1.87	0.00	0.00	0.00	0.00	0.00	0.00	2.16	0.00	0.00	0.00
SiO_2	49.60	53.54	48.29	52.02	47.95	51.63	50.58	54.69	49.60	53.54	48.29	52.02	47.95	51.63	49.42	53.34	61.96	59.94	59.42	61.70
SUM	100.00	100.00	100.00	100.00	100.00	100.00	100.00	100.00	100.00	100.00	100.00	100.00	100.00	100.00	100.00	100.00	100.00	100.00	100.00	100.00

Divalent manganese does not crystallize in the 1050-1150ºC melt temperature range regardless of the presence or absence of Fe^{3+} and Al^{3+}. Divalent manganese only crystallizes as $MnCr_2O_4$ spinel in the presence of Al^{3+} and Cr^{3+}. The data in Table 1-3 and Table 1-4 demonstrates that the spinels analyzed in nuclear waste glasses are solid solutions of $NiFe_2O_4$, $NiCr_2O_4$, and $MnCr_2O_4$.

Using this qualitative approach, the data in Table 1-3 and Table 1-4 indicate that the OSPE diminishes for the formation of spinels in nuclear waste glasses is $Ni \approx Fe^{2+} > Mg^{2+} > Mn^{2+}$ in agreement with the sequences determined in previous studies in simpler systems [39, 61]. In addition, the presence of $LiCr(SiO_3)_2$ as a phase in Table 1-3 is an indication that $LiCrO_4$ in the presence of excess SiO_2 ($LiCr(SiO_3)_2 = LiCrO_4 + 2SiO_2$) may also be present in nuclear waste glasses as a quasicrystalline species similar to $LiFeO_4$ and $NaFeO_4$ quasicrystals observed previously during crucible and pilot scale melter tests [16, 41].

It should also be recognized that the melt has a dynamic equilibrium between the aluminate, ferrate, and chromate quasicrystals formed with the A and B cations and the silicate quasicrystals formed with A and B cations in the spinel structure (see Equation 3 and Figure 1-1). Strong evidence that the cation Li is primarily present as a silicate quasicrystalline species comes from the ubiquitous formation of $Li_2Si_2O_5$ as a phase during the determination of all TTT diagrams for simulated waste glasses [50, 51, 52]. Since little to no Li substitutes into the nepheline structure (it is too small for the 8-9 coordinated M1 sites in nepheline [69]), it crystallizes out as a separate silicate phase. In the absence of Fe^{3+}, Al^{3+}, Ni^{2+}, Fe^{2+}, Mn^{2+}, and Mg^{2+} from the waste, e.g. the heat treatment of an alkali borosilicate frit (F165) at 700ºC for 24 hours, this lithium disilicate phase is the only phase to form. Likewise, a Mn^{2+}-Fe^{3+} rich melt (Table 1-3) that was amorphous when held at 1050ºC for 4 hours is heat treated for 24 hours, the disilicate $Ca(Mn,Ca)Si_2O_6$ phase (bustamite) crystallizes. Thus, it appears that Ca^{2+}, Mn^{2+} and Li^{+} may all be strongly associated with silicate quasicrystals instead of the aluminate, ferrate, or chromate quasicrystals.

The distribution of the chromate, ferrate, aluminate, and silicate quasicrystalline groups in the melt is temperature dependent, but the degree of order (normal spinel vs. inverse spinel structure), which determines the coordination of the trivalent cations in crystalline spinel, is also a strong function of temperature [70]. Therefore, the exchange reactions between $^{[4]}Cr^{3+}_{(melt)}$- $^{[6]}Cr^{3+}_{(crystal),}$ $^{[4]}Fe^{3+}_{(melt)}$-$^{[6]}Fe^{3+}_{(crystal),}$ and $^{[4]}Al^{3+}_{(melt)}$-$^{[6]}Al^{3+}_{(crystal)}$ define the shape of the liquidus in these complex 15 component systems. Since the ferrite spinels like $NiFe_2O_4$, have an inverse spinel structure, $^{[6]}Mg^{2+}$, $^{[6]}Zn^{2+}$, $^{[6]}Fe^{2+}$, $^{[6]}Ni^{2+}$ are in octahedral coordination and half of the Fe^{3+} is in octahedral coordination ($^{[6]}Fe^{3+}$), while in the chromate and aluminate spinels all the divalent species are tetrahedrally coordinated and $^{[6]}Cr^{3+}$ and $^{[6]}Al^{3+}$are octahedrally coordinated [39, 60, 61], exchange reactions of the following type between the melt species (left hand side, LHS) and the primary crystalline phases (right hand side, RHS) are likely:

Equation 7 for normal spinels

$$\underset{\text{melt}}{2^{[4\text{-}6]}Ni_{0.5}{}^{[4]}AlO_2} + \underset{\text{melt}}{2(Na,Li)^{[4]}CrO_2} + \underset{\text{melt}}{2(K,Na)^{[4]}AlO_2} + \underset{\text{melt}}{(K,Na)_2SiO_3} + \underset{\text{melt}}{5SiO_2} \quad \leftrightarrow$$

$$\underset{\text{normal spinel}}{^{[4]}Ni^{[6]}Cr_2O_4} + \underset{\text{nepheline}}{4(K,Na)^{[4]}AlSiO_4} + \underset{\text{disilicate}}{(Na,Li)_2Si_2O_5}$$

Equation 8 for inverse spinels

$$2^{[4\text{-}6]}Ni_{0.5}{}^{[4]}AlO_2 + 2(Na,Li)^{[4]}FeO_2 + 2(K,Na)^{[4]}AlO_2 + (K,Na)_2SiO_3 + 5SiO_2 \leftrightarrow$$
melt melt melt melt melt

$$^{[6]}Ni^{[4]}Fe^{[6]}FeO_4 + 4(K,Na)^{[4]}AlSiO_4 + (Na,Li)_2Si_2O_5$$
inverse spinel nepheline disilicate

where Ni^{2+} represents any of the divalent transition metals. Note that in acmite the coordination of Ni and Fe is also $^{[6]}Ni^{[4]}Fe^{[6]}Fe$ as it is in the inverse $NiFe_2O_4$ spinel so a similar reaction could be written with acmite as the crystalline species on the RHS of Equation 8.

Reactions such as Equation 7 and Equation 8

explain why "precursor" $NaFeO_2$ [16], $LiFeO_2$ [41] and $LiCrO_2$ identified in this study, that have a spinel structure, are observed during feed to glass conversion of waste/frit mixtures. These ferrate and chromate species are transient precursors, which dissolve in the later stages of feed to glass conversion and then convert to insoluble $NiFe_2O_4$ spinels by the exchange of an A atomic species for a B atomic species in the spinel structure (see Figure 1-1). The formation of the $NiFe_2O_4$-$NiCr_2O_4$ spinels probably occurs by one of the quasicrystalline exchange reactions proposed above.

1.5 Objectives of this Report

The subsequent discussions presented in this report address the following topics:

- The measurements supporting the determination of liquidus temperature for the glasses with higher TiO_2 content are presented and reviewed;
- The impact of the studies of durability and viscosity on the use of the liquidus results for model evaluation and development is discussed.

The results are provided for the attempts (1) to use the 2001 current model to predict the T_L values for the glasses with higher TiO_2 content and (2) to refit the coefficients (i.e., the a, b, c, and d terms) of Equation 1. Given the unsatisfactory results from these initial efforts, a decision was made to explore revising the values for selected speciation terms of Table 1-1 above. However, in pursuing this approach, there was a need to balance the statistical and crystal theory perspectives as the viability of these efforts was evaluated. A discussion of these aspects of the investigation is provided leading to the T_L model recommended for when SWPF becomes operational.

1.6 Quality Assurance

Requirements for performing reviews of technical reports and the extent of review are established in manual E7 2.60. SRNL documents the extent and type of review using the SRNL Technical Report Design Checklist contained in WSRC-IM-2002-00011, Rev. 2. All of the liquidus temperature-composition models presented in this report were conducted using JMP Version 11.1.1 or using JMP Pro Version 11.2.1 [71] and checked using E7 2.60.

This report addresses the integration of SWPF process streams enriched in Ti, Na, and Cs into the DWPF glass property models as set forth in Technical Task Request (TTR) X-TTR-S-00012 of April 24, 2014. The details of how the integration of the SWPF process stream components were integrated into the

DWPF glass property models is given in the Task Technical and Quality Assurance Plan (TTQAP) given in Reference 72.

2.0 DWPF Process/Product (P/P) Modeling Constraints

2.1 Modeling Constraints Common to PCCS Models

For all the PCCS models and validation data, various constraints are applied on the data. The first requires that the chemical composition of the glass, on an oxide basis, be within 100±5 weight percent (wt%) [73]. The "sum of oxides" constraint minimizes the impact of analytic errors during modeling and validation.

The glass REDOX, expressed as the $Fe^{2+}/\Sigma Fe$ ratio, must be <0.33, which is the upper limit of processability in the DWPF melter. This is because REDOX values <0.33 have been shown not to impact glass durability [74, 75, 76], glass viscosity, or glass liquidus values, while higher REDOX ratios (more reducing values) can impact these properties.

The alkali (ΣR_2O where R=Rb, Cs, Na, Li, or K) and alumina (Al_2O_3) constraints shown in Figure 2-1 were developed after the DWPF durability model (THERMO™) was developed to ensure that the durability response of a glass could be modeled. The alkali and alumina constraints replaced the "homogeneity constraint" and became known as the "reduction of constraints (ROC)" as discussed in Reference 77 and the references contained therein. The ROC within PCCS is used in conjunction with the P/P models to determine whether a glass can be processed in DWPF. The ROC as shown in Figure 2-1 has worked for DWPF glasses with 0-2.00 wt% TiO_2. Recent investigations [77] have shown that for glasses such as the SWPF glasses with TiO_2>2.00 wt% that the ROC constraint has to be Al_2O_3≥4.00 wt%, which alters the Figure 2-1 constraints to those shown in Figure 2-2.

Moreover, a given glass must be homogeneous, i.e. not phase separated by liquid-liquid amorphous phase separation (APS). Regions of APS are known to form due to low Al_2O_3 (≤3.00 wt%), high P_2O_5 (≥2.25 wt%), or high B_2O_3 (≥14.00 wt%) concentrations in HLW glasses, and so these compositions are excluded from modeling (see Figure 2-1). Sometimes an X-ray Diffraction (XRD) of an as-quenched glass will show a double amorphous hump rather than a single amorphous hump, which is also an indication of APS. Occasionally, Scanning Electron Microscopy (SEM) or Transmission Electron Microscopy (TEM) is necessary to make the determination of whether a glass is phase separated or not.[4, 5] In References 4 and 5, a "homogeneity constraint" based on glass composition was developed to distinguish between homogeneous and phase separated glasses. Likewise, glasses for modeling should not be phase separated because phase separated glasses can give anomalous durability [4, 5, 78, 79, 80], viscosity [81], and liquidus [82] responses. While phase separated glasses can exhibit anomalous liquidus measurements, there were 36 of the 105 data points used in the 2001 historic liquidus model that failed the original ROC (Figure 2-1). Comparison of the historic model with and without these 36 points showed little impact. Since the 36 data points were high leverage points in the 2001 model and all the liquidus phases were spinel, these 36 data points were retained in the current modeling effort. Due to the competition between Al^{3+} and Ti^{4+} for alkali MRO discussed in Section 4.3.3, the ROC was retained for the SWPF glasses.

The constraints, without the uncertainties factored into the values shown, as summarized graphically in Figure 2-1 and Figure 2-2 are applied to the modeling data (composition and property) so that model accuracy is maximized and model error is minimized by ensuring complete glass analyses and no anomalous property responses.

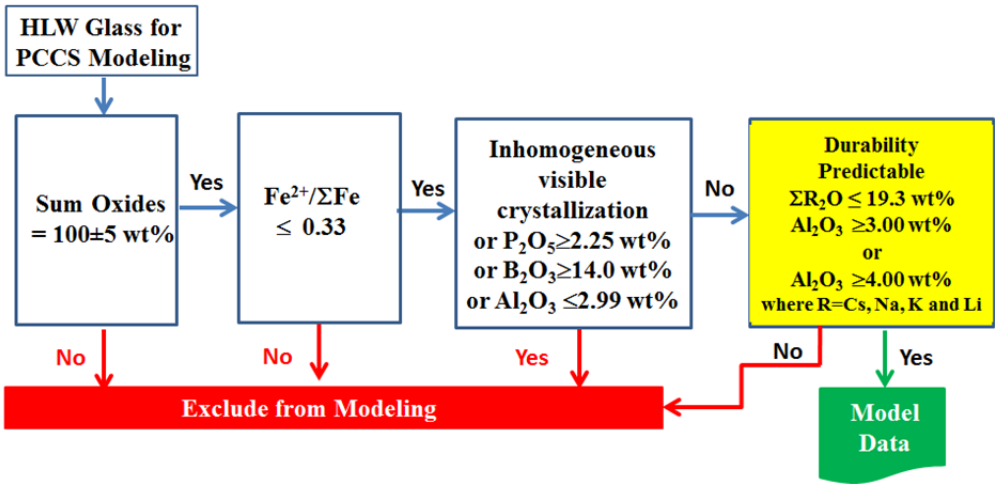

Figure 2-1. Graphical Representation of the Constraints Applied to the Choice of Model and Validation Data for the Durability, Viscosity, and Liquidus P/P Models for glasses with 0-2.00 wt% TiO_2. The Al_2O_3 term in the inhomogeneous by visible crystallization is 2.99 wt% to accommodate the Waste Compliance Plan (WCP) Purex glass which contains 2.99 wt% Al_2O_3.

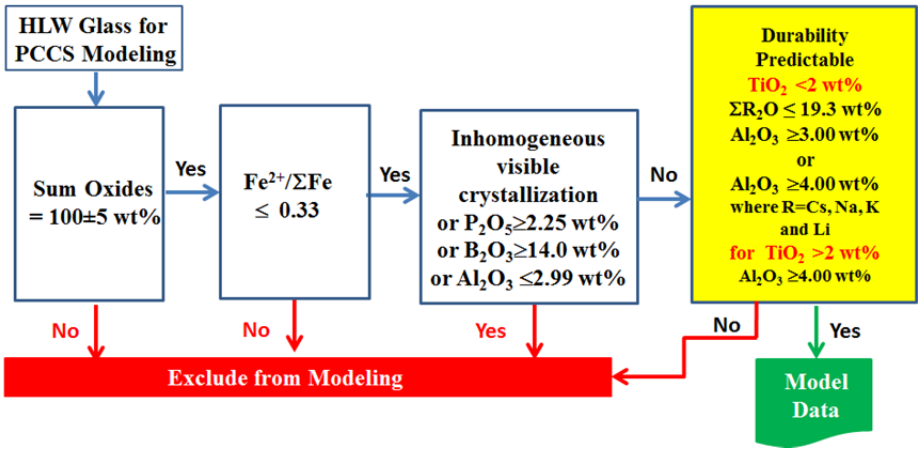

Figure 2-2. Graphical Representation of the Constraints Applied to the Choice of Model and Validation Data for the Durability, Viscosity, and Liquidus P/P Models for glasses with 0-2.00 wt% TiO_2 and glasses with ≥ 2.00 wt% TiO_2. The Al_2O_3 term in the "inhomogeneous by visible crystallization" box is 2.99 wt% to accommodate the WCP Purex glass.

2.2 Modeling Constraints Unique to the PCCS Liquidus Model

The liquidus model has only one additional modeling constraint, which is that the major phase on the liquidus boundary is a spinel. This unique constraint exists due to the quasicrystalline theory involved in the model, which is based on the incongruent melting of pyroxene subliquidus phases to spinel at the liquidus as discussed in the previous sections.

Other experimental constraints unique to the liquidus measurement are addressed in the American Society for Testing and Materials (ASTM) liquidus procedure (ASTM C-1720), where the liquidus temperature measurement should be approached from a lower temperature and not from a higher temperature due to thermodynamic and kinetic considerations. The initial glass, before liquidus measurement should be amorphous and not crystallized.

3.0 Experimental

3.1 Historic Liquidus Model

Approximately 50 glasses designated the Extreme Composition Matrix, representing waste glass extremes in Al_2O_3 and Fe_2O_3 content,* were fabricated at SRNL from reagent grade oxides, carbonates, and hydroxides, in high purity Al_2O_3 crucibles at 1150°C, the nominal DWPF melt temperature. Due to inherent co-linearity of species in the waste, these glasses represent composition extremes but lack variations amongst individual components. The glasses were made in both reduced and oxidized states spanning $Fe^{+2}/\Sigma Fe$ ratios of 0.01 to 0.47. The glasses were held at the melt temperature for 4 hours, air quenched in the crucible, removed, and analyzed by x-ray diffraction to ensure that the sample was amorphous. The glasses were sent to both Corning Engineering Laboratory Services (CELS) †† and Sharp-Shurtz (now Owens Corning Testing) for liquidus temperature (T_L) measurements by ASTM C829 [83] and to CELS for replicate chemical analyses. The T_L values of a subset of 6 glasses, all highly reduced, were measured three to five times by CELS over a 4 year time frame. These same glasses were also analyzed by Pacific Northwest National Laboratory (PNNL) in duplicate using a recently developed isothermal liquidus temperature procedure [84]. When replicate T_L measurements made by the various laboratories were in disagreement, confirmation testing at SRNL was performed using isothermal T_L measurement. Glasses used in liquidus modeling are given in Appendix A, Table A1 and in References 6, 7, and 8.

The compositions of the SRNL glasses whose liquidus temperature measurements were used in modeling were primarily analyzed by CELS; the compositions for these glasses are also provided in Appendix A, Table A1. CELS analyzed most of the glasses in duplicate† so that any effects of short term instrument bias on the whole element chemistry would be minimized. CELS analyzed the various frits six times. All CELS composition analyses are traceable to the NBS777 standard glass. These data indicate little random or systematic variation for these analyses. Two glasses (AH 168AL-1988 and AH 168FE-RED-1988) were analyzed by the Analytic Development Division (ADD) of SRNL. These samples were prepared using dissolution by either Na_2O_2 with a hydrochloric acid (HCl) uptake or HCl/HF(hydrofluoric acid)/microwave digestion followed by analysis using Inductively Coupled Plasma (ICP-ES) Emission Spectroscopy and Atomic Absorption (AA) [85]. The $Fe^{2+}/\Sigma Fe$ analyses were performed on selected glasses. For those glasses without $Fe^{2+}/\Sigma Fe$ determinations, glasses that were fabricated without the addition of a reductant, the $Fe^{2+}/\Sigma Fe$ values were assumed to be one-half the detection limit [86] for this measurement, $Fe^{2+}/\Sigma Fe = \frac{1}{2}(0.03) = 0.015$.

A second set of 51 compositions designated as the DWPF Statistically Designed Matrix was designed by SRNL to cover the range of waste glass extremes in Al_2O_3 and Fe_2O_3. This data set, designated the "SG" glasses, included two glasses that were compositional replicates of each other (i.e., SG05 and SG18). These glasses were made at PNNL from reagent grade chemicals, melted for 1 hour in Pt-Rh crucibles, quenched on either a stainless steel plate or into water, ground, remelted, quenched again and reground again before liquidus measurement. Glasses were melted at a variety of temperatures ranging between 1107ºC and 1384ºC. The compositions were measured by SRNL in duplicate [6]. The details of the glass fabrication and T_L measurement are available elsewhere [59]. The precision of the PNNL isothermal temperature method, which became ASTM 1720 [84], was reported to be ±12°C for bias-corrected

* The glasses were fabricated with "waste loadings" calculated on an oxide basis and varying between 25 and 35 wt% for high Fe_2O_3 containing Purex waste, high Al_2O_3 HM waste, and average waste (a mixture of the two).

†† ASTM C829 states that a precision of ±10°C is achievable for T_L measurement with clear glasses tested in the same furnace. No precision is given for glasses tested in different furnaces or for opaque glasses. CELS provided estimates of ±20°C (twice the ASTM value) for black opaque waste glasses.

† Two dissolutions were performed (one on each day) with each dissolution analyzed in duplicate.

liquidus measurements [59] based on replicate analyses of a waste glass standard (SP-1).[‡] During a subsequent study (designated the SG1 study) that included the effect of variable quench rate, the long term precision of the SP-1 glass was found to be as large as ±30°C [6, 59].

The liquidus temperature measurements and compositions for the SG glasses are provided in Appendix A, Table A1. Only those SG Study glasses exhibiting spinel[†], whether or not it was in conjunction with clinopyroxene, were used for modeling. This constraint provided 59 measured liquidus temperatures for 44 different glass compositions that were pooled with the SRNL extreme composition study glasses. As with the extreme composition study glasses, the short-term PNNL liquidus temperature measurements from the SG Study were averaged, e.g. the T_L measurements for the SG06(2), SG18(7), SG18B(5), SG25(2), and SG37(2). The seven SG18 and five SG18B measurements were averaged over the various PNNL furnaces used for heat-treatment into two sets of three values each because the use of different furnaces was believed to have introduced the observed long-term biases. The averaging decreases the unique SG model data to 50 liquidus temperatures for a total modeling population of 105 measurements.

3.2 SWPF Liquidus Model Database

The SWPF glasses were made and analyzed by VSL. The details of the glass fabrication are given in Reference 13. The chemical compositions were measured by X-ray Fluorescence (XRF) and other methods. Since XRF cannot measure light elements such as B and Li, the glasses were dissolved and analyzed by Direct Current Plasma Emission Spectrometry (DCP) for these two elements. For each glass, two XRF and two DCP preparations were performed and two reads on each were performed on different days for different elements. Therefore, each glass had two measurements for each cation in the glass. A glass standard, the SRNL Environmental Assessment (EA) glass was used. The EA glass had been manufactured and analyzed by CELS ten replicate times, and the analyses were validated by ten additional analyses by SRNL ADD [87, 88]. The details of the SWPF glass measurements and bias correction to the EA glass standards are discussed elsewhere [89]. The biased corrected glass compositions are given in Appendix A, Table A2.

The liquidus temperature measurements, which were conducted by VSL using ASTM 1720 and provided to SRNL [14], are given in Appendix A, Table A2. VSL conducted the measurement of T_L based on the uniform temperature method described in ASTM C1720 [84]. For this method, samples of each study glass are subjected to multiple heat treatments at different temperatures and time durations (see ASTM 1720 for details and see Appendix A for actual conditions used). The heat treated samples are then analyzed by XRD to identify and quantify the crystal content. Heat treatments of the glasses with higher TiO_2 content were performed between 650°C and 1200°C.

Based upon the experimental results, VSL provided T_L values for 43 of the 50 study glasses. Quantitative data could not be obtained for glass samples that crystallized titanium-containing phases (i.e., lithium titanosilicate and pseudobrookite) due to the lack of suitable calibration standards; T_L determinations were not performed for these glasses or for glasses that did not show sufficient crystallinity (see ASTM 1720 which defines the sufficient crystallinity for different types of diagnostic equipment). The rows of Table A2 that are shaded were not included in the determination of T_L values.

Glasses SWPF-01 through SWPF-12 were excluded from modeling for the following reasons.

- SWPF-08 was visually inhomogeneous and there was no suitable calibration curve for T_L measurement.

[‡] The SP-1 glass was used by PNNL during the SG Study to correct the liquidus temperature measurements on a furnace to furnace basis by between 1 and 33ºC. The accepted value for the SP-1 glass is 1040ºC [91].

[†] As in one of the SRNL model data (i.e., one of the DWPF Startup Frit glasses), some of the glasses exhibit both spinel and (clino)pyroxene to the resolution of the liquidus temperature measurement.

- SWPF-01 through SWPF-09 contained TiO_2>2.00 wt% and Al_2O_3<4.00 wt%, i.e. it failed the revised ROC for high TiO_2 containing glasses in Figure 2-2. (Note SWPF-03, 04, 08, 09 also did not have suitable calibration curves for T_L measurement.)
- SWPF-11 exhibited no liquidus phase and so a regression was not performed.
- SWPF-12 contained unreacted Fe_2O_3 (see Reference 14) and was, therefore, not a glass. In addition no suitable calibration curve existed for T_L measurement.
- SWPF-14 contained pyroxene (acmite/agerine) as the liquidus phase and no suitable calibration curve existed for T_L measurement. Note that acmite/agerine is a lower temperature phase that will melt to spinel at a higher temperature.

This left a modeling pool of 37 glasses, all of which had spinel as a primary phase. The 37 spinel T_L values span a range of 898°C to 1163°C as shown in Appendix A, Table A2.

In the following sections, a closer look at the determination of T_L values is provided; these values are reviewed in light of the approach used for modeling the relationship between T_L and composition for DWPF. The impact of the conclusions from the studies of the durability and viscosity of these glasses with higher TiO_2 content on the investigation of T_L is discussed.

3.3 Liquidus Temperature Determinations

As discussed above, VSL's experimental results led to a set of values for temperature and crystal content (phase and volume percent) for each study glass that contained sufficient crystallinity to be measured and with suitable X-ray diffraction calibration standards for quantitate percent crystallinity determinations to be made. Two methods for determining the T_L for a glass from such data are detailed in the ASTM 1720 [84] procedure:

- Conduct a least squares, linear fit of the temperature (T) values to the crystal percent (%C) values (i.e., $T = a + b \times \%C$). This is the method used by VSL, and the T_L determined by this method is the estimate of the y-intercept, a)
- Conduct a least squares, linear fit of the crystal percent (%C) values to the temperature (T) values (i.e., $\%C = a + b \times T$). This is designated as an Alternate Method, and T_L is determined from the estimates of a and b by –a/b.

In general, the two methods yield very similar T_L values for situations with a strong linear relationship between T and %C. The coefficient of determination (i.e., the R^2 value) from the least squares, linear fitting process is a measure of this relationship. The value of R^2 falls between 0 and 1, and it represents the fraction of the variation in the y values of the regression that is explained by the linear relationship (i.e., $y = a + bx$) to the x values. A larger value for R^2 indicates a stronger linear relationship between T and %C. Exhibit A1 of Appendix A was prepared to offer more insight into this aspect of T_L determinations. In this exhibit, the two linear fitting approaches (Alternate Method and VSL) are presented. The resulting T_L determinations are provided in Table 3-1. For completeness, this table also includes (1) the primary crystalline phase determined by VSL and (2) those study glasses for which no T_L determination was made. Those situations where the results for the VSL method yielded R^2 values less than 0.95 are shaded in this table. The difference between the T_L's from the VSL and alternate methods for several of these situations is greater than 10°C with the difference for SWPF-50 being more than 50°C. These results reflect the known difficulties in measuring the T_L values for opaque black HLW glasses as discussed in ASTM C1720.

The primary factor in selecting between the two methods was determined to be consistent with T_L data utilized in the previous modeling effort. A review of the previous study confirmed that the extrapolation

method used by VSL is the same method used for that study [6]; thus, the VSL T_L values were used for the current model evaluation and development efforts.

Table 3-1. T_L Determinations and Primary Crystalline Phases.

VSL T_L (°C)	Primary Phase	Glass ID	VSL ID	Alternate Method Extrapolation Using Crystal % Regressed on Temperature		
				Estimate Intercept	Estimate Temperature Slope	Alternate T_L (°C)
939.5	clinopyroxene	SWPF-01	GAP-15	264.4193	-0.2806	942.5
901.1	spinel	SWPF-02	GAP-22	25.6630	-0.0282	909.2
.	Li_2TiSiO_5	SWPF-03	GAP-43			
.	Li_2TiSiO_5	SWPF-04	GAP-31			
1034.4	spinel	SWPF-05	GAP-33	27.3013	-0.0260	1048.4
742.2	spinel	SWPF-06	GAP-38	125.6952	-0.1694	742.2
979.8	spinel	SWPF-07	GAP-21	23.7677	-0.0242	980.3
.	pseudobrookite	SWPF-08	GAP-37			
.	Li_2TiSiO_5	SWPF-09	GAP-44			
1001.7	spinel	SWPF-10	GAP-47	30.3776	-0.0303	1002.3
no TL		SWPF-11	GAP-10			
.	pseudobrookite	SWPF-12	GAP-34			
1048.0	spinel	SWPF-13	GAP-19	39.7429	-0.0377	1053.3
.	clinopyroxene	SWPF-14	GAP-12			
969.6	spinel	SWPF-15	GAP-14	89.4983	-0.0923	969.7
969.6	spinel	SWPF-16	GAP-26	19.0777	-0.0196	974.3
923.1	spinel	SWPF-17	GAP-05	8.3397	-0.0090	927.1
907.7	spinel	SWPF-18	GAP-29	26.2928	-0.0289	911.3
897.9	spinel	SWPF-19	GAP-35	21.7765	-0.0242	899.1
1088.2	spinel	SWPF-20	GAP-46	29.5387	-0.0270	1092.7
1044.0	spinel	SWPF-21	GAP-41	36.0451	-0.0345	1044.7
1037.9	spinel	SWPF-22	GAP-20	18.6569	-0.0178	1050.2
938.4	spinel	SWPF-23	GAP-23	14.7962	-0.0157	940.1
1088.9	spinel	SWPF-24	GAP-42	21.9763	-0.0202	1090
930.9	spinel	SWPF-25	GAP-17	21.6151	-0.0232	931.3
1052.6	spinel	SWPF-26	GAP-06	24.3822	-0.0230	1059.8
1162.6	spinel	SWPF-27	GAP-24	34.5231	-0.0296	1165
1058.3	spinel	SWPF-28	GAP-50	31.2149	-0.0295	1059.4
1047.4	spinel	SWPF-29	GAP-32	23.2527	-0.0222	1047.4
1136.4	spinel	SWPF-30	GAP-16	21.7810	-0.0192	1136.5
1096.8	spinel	SWPF-31	GAP-30	27.7800	-0.0252	1101.5
1049.0	spinel	SWPF-32	GAP-09	20.7510	-0.0198	1049.4
1096.9	spinel	SWPF-33	GAP-40	19.8601	-0.0179	1106.8
1075.8	spinel	SWPF-34	GAP-36	16.6354	-0.0153	1084.5
1114.6	spinel	SWPF-35	GAP-03	26.4383	-0.0237	1116.2
1076.7	spinel	SWPF-36	GAP-11	30.1264	-0.0276	1090.3
1156.8	spinel	SWPF-37	GAP-07	13.1248	-0.0113	1161.7
1084.3	spinel	SWPF-38	GAP-13	25.4185	-0.0234	1086.2
954.1	spinel	SWPF-39	GAP-49	14.4712	-0.0151	956.1
1130.4	spinel	SWPF-40	GAP-48	30.4049	-0.0268	1133.2
911.9	spinel	SWPF-41	GAP-04	26.8363	-0.0293	916.3
960.6	spinel	SWPF-42	GAP-27	8.8713	-0.0091	976.6
1090.9	spinel	SWPF-43	GAP-28	33.3840	-0.0305	1096
1031.3	spinel	SWPF-44	GAP-01	14.0063	-0.0135	1035.6
1060.0	spinel	SWPF-45	GAP-08	19.0397	-0.0176	1084.4
967.7	spinel	SWPF-46	GAP-39	15.3987	-0.0159	968
1069.2	spinel	SWPF-47	GAP-45	16.8821	-0.0157	1072.2
1075.7	spinel	SWPF-48	GAP-25	23.4743	-0.0218	1077.2
912.9	spinel	SWPF-49	GAP-02	16.4189	-0.0180	914.4
1141.1	spinel	SWPF-50	GAP-18	19.9718	-0.0168	1192.2

Note: Those situations where the results for the VSL method of extrapolation yielded R^2 values less than 0.95 are shaded in this table.

3.4 SWPF (TiO_2-only) Liquidus Validation Database

References 90-91 were studies designed to maximize waste loading in defense waste glasses. These high waste loaded glasses [90, 91] are, therefore, used in this study to validate the TiO_2 term in the SWPF liquidus model.

The details of the composition and liquidus measurements for the TiO_2-only validation glasses are given in References 90-91 and include dissolution of the glasses by the Process Science Analytical Laboratory (PSAL) using the methods given in ASTM C1463 [92] for dissolution followed by ICP-ES for cations and Ion Chromatography (IC) for anions. The liquidus temperature of these glasses were measured by PNNL using ASTM 1720 [84] and the data regressed the same way as the historic and SWPF liquidus data. Glasses that were omitted as validation data included the following:

- HWL-01 through HWL-06, HWL-08, and FY09EM21-01, FY09EM21-03, FY09EM21-04, FY09EM21-10, FY09EM21-13, FY09EM21-22 and FY09EM21-24, which crystallized upon quenching
- HWL-15, HWL-18, FY09EM21-05, FY09EM21-08, FY09EM21-11, FY09EM21-14, and FY09EM21-16, which contained > 2.00 wt% TiO_2 and $Al_2O_3 < 4.00$ wt%
- FY09EM21-14 which had over 14 wt% B_2O_3 and
- FY09EM21-05, FY09EM21-11, FY09EM21-14, FY09EM21-18, FY09EM21-19, and FY09EM21-23 which did not precipitate spinel on the liquidus.

This left a validation pool of 20 glasses where the eight HWL glasses were the same glasses used for validation of the viscosity model and twelve FY09 glasses were a subset of those used for the viscosity model. The compositions and measured liquidus values for the validation data are given in Appendix A, Table A3.

3.5 Quasicrystalline Glass Experiments

To evaluate the preferred partitioning between the divalent and trivalent transition metals (Cr^{3+}, Ni^{2+}, Fe^{3+}, Mn^{2+}, and Al^{3+}) and the OSPE between the melt and the spinel liquidus phases, glasses containing individual divalent-trivalent pairs were examined in the presence of 4 wt% TiO_2, e.g. Ni^{2+}-Cr^{3+} was examined in the absence of Ni^{2+}-Fe^{3+} and vice versa similar to Table 1-3 and Table 1-4. To examine the role of Al^{3+} in the presence of 4 wt% TiO_2, the Ni^{2+}-Cr^{3+} and Ni^{2+}-Fe^{3+} pairs were examined in the absence and presence of Al^{3+}. In addition, the formation of phases in the absence of Cr^{3+} and Fe^{3+} were examined, e.g. Ni^{2+}-Al^{3+}, Mg^{2+}-Al^{3+}, and Mn^{2+}-Al^{3+} pairs.

Glasses were made from an average DWPF (Stage I) waste and a borosilicate frit (F202) as given in Table 1-4 were remade to contain 4 wt% TiO_2. Glasses were melted for 4 hours in Pt crucibles at the melt temperature of 1150°C and at the DWPF liquidus control temperature of 1050°C. The Fe_2O_3 in the Fe^{3+} only experiments (no Al_2O_3) varied from 19.96 to 20.69 wt%, while the Fe_2O_3 in the Fe^{3+}-Al^{3+} coupled experiments varied from 18.53-19.17 wt% with an Al_2O_3 content of 6.84-7.07 wt%. The Cr_2O_3 in the Cr^{3+} only (no Al_2O_3) experiments varied from 19.96-20.69 wt%, while the Cr_2O_3 in the Cr^{3+}-Al^{3+} coupled experiments varied from 18.53-19.17 wt% with an Al_2O_3 content of 6.84-7.07 wt%. The Al_2O_3 content in the Al^{3+} only experiments varied from 8.48-8.84 wt% and SiO_2 was substituted for the missing Fe_2O_3 and Cr_2O_3 in order to allow the glasses to melt at 1150ºC. The as-made compositions are given in Table 3-2. Glasses were air quenched in their crucibles. The resulting glasses were analyzed by XRD.

Table 3-2. Quasi-Chemical Glass Compositions for the SWPF Liquidus Model (wt% as-batched)

	MnFe Only	MnFe Only	MgFe Only	MgFe Only	NiCr Only	NiCr Only	MnCr Only	MnCr Only	MgCr Only	MgCr Only	NiAl w/o Fe/Cr	MnAl w/o Fe/Cr	MgAl w/o Fe/Cr
	Al_2O_3	No Al_2O_3	Al_2O_3	No Al_2O_3	Al_2O_3	No Al_2O_3	Al_2O_3	No Al_2O_3	Al_2O_3	No Al_2O_3	Al_2O_3	Al_2O_3	Al_2O_3
	6.89	0.00	6.84	0.00	7.07	0.00	6.89	0.00	6.84	0.00	8.84	8.54	8.48
	7.10	7.65	7.05	7.59	7.29	7.87	7.10	7.65	7.05	7.59	9.10	8.81	8.74
	0.00	0.00	0.00	0.00	19.17	20.69	18.66	20.11	18.53	19.96	0.00	0.00	0.00
	18.66	20.11	18.53	19.96	0.00	0.00	0.00	0.00	0.00	0.00	0.00	0.00	0.00
	0.00	0.00	0.00	0.00	0.00	0.00	0.00	0.00	0.00	0.00	0.00	0.00	0.00
	3.05	3.28	3.03	3.26	3.13	3.38	3.05	3.28	3.03	3.26	3.92	3.79	3.75
	4.21	4.54	4.19	4.51	4.33	4.67	4.21	4.54	4.19	4.51	5.41	5.23	5.18
	0.00	0.00	4.78	5.15	0.00	0.00	0.00	0.00	4.78	5.15	0.00	0.00	5.92
	4.14	4.46	0.00	0.00	0.00	0.00	4.14	4.46	0.00	0.00	0.00	5.14	0.00
	5.59	6.02	5.55	5.97	5.74	6.20	5.59	6.02	5.55	5.97	7.17	6.94	6.88
	0.00	0.00	0.00	0.00	1.66	1.79	0.00	0.00	0.00	0.00	2.07	0.00	0.00
	46.36	49.94	46.04	49.57	47.61	51.40	46.36	49.94	46.04	49.57	59.48	57.54	57.04
	4.00	4.00	4.00	4.00	4.00	4.00	4.00	4.00	4.00	4.00	4.00	4.00	4.00
	100.00	100.00	100.00	100.00	100.00	100.00	100.00	100.00	100.00	100.00	100.00	100.00	100.00

4.0 T_L Model Evaluation and Development

As SWPF becomes operational, DWPF processing control is to continue to rely on PCCS to make SME acceptability decisions based upon measurements of samples from the SME. Work has already been completed to update the durability and viscosity models [77, 93] so that the necessary changes for these models may be incorporated into the revision of PCCS that is needed to support DWPF's processing once SWPF becomes operational. The primary crystalline phases of the 37 SWPF model glasses, whose T_L values were discussed in Sections 3.2 and 3.3, are spinels; this is a positive outcome that suggests that the 2001 historic T_L model (one based on a spinel primary crystalline phase) may be adequate or that it may be revised to adequately support DWPF's future processing with SWPF operational.

4.1 Evaluation of the 2001 Historic Model with the SWPF Data

Thus, the first decision of interest is: Are the SWPF T_L values adequately predicted by the 2001 historic model that does have a TiO_2 term or does the TiO_2 term need to be refit? Exhibit 4-1 provides a graphical answer to that question. In this plot, the measured T_L values for the higher SWPF TiO_2 glasses are represented by open red circles, ○, and these values are plotted along with predictions and confidence intervals for the 2001 historic model (that are shown as lines). While the current model was developed for $1/T_L$ in Kelvin, the T_L data of this plot have been expressed directly in degrees Celsius. If the data were perfectly predicted, they would all fall along the green line, or if they were adequately predicted, the vast majority of the data would fall within the 95% confidence intervals. Neither of these patterns is seen for the T_L values of the higher TiO_2 SWPF glasses. In fact, the vast majority of these data fall above the upper 95% confidence limit, which indicates that the current model under-predicts the measured T_L values for the higher SWPF TiO_2 glasses. Since for T_L predictions, PCCS imposes a constraint with an upper limit of 1050°C, these "prediction-misses" are in the wrong direction (i.e., they do not lead to a conservative outcome – that is, operating at a falsely low predicted temperature could result in substantial crystallization within the melter vessel). Based upon these results, the 2001 historic T_L model, without any coefficient and/or parameter refitting, is inappropriate for use by DWPF once SWPF is operational.

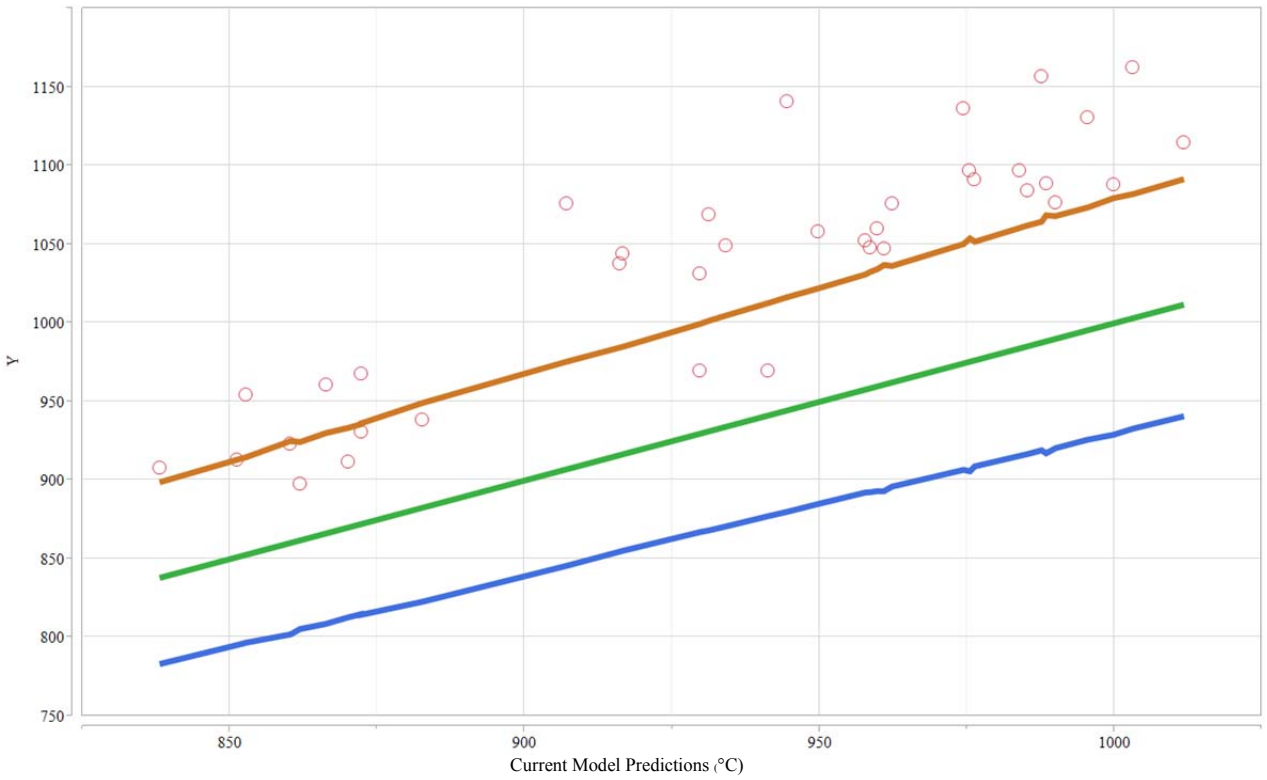

Y-axis Legend: ○ - Measured T_L; Green Line – Predicted TL; Blue Line – Lower 95% Confidence Limit for an Individual Prediction; and Orange Line – Upper 95% Confidence Limit for an Individual Prediction

Exhibit 4-1. Measured T_L Values for Higher TiO_2 Glasses versus 2001 Historic Model Predictions

4.2 Trials Re-fitting of the Parameters a, b, c, and d of the 2001 Historic Model

As discussed earlier, the 2001 historic T_L model is given by Equation 1 with the estimates of the parameters: a = –0.000260, b = –0.000566, c = –0.000153, and d = –0.00144 and with the ϕ coefficients representing the distribution of the various species, i.e., the speciation values, provided in Table 1-1. Given the need to modify the 2001 historic model, an approach was taken to add the 37 T_L data points to the modeling data set (leading to 142 data points) and to attempt an initial revision involving only a re-fitting of the a, b, c, and d parameters (i.e., while maintaining the speciation values of Table 1-1).

Exhibit 4-2 provides the results from this fitting process, which shows an R^2 value of ~ 0.74 and a RMSE value of 54.2°C, when translated from 1/K to °C. There is also an indication of a statistically significant lack of fit for the model (i.e., p-value for the lack of fit test is 0.0061, which indicates a significant lack of fit at the 5% significance level). While these metrics of the resulting model are poor when compared to those cited in Section 1 for the 2001 historic model, the poor performance of the re-fitted model is also illustrated by the graphics in Exhibit 4-2. The vast majority of the T_L values for the higher TiO_2 glasses (which are once again represented by the open red circles, ○) fall below the fitted line (correspondingly, the residuals for these glasses, in general, are negative). Given in this case, that these results are in 1/K, the pattern for the higher TiO_2 glasses, suggests that the re-fitted model is under-predicting the T_L response for these glasses. As discussed above, this is an unacceptable outcome, and this re-fitted model is inadequate for use after joint DWPF and SWPF operation begins.

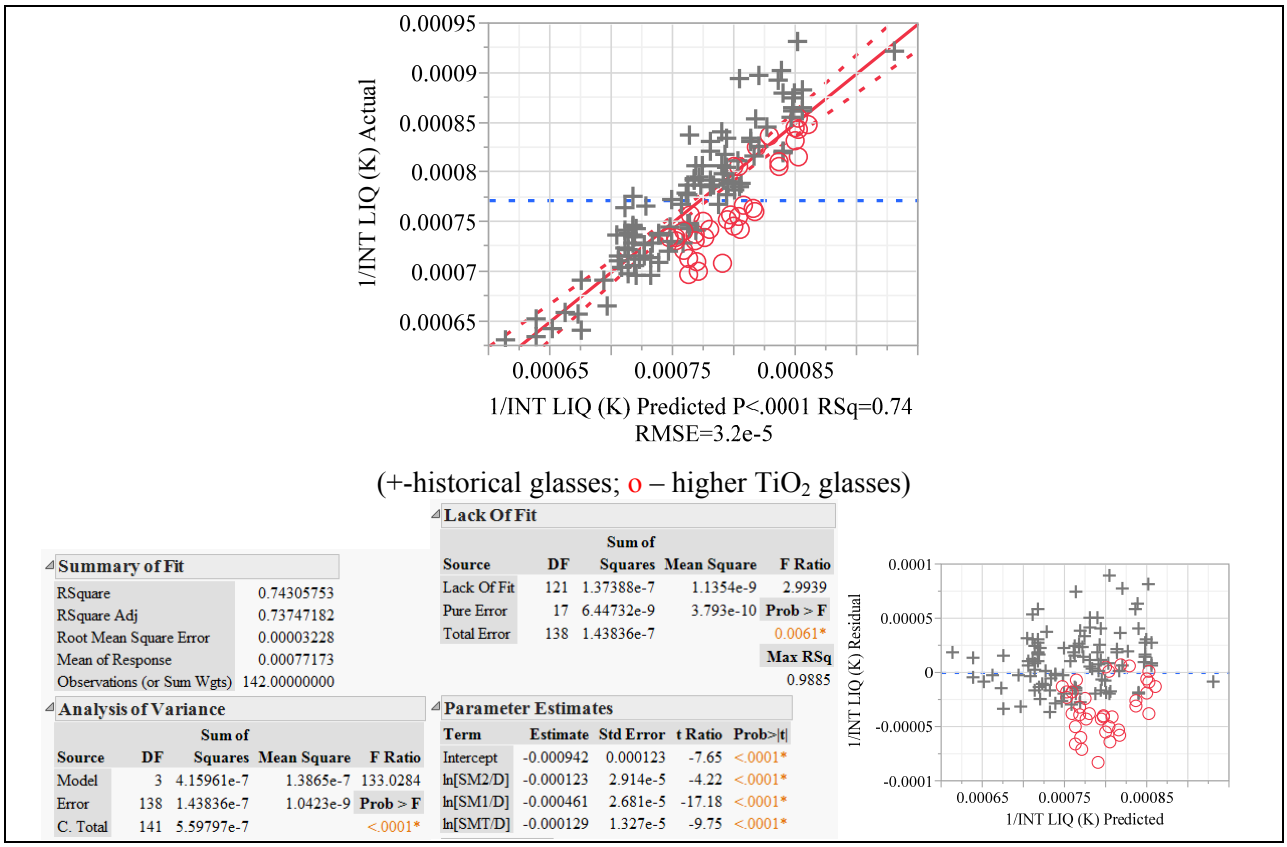

Exhibit 4-2. Re-fitting of the a, b, c, and d Parameters of the Current T_L Model

4.3 Trials Exploring the Use of Different Speciation Values

With the poor results from the initial attempts at using the 2001 historic T_L model and a simple re-fit of the model parameters, the next phase of study involved the investigation into modifying the speciation values (ϕ coefficients) of

Table 1-1. The speciation values utilized by the 2001 historic model were selected based upon a "trial and error" approach [6]. Guidance for this approach was provided by the information in Table 1-2 (this information appears in [6, 7, 8]), and the interpretation of the results from each "trial" (i.e., a fitted model utilizing a set of candidate speciation values fitted to a subset of the available model data) involved balancing the statistical and crystal chemistry theories. For a candidate set of speciation values, there are two questions: Did the statistical metrics associated with the resulting fitted model indicate an adequate result? And are the candidate speciation values supported by known crystal chemistry? The statistical perspective drives the "trial and error" process, but crystal chemistry trumps the statistics, when necessary to maintain a mechanistic approach to modeling.

4.3.1 *Quasicrystalline Rational for Re-speciation of TiO_2 Only*

The simplest trial approach was to refit only the TiO_2 ϕ coefficient. All the liquidus phases of the 37 SWPF Model glasses, after screening for homogeneity and ROC, were spinels. In particular, the spinels had been identified by whole pattern XRD fitting and shown to be most similar to magnetite, $FeO \bullet Fe_2O_3$. Magnetite spinels are known to take up to ~20 wt% TiO_2 into their structure [94]. In addition, phase equilibria has shown that magnetite forms a solid solution with ulvospinel (Fe_2TiO_4), where ulvospinel has a magnetite like structure [60], as shown in Figure 4-1. Titanium can enter the spinel structure by linked replacement of $2Fe^{3+}$ in the octahedral site (6 coordinated) by Fe^{2+} + Ti^{4+} [94]. Complete replacement leads to ulvospinel. Other divalent (+2) cations can participate in the linked replacement instead of Fe^{2+} as these inverse spinels can form defect structures [60].

It is known that titanium acts as both a network modifier and as a network former in melts because Ti is surrounded by both non-bridging and bridging oxygen bonds [29]. Titanium oxide (TiO_4) polyhedra exist in natural melts where Ti is 5-coordinated ($^{[5]}Ti$). This causes heterogeneities in the melt that can lead to crystallization [60] and TiO_2 is a known crystallizing agent in both commercial glasses [95] and in defense HLW glasses [55]. So $^{[5]}Ti$ in a melt can easily form $^{[6]}Ti$ in a spinel liquidus phase depending on its OSPE.

The OSPE of Ti^{3+} was discussed in Section 1.4.3 as being $Cr^{3+} > Ni^{2+} > Ti^{3+} > Fe^{2+} > Fe^{3+} > Mn^{2+}$ according to Bragg and Claringbull [39], while the order of the OSPE from Navrotsky and Kleppa [61] is repeated below for those cations with large OSPEs (Cr^{3+} to Cu^{2+} with decreasing OSPE, Fe^{2+} to Mn^{2+} with small to zero tetrahedral site preference and Zn^{2+} with large tetrahedral site preference).

$$Cr^{3+} > Mn^{3+} > Ni^{2+} > Al^{3+} > Cu^{2+} > Fe^{2+} > Mg^{2+} > Co^{2+} > Ga^{3+} > Fe^{3+} > Mn^{2+} > Zn^{2+}$$

Navrotsky and Kleppa [61] maintain that the OSPE of Ti^{4+} is unknown but classify Ti^{4+} as an element with a large OSPE similar to Ti^{3+}. Ottonello [96] and Burns [97], however, classify the OSPE of Ti^{4+} as zero similar to Fe^{3+} and Mn^{2+}. A low or zero OSPE for Ti^{4+} would favor an inverse spinel depending on the site preference energies of the other ions in the structure [97]. Therefore, the linked replacement of $2Fe^{3+}$ in the octahedral site (6 coordinated) by Fe^{2+} + Ti^{4+} may well be driven by Ni^{2+} + Ti^{4+} substitutions since Ni^{2+} has a high OSPE and Ni spinels are always inverse spinels. Therefore, refitting only the TiO_2 ϕ coefficient was explored preferentially to refitting additional ϕ coefficients.

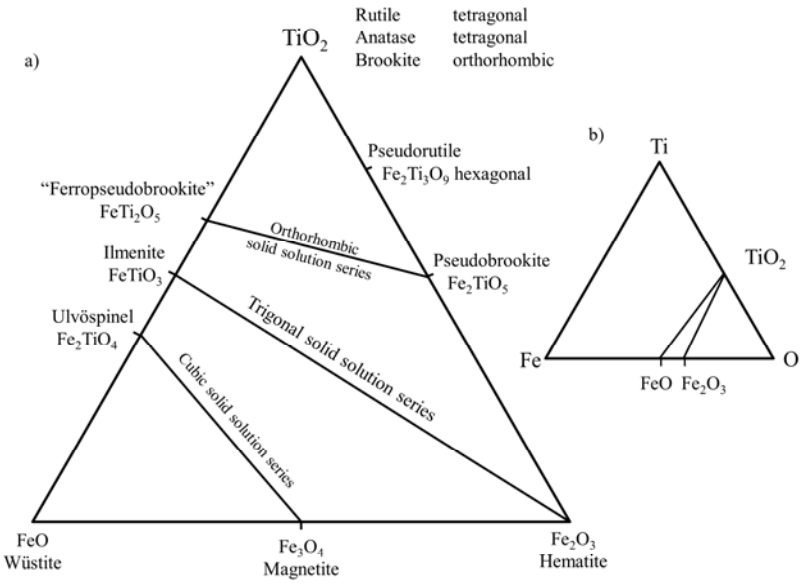

Figure 4-1. Large Region of Solid Solutions is Exhibited between FeO, Fe_2O_3, and TiO_2.[94]

4.3.2 *Trials Re-Speciating for TiO_2 Only*

The trial-and-error approach to selecting speciation values for TiO_2 led to the speciation values provided in Table 4-1. Using these values and re-fitting the parameters a, b, c, and d of Equation 1 to the full modeling data set led to the results provided in Exhibit 4-3. The R^2 value is ~0.841 and the RMSE, expressed in °C, is 42.7 °C. The p-value for the lack of fit statistic is 0.0815, indicating no statistically significant (at 5% significance) lack of fit for this model. However, modeling efforts continued in an attempt to improve the R^2 and RMSE by looking at interactions of TiO_2 with alkali, iron, and alumina.

Table 4-1. Modified Values of the ϕ Coefficients for TiO_2 Only

	Pyroxene-like Precursors			Nepheline-like Precursors		
	M2	**M1**	**MT**	**N1**	**T1**	**SUM**
Al_2O_3	0	0.0607	0.9393	0	0	1.0000
B_2O_3	0	0	0	0	0	0.0000
CaO	0.029	0	0	0	0	0.0290
Cr_2O_3	0	0.9202	0	0	0	0.9202
Fe_2O_3	0	0.1079	0.0193	0	0.6094	0.7366
K_2O	0.3041	0	0	0.1049	0	0.4090
Li_2O	0.1745	0	0	0.1068	0	0.2813
MgO	0.0167	0.0223	0	0	0	0.0390
MnO	0.994	0.006	0	0	0	1.0000
Na_2O	0.1671	0	0	0.2518	0	0.4189
NiO	0	0.1079	0	0	0	0.1079
SiO_2	0	0	0.0193	0	0.0133	0.0326
TiO_2	**0**	**0.08128**	**0**	**0**	**0.41**	**0.49128**
U_3O_8	0	0	0	0	0	0.0000
ZrO_2	0	0.0458	0	0	0	0.0458

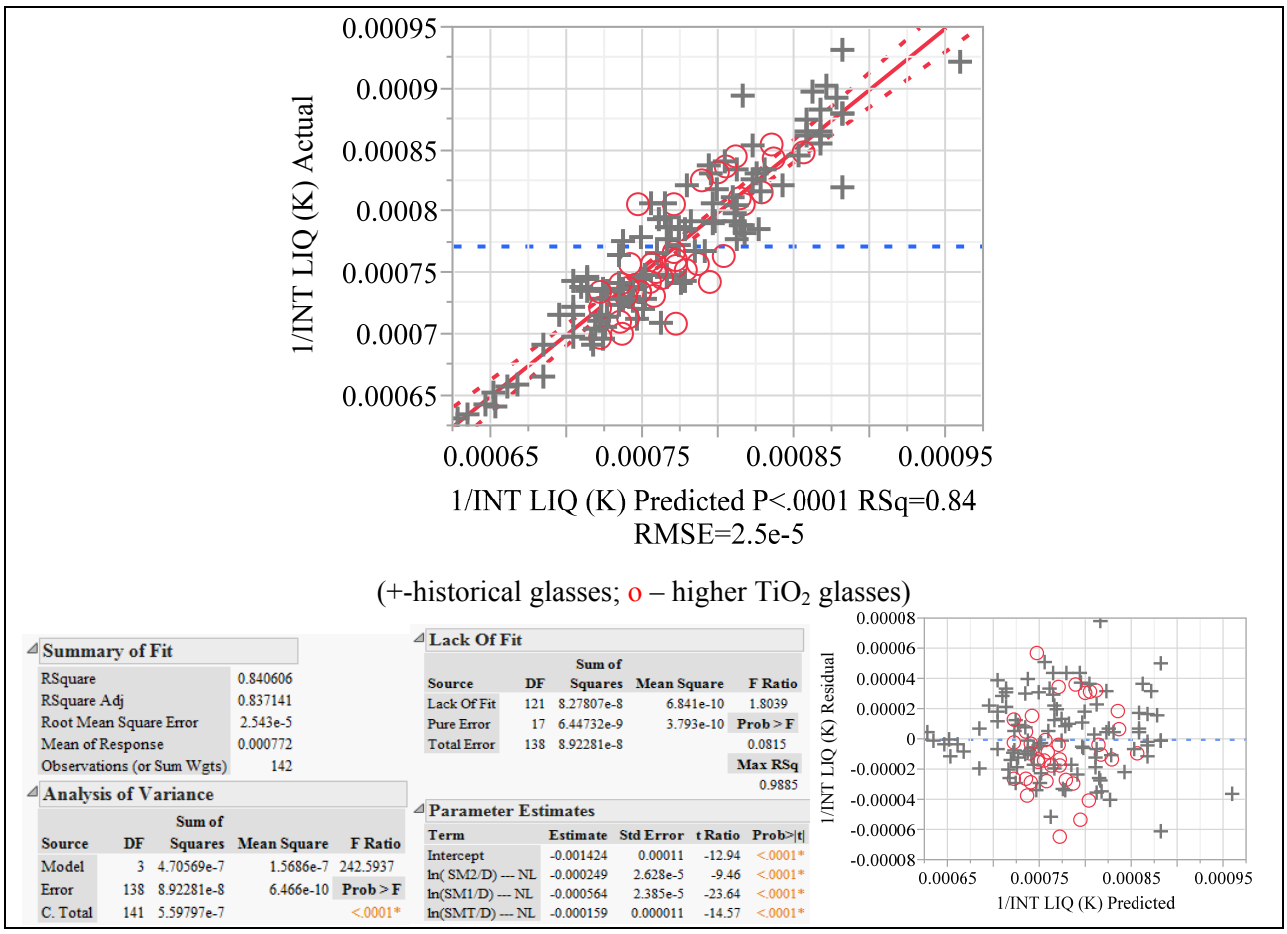

Exhibit 4-3. Modifying the TiO_2 Speciation Values and Re-fitting of the a, b, c, and d Parameters of the T_L Model

4.3.3 *Quasicrystalline Rationale for Re-speciation of Al_2O_3, Fe_2O_3, Li_2O, Na_2O, and TiO_2*

The rationale for examining the TiO_2 (ϕ coefficient) has already been discussed in Section 4.3.1. Because of the linked replacement of $2Fe^{3+}$ in the octahedral site (6 coordinated) by $Fe^{2+} + Ti^{4+}$ [94], it is logical to examine the impact of re-fitting the Fe_2O_3 term. Note that the liquidus model does not include Fe^{2+} and it is likely that Mn^{2+} or Ni^{2+} cations are participating in the linked replacement instead of or along with any Fe^{2+}. This is supported by the quasicrystalline glass experiments described in Section 3.5 and the results shown in Table 4-2, which demonstrated that, in the presence of Ni^{+2}, Fe^{+3} and Ti^{+4} the glass remains amorphous, while in the presence of Ni^{+2}, Fe^{+3}, Al^{+3} and Ti^{+4}, the strong OSPE of nickel compared to the weaker OSPE of iron, aluminum and titanium forms inverse spinels in the magnetite-structured group of spinels. In other words, Al^{+3} containing MRO's such as $NiAlO_2$ act as precursor complexes to forming the inverse spinels when the Al^{+3} and the Fe^{+3} MRO's switch divalent partners due to the OSPE.

Square pyramids (titanyl groups) with five coordinated ([5]) titanium as $^{[5]}TiO_5$, are the predominant MRO in Ti-rich silicate glasses as determined by X-ray Absorption Fine Structure (XAFS) studies [98]. Farges and others [99] demonstrated that the titanyl groups can cross link with SiO_2 tetrahedra acting as a glass homogenizer, while octahedral $^{[6]}Ti$ can act to cause liquid immiscibility in glasses [99]. TiO_2 acts as a network modifier ($^{[6]}Ti$) in glasses that are less polymerized and as a network former ($^{[4]}Ti$) in high

TiO_2 containing glasses [98, 99]. For example, $^{[5]}TiO_5$ increases compared to $^{[6]}TiO_6$ as Al substitutes for Si in $CaMgSi_2O_6$-$CaTiAl_2O_6$ glasses, as the glasses become more polymerized [29].

While $^{[5]}$Ti is the predominate coordination of Ti in glass as discussed above, Marumo, et al.[100] noted that tetrahedral $^{[4]}$Ti increases with increasing Ti content and octahedral $^{[6]}$Ti is favored at low Ti contents in glass. This was verified in the DWPF high TiO_2 containing glass viscosity report [93], because in glasses up to ~6 wt% TiO_2, the Ti acted predominately as a network modifier creating one non-bridging oxygen (NBO), i.e. as $^{[6]}$Ti. At concentrations of TiO_2 >7 wt%, the Ti is predominately $^{[4]}$Ti and acted as a network former. The exact TiO_2 concentration at which TiO_2 switches from a network modifier to a network former lie somewhere between ~6.00 and 8.00 wt% TiO_2 for DWPF type glasses and additional studies would have to be performed to determine this limit.

A competition between Al and Ti in glasses to form MRO alkali aluminate versus alkali titanyl complexes, i.e. $LiAlO_2$ versus $LiTiO_2$, is documented in the literature [101, 102]. The coordination of Ti is also known to decrease from 5-fold in glass to 4-fold with the addition of Al_2O_3 as tetrahedral (4-fold) alkali groups such as $NaAlO_2$, $NaTiO_2$ and their Li or K analogs form [102, 101]. These literature citations note that the concentration of $^{[5]}$Ti is higher in alkali silicate glasses versus alkaline earth silicate glasses, where the concentration of $^{[4]}$Ti, is higher. Differences also occur among the various types of alkali. The competition between Al and Ti for alkali as $(Na,Li)AlO_2$ and $(Na,Li)TiO_2$ MRO groups was noted in the DWPF high TiO_2 containing glass durability report [77] since the alkali and alumina terms are linked in the ROC term. So for this reason the Li_2O and Na_2O and Al_2O_3 terms (ϕ coefficients) were re-speciated. Since the liquidus data contains only a few K_2O glasses, and K_2O is a minor component, the historic K_2O term (ϕ coefficient) was considered adequate and a revised term was not deemed necessary. Since Cs_2O does not enter the pyroxene precursor structure, there was no need for a Cs_2O term in the liquidus model. For this reason there was no Cs_2O in the 2001 historic liquidus model and a Cs_2O term was not deemed necessary in the liquidus model update.

When titanium dioxide is tetrahedral ($^{[4]}$Ti), it can substitute for SiO_2 in glasses at temperatures below the glass transition temperature [99]. Indeed, titanium rich acmites, which melts incongruently to spinel, have been made at high pressures under hydrothermal conditions that show that a $NaFeSi_2O_6$ acmite can undergo a substitution of $^{[4]}$Ti for $^{[4]}$Si creating an $NaTiFeSiO_6$ acmite or a coupled substitution of $^{[4]}$Ti for $^{[4]}$Si and $^{[4]}$Al for $^{[4]}$Fe making an $NaTiAlSiO_6$ pyroxene related to jadeite ($NaAlSi_2O_6$) [64]. This is not a concern at liquidus temperatures so the SiO_2 term was not redetermined.

Lastly, because the spinel liquidus quasicrystalline model is based on the elemental species found in the pyroxene acmite from which they precipitate after incongruent melting, a short discussion of the elemental speciation in acmite is warranted. In acmites, the sodium and/or potassium in the chemical composition varies directly with the ferric iron, titanium and aluminum. Sodium and potassium also vary inversely with calcium content [103, 104]. High titanium acmite-agerines are accompanied by lower Fe^{3+} content and often a substitution of $Na(Mg,Fe)_{0.5}Ti_{0.5}Si_2O_6$ for $NaFeSi_2O_6$ [104]. The coupled interactions between iron and titanium and alkali and titanium gives additional rationale as to why redetermination of the Al_2O_3, Fe_2O_3, Li_2O, Na_2O, and TiO_2 terms (ϕ coefficients) was examined.

Solid Solutions Formed in Limited Component Waste Glasses Melted at 1050°C and 1150°C with 4 wt% TiO_2.

ly lent ion ent	Fe^{3+} and Ti^{4+}	Fe^{3+}, Al^{3+} and Ti^{4+}	Cr^{3+} and Ti^{4+}	Cr^{3+}, Al^{3+}, Ti^{4+}	Al^{3+} and Ti^{4+}
emperature of 1150°C					
$^{2+}$	Amorphous	$NiFe_2O_4$	Cr_2O_3	Cr_2O_3	Amorphous
$^{2+}$	Amorphous	Fe_9TiO_{15} ($4Fe_2O_3$•$FeTiO_3$)	Cr_2O_3	$MnCr_2O_4$ + Cr_2O_3	Amorphous
$^{2+}$	Amorphous	Fe_9TiO_{15} ($4Fe_2O_3$•$FeTiO_3$)	$MgCr_2O_4$ + Cr_2O_3	$MgCr_2O_4$ + Cr_2O_3	Amorphous
emperature of 1050°C					
$^{2+}$	$Li_2NiFe_2O_4$	$NiFe_2O_4$	Cr_2O_3	Cr_2O_3	SiO_2
$^{2+}$	Amorphous	Fe_9TiO_{15} ($4Fe_2O_3$•$FeTiO_3$)	Cr_2O_3	$MnCr_2O_4$ + Cr_2O_3	SiO_2
$^{2+}$	Amorphous	Fe_9TiO_{15} ($4Fe_2O_3$•$FeTiO_3$)	Cr_2O_3	$MgCr_2O_4$ + Cr_2O_3	SiO_2

4.3.4 *Trials Re-Speciating for Al_2O_3, Fe_2O_3, Li_2O, Na_2O, and TiO_2*

While selecting new values for the speciation of TiO_2 did lead to an acceptable outcome, a more aggressive selection of specification values, prompted by known crystal chemistry, was also investigated. In this effort, the speciation values for the following oxides were evaluated by the trial-and-error approach: Al_2O_3, Fe_2O_3, Li_2O, Na_2O, and TiO_2. This led to the candidate speciation values appearing in Table 4-3. The resulting speciation values from this effort were reviewed relative to their agreement with the known crystal chemistry of Al^{+3} described in Section 1.4.4 and Equation 8 (from Reference 6). As shown in Equation 8, Al^{+3} is always [4]-coordinated in the melt and in crystals formed on the liquidus, which are primarily nepheline. This speciation is also based on the fact that electron microprobe analyses of the spinels in DWPF like glasses have minimal Al in them [7] indicating that Al^{+3} is not preferentially speciating into an octahedral position in either a normal or inverse spinel (Equation 7 or Equation 8). This conclusion is also supported by the quasicrystalline glass experiments described in Section 3.5 and the results shown in Table 4-2. When Al^{3+} is present, only Ni-Fe inverse spinels or Cr rich normal spinels form. When Al^{3+} alone is present in a glass in conjunction with a divalent species such as nickel, magnesium or manganese, no spinels form.

Thus, the speciation values in Table 4-3 are in question; however, for completeness, they were utilized in re-fitting the parameters a, b, c, and d of Equation 1 for all of the modeling data. The results from this fitting process are provided in Exhibit 4-4. The R^2 value is ~0.867 and the RMSE, expressed in °C, is 39.0 °C. The p-value for the lack of fit statistic is 0.1769, indicating no statistically significant (at 5% significance) lack of fit for this model.

Table 4-3. Aggressively Modified Values of the ϕ Coefficients

	Pyroxene-like Precursors			Nepheline-like Precursors		
	M2	**M1**	**MT**	**N1**	**T1**	**SUM**
Al_2O_3	**0**	**0.031701**	**0.361046**	**0**	**0.02432**	**0.417067**
B_2O_3	0	0	0	0	0	0.0000
CaO	0.029	0	0	0	0	0.0290
Cr_2O_3	0	0.9202	0	0	0	0.9202
Fe_2O_3	**0**	**0.08104**	**0.02689**	**0**	**0.180304**	**0.288234**
K_2O	0.3041	0	0	0.1049	0	0.4090
Li_2O	**0.131343**	**0**	**0**	**0.046091**	**0**	**0.177434**
MgO	0.0167	0.0223	0	0	0	0.0390
MnO	0.994	0.006	0	0	0	1.0000
Na_2O	**0.069168**	**0**	**0**	**0.094959**	**0**	**0.164127**
NiO	0	0.1079	0	0	0	0.1079
SiO_2	0	0	0.0193	0	0.0133	0.0326
TiO_2	**0**	**0.038098**	**0**	**0**	**0.042829**	**0.080927**
U_3O_8	0	0	0	0	0	0.0000
ZrO_2	0	0.0458	0	0	0	0.0458

4.3.5 *Quasicrystalline Rationale for Re-speciation of Fe_2O_3, Li_2O, Na_2O, and TiO_2 Only*

As stated in the previous section (Section 4.3.3) and the data given in Table 4-2, DWPF-type glass only crystallizes spinels when $^{[4]}Al^{+3}$ is present in conjunction with Ni^{+2}, Fe^{+3}, and Ti^{+4}. The strong OSPE of nickel compared to the weaker OSPE of iron, aluminum, and titanium causes the $NiAlO_2$ MRO in the melt to switch partners and form $NiFeO_2$ MRO that form the inverse magnetite-structured spinels.

The main driver for not re-speciating Al_2O_3 is that $^{[4]}Al^{+3}$ does not change from tetrahedral to octahedral coordination in Equation 7 and Equation 8 and the quasicrystalline studies provided in Table 4-2 supports the quasicrystalline melt-crystal exchange reactions given in Equation 7 and Equation 8, i.e. the phases observed in Table 4-2 for glasses with TiO_2 present are identical to the phases in Table 1-4 when TiO_2 was absent in the melts. While there is a competition between Al and Ti for alkali to form MRO in the melt, the same crystalline species are being seen on the RHS of Equation 7 and Equation 8 when TiO_2 is present or absent in the glasses. Additional rationale for not re-speciating Al_2O_3 is that the pyroxene precursors should be high in $^{[4]}Al^{+3}$ and it is not when Al_2O_3 is speciated. Likewise, the sums of $^{[6]}Fe$ and $^{[6]}Ti$ should be higher, not lower, than the values determined in Table 4-3 when Al_2O_3 was re-speciated, i.e. compare Table 4-3 to

Table 1-1. Therefore, it was decided to retain the 2001 historic liquidus model Al_2O_3 term (ϕ coefficient) and only refit the Fe_2O_3, Li_2O, Na_2O, and TiO_2 parameters (ϕ coefficients).

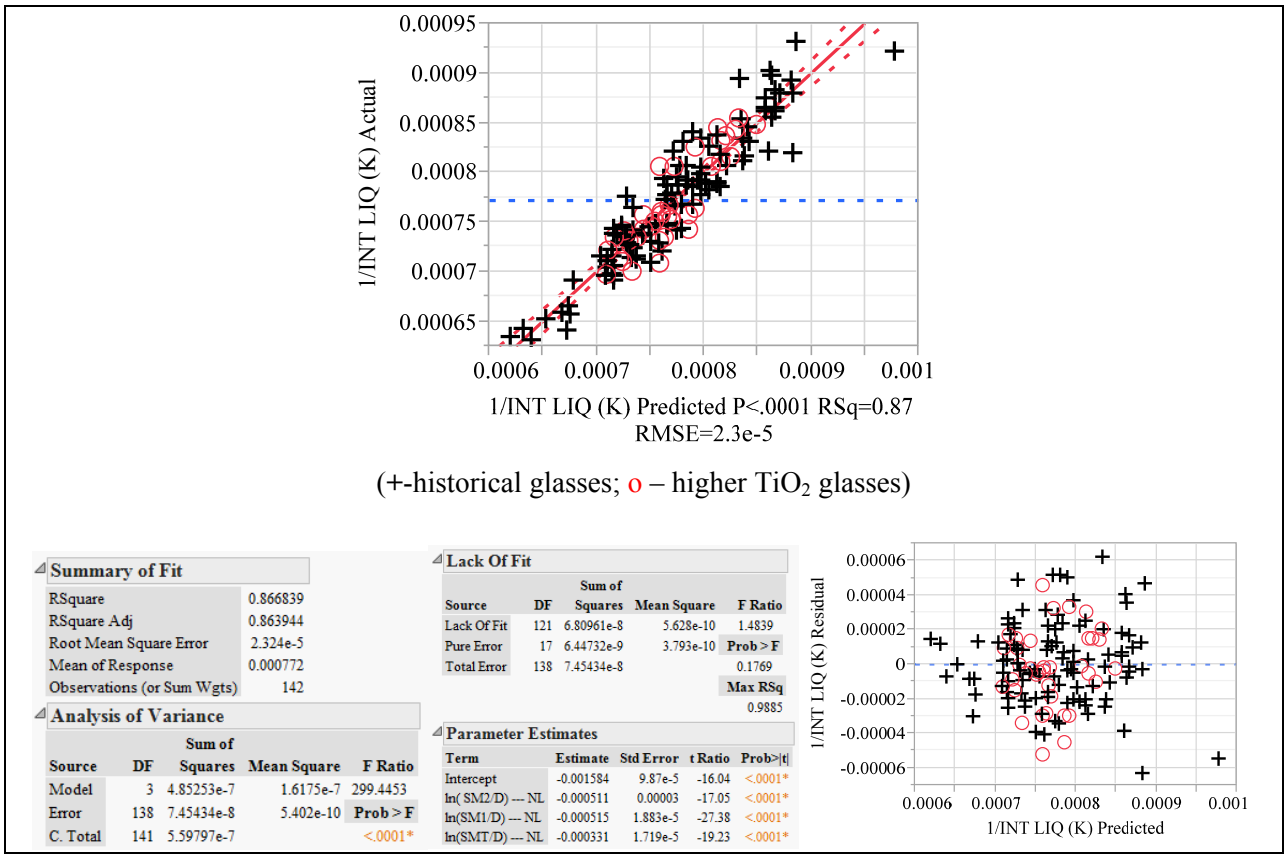

Exhibit 4-4. Aggressively Modifying Speciation Values and Re-fitting of the a, b, c, and d Parameters of the T_L Model.

4.3.6 *Final Model Re-speciating for Fe_2O_3, Li_2O, Na_2O, and TiO_2*

To align the statistical investigation more closely with the known crystal chemistry the speciation values for Al_2O_3 were held to the values of Table 4-4, while the following oxides were evaluated by the trial-and-error approach: Fe_2O_3, Li_2O, Na_2O, and TiO_2. This led to the candidate speciation values appearing in Table 4-4. These values were utilized in re-fitting the parameters a, b, c, and d of Equation 1 for all of the modeling data. The results from this fitting process are provided in Exhibit 4-5. The R^2 value is ~0.856 and the RMSE, expressed in °C, is 40.6 °C. The p-value for the lack of fit statistic is 0.1281, indicating no statistically significant (at 5% significance) lack of fit for this model.

The column labelled "sum" can be used to calculate "1-sum," which is the solvent or glassy phase since the liquidus model is a solvent-solute model [6, 7, 8] The speciation in Table 4-4, when compared to the speciation in the 2001 historic DWPF liquidus (

Table 1-1), indicates that more Fe_2O_3 is going into the pyroxene/spinel crystals and less into the glass while simultaneously allowing more TiO_2 into the glass. This is consistent with the identification of magnetite spinels as the liquidus phases for higher TiO_2 containing SWPF glasses.

Table 4-4. Modified Values of the ϕ Coefficients in Red with those for Al_2O_3 Fixed

	Pyroxene-like Precursors			Nepheline-like Precursors		
	M2	**M1**	**MT**	**N1**	**T1**	**SUM**
Al_2O_3	0	0.0607	0.9393	0	0	1
B_2O_3	0	0	0	0	0	0.0000
CaO	0.029	0	0	0	0	0.0290
Cr_2O_3	0	0.9202	0	0	0	0.9202
Fe_2O_3	**0**	**0.127347**	**0.223553**	**0**	**0.503634**	**0.854534**
K_2O	0.3041	0	0	0.1049	0	0.4090
Li_2O	**0.140267**	**0**	**0**	**0.064189**	**0**	**0.204456**
MgO	0.0167	0.0223	0	0	0	0.0390
MnO	0.994	0.006	0	0	0	1.0000
Na_2O	**0.077275**	**0**	**0**	**0.136697**	**0**	**0.213972**
NiO	0	0.1079	0	0	0	0.1079
SiO_2	0	0	0.0193	0	0.0133	0.0326
TiO_2	**0**	**0.047186**	**0**	**0**	**0.148511**	**0.195697**
U_3O_8	0	0	0	0	0	0.0000
ZrO_2	0	0.0458	0	0	0	0.0458

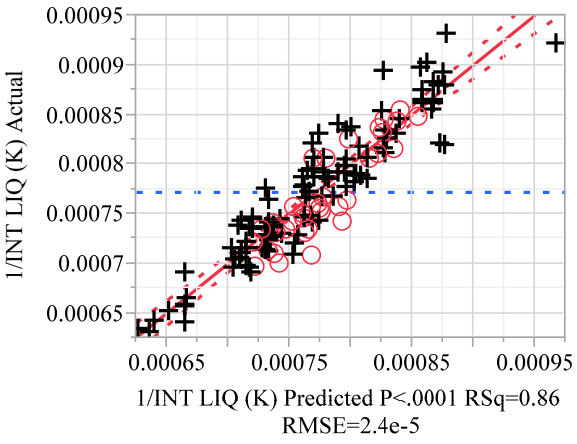

(+-historical glasses; o – higher TiO_2 glasses)

Summary of Fit

RSquare	0.855967
RSquare Adj	0.852836
Root Mean Square Error	2.417e-5
Mean of Response	0.000772
Observations (or Sum Wgts)	142

Analysis of Variance

Source	DF	Sum of Squares	Mean Square	F Ratio
Model	3	4.79167e-7	1.5972e-7	273.3706
Error	138	8.06294e-8	5.843e-10	Prob > F
C. Total	141	5.59797e-7		<.0001*

Lack Of Fit

Source	DF	Sum of Squares	Mean Square	F Ratio
Lack Of Fit	121	7.41821e-8	6.131e-10	1.6165
Pure Error	17	6.44732e-9	3.793e-10	Prob > F
Total Error	138	8.06294e-8		0.1281
				Max RSq
				0.9885

Parameter Estimates

Term	Estimate	Std Error	t Ratio	Prob>|t|	Lower 95%	Upper 95%
Intercept	-0.002023544	0.000123	-16.45	<.0001*	-0.002266800	-0.001780287
ln(SM2/D) --- NL	-0.000353617	0.000024	-14.75	<.0001*	-0.000401015	-0.000306220
ln(SM1/D) --- NL	-0.000691213	2.71e-5	-25.50	<.0001*	-0.000744805	-0.000637621
ln(SMT/D) --- NL	-0.000389016	2.031e-5	-19.15	<.0001*	-0.000429174	-0.000348858

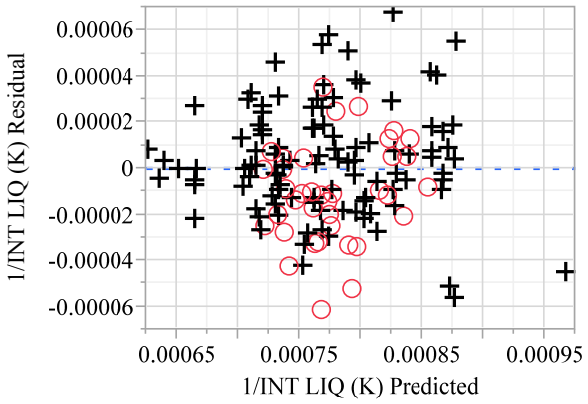

Exhibit 4-5. Modifying Speciation Values with Those for Al_2O_3 Fixed and Re-fitting of the a, b, c, and d Parameters of the T_L Model.

5.0 T_L Model Recommendation and Evaluations

In this section, the recommended T_L model is provided, data available for an independent evaluation of this model is provided and discussed, and an evaluation of the impact of the recommended model on PCCS is provided.

5.1 Model Evaluations Against 2001 Historic and SWPF Data Sets

A closer expanded look at the SWPF liquidus results, in degrees C, comparable to the fitting process of Exhibit 4-5 is provided in Exhibit 5-1. This exhibit provides a plot of the measured and predicted T_L values for the model data. For values perfectly predicted, the measured values would fall along the middle line of this plot. The two lines bounding the mid-line form a prediction interval (for an individual prediction) at a 95% confidence level. The SWPF-50 glass is the glass whose T_L measurement is the most under-predicted for these model data. In Section 2.1, the T_L measurement for this glass was called out as being a somewhat questionable result.

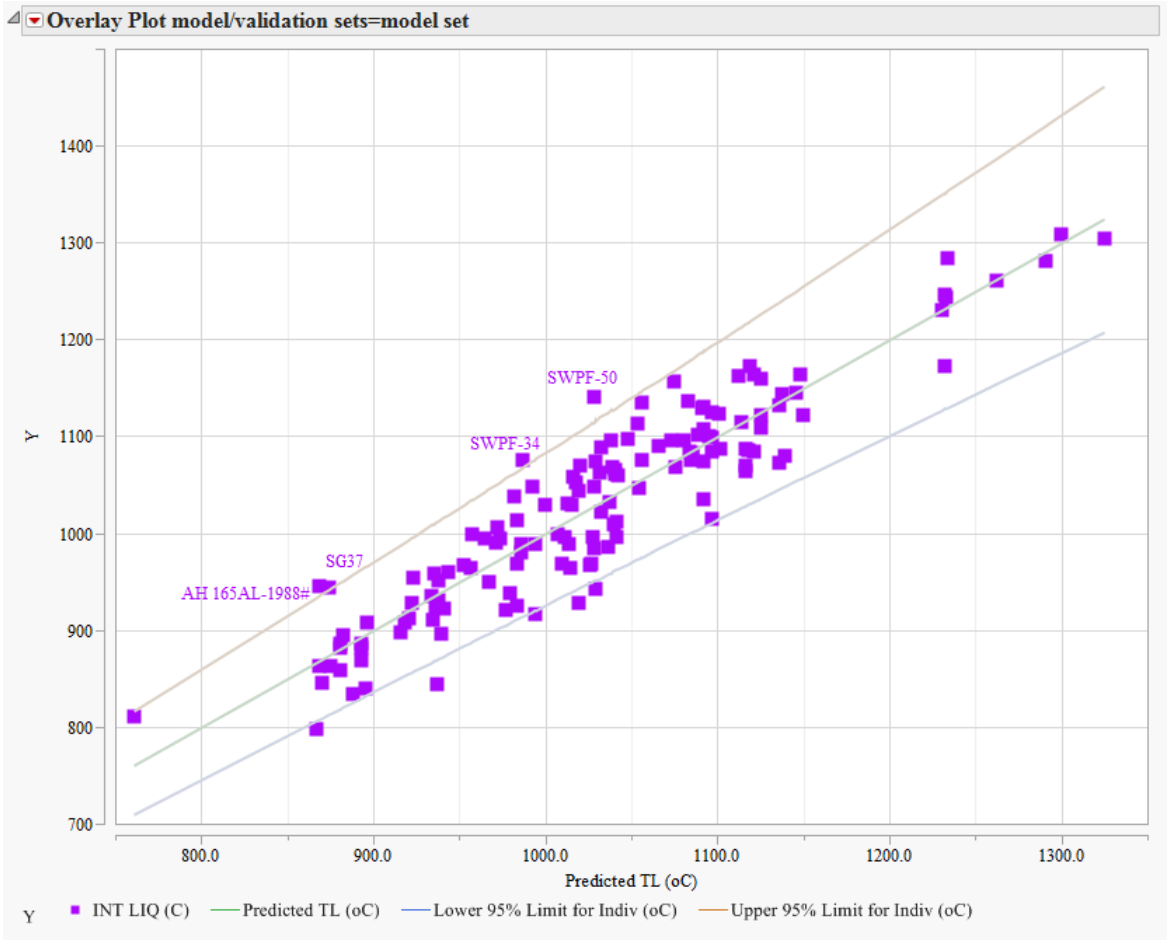

Exhibit 5-1. Predictability of Model Data (2001 Historic and SWPF Data Sets).

5.2 Model Evaluations Against Validation Data

Twenty data points from previous studies were identified and used for an independent evaluation of the recommended SWPF model's performance [90, 91]. The glass identifiers, the compositions, and measured T_L values of these validation data appear in Table A4 in Appendix A. A plot of the validation data, similar to that above for the model data, is provided in Exhibit 5-2. Only one glass, FY09EM21-25, has a T_L measurement that is under-predicted (above the upper limit of the 95% confidence interval) which validates the new SWPF liquidus model. This glass had a liquidus well below DWPF operating temperatures, i.e. 858°C (see Table A4 in Appendix A).

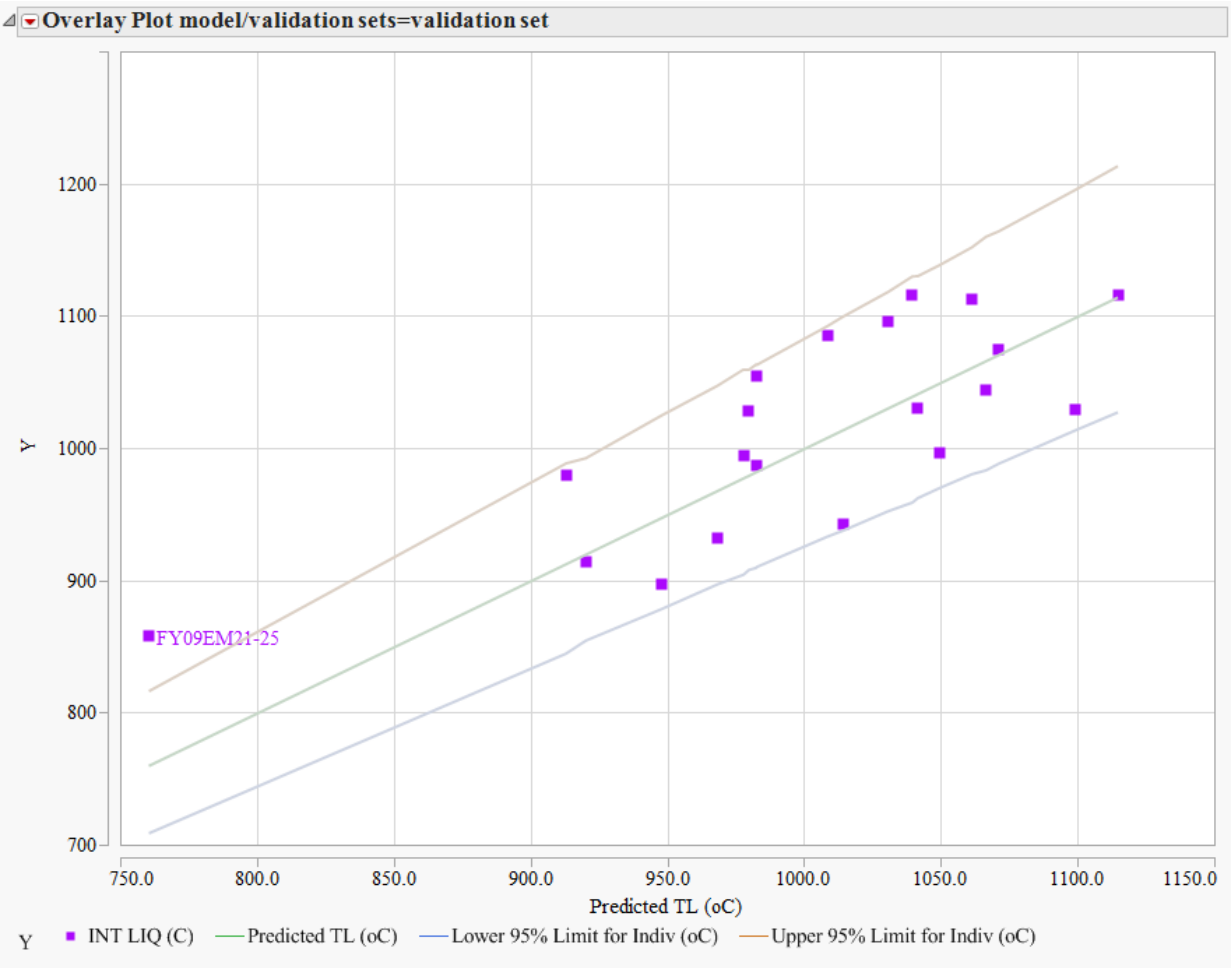

Exhibit 5-2. Predictability of Validation Data.

5.3 Recommended SWPF T_L Model

Based upon the acceptable outcome from the fitting process of Section 4.3.6 where the ϕ coefficients for Fe_2O_3, Li_2O, Na_2O, and TiO_2 were refit, and the validation described in Section 5.2, the following T_L model is recommended for use in PCCS for all glasses including sludge only and coupled flowsheet glasses with TiO_2 values up to 6.0 wt%:

Equation 9.

$$T_L(^{\circ}C) = \left\{-0.00035361 \times \ln(M_2) - 0.00069121 \times \ln(M_1) - 0.00038901 \times \ln(M_T) - 0.00202354\right\}^{-1} - 273$$

where

$$\Sigma_{MT} \equiv \phi_{MT,SiO_2} z_{SiO_2} + \phi_{MT,Al_2O_3} z_{Al_2O_3} + \phi_{MT,Fe_2O_3} z_{Fe_2O_3}$$

$$\Sigma_{M1} \equiv \phi_{M1,Al_2O_3} z_{Al_2O_3} + \phi_{M1,Fe_2O_3} z_{Fe_2O_3} + \phi_{M1,TiO_2} z_{TiO_2} + \phi_{M1,Cr_2O_3} z_{Cr_2O_3} + \phi_{M1,ZrO_2} z_{ZrO_2} + \phi_{M1,NiO} z_{NiO} + \phi_{M1,MgO} z_{MgO} + \phi_{M1,MnO} z_{MnO}$$

$$\Sigma_{M2} \equiv \phi_{M2,NiO} z_{NiO} + \phi_{M2,MgO} z_{MgO} + \phi_{M2,MnO} z_{MnO} + \phi_{M2,CaO} z_{CaO} + \phi_{M2,K_2O} z_{K_2O} + \phi_{M2,Li_2O} z_{Li_2O} + \phi_{M2,Na_2O} z_{Na_2O}$$

$$\Sigma_{T1} \equiv \phi_{T1,SiO_2} z_{SiO_2} + \phi_{T1,Al_2O_3} z_{Al_2O_3} + \phi_{T1,Fe_2O_3} z_{Fe_2O_3} + \phi_{T1,TiO_2} z_{TiO_2}$$

$$\Sigma_{N1} \equiv \phi_{N1,K_2O} z_{K_2O} + \phi_{N1,Li_2O} z_{Li_2O} + \phi_{N1,Na_2O} z_{Na_2O}$$

$$M_2 \equiv \frac{\Sigma_{M2}}{\Sigma}, M_1 \equiv \frac{\Sigma_{M1}}{\Sigma}, M_T \equiv \frac{\Sigma_{MT}}{\Sigma}, \text{and } \Sigma \equiv \Sigma_{M2} + \Sigma_{M1} + \Sigma_{MT} + \Sigma_{T1} + \Sigma_{N1}, \text{ and}$$

these speciation values are given in Table 4-4.

5.4 Evaluation of the Impact on PCCS

The impact on PCCS of the recommended T_L model is discussed in this section. Obviously, the fitted parameters of the recommended model will replace those for the current model in PCCS (when SWPF becomes operational) in satisfying the T_L constraint: Liquidus Temperature ≤ 1050 °C (as described in the technical basis document for PCCS [105]).

Two other PCCS aspects that must be addressed for the recommended model are the determination of the T_L Property Acceptability Region (PAR) and the determination between the T_L Measurement Acceptability Region (MAR) for the recommended model[f]. The close agreement of the approach leading to the recommended model and that used for the current PCCS model [6] simplifies the changes needed to update PCCS. In essence, the uncertainties for the PAR and MAR for the recommended model are addressed in a manner almost identical to those discussed in References 6 and 105; only slight modifications are needed. For completeness, Appendix B provides a full discussion of the approach to addressing the PAR aspects and Appendix C provides a full discussion (which is almost identical to that in References 6 and 105) for the MAR aspects. The discussions in these appendices will provide the appropriate guidance for the necessary changes to the technical basis document for PCCS.

6.0 Conclusions

An SWPF liquidus model has been developed for higher TiO_2 containing glasses by revising the TiO_2, Na_2O, Li_2O and Fe_2O_3 coefficients of the 2001 historic DWPF liquidus model and revising the model coefficients (a, b, c, and d) as shown in the equation below. The form of the new model developed in this study to predict spinel liquidus temperature, T_L, from composition is defined as:

$$T_L(^\circ C) = \{a \ln(M_2) + b \ln(M_1) + c \ln(M_T) + d\}^{-1} - 273$$

where

$$\Sigma_{MT} \equiv \phi_{MT,SiO_2} z_{SiO_2} + \phi_{MT,Al_2O_3} z_{Al_2O_3} + \phi_{MT,Fe_2O_3} z_{Fe_2O_3}$$

$$\Sigma_{M1} \equiv \phi_{M1,Al_2O_3} z_{Al_2O_3} + \phi_{M1,Fe_2O_3} z_{Fe_2O_3} + \phi_{M1,TiO_2} z_{TiO_2} + \phi_{M1,Cr_2O_3} z_{Cr_2O_3} + \phi_{M1,ZrO_2} z_{ZrO_2} + \phi_{M1,NiO} z_{NiO} + \phi_{M1,MgO} z_{MgO} + \phi_{M1,MnO} z_{MnO}$$

$$\Sigma_{M2} \equiv \phi_{M2,NiO} z_{NiO} + \phi_{M2,MgO} z_{MgO} + \phi_{M2,MnO} z_{MnO} + \phi_{M2,CaO} z_{CaO} + \phi_{M2,K_2O} z_{K_2O} + \phi_{M2,Li_2O} z_{Li_2O} + \phi_{M2,Na_2O} z_{Na_2O}$$

$$\Sigma_{T1} \equiv \phi_{T1,SiO_2} z_{SiO_2} + \phi_{T1,Al_2O_3} z_{Al_2O_3} + \phi_{T1,Fe_2O_3} z_{Fe_2O_3} + \phi_{T1,TiO_2} z_{TiO_2}$$

$$\Sigma_{N1} \equiv \phi_{N1,K_2O} z_{K_2O} + \phi_{N1,Li_2O} z_{Li_2O} + \phi_{N1,Na_2O} z_{Na_2O}$$

and

$$M_2 \equiv \frac{\Sigma_{M2}}{\Sigma}, M_1 \equiv \frac{\Sigma_{M1}}{\Sigma}, M_T \equiv \frac{\Sigma_{MT}}{\Sigma}, \text{and } \Sigma \equiv \Sigma_{M2} + \Sigma_{M1} + \Sigma_{MT} + \Sigma_{T1} + \Sigma_{N1}.$$

[f] In PCCS, the PAR is utilized to address the property-composition model uncertainty and the MAR is used to address the measurement uncertainty; so that these uncertainties can be appropriately integrated into the constraints imposed by PCCS.

Assuming that pyroxene-like melt phase complexes or precursors control crystallization in expected DWPF glasses, the new ϕ coefficients representing the distribution of the various species in the pyroxene-like precursors are provided in Table 4-4 of the report. The least-squares results for the ($1/T_L$) versus the above expression for 142 model data representing DWPF compositions were used to estimate the parameters in the above model yielding a = –0.000353617, b = –0.000691213, c = –0.000389016, and d = –0.00202354. The summary statistics for the least-squares fit obtained were R^2 = 0.856 and s_r = $2.417x10^{-5}K^{-1}$, and the results indicated no significant lack-of-fit. (The RMSE value may be re-expressed as 40.6°C.)

Two additional SRNL/PNNL liquidus studies were examined at TiO_2 concentrations up to 6.52 wt%. The SWPF liquidus model was also shown to be valid up to 4.286 wt% CaO (in the validation data) and 2.65 wt% MgO (in the historical and high TiO_2 data). This means that CaO and/or MgO can be added to frit compositions up to these concentrations since CaO is known to suppress nepheline crystallization and MgO is known to improve glass durability and reduce DWPF refractory corrosion and wear. While the SWPF liquidus model has been modeled/validated up to ~6 wt% (actual measured value of 5.85 wt% TiO_2), the role of TiO_2 on liquidus of DWPF-type glasses switches from being a network modifier to being a network former somewhere between 6.62 and 8.38 wt% TiO_2. The exact region at which this switch occurs has not been investigated so the usage of the SWPF liquidus model and other models will be limited to ~6.0 wt% TiO_2, which has been the range investigated in all the SWPF modeling studies.

The ultimate limit on the amount of TiO_2 that can be accommodated from SWPF will be determined by the three PCCS models, the waste composition of a given sludge batch, the waste loading of the sludge batch, and the frit used for vitrification. Once a component like TiO_2 is present at larger concentrations than 2 wt%, the interactions of that component with other components in the melter feed must be considered simultaneously, i.e. an individual solubility limit cannot be defined to globally account for the interactions with all the remaining sludge/frit composition variables.

Only the ϕ parameters for TiO_2, Fe_2O_3, Li_2O, and Na_2O were refit along with the equation coefficients for M_2, M_1, M_T and the intercept. It is known that TiO_4 or TiO_5 melt species can compete with Al^{3+} for alkali bonding and it is known that TiO_4 or TiO_5 melt species have a coupled impact with Fe^{3+} on their joint solubility in a melt or glass which is why the TiO_2, Fe_2O_3, Na_2O and Li_2O coefficients were refit in the liquidus model. The Al_2O_3 term was not refit as Al^{3+} remains tetrahedrally coordinated as AlO_4 in both the melt and in the crystalline state.

Appendix A. Supporting Tables and Exhibits

Table A1. T_L and Compositional Information for 2001 Model Data

(values are in wt%)

Sample ID	INT LIQ (C)	Al2O3	B2O3	BaO	CaO	Cr2O3	Cs2O	CuO	Cu2O	FeO	Fe2O3	K2O	La2O3
AH-131Fe-AB-PNNL	1108	2.25	7.33	0.00	1.01	0.00	0.00	0.00	0.00	5.86	11.09	0.00	0.00
AH-165Fe-AB-PNNL	1099.5	1.42	7.28	0.00	1.40	0.00	0.00	0.00	0.00	5.46	10.93	0.00	0.00
AH-168Av-AB-PNNL	969	5.31	12.65	0.02	0.70	0.00	0.00	0.00	0.00	0.63	10.90	0.05	0.01
AH-200Fe-AB-PNNL	1087.5	2.07	10.10	0.00	0.92	0.00	0.00	0.00	0.00	5.90	9.84	3.15	0.00
AH-202Fe-AB-PNNL	1122.5	1.36	7.08	0.00	0.96	0.00	0.00	0.00	0.00	6.90	8.93	3.28	0.00
SG01	1124	2.50	10.23	0.00	1.98	0.09	0.00	0.00	0.00	0.19	13.95	3.79	0.00
SG03	1164	3.95	9.42	0.00	1.52	0.24	0.00	0.00	0.00	0.16	11.62	2.07	0.00
SG04	1261	8.28	4.89	0.00	0.32	0.08	0.00	0.00	0.00	0.20	14.50	1.49	0.00
SG05	1084	5.60	7.73	0.00	1.15	0.20	0.00	0.00	0.00	0.14	10.49	2.67	0.00
SG05b	1082	5.56	7.84	0.00	1.14	0.19	0.00	0.00	0.00	0.14	10.21	2.51	0.00
SG06	921	7.90	5.01	0.00	2.00	0.09	0.00	0.00	0.00	0.19	14.06	3.77	0.00
SG07	950	8.11	10.62	0.00	0.31	0.29	0.00	0.00	0.00	0.04	5.77	3.64	0.00
SG08	1114	4.12	6.50	0.00	1.57	0.14	0.00	0.00	0.00	0.17	12.34	3.21	0.00
SG09	1173	8.21	10.11	0.00	2.01	0.28	0.00	0.00	0.00	0.20	14.62	1.51	0.00
SG10	1098	4.03	6.65	0.00	0.75	0.25	0.00	0.00	0.00	0.11	8.12	3.22	0.00
SG11	895	3.86	9.48	0.00	0.76	0.14	0.00	0.00	0.00	0.11	8.00	2.10	0.00
SG12	1030	2.59	5.01	0.00	0.32	0.28	0.00	0.00	0.00	0.13	14.53	1.50	0.00
SG13	1063	2.56	9.75	0.00	0.32	0.28	0.00	0.00	0.00	0.29	8.13	1.48	0.00
SG14	951	2.66	11.00	0.00	0.31	0.09	0.00	0.00	0.00	0.14	14.93	3.73	0.00
SG16	995	6.93	6.33	0.00	1.57	0.14	0.00	0.00	0.00	0.11	8.28	2.06	0.00
SG17	1075	3.97	7.92	0.00	1.59	0.14	0.00	0.00	0.00	0.17	12.19	3.23	0.00
SG18	859	2.52	10.43	0.00	0.33	0.28	0.00	0.00	0.00	0.08	14.27	1.50	0.00
SG18	883	2.52	10.43	0.00	0.33	0.28	0.00	0.00	0.00	0.08	14.27	1.50	0.00
SG18	886.5	2.52	10.43	0.00	0.33	0.28	0.00	0.00	0.00	0.08	14.27	1.50	0.00
SG18b	869	2.67	10.28	0.00	0.32	0.28	0.00	0.00	0.00	0.08	14.61	1.46	0.00
SG18b	883	2.67	10.28	0.00	0.32	0.28	0.00	0.00	0.00	0.08	14.61	1.46	0.00
SG18b	886.5	2.67	10.28	0.00	0.32	0.28	0.00	0.00	0.00	0.08	14.61	1.46	0.00
SG19	929	6.59	10.31	0.00	0.31	0.28	0.00	0.00	0.00	0.08	5.72	3.72	0.00
SG20(s,c)	799	8.34	4.97	0.00	1.95	0.10	0.00	0.00	0.00	0.08	6.03	1.52	0.00
SG21	987	3.97	8.93	0.00	1.59	0.24	0.00	0.00	0.00	0.11	7.77	2.04	0.00
SG22	1145	6.94	6.54	0.00	1.53	0.25	0.00	0.00	0.00	0.17	12.57	2.10	0.00
SG23	1069	4.27	6.52	0.00	1.58	0.25	0.00	0.00	0.00	0.11	7.87	3.14	0.00
SG25	1309.5	7.91	11.54	0.00	0.35	0.09	0.00	0.00	0.00	0.19	14.21	3.66	0.00
SG26	1071	4.07	6.69	0.00	0.77	0.24	0.00	0.00	0.00	0.17	12.35	2.07	0.00
SG27	1086	6.95	9.43	0.00	1.53	0.25	0.00	0.00	0.00	0.15	10.91	3.25	0.00
SG29	811	8.14	5.15	0.00	0.32	0.10	0.00	0.00	0.00	0.08	5.76	1.54	0.00
SG30	1030	8.03	5.09	0.00	1.92	0.10	0.00	0.00	0.00	0.08	5.81	3.67	0.00
SG31	1081	8.36	11.10	0.00	2.00	0.09	0.00	0.00	0.00	0.08	15.09	3.70	0.00
SG32	1132	8.21	10.58	0.00	0.32	0.10	0.00	0.00	0.00	0.31	14.54	1.51	0.00
SG33	943	8.36	10.43	0.00	1.95	0.28	0.00	0.00	0.00	0.13	6.04	3.77	0.00
SG34	1282	8.33	9.61	0.00	1.96	0.27	0.00	0.00	0.00	0.20	14.41	1.50	0.00
SG35	1231	8.12	5.31	0.00	0.32	0.28	0.00	0.00	0.00	0.19	13.66	3.67	0.00
SG37	944.5	2.63	10.29	0.00	1.96	0.30	0.00	0.00	0.00	0.11	5.67	3.83	0.00
SG38	897	2.67	11.13	0.00	0.32	0.09	0.00	0.00	0.00	0.20	14.50	3.71	0.00

Table A1. T_L and Compositional Information for 2001 Model Data *(continued)*
(values are in wt%)

Sample ID	INT LIQ (C)	Al2O3	B2O3	BaO	CaO	Cr2O3	Cs2O	CuO	Cu2O	FeO	Fe2O3	K2O	La2O3
SG39	1164	2.61	5.44	0.00	1.96	0.28	0.00	0.00	0.00	0.22	14.13	1.48	0.00
SG40	1173	8.20	10.80	0.00	0.31	0.29	0.00	0.00	0.00	0.08	5.86	1.44	0.00
SG41	1304	8.10	11.12	0.00	1.98	0.08	0.00	0.00	0.00	0.20	14.32	1.61	0.00
SG42	990	4.55	9.15	0.00	0.74	0.23	0.00	0.00	0.00	0.16	12.04	3.23	0.00
SG43	924	6.77	8.80	0.00	0.73	0.15	0.00	0.00	0.00	0.11	7.95	3.23	0.00
SG44	1244	7.00	9.19	0.00	0.74	0.15	0.00	0.00	0.00	0.17	12.59	2.13	0.00
SG45(s,c)	936	2.61	10.56	0.00	1.96	0.10	0.00	0.00	0.00	0.08	5.72	1.53	0.00
SG46	1247	2.65	5.22	0.00	0.31	0.28	0.00	0.00	0.00	0.20	14.59	3.88	0.00
SG47	1144	2.67	5.03	0.00	1.97	0.28	0.00	0.00	0.00	0.20	14.73	1.52	0.00
SG50	1285	2.65	5.42	0.00	1.98	0.28	0.00	0.00	0.00	0.20	14.71	3.72	0.00
SG51	1033	7.98	5.22	0.00	1.95	0.28	0.00	0.00	0.00	0.20	14.64	3.72	0.00
AH 131AL-1992#	835	13.50	10.90	0.00	0.38	0.00	0.00	0.00	0.00	0.09	4.58	0.00	0.36
AH 131AL-1985	863	14.05	11.35	0.00	0.39	0.00	0.00	0.00	0.00	0.13	3.99	0.05	0.35
AH 131AV-1985 - No La	990	7.18	10.88	0.06	0.74	0.07	0.00	0.00	0.00	0.27	11.40	0.04	0.00
AH 131AV-1992 - No La#	995	4.39	7.60	0.00	0.76	0.00	0.00	0.00	0.00	0.29	11.57	0.00	0.00
AH 131 FE -RED-1992-No La#	1075	2.25	7.33	0.00	1.01	0.00	0.00	0.00	0.00	5.86	11.09	0.00	0.00
AH 165AL-1985(h)	863	13.30	7.57	0.29	0.52	0.00	0.00	0.00	0.00	0.04	4.12	0.05	0.00
AH 165AL-1992#	840	13.40	7.34	0.00	0.51	0.00	0.00	0.00	0.00	0.12	4.70	0.00	0.00
AH 165AV -1985	917	5.34	7.33	0.02	0.69	0.05	0.00	0.00	0.00	0.20	11.88	0.06	0.00
AH 165AV-REVISED LIQ - 1988	1006	5.08	7.27	0.02	0.88	0.03	0.00	0.00	0.00	0.20	11.78	0.09	0.00
AH 165AV - 1992#	1000	5.17	6.57	0.00	1.04	0.00	0.00	0.00	0.00	0.19	11.38	0.00	0.00
AH165FE-RED-1985	1102	1.28	7.48	0.28	1.49	0.01	0.01	0.00	0.00	6.65	9.71	0.03	0.01
AH 165FE-RED -1992#	1085	1.42	7.28	0.00	1.40	0.00	0.00	0.00	0.00	5.46	10.93	0.00	0.00
AH165FE-OX-1996# (not ox)	1135	1.45	7.36	0.00	1.42	0.00	0.00	0.00	0.00	5.99	10.54	0.03	0.00
AH 168AL-1988#	846	14.16	12.11	0.01	0.44	0.00	0.00	0.00	0.00	0.02	3.43	0.23	0.00
AH 168AV-1985	1014	5.31	12.65	0.02	0.70	0.00	0.00	0.00	0.00	0.63	10.90	0.05	0.01
AH 168AV-1988	925	5.31	12.65	0.02	0.70	0.00	0.00	0.00	0.00	0.63	10.90	0.05	0.01
AH 168AV-1992	990	5.58	10.60	0.00	0.68	0.00	0.00	0.00	0.00	0.61	10.51	0.00	0.00
AH 168AV-1992(peeler)	980	5.58	10.60	0.00	0.68	0.00	0.00	0.00	0.00	0.61	10.51	0.00	0.00
AH 168FE-RED-1988	1022	1.44	11.73	0.02	1.05	0.01	0.00	0.00	0.00	5.20	7.85	0.06	0.00
AH 168FE-RED (?)-1992	1085	2.47	11.40	0.00	1.35	0.00	0.00	0.00	0.00	6.22	9.39	0.00	0.00
AH 168 FE-OX-1996#	1130	3.29	12.00	0.00	1.29	0.00	0.00	0.00	0.00	0.38	16.98	0.03	0.00
AH 200AL - 1988#	929	13.85	10.30	0.00	0.56	0.00	0.00	0.00	0.00	0.02	3.95	3.29	0.00
AH 200AL -1992#	845	13.40	10.20	0.00	0.54	0.00	0.00	0.00	0.00	0.06	4.40	3.12	0.00
AH200AV(AH-8)-1988#	996	5.88	10.10	0.00	0.69	0.02	0.04	0.00	0.00	0.29	11.28	3.08	0.00
AH 200AV - 1988#	997	5.16	10.24	0.03	0.88	0.00	0.00	0.00	0.00	0.08	11.21	3.18	0.01
AH 200AV - 1992#	985	5.14	10.30	0.00	0.63	0.00	0.00	0.00	0.00	0.08	11.81	3.18	0.00
AH 200FE-RED-1988	1126	1.39	10.35	0.01	0.97	0.01	0.00	0.00	0.00	6.01	9.92	3.31	0.01
AH 200FE-RED-1992#	1065	2.07	10.10	0.00	0.92	0.00	0.00	0.00	0.00	5.90	9.84	3.15	0.00
AH 200FE-1992(peeler)#	1070	2.07	10.10	0.00	0.92	0.00	0.00	0.00	0.00	5.90	9.84	3.15	0.00
AH 202AL - 1988 (AH131Fe/Av?)	959	13.70	7.53	0.02	0.40	0.00	0.00	0.00	0.00	0.07	3.81	3.45	0.00
AH 202AL (Pt not good) - 1992#	965	13.90	7.42	0.00	0.41	0.00	0.00	0.00	0.00	0.19	4.19	3.32	0.00
AH202AV (AH-10) - 1985#	965	5.14	7.59	0.00	0.68	0.01	0.05	0.00	0.00	0.14	11.14	3.09	0.00
AH 202AV - 1988#	967	4.98	7.55	0.02	0.72	0.00	0.00	0.00	0.00	0.08	11.66	3.45	0.01

Table A1. T_L and Compositional Information for 2001 Model Data *(continued)*
(values are in wt%)

Sample ID	INT LIQ (C)	Al2O3	B2O3	BaO	CaO	Cr2O3	Cs2O	CuO	Cu2O	FeO	Fe2O3	K2O	La2O3
AH 202AV - 1992#	1010	4.96	7.44	0.00	0.72	0.00	0.00	0.00	0.00	0.14	11.75	3.33	0.00
AH 202FE-RED - 1988#	1123	1.38	7.32	0.02	1.01	0.01	0.00	0.00	0.00	6.88	9.86	3.47	0.01
AH 202FE-RED-1992#	1110	1.36	7.08	0.00	0.96	0.00	0.00	0.00	0.00	6.90	8.93	3.28	0.00
AH 202FE-1992(peeler)#	1160	1.36	7.08	0.00	0.96	0.00	0.00	0.00	0.00	6.90	8.93	3.28	0.00
AH 202FE-OX - 1996#	1100	0.99	7.34	0.00	1.36	0.00	0.00	0.00	0.00	0.62	15.31	3.26	0.00
AH-5-1985#	991	5.48	6.95	0.00	0.66	0.00	0.00	0.00	0.00	0.19	11.19	3.16	0.00
AH-9-1985#	1000	6.04	8.75	0.00	0.69	0.01	0.05	0.00	0.00	0.16	11.43	3.13	0.00
AH-13 -1985#	1096	6.48	6.41	0.00	1.25	0.01	0.05	0.00	0.00	0.06	13.53	3.06	0.00
AH-16-1985#	1073	6.36	7.20	0.00	1.26	0.08	0.03	0.00	0.00	0.19	13.19	3.06	0.00
DWPF STARTUP FRIT (10/26/87)	1066	4.59	8.49	0.12	1.45	0.09	0.01	0.00	0.00	0.19	13.89	2.68	0.00
DWPF STARTUP FRIT (10/28/87)	1062	4.67	8.66	0.08	1.44	0.10	0.01	0.00	0.00	0.19	13.99	2.69	0.00
DWPF STARTUP FRIT (10/27/87) (s,p)	1012	4.53	8.37	0.10	1.51	0.09	0.01	0.00	0.00	0.19	14.08	2.74	0.00
DWPF STARTUP FRIT (10/27/87)	997	4.53	8.37	0.10	1.51	0.09	0.01	0.00	0.00	0.19	14.08	2.74	0.00
Carters 165 Black Frit	909	4.62	6.84	0.11	1.58	0.00	0.00	0.00	0.00	0.16	11.43	0.13	0.00
AH 131 FE-1992 (peeler)-No La#	1035	2.25	7.33	0.00	1.01	0.00	0.00	0.00	0.00	5.86	11.09	0.00	0.00
AH 165AL-1988#	946	13.30	7.57	0.29	0.52	0.00	0.00	0.00	0.00	0.04	4.12	0.05	0.00
AH 165 FE-1992 (peeler)#	1015	1.42	7.28	0.00	1.40	0.00	0.00	0.00	0.00	5.46	10.93	0.00	0.00

Sample ID	INT LIQ (C)	Li2O	MgO	MnO	Na2O	NiO	SiO2	SrO	ThO2	TiO2	U3O8	ZrO2
AH-131Fe-AB-PNNL	1108	4.09	0.66	0.93	10.90	2.56	51.40	0.00	0.00	0.05	0.00	0.87
AH-165Fe-AB-PNNL	1099.5	4.05	0.65	1.07	10.70	2.97	52.00	0.00	0.00	0.00	0.00	0.85
AH-168Av-AB-PNNL	969	4.28	0.73	2.72	10.30	0.98	50.40	0.00	0.00	0.06	0.00	0.76
AH-200Fe-AB-PNNL	1087.5	2.59	1.21	0.95	10.60	2.57	47.40	0.00	0.00	1.78	0.00	0.02
AH-202Fe-AB-PNNL	1122.5	4.27	1.26	0.95	7.62	2.73	52.50	0.00	0.00	1.72	0.00	0.02
SG01	1124	5.89	0.49	0.97	6.22	2.13	42.71	0.00	0.00	0.65	4.48	0.00
SG03	1164	3.41	1.88	2.41	9.90	1.56	46.64	0.00	0.00	0.28	3.52	0.00
SG04	1261	5.99	2.58	0.96	6.17	2.06	51.75	0.00	0.00	0.16	0.26	0.00
SG05	1084	4.44	1.56	1.96	8.48	1.10	52.27	0.00	0.00	0.40	2.51	0.00
SG05b	1082	4.02	1.43	1.97	8.57	1.08	51.07	0.00	0.00	0.42	2.39	0.00
SG06	921	2.97	0.50	0.98	10.95	0.05	47.93	0.00	0.00	0.65	0.26	0.00
SG07	950	5.43	2.29	2.91	6.03	0.06	53.29	0.00	0.00	0.17	0.26	0.00
SG08	1114	3.44	2.06	2.43	7.54	0.56	54.26	0.00	0.00	0.28	1.54	0.00
SG09	1173	5.78	0.52	0.98	6.30	0.05	43.96	0.00	0.00	0.16	4.81	0.00
SG10	1098	5.25	2.03	2.45	7.47	1.61	54.17	0.00	0.00	0.28	3.62	0.00
SG11	895	5.11	1.94	1.48	9.72	0.57	53.48	0.00	0.00	0.29	1.54	0.00
SG12	1030	3.04	2.48	0.97	11.14	0.04	56.35	0.00	0.00	0.16	0.27	0.00
SG13	1063	5.87	0.50	2.88	5.99	2.14	56.71	0.00	0.00	0.16	0.27	0.00
SG14	951	2.74	2.60	2.93	11.28	0.05	43.34	0.00	0.00	0.17	5.14	0.00
SG16	995	5.18	2.01	2.38	9.87	0.56	50.08	0.00	0.00	0.52	3.67	0.00
SG17	1075	5.32	0.98	1.45	9.98	1.59	45.72	0.00	0.00	0.53	3.58	0.00
SG18	859	5.90	0.47	2.84	10.85	0.04	46.78	0.00	0.00	0.64	0.27	0.00
SG18	883	5.90	0.47	2.84	10.85	0.04	46.78	0.00	0.00	0.64	0.27	0.00
SG18	886.5	5.90	0.47	2.84	10.85	0.04	46.78	0.00	0.00	0.64	0.27	0.00

Table A1. T_L and Compositional Information for 2001 Model Data *(continued)*
(values are in wt%)

Sample ID	INT LIQ (C)	Li2O	MgO	MnO	Na2O	NiO	SiO2	SrO	ThO2	TiO2	U3O8	ZrO2
SG18b	869	5.89	0.49	2.87	10.89	0.04	47.77	0.00	0.00	0.64	0.27	0.00
SG18b	883	5.89	0.49	2.87	10.89	0.04	47.77	0.00	0.00	0.64	0.27	0.00
SG18b	886.5	5.89	0.49	2.87	10.89	0.04	47.77	0.00	0.00	0.64	0.27	0.00
SG19	929	5.91	0.49	0.95	10.90	2.15	44.38	0.00	0.00	0.18	4.65	0.00
SG20(s,c)	799	5.90	2.56	0.99	11.05	0.06	51.51	0.00	0.00	0.64	4.98	0.00
SG21	987	5.17	0.97	2.31	7.23	1.60	53.43	0.00	0.00	0.52	1.58	0.00
SG22	1145	5.19	1.01	1.46	9.84	1.58	50.01	0.00	0.00	0.28	1.61	0.00
SG23	1069	3.39	1.88	1.48	9.93	1.58	53.45	0.00	0.00	0.54	1.49	0.00
SG25	1309.5	2.72	2.37	0.99	6.59	2.06	47.05	0.00	0.00	0.17	0.26	0.00
SG26	1071	3.75	1.00	1.46	10.07	0.58	52.27	0.00	0.00	0.52	3.66	0.00
SG27	1086	5.11	1.98	1.48	7.44	0.58	47.15	0.00	0.00	0.29	3.62	0.00
SG29	811	6.16	0.48	2.91	11.20	0.05	51.42	0.00	0.00	0.65	4.65	0.00
SG30	1030	5.37	2.37	2.85	10.90	2.06	44.10	0.00	0.00	0.18	4.50	0.00
SG31	1081	5.34	2.65	2.93	6.23	0.06	43.11	0.00	0.00	0.65	0.26	0.00
SG32	1132	5.97	0.49	0.97	10.94	2.08	42.96	0.00	0.00	0.63	0.27	0.00
SG33	943	5.91	0.52	2.86	10.62	2.11	47.55	0.00	0.00	0.61	0.26	0.00
SG34	1282	2.99	2.52	2.85	6.35	0.05	42.05	0.00	0.00	0.64	4.76	0.00
SG35	1231	6.06	2.38	2.89	10.95	2.13	41.80	0.00	0.00	0.65	0.26	0.00
SG37	944.5	5.88	2.40	0.98	6.04	0.32	58.23	0.00	0.00	0.66	0.26	0.00
SG38	897	2.71	2.57	2.97	11.28	0.06	43.29	0.00	0.00	0.65	5.07	0.00
SG39	1164	3.01	0.50	2.87	11.16	2.12	52.23	0.00	0.00	0.64	0.26	0.00
SG40	1173	2.65	2.39	0.97	10.96	2.08	46.93	0.00	0.00	0.66	4.71	0.00
SG41	1304	2.75	0.52	2.94	6.52	2.02	42.42	0.00	0.00	0.18	4.90	0.00
SG42	990	5.10	1.94	2.41	9.78	0.57	45.99	0.00	0.00	0.54	1.58	0.00
SG43	924	3.77	0.98	2.45	9.69	0.58	51.54	0.00	0.00	0.28	1.61	0.00
SG44	1244	3.71	1.98	1.46	7.55	1.59	51.02	0.00	0.00	0.53	1.67	0.00
SG45(s,c)	936	2.96	2.43	2.94	10.80	2.14	55.89	0.00	0.00	0.17	0.26	0.00
SG46	1247	5.85	2.49	0.99	6.46	2.10	49.20	0.00	0.00	0.64	4.90	0.00
SG47	1144	5.83	2.48	1.00	11.08	2.06	45.57	0.00	0.00	0.18	5.00	0.00
SG50	1285	3.02	0.50	2.89	6.30	2.10	49.32	0.00	0.00	0.64	4.81	0.00
SG51	1033	2.99	0.50	0.96	10.90	0.05	48.89	0.00	0.00	0.16	0.26	0.00
AH 131AL-1992#	835	4.09	1.38	2.51	14.10	0.63	46.40	0.00	0.00	0.72	0.00	0.34
AH 131AL-1985	863	4.19	1.42	2.69	14.90	0.61	44.60	0.00	0.00	0.77	0.00	0.39
AH 131AV-1985 - No La	990	3.88	1.28	0.82	14.30	1.08	45.20	0.00	0.00	0.70	0.00	0.32
AH 131AV-1992 - No La#	995	4.25	0.67	2.59	9.86	1.04	54.99	0.00	0.00	0.06	0.00	0.88
AH 131 FE -RED-1992-No La#	1075	4.09	0.66	0.93	10.90	2.56	51.40	0.00	0.00	0.05	0.00	0.87
AH 165AL-1985(h)	863	4.28	0.67	2.75	11.10	0.57	52.70	0.01	0.00	0.06	0.00	0.97
AH 165AL-1992#	840	4.20	0.66	2.62	10.60	0.67	53.60	0.00	0.00	0.00	0.00	0.79
AH 165AV -1985	917	5.11	0.73	2.78	10.30	1.07	53.10	0.00	0.00	0.17	0.00	0.72
AH 165AV-REVISED LIQ - 1988	1006	5.09	0.69	2.76	10.23	1.02	53.27	0.00	0.00	0.11	0.00	0.79
AH 165AV - 1992#	1000	5.02	0.66	2.57	9.96	1.01	55.29	0.00	0.00	0.00	0.00	0.76
AH165FE-RED-1985	1102	4.18	0.66	1.13	11.20	3.05	51.70	0.01	0.00	0.06	0.00	0.95
AH 165FE-RED -1992#	1085	4.05	0.65	1.07	10.70	2.97	52.00	0.00	0.00	0.00	0.00	0.85

Table A1. T_L and Compositional Information for 2001 Model Data *(continued)*
(values are in wt%)

Sample ID	INT LIQ (C)	Li2O	MgO	MnO	Na2O	NiO	SiO2	SrO	ThO2	TiO2	U3O8	ZrO2
AH165FE-OX-1996# (not ox)	1135	4.27	0.64	1.01	11.20	2.58	49.60	0.01	0.00	0.00	0.00	0.87
AH 168AL-1988#	846	4.24	0.71	2.66	10.42	0.53	47.66	0.01	0.00	0.05	0.00	0.67
AH 168AV-1985	1014	4.28	0.73	2.72	10.30	0.98	50.40	0.00	0.00	0.06	0.00	0.76
AH 168AV-1988	925	4.28	0.73	2.72	10.30	0.98	50.40	0.00	0.00	0.06	0.00	0.76
AH 168AV-1992	990	4.24	0.74	2.64	10.10	1.02	51.60	0.00	0.00	0.00	0.00	0.69
AH 168AV-1992(peeler)	980	4.24	0.74	2.64	10.10	1.02	51.60	0.00	0.00	0.00	0.00	0.69
AH 168FE-RED-1988	1022	4.17	0.71	0.74	11.15	2.77	53.05	0.01	0.00	0.04	0.00	0.67
AH 168FE-RED (?)-1992	1085	4.12	0.71	0.98	10.80	2.82	48.30	0.00	0.00	0.00	0.00	0.67
AH 168 FE-OX-1996#	1130	4.00	0.68	0.96	13.80	2.72	42.50	0.00	0.00	0.00	0.00	0.71
AH 200AL - 1988#	929	2.58	1.25	2.60	10.90	0.55	47.70	0.00	0.00	1.76	0.00	0.03
AH 200AL -1992#	845	2.65	1.25	2.49	10.60	0.61	48.40	0.00	0.00	1.70	0.00	0.03
AH200AV(AH-8)-1988#	996	3.17	1.20	2.68	9.76	0.97	49.00	0.05	0.00	1.32	0.00	0.01
AH 200AV - 1988#	997	2.71	1.27	2.75	10.10	1.00	49.22	0.00	0.00	1.58	0.00	0.02
AH 200AV - 1992#	985	2.68	1.22	2.55	9.77	1.02	49.50	0.00	0.00	1.41	0.00	0.02
AH 200FE-RED-1988	1126	2.49	1.27	1.03	11.00	2.74	47.40	0.00	0.00	1.85	0.00	0.03
AH 200FE-RED-1992#	1065	2.59	1.21	0.95	10.60	2.57	47.40	0.00	0.00	1.78	0.00	0.02
AH 200FE-1992(peeler)#	1070	2.59	1.21	0.95	10.60	2.57	47.40	0.00	0.00	1.78	0.00	0.02
AH 202AL - 1988 (AH131Fe/Av?)	959	4.28	1.30	2.64	7.56	0.56	52.15	0.00	0.00	1.77	0.00	0.03
AH 202AL (Pt not good) - 1992#	965	4.18	1.28	2.51	7.34	0.62	52.40	0.00	0.00	1.71	0.00	0.03
AH202AV (AH-10) - 1985#	965	4.44	1.11	2.67	6.83	0.96	54.20	0.05	0.00	1.30	0.00	0.01
AH 202AV - 1988#	967	4.37	1.31	2.67	6.75	0.96	53.30	0.00	0.00	1.41	0.00	0.03
AH 202AV - 1992#	1010	4.27	1.30	2.59	6.55	1.00	54.10	0.00	0.00	1.37	0.00	0.03
AH 202FE-RED - 1988#	1123	4.20	1.31	1.04	7.73	2.87	51.00	0.01	0.00	1.84	0.00	0.04
AH 202FE-RED-1992#	1110	4.27	1.26	0.95	7.62	2.73	52.50	0.00	0.00	1.72	0.00	0.02
AH 202FE-1992(peeler)#	1160	4.27	1.26	0.95	7.62	2.73	52.50	0.00	0.00	1.72	0.00	0.02
AH 202FE-OX - 1996#	1100	4.36	1.31	0.96	7.77	2.66	50.10	0.00	0.00	1.75	0.00	0.02
AH-5-1985#	991	3.77	0.60	2.64	9.24	0.96	53.08	0.00	0.00	1.31	0.00	0.01
AH-9-1985#	1000	3.47	0.58	2.64	9.20	0.97	50.88	0.05	0.00	1.33	0.00	0.01
AH-13 -1985#	1096	3.32	0.49	3.25	8.80	1.14	49.00	0.05	0.00	1.29	0.00	0.03
AH-16-1985#	1073	4.06	1.00	3.22	6.54	1.10	50.20	0.07	0.00	1.30	0.00	0.01
DWPF STARTUP FRIT (10/26/87)	1066	3.22	0.86	1.93	11.50	1.10	48.10	0.00	0.00	1.16	0.00	0.13
DWPF STARTUP FRIT (10/28/87)	1062	3.32	0.81	1.89	11.60	1.11	47.60	0.00	0.00	1.21	0.00	0.07
DWPF STARTUP FRIT (10/27/87) (s,p)	1012	3.21	0.86	1.97	11.50	1.11	48.00	0.00	0.00	1.16	0.00	0.12
DWPF STARTUP FRIT (10/27/87)	997	3.21	0.86	1.97	11.50	1.11	48.00	0.00	0.00	1.16	0.00	0.12
Carters 165 Black Frit	909	4.94	0.75	1.96	11.20	0.84	54.40	0.00	0.00	0.23	0.00	0.71
AH 131 FE-1992 (peeler)-No La#	1035	4.09	0.66	0.93	10.90	2.56	51.40	0.00	0.00	0.05	0.00	0.87
AH 165AL-1988#	946	4.28	0.67	2.75	11.10	0.57	52.70	0.01	0.00	0.06	0.00	0.97
AH 165 FE-1992 (peeler)#	1015	4.05	0.65	1.07	10.70	2.97	52.00	0.00	0.00	0.00	0.00	0.85

Table A2. T_L and Compositional Information for Higher TiO_2 Glasses

(values are in wt%)

Sample ID	INT LIQ (C)	Al2O3	B2O3	BaO	CaO	Ce2O3	CoO	Cr2O3	Cs2O	CuO	Cu2O	Fe2O3	K2O	La2O3	Li2O
SWPF-13	1048	13.38	4.57	0.21	0.22	0.19	0.05	0.19	1.11	0.06	0.05	4.98	0.23	0.12	6.81
SWPF-15	969.6	13.35	10.14	0.23	1.98	0.24	0.05	0.19	1.26	0.05	0.05	4.83	0.22	0.15	6.76
SWPF-16	969.6	6.62	7.96	0.11	1.04	0.10	0.06	0.11	0.72	0.04	0.03	7.64	0.14	0.06	5.46
SWPF-17	923.1	6.31	5.93	0.06	0.66	0.06	0.04	0.05	1.09	0.02	0.02	7.51	0.09	0.03	2.64
SWPF-18	907.7	6.24	5.89	0.06	0.65	0.06	0.05	0.05	1.09	0.02	0.02	7.49	0.08	0.03	5.68
SWPF-19	897.9	6.28	5.91	0.18	1.55	0.14	0.06	0.14	0.62	0.05	0.04	7.50	0.19	0.04	2.65
SWPF-20	1088.2	6.31	5.79	0.19	1.54	0.15	0.10	0.14	0.66	0.04	0.04	12.75	0.17	0.04	5.57
SWPF-21	1044	6.18	5.78	0.06	1.56	0.06	0.05	0.05	1.02	0.02	0.02	8.09	0.09	0.03	2.57
SWPF-22	1037.9	6.18	7.10	0.06	1.54	0.05	0.04	0.05	1.09	0.02	0.02	12.84	0.09	0.03	2.61
SWPF-23	938.4	6.14	8.35	0.17	0.68	0.11	0.06	0.14	0.54	0.05	0.04	7.57	0.19	0.09	2.53
SWPF-24	1088.9	6.25	8.55	0.06	0.67	0.06	0.04	0.05	0.99	0.02	0.02	12.80	0.10	0.03	2.56
SWPF-25	930.9	6.17	8.64	0.06	1.61	0.06	0.04	0.06	0.55	0.02	0.02	7.48	0.09	0.03	5.52
SWPF-26	1052.6	6.16	8.66	0.06	1.55	0.06	0.04	0.06	1.02	0.02	0.02	7.51	0.09	0.03	5.61
SWPF-27	1162.6	10.88	5.74	0.06	0.69	0.07	0.05	0.05	0.59	0.03	0.02	7.54	0.10	0.03	5.47
SWPF-28	1058.3	10.88	5.85	0.06	0.68	0.06	0.04	0.06	1.00	0.02	0.02	7.71	0.09	0.03	5.29
SWPF-29	1047.4	10.90	5.69	0.18	1.58	0.17	0.08	0.14	1.00	0.04	0.04	7.73	0.18	0.12	5.35
SWPF-30	1136.4	10.96	8.64	0.18	0.67	0.20	0.07	0.14	1.07	0.04	0.04	7.49	0.17	0.07	2.61
SWPF-31	1096.8	10.98	8.77	0.06	1.55	0.07	0.04	0.04	0.65	0.02	0.01	7.52	0.08	0.03	2.47
SWPF-32	1049	6.95	5.90	0.11	1.10	0.10	0.04	0.08	0.89	0.03	0.03	7.08	0.13	0.03	5.11
SWPF-33	1096.9	7.67	8.38	0.11	1.07	0.11	0.05	0.09	0.75	0.04	0.04	8.52	0.15	0.03	4.88
SWPF-34	1075.8	10.30	6.43	0.10	0.98	0.10	0.05	0.08	0.82	0.03	0.03	6.46	0.12	0.06	3.09
SWPF-35	1114.6	7.77	8.87	0.10	1.08	0.11	0.04	0.08	0.83	0.03	0.03	10.58	0.12	0.03	5.32
SWPF-36	1076.7	11.34	6.53	0.13	1.10	0.10	0.06	0.08	0.90	0.03	0.03	7.00	0.13	0.04	5.37
SWPF-37	1156.8	5.13	7.81	0.11	1.10	0.11	0.05	0.10	0.79	0.03	0.03	9.63	0.13	0.04	4.63
SWPF-38	1084.3	5.54	7.63	0.10	1.05	0.10	0.04	0.09	0.75	0.03	0.03	11.28	0.13	0.03	2.26
SWPF-39	954.1	6.04	5.88	0.10	1.07	0.09	0.06	0.09	0.81	0.03	0.02	7.03	0.12	0.04	4.95
SWPF-40	1130.4	10.85	7.73	0.13	1.19	0.13	0.04	0.10	0.85	0.04	0.03	9.42	0.14	0.03	4.55
SWPF-41	911.9	5.75	8.36	0.11	1.07	0.10	0.05	0.10	0.86	0.03	0.03	6.38	0.12	0.07	5.99
SWPF-42	960.6	5.91	6.78	0.09	1.00	0.11	0.04	0.08	0.78	0.03	0.03	6.21	0.12	0.04	2.26
SWPF-43	1090.9	6.57	5.86	0.09	1.14	0.09	0.05	0.09	0.75	0.03	0.03	11.08	0.12	0.06	5.38
SWPF-44	1031.3	6.83	7.24	0.10	1.21	0.11	0.05	0.08	0.76	0.04	0.03	6.67	0.13	0.07	5.02
SWPF-45	1060	6.67	6.56	0.11	1.09	0.08	0.06	0.08	0.79	0.03	0.03	10.26	0.13	0.03	2.35
SWPF-46	967.7	6.32	6.05	0.10	1.10	0.14	0.06	0.10	0.76	0.04	0.03	6.95	0.13	0.05	3.46
SWPF-47	1069.2	7.98	7.80	0.10	1.14	0.10	0.04	0.09	0.76	0.03	0.03	6.68	0.13	0.05	4.41
SWPF-48	1075.7	9.28	8.04	0.11	1.13	0.10	0.04	0.06	0.87	0.03	0.03	7.18	0.11	0.06	3.75
SWPF-49	912.9	5.74	8.27	0.13	1.07	0.11	0.06	0.10	0.87	0.03	0.03	7.22	0.13	0.04	3.56
SWPF-50	1141.1	11.06	6.23	0.12	1.11	0.09	0.05	0.10	0.76	0.04	0.03	6.90	0.14	0.06	5.67

Table A2. T_L and Compositional Information for Higher TiO_2 Glasses *(continued)*
(values are in wt%)

Sample ID	INT LIQ (C)	MgO	MnO	Na2O	NiO	PbO	RuO2	SO4	SiO2	ThO2	TiO2	U3O8	ZnO	ZrO2
SWPF-13	1048	1.92	4.08	8.03	0.00	0.23	0.14	0.32	45.15	0.00	1.95	6.24	0.20	0.22
SWPF-15	969.6	0.00	3.99	8.18	0.00	0.22	0.11	0.30	40.10	0.95	5.85	0.86	0.19	0.23
SWPF-16	969.6	0.95	1.96	9.75	0.65	0.11	0.13	0.23	49.30	0.37	3.96	2.92	0.10	0.11
SWPF-17	923.1	1.41	1.17	14.84	0.51	0.06	0.12	0.16	51.02	0.24	4.90	1.52	0.06	0.06
SWPF-18	907.7	0.47	1.17	15.42	1.47	0.06	0.12	0.18	48.88	0.71	2.92	1.52	0.05	0.05
SWPF-19	897.9	0.48	3.08	14.23	0.49	0.16	0.13	0.28	51.12	0.24	2.98	1.52	0.14	0.17
SWPF-20	1088.2	1.40	1.16	10.53	0.50	0.16	0.12	0.34	45.12	0.71	4.96	1.48	0.15	0.17
SWPF-21	1044	0.47	3.16	15.39	1.50	0.05	0.13	0.18	43.46	0.71	4.97	4.57	0.05	0.05
SWPF-22	1037.9	0.48	3.10	15.33	0.50	0.06	0.12	0.24	43.67	0.27	3.00	1.52	0.05	0.05
SWPF-23	938.4	1.26	1.20	15.44	0.50	0.17	0.12	0.28	43.70	0.83	4.90	4.53	0.14	0.17
SWPF-24	1088.9	0.46	1.17	10.48	0.50	0.05	0.13	0.20	46.96	0.80	2.93	4.46	0.06	0.05
SWPF-25	930.9	0.46	3.11	10.34	0.50	0.06	0.11	0.15	45.36	0.81	4.82	4.43	0.05	0.05
SWPF-26	1052.6	1.40	3.13	10.38	1.47	0.06	0.11	0.17	45.23	0.26	2.93	4.45	0.06	0.05
SWPF-27	1162.6	0.49	3.13	10.53	1.45	0.05	0.13	0.17	43.94	0.27	4.86	4.03	0.06	0.05
SWPF-28	1058.3	1.41	3.17	11.09	0.50	0.05	0.13	0.16	43.76	0.82	2.96	4.59	0.06	0.05
SWPF-29	1047.4	0.47	1.19	10.31	0.51	0.17	0.12	0.29	43.89	0.27	4.91	4.52	0.15	0.16
SWPF-30	1136.4	0.46	3.05	12.43	0.49	0.16	0.13	0.28	43.88	0.82	4.93	1.52	0.15	0.17
SWPF-31	1096.8	1.36	1.17	14.81	1.50	0.05	0.14	0.18	43.72	0.84	3.00	1.53	0.05	0.05
SWPF-32	1049	0.80	1.85	10.06	0.96	0.10	0.13	0.22	50.74	0.52	4.68	2.63	0.09	0.10
SWPF-33	1096.9	0.90	1.89	10.30	0.98	0.11	0.12	0.25	44.80	0.53	3.91	4.66	0.10	0.11
SWPF-34	1075.8	1.02	1.92	15.81	0.99	0.10	0.13	0.21	45.65	0.55	3.67	1.58	0.09	0.11
SWPF-35	1114.6	1.08	2.49	10.18	0.90	0.11	0.11	0.25	43.62	0.54	4.31	1.92	0.09	0.10
SWPF-36	1076.7	1.05	2.02	10.37	1.09	0.10	0.13	0.23	46.39	0.56	4.13	1.27	0.11	0.11
SWPF-37	1156.8	0.93	1.84	9.43	1.04	0.11	0.13	0.23	49.68	0.52	3.82	2.78	0.09	0.11
SWPF-38	1084.3	1.00	2.27	13.32	0.99	0.10	0.13	0.25	44.93	0.56	4.02	3.63	0.09	0.09
SWPF-39	954.1	0.93	1.74	14.24	0.96	0.09	0.12	0.21	49.39	0.52	3.90	1.76	0.08	0.09
SWPF-40	1130.4	1.02	2.72	12.87	0.92	0.11	0.11	0.26	41.65	0.55	3.86	1.40	0.11	0.13
SWPF-41	911.9	0.95	2.37	11.53	0.99	0.11	0.13	0.22	48.64	0.56	4.06	1.82	0.10	0.11
SWPF-42	960.6	0.96	1.73	14.48	0.91	0.09	0.13	0.21	50.58	0.58	3.75	3.25	0.09	0.10
SWPF-43	1090.9	1.01	1.97	11.60	0.99	0.10	0.11	0.25	45.68	0.57	3.97	2.68	0.09	0.10
SWPF-44	1031.3	0.96	2.37	10.59	1.01	0.11	0.12	0.23	47.61	0.57	3.98	4.40	0.10	0.11
SWPF-45	1060	1.03	1.73	13.83	0.90	0.10	0.13	0.24	48.47	0.49	3.67	1.36	0.09	0.11
SWPF-46	967.7	0.91	1.81	15.57	1.09	0.11	0.12	0.23	46.22	0.54	3.71	4.52	0.10	0.11
SWPF-47	1069.2	1.14	2.10	13.22	1.09	0.12	0.12	0.23	43.35	0.62	4.76	4.16	0.10	0.11
SWPF-48	1075.7	1.06	2.37	12.47	1.12	0.10	0.13	0.22	46.11	0.59	3.84	1.49	0.09	0.10
SWPF-49	912.9	0.85	1.75	15.44	0.92	0.12	0.12	0.24	47.29	0.57	3.38	2.10	0.10	0.13
SWPF-50	1141.1	0.97	2.22	12.22	0.89	0.12	0.11	0.24	42.58	0.55	3.66	4.40	0.10	0.11

Table A3. Measurements Supporting Liquidus Temperature Determinations

(The shaded rows (i.e., excluded values) identify a heat-treated glass sample with an experimental outcome containing a crystalline phase without an appropriate standard calibration to assess the crystal fraction. These values were not used in the determination of T_L values)

Glass ID	VSL ID	Temperature (oC)	% Crystals	1 => excluded
SWPF-44	GAP-01	804.2	3	0
SWPF-44	GAP-01	853.7	2.6	0
SWPF-44	GAP-01	903.3	1.9	0
SWPF-44	GAP-01	952.8	1	0
SWPF-49	GAP-02	705	3.8	0
SWPF-49	GAP-02	754.6	2.9	0
SWPF-49	GAP-02	804.2	1.8	0
SWPF-49	GAP-02	853.7	1.2	0
SWPF-35	GAP-03	853.7	6.3	0
SWPF-35	GAP-03	952.8	3.6	0
SWPF-35	GAP-03	1002.4	2.9	0
SWPF-35	GAP-03	1052	1.5	0
SWPF-41	GAP-04	705	4.5	1
SWPF-41	GAP-04	754.6	2.7	1
SWPF-41	GAP-04	804.2	3.5	0
SWPF-41	GAP-04	853.7	1.3	0
SWPF-41	GAP-04	878.5	1.3	0
SWPF-41	GAP-04	903.3	0.5	0
SWPF-17	GAP-05	705	1.8	1
SWPF-17	GAP-05	754.6	1.5	0
SWPF-17	GAP-05	804.2	1.2	0
SWPF-17	GAP-05	828.9	0.9	0
SWPF-17	GAP-05	853.7	0.6	0
SWPF-26	GAP-06	804.2	5.9	0
SWPF-26	GAP-06	853.7	4.4	0
SWPF-26	GAP-06	903.3	3.8	0
SWPF-26	GAP-06	952.8	3	0
SWPF-26	GAP-06	1002.4	0.9	0
SWPF-37	GAP-07	804.2	2.6	1
SWPF-37	GAP-07	853.7	3.6	0
SWPF-37	GAP-07	903.3	2.7	0
SWPF-37	GAP-07	952.8	2.4	0
SWPF-37	GAP-07	1002.4	1.9	0
SWPF-37	GAP-07	1052	1.2	0
SWPF-45	GAP-08	804.2	4.8	0
SWPF-45	GAP-08	853.7	3.6	0
SWPF-45	GAP-08	903.3	3.9	0
SWPF-45	GAP-08	952.8	2.7	0
SWPF-45	GAP-08	1002.4	0.9	0
SWPF-32	GAP-09	804.2	3.5	1
SWPF-32	GAP-09	853.7	3.8	0
SWPF-32	GAP-09	903.3	3	0
SWPF-32	GAP-09	952.8	1.9	0
SWPF-32	GAP-09	1002.4	0.9	0
SWPF-11	GAP-10	655.5	0.4	1
SWPF-36	GAP-11	878.5	6.2	0
SWPF-36	GAP-11	903.3	4.2	0
SWPF-36	GAP-11	952.8	4.5	0
SWPF-36	GAP-11	1002.4	2.7	0
SWPF-36	GAP-11	1052	0.7	0
SWPF-14	GAP-12	705	14.7	1
SWPF-14	GAP-12	729.8	11.3	1
SWPF-14	GAP-12	754.6	5.7	1
SWPF-38	GAP-13	853.7	5.4	0
SWPF-38	GAP-13	903.3	4.1	0
SWPF-38	GAP-13	952.8	3.5	0
SWPF-38	GAP-13	1002.4	1.9	0
SWPF-38	GAP-13	1052	0.7	0
SWPF-15	GAP-14	804.2	4.4	1
SWPF-15	GAP-14	853.7	4.8	1
SWPF-15	GAP-14	878.5	8.3	0
SWPF-15	GAP-14	903.3	6.3	0
SWPF-15	GAP-14	952.8	1.5	0
SWPF-01	GAP-15	705	60.5	1
SWPF-01	GAP-15	754.6	43.2	1
SWPF-01	GAP-15	804.2	37.3	0
SWPF-01	GAP-15	853.7	27.9	0
SWPF-01	GAP-15	903.3	9.5	0
SWPF-30	GAP-16	853.7	5.4	0
SWPF-30	GAP-16	903.3	4.5	0
SWPF-30	GAP-16	952.8	3.5	0
SWPF-30	GAP-16	1002.4	2.6	0
SWPF-30	GAP-16	1052	1.6	0
SWPF-25	GAP-17	754.6	4.2	1
SWPF-25	GAP-17	804.2	2.9	0
SWPF-25	GAP-17	853.7	1.9	0
SWPF-25	GAP-17	903.3	0.6	0
SWPF-50	GAP-18	804.2	6.6	0
SWPF-50	GAP-18	853.7	6.2	0
SWPF-50	GAP-18	903.3	3.8	0
SWPF-50	GAP-18	952.8	4.1	0
SWPF-50	GAP-18	1002.4	3.5	0
SWPF-13	GAP-19	853.7	8	0
SWPF-13	GAP-19	903.3	5.1	0
SWPF-13	GAP-19	952.8	3.5	0
SWPF-13	GAP-19	1002.4	2.3	0
SWPF-22	GAP-20	804.2	4.2	0
SWPF-22	GAP-20	853.7	3.9	0
SWPF-22	GAP-20	903.3	2.3	0
SWPF-22	GAP-20	952.8	1.8	0
SWPF-07	GAP-21	754.6	2.7	1
SWPF-07	GAP-21	804.2	2.1	1
SWPF-07	GAP-21	853.7	1.8	1
SWPF-07	GAP-21	878.5	1.8	1
SWPF-07	GAP-21	903.3	1.9	0
SWPF-07	GAP-21	928.1	1.2	0
SWPF-07	GAP-21	952.8	0.7	0
SWPF-02	GAP-22	754.6	19.9	1
SWPF-02	GAP-22	804.2	1.2	1
SWPF-02	GAP-22	828.9	2.1	0
SWPF-02	GAP-22	853.7	1.9	0
SWPF-02	GAP-22	878.5	0.7	0
SWPF-23	GAP-23	754.6	3	0
SWPF-23	GAP-23	804.2	2.1	0
SWPF-23	GAP-23	853.7	1.2	0
SWPF-23	GAP-23	903.3	0.7	0
SWPF-27	GAP-24	903.3	7.7	0
SWPF-27	GAP-24	1002.4	4.7	0
SWPF-27	GAP-24	1052	3.8	0
SWPF-27	GAP-24	1101.5	1.6	0
SWPF-48	GAP-25	853.7	4.8	0
SWPF-48	GAP-25	903.3	3.8	0
SWPF-48	GAP-25	952.8	2.9	0
SWPF-48	GAP-25	1002.4	1.5	0
SWPF-16	GAP-26	754.6	2.1	1
SWPF-16	GAP-26	804.2	3.3	0
SWPF-16	GAP-26	853.7	2.6	0
SWPF-16	GAP-26	903.3	1	0
SWPF-16	GAP-26	952.8	0.6	0
SWPF-42	GAP-27	705	25.7	1
SWPF-42	GAP-27	754.6	2.1	0
SWPF-42	GAP-27	804.2	1.4	0
SWPF-42	GAP-27	853.7	1.2	0
SWPF-43	GAP-28	853.7	7.7	0
SWPF-43	GAP-28	903.3	5.9	0
SWPF-43	GAP-28	952.8	3.9	0
SWPF-43	GAP-28	1002.4	2.4	0
SWPF-43	GAP-28	1052	1.9	0
SWPF-18	GAP-29	705	5.3	1
SWPF-18	GAP-29	754.6	4.8	0
SWPF-18	GAP-29	804.2	2.9	0
SWPF-18	GAP-29	853.7	1.2	0

Table A3. Measurements Supporting Liquidus Temperature Determinations

(continued)

(The shaded rows (i.e., excluded values) identify a heat-treated glass sample with an experimental outcome containing a crystalline phase without an appropriate standard calibration to assess the crystal fraction. These values were not used in the determination of T_L values)

Glass ID	VSL ID	Temperature (oC)	% Crystals	1 => excluded
SWPF-18	GAP-29	903.3	0.6	0
SWPF-31	GAP-30	903.3	4.7	0
SWPF-31	GAP-30	952.8	4.1	0
SWPF-31	GAP-30	1002.4	2.7	0
SWPF-31	GAP-30	1052	1	0
SWPF-04	GAP-31	705	8.1	1
SWPF-04	GAP-31	754.6	3.1	1
SWPF-04	GAP-31	804.2	7.8	1
SWPF-04	GAP-31	853.7	6.9	1
SWPF-04	GAP-31	878.5	3.3	1
SWPF-29	GAP-32	754.6	6.6	1
SWPF-29	GAP-32	804.2	4.7	1
SWPF-29	GAP-32	853.7	3.2	1
SWPF-29	GAP-32	903.3	3.2	0
SWPF-29	GAP-32	952.8	2.1	0
SWPF-29	GAP-32	1002.4	1	0
SWPF-05	GAP-33	804.2	5.9	0
SWPF-05	GAP-33	853.7	5.6	0
SWPF-05	GAP-33	903.3	4.1	0
SWPF-05	GAP-33	952.8	2.1	0
SWPF-12	GAP-34	952.8	8.9	1
SWPF-12	GAP-34	1002.4	4.8	1
SWPF-12	GAP-34	1052	4.1	1
SWPF-12	GAP-34	1101.5	3.6	1
SWPF-12	GAP-34	1151.1	3.9	1
SWPF-12	GAP-34	1200.6	4.8	1
SWPF-19	GAP-35	705	2.7	1
SWPF-19	GAP-35	754.6	2.3	1
SWPF-19	GAP-35	804.2	2.4	0
SWPF-19	GAP-35	828.9	1.6	0
SWPF-19	GAP-35	853.7	1	0
SWPF-19	GAP-35	878.5	0.6	0
SWPF-34	GAP-36	804.2	4.2	0
SWPF-34	GAP-36	853.7	3.9	0
SWPF-34	GAP-36	903.3	2.4	0
SWPF-34	GAP-36	952.8	2.1	0
SWPF-34	GAP-36	1002.4	1.3	0
SWPF-08	GAP-37	952.8	10.1	1
SWPF-08	GAP-37	1002.4	8.5	1
SWPF-08	GAP-37	1052	7.9	1
SWPF-08	GAP-37	1151.1	6.7	1
SWPF-08	GAP-37	1200.6	4.2	1
SWPF-06	GAP-38	655.5	10.8	1
SWPF-06	GAP-38	705	6.3	0
SWPF-06	GAP-38	729.8	2.1	0
SWPF-46	GAP-39	655.5	5	0
SWPF-46	GAP-39	705	4.2	0
SWPF-46	GAP-39	754.6	3.3	0
SWPF-46	GAP-39	853.7	1.9	0
SWPF-46	GAP-39	903.3	1	0
SWPF-33	GAP-40	804.2	5.1	0
SWPF-33	GAP-40	903.3	3.9	0
SWPF-33	GAP-40	952.8	3	0
SWPF-33	GAP-40	1002.4	2.3	0
SWPF-33	GAP-40	1052	0.4	0
SWPF-21	GAP-41	853.7	6.5	0
SWPF-21	GAP-41	903.3	5.1	0
SWPF-21	GAP-41	952.8	3	0
SWPF-21	GAP-41	1002.4	1.5	0
SWPF-24	GAP-42	903.3	2.1	1
SWPF-24	GAP-42	952.8	2.7	0
SWPF-24	GAP-42	1002.4	1.9	0
SWPF-24	GAP-42	1052	0.7	0
SWPF-03	GAP-43	804.2	12.6	1
SWPF-03	GAP-43	853.7	11.4	1
SWPF-03	GAP-43	878.5	8	1
SWPF-03	GAP-43	903.3	2.8	1
SWPF-09	GAP-44	754.6	12.8	1
SWPF-09	GAP-44	804.2	7.9	1
SWPF-09	GAP-44	828.9	9.7	1
SWPF-09	GAP-44	853.7	7.5	1
SWPF-09	GAP-44	878.5	4.6	1
SWPF-47	GAP-45	754.6	4.1	1
SWPF-47	GAP-45	804.2	4.1	0
SWPF-47	GAP-45	853.7	3.6	0
SWPF-47	GAP-45	903.3	2.7	0
SWPF-47	GAP-45	952.8	1.8	0
SWPF-20	GAP-46	804.2	5.4	1
SWPF-20	GAP-46	853.7	6.8	0
SWPF-20	GAP-46	903.3	4.5	0
SWPF-20	GAP-46	952.8	3.9	0
SWPF-20	GAP-46	1002.4	2.7	0
SWPF-20	GAP-46	1052	1	0
SWPF-10	GAP-47	853.7	0.5	1
SWPF-10	GAP-47	878.5	3.8	1
SWPF-10	GAP-47	903.3	2.9	1
SWPF-10	GAP-47	928.1	2.2	0
SWPF-10	GAP-47	952.8	1.6	0
SWPF-10	GAP-47	977.6	0.7	0
SWPF-40	GAP-48	853.7	7.2	0
SWPF-40	GAP-48	903.3	6.6	0
SWPF-40	GAP-48	952.8	4.8	0
SWPF-40	GAP-48	1002.4	3.5	0
SWPF-40	GAP-48	1052	2.1	0
SWPF-39	GAP-49	705	4.5	1
SWPF-39	GAP-49	754.6	3	0
SWPF-39	GAP-49	804.2	2.4	0
SWPF-39	GAP-49	853.7	1.5	0
SWPF-28	GAP-50	804.2	7.7	0
SWPF-28	GAP-50	853.7	6	0
SWPF-28	GAP-50	903.3	4.4	0
SWPF-28	GAP-50	952.8	3	0
SWPF-28	GAP-50	1002.4	1.9	0

Table A4. T_L and Compositional Information for Validation Data

(values are in wt%)

Sample ID	INT LIQ (C)	Al2O3	B2O3	BaO	CaO	CdO	Ce2O3	Cr2O3	CuO	Cu2O	Fe2O3	K2O	La2O3
FY09EM21-02	980	4.341	5.142	0.089	0.007	0.250	0.360	0.012	0.068	0.061	20.859	0.000	0.090
FY09EM21-06	995	4.593	11.387	0.080	0.032	0.245	0.342	0.181	0.066	0.059	5.291	0.000	0.092
FY09EM21-07	1055	4.980	13.508	0.006	4.158	0.006	0.006	0.007	0.003	0.003	17.162	0.000	0.006
FY09EM21-09	1075	13.413	9.407	0.006	3.154	0.006	0.006	0.130	0.003	0.003	10.732	0.000	0.006
FY09EM21-12	1096	4.820	5.155	0.006	0.007	0.006	0.009	0.017	0.003	0.003	15.848	0.000	0.006
FY09EM21-15	1116	5.507	4.605	0.096	3.332	0.214	0.346	0.134	0.067	0.060	7.920	0.000	0.091
FY09EM21-17	898	7.827	4.699	0.095	0.118	0.274	0.374	0.011	0.074	0.066	14.295	0.000	0.099
FY09EM21-20	1044.5	6.321	5.301	0.006	0.007	0.006	0.006	0.152	0.003	0.003	11.465	0.000	0.006
FY09EM21-21	932.5	4.962	8.952	0.087	0.007	0.284	0.358	0.184	0.068	0.061	19.491	0.000	0.086
FY09EM21-25	858	6.544	4.882	0.006	4.286	0.006	0.006	0.159	0.007	0.006	7.789	0.000	0.006
FY09EM21-26	943	14.019	7.383	0.006	0.008	0.006	0.006	0.131	0.003	0.003	4.956	0.000	0.006
FY09EM21-27	1116.5	7.480	6.868	0.044	1.908	0.135	0.184	0.088	0.035	0.031	12.771	0.000	0.047
HWL-07	1113	6.820	5.130	0.120	1.520	0.000	0.270	0.160	0.025	0.022	16.410	0.110	0.100
HWL-09	987	4.500	11.920	0.080	0.870	0.000	0.190	0.100	0.015	0.013	10.400	0.060	0.070
HWL-10	1031	5.160	11.030	0.090	1.000	0.000	0.210	0.110	0.015	0.013	11.920	0.070	0.080
HWL-14	1086	5.820	4.510	0.100	1.130	0.000	0.240	0.130	0.020	0.018	13.440	0.080	0.090
HWL-16	997	4.440	11.510	0.080	1.030	0.000	0.270	0.100	0.015	0.013	12.380	0.060	0.090
HWL-17	1030	5.050	10.620	0.090	1.170	0.000	0.300	0.110	0.015	0.013	14.080	0.070	0.100
HWL-19	914	4.440	5.120	0.080	1.030	0.000	0.270	0.100	0.015	0.013	12.380	0.060	0.090
HWL-20	1029	5.050	4.720	0.090	1.170	0.000	0.300	0.110	0.015	0.013	14.080	0.070	0.100

Sample ID	INT LIQ (C)	Li2O	MgO	MnO	Na2O	NiO	PbO	SO4	SiO2	TiO2	ZnO	ZrO2
FY09EM21-02	980	4.072	1.561	0.317	17.393	0.007	0.184	0.485	41.335	2.175	0.134	0.201
FY09EM21-06	995	3.898	0.009	5.495	14.664	2.712	0.185	0.431	43.084	6.304	0.138	0.193
FY09EM21-07	1055	3.889	1.478	5.399	12.709	0.070	0.005	0.075	33.266	2.126	0.006	0.007
FY09EM21-09	1075	6.826	0.009	2.050	9.982	0.664	0.005	0.075	40.562	2.666	0.006	0.007
FY09EM21-12	1096	6.648	0.009	4.724	10.004	1.897	0.005	0.075	47.360	2.105	0.006	0.007
FY09EM21-15	1116	5.884	1.450	5.297	9.941	2.593	0.181	0.436	49.348	1.974	0.132	0.187
FY09EM21-17	898	6.908	0.009	0.597	15.034	0.007	0.205	0.491	40.839	6.526	0.139	0.206
FY09EM21-20	1044.5	3.964	1.279	0.298	17.007	2.640	0.005	0.075	47.345	2.093	0.006	0.007
FY09EM21-21	932.5	6.975	0.009	1.021	14.426	0.007	0.211	0.474	39.049	2.106	0.132	0.198
FY09EM21-25	858	3.959	0.009	5.710	15.404	0.007	0.005	0.075	48.295	2.137	0.006	0.013
FY09EM21-26	943	4.039	1.548	5.243	11.929	0.007	0.005	0.075	44.912	5.176	0.006	0.007
FY09EM21-27	1116.5	5.012	0.729	2.682	12.672	1.284	0.104	0.247	42.946	4.119	0.068	0.109
HWL-07	1113	5.130	0.220	2.410	12.180	0.600	0.120	0.000	46.870	1.290	0.080	0.290
HWL-09	987	5.300	0.140	3.360	7.960	0.670	0.110	0.000	50.290	2.340	0.040	0.770
HWL-10	1031	4.900	0.160	3.850	8.970	0.770	0.130	0.000	46.970	2.690	0.040	0.890
HWL-14	1086	4.510	0.180	4.340	13.940	0.870	0.140	0.000	45.330	3.030	0.050	1.000
HWL-16	997	3.840	0.170	2.670	8.550	0.350	0.140	0.000	49.850	3.130	0.030	0.660
HWL-17	1030	3.540	0.190	3.040	9.590	0.400	0.150	0.000	46.390	3.560	0.030	0.750
HWL-19	914	5.120	0.170	2.670	13.030	0.350	0.140	0.000	50.490	3.130	0.030	0.660
HWL-20	1029	4.720	0.190	3.040	13.720	0.400	0.150	0.000	46.980	3.560	0.030	0.750

Exhibit A1. Liquidus Temperature Determinations

Bivariate Fit of y By x Glass ID=SWPF-01, VSL ID=GAP-15, Regression=% crys fit to temp

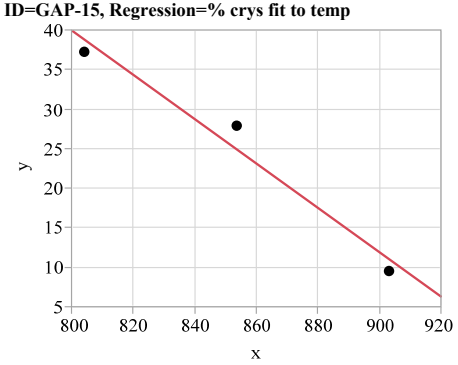

Linear Fit

Linear Fit
y = 264.4193 - 0.2805552*x

Summary of Fit

RSquare	0.966453
RSquare Adj	0.932907
Root Mean Square Error	3.662782
Mean of Response	24.9
Observations (or Sum Wgts)	3

Analysis of Variance

Source	DF	Sum of Squares	Mean Square	F Ratio
Model	1	386.50403	386.504	28.8093
Error	1	13.41597	13.416	**Prob > F**
C. Total	2	399.92000		0.1173

Parameter Estimates

Term	Estimate	Std Error	t Ratio	Prob>|t|
Intercept	264.4193	44.6747	5.92	0.1066
x	-0.280555	0.05227	-5.37	0.1173

Bivariate Fit of y By x Glass ID=SWPF-01, VSL ID=GAP-15, Regression=temps fit to % crys

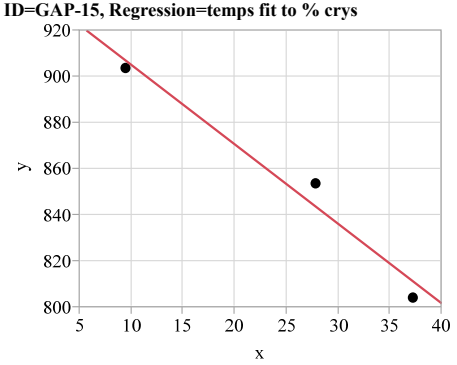

Linear Fit

Linear Fit
y = 939.50858 - 3.444789*x

Summary of Fit

RSquare	0.966453
RSquare Adj	0.932907
Root Mean Square Error	12.83463
Mean of Response	853.7333
Observations (or Sum Wgts)	3

Analysis of Variance

Source	DF	Sum of Squares	Mean Square	F Ratio
Model	1	4745.6791	4745.68	28.8093
Error	1	164.7276	164.73	**Prob > F**
C. Total	2	4910.4067		0.1173

Parameter Estimates

Term	Estimate	Std Error	t Ratio	Prob>|t|
Intercept	939.50858	17.61511	53.34	0.0119*
x	-3.444789	0.641795	-5.37	0.1173

Bivariate Fit of y By x Glass ID=SWPF-02, VSL ID=GAP-22, Regression=% crys fit to temp

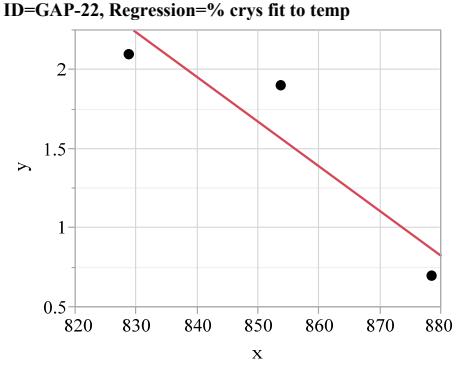

Linear Fit

Linear Fit
y = 25.663038 - 0.0282258*x

Summary of Fit

RSquare	0.854651
RSquare Adj	0.709302
Root Mean Square Error	0.408248
Mean of Response	1.566667
Observations (or Sum Wgts)	3

Analysis of Variance

Source	DF	Sum of Squares	Mean Square	F Ratio
Model	1	0.9800000	0.980000	5.8800
Error	1	0.1666667	0.166667	**Prob > F**
C. Total	2	1.1466667		0.2490

Parameter Estimates

Term	Estimate	Std Error	t Ratio	Prob>|t|
Intercept	25.663038	9.939971	2.58	0.2353
x	-0.028226	0.01164	-2.42	0.2490

Bivariate Fit of y By x Glass ID=SWPF-02, VSL ID=GAP-22, Regression=temps fit to % crys

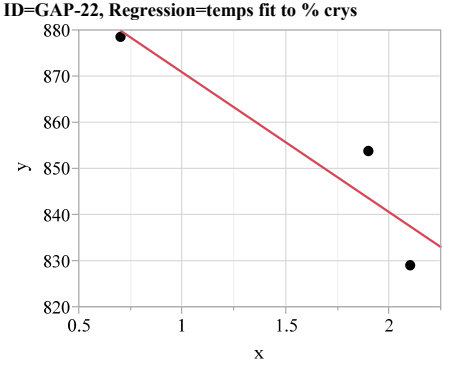

Linear Fit

Linear Fit
y = 901.13721 - 30.27907*x

Summary of Fit

RSquare	0.854651
RSquare Adj	0.709302
Root Mean Square Error	13.37126
Mean of Response	853.7
Observations (or Sum Wgts)	3

Analysis of Variance

Source	DF	Sum of Squares	Mean Square	F Ratio
Model	1	1051.2893	1051.29	5.8800
Error	1	178.7907	178.79	**Prob > F**
C. Total	2	1230.0800		0.2490

Parameter Estimates

Term	Estimate	Std Error	t Ratio	Prob>|t|
Intercept	901.13721	21.03091	42.85	0.0149*
x	-30.27907	12.48688	-2.42	0.2490

Exhibit A1. Liquidus Temperature Determinations

Bivariate Fit of y By x Glass ID=SWPF-05, VSL ID=GAP-33, Regression=% crys fit to temp

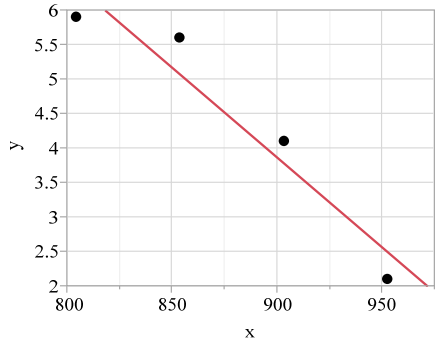

Linear Fit
y = 27.301254 - 0.0260401*x

Summary of Fit

RSquare	0.917658
RSquare Adj	0.876487
Root Mean Square Error	0.610998
Mean of Response	4.425
Observations (or Sum Wgts)	4

Analysis of Variance

Source	DF	Sum of Squares	Mean Square	F Ratio
Model	1	8.3208632	8.32086	22.2889
Error	2	0.7466368	0.37332	Prob > F
C. Total	3	9.0675000		0.0421*

Parameter Estimates

Term	Estimate	Std Error	t Ratio	Prob>|t|
Intercept	27.301254	4.855141	5.62	0.0302*
x	-0.02604	0.005516	-4.72	0.0421*

Bivariate Fit of y By x Glass ID=SWPF-05, VSL ID=GAP-33, Regression=temps fit to % crys

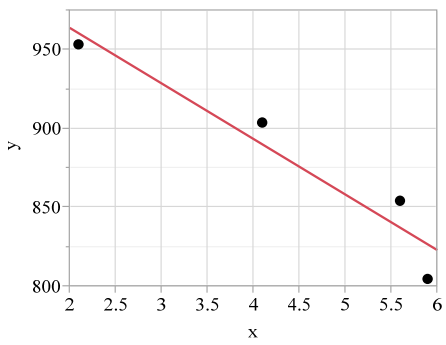

Linear Fit
y = 1034.4376 - 35.240143*x

Summary of Fit

RSquare	0.917658
RSquare Adj	0.876487
Root Mean Square Error	22.47693
Mean of Response	878.5
Observations (or Sum Wgts)	4

Analysis of Variance

Source	DF	Sum of Squares	Mean Square	F Ratio
Model	1	11260.635	11260.6	22.2889
Error	2	1010.425	505.2	Prob > F
C. Total	3	12271.060		0.0421*

Parameter Estimates

Term	Estimate	Std Error	t Ratio	Prob>|t|
Intercept	1034.4376	34.88944	29.65	0.0011*
x	-35.24014	7.46437	-4.72	0.0421*

Bivariate Fit of y By x Glass ID=SWPF-06, VSL ID=GAP-38, Regression=% crys fit to temp

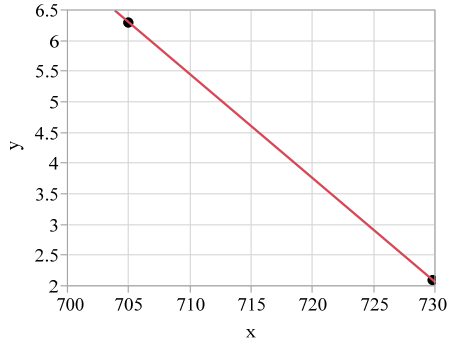

Linear Fit
y = 125.69516 - 0.1693548*x

Summary of Fit

RSquare	1
RSquare Adj	.
Root Mean Square Error	.
Mean of Response	4.2
Observations (or Sum Wgts)	2

Analysis of Variance

Source	DF	Sum of Squares	Mean Square	F Ratio
Model	1	8.8200000	8.82000	.
Error	0	0.0000000	.	Prob > F
C. Total	1	8.8200000		.

Parameter Estimates

Term	Estimate	Std Error	t Ratio	Prob>|t|
Intercept	125.69516	.	.	.
x	-0.169355	.	.	.

Bivariate Fit of y By x Glass ID=SWPF-06, VSL ID=GAP-38, Regression=temps fit to % crys

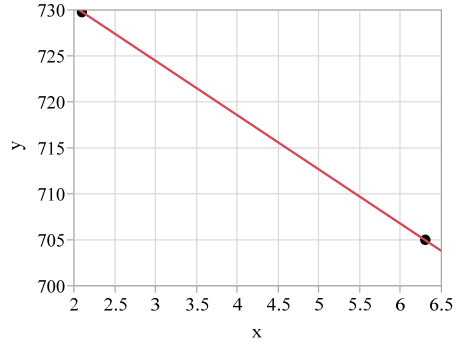

Linear Fit
y = 742.2 - 5.9047619*x

Summary of Fit

RSquare	1
RSquare Adj	.
Root Mean Square Error	.
Mean of Response	717.4
Observations (or Sum Wgts)	2

Analysis of Variance

Source	DF	Sum of Squares	Mean Square	F Ratio
Model	1	307.52000	307.520	.
Error	0	0.00000	.	Prob > F
C. Total	1	307.52000		.

Parameter Estimates

Term	Estimate	Std Error	t Ratio	Prob>|t|
Intercept	742.2	.	.	.
x	-5.904762	.	.	.

Exhibit A1. Liquidus Temperature Determinations

Bivariate Fit of y By x Glass ID=SWPF-07, VSL ID=GAP-21, Regression=% crys fit to temp

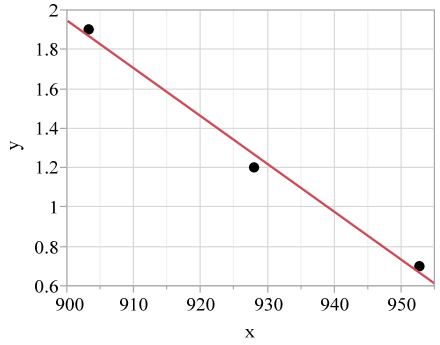

Linear Fit
y = 23.767747 - 0.0242451*x

Summary of Fit

RSquare	0.991047
RSquare Adj	0.982094
Root Mean Square Error	0.08066
Mean of Response	1.266667
Observations (or Sum Wgts)	3

Analysis of Variance

Source	DF	Sum of Squares	Mean Square	F Ratio
Model	1	0.72016065	0.720161	110.6914
Error	1	0.00650602	0.006506	**Prob > F**
C. Total	2	0.72666667		0.0603

Parameter Estimates

Term	Estimate	Std Error	t Ratio	Prob>|t|
Intercept	23.767747	2.13919	11.11	0.0571
x	-0.024245	0.002304	-10.52	0.0603

Bivariate Fit of y By x Glass ID=SWPF-07, VSL ID=GAP-21, Regression=temps fit to % crys

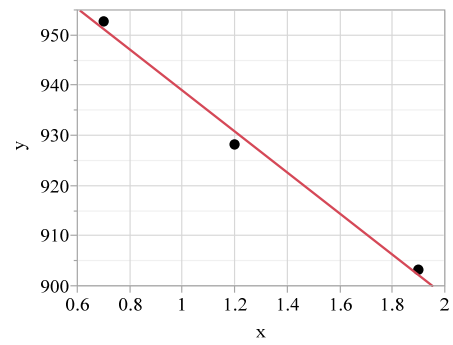

Linear Fit
y = 979.84312 - 40.876147*x

Summary of Fit

RSquare	0.991047
RSquare Adj	0.982094
Root Mean Square Error	3.311926
Mean of Response	928.0667
Observations (or Sum Wgts)	3

Analysis of Variance

Source	DF	Sum of Squares	Mean Square	F Ratio
Model	1	1214.1578	1214.16	110.6914
Error	1	10.9689	10.97	**Prob > F**
C. Total	2	1225.1267		0.0603

Parameter Estimates

Term	Estimate	Std Error	t Ratio	Prob>|t|
Intercept	979.84312	5.279676	185.59	0.0034*
x	-40.87615	3.885197	-10.52	0.0603

Bivariate Fit of y By x Glass ID=SWPF-10, VSL ID=GAP-47, Regression=% crys fit to temp

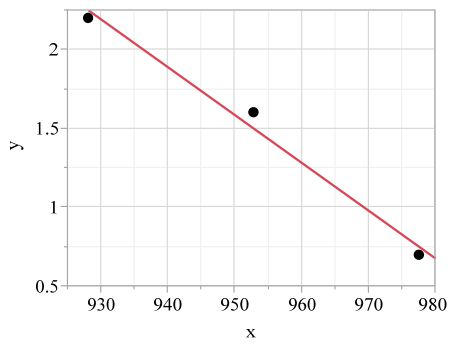

Linear Fit
y = 30.377587 - 0.0303071*x

Summary of Fit

RSquare	0.987107
RSquare Adj	0.974213
Root Mean Square Error	0.121237
Mean of Response	1.5
Observations (or Sum Wgts)	3

Analysis of Variance

Source	DF	Sum of Squares	Mean Square	F Ratio
Model	1	1.1253015	1.12530	76.5590
Error	1	0.0146985	0.01470	**Prob > F**
C. Total	2	1.1400000		0.0724

Parameter Estimates

Term	Estimate	Std Error	t Ratio	Prob>|t|
Intercept	30.377587	3.301112	9.20	0.0689
x	-0.030307	0.003464	-8.75	0.0724

Bivariate Fit of y By x Glass ID=SWPF-10, VSL ID=GAP-47, Regression=temps fit to % crys

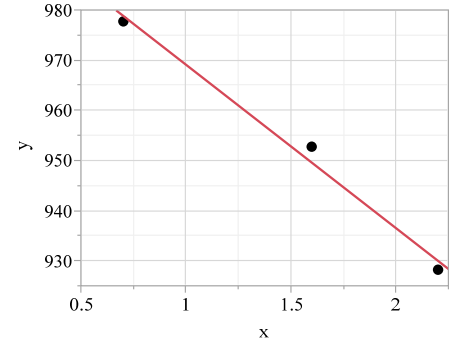

Linear Fit
y = 1001.6886 - 32.570175*x

Summary of Fit

RSquare	0.987107
RSquare Adj	0.974213
Root Mean Square Error	3.974425
Mean of Response	952.8333
Observations (or Sum Wgts)	3

Analysis of Variance

Source	DF	Sum of Squares	Mean Square	F Ratio
Model	1	1209.3306	1209.33	76.5590
Error	1	15.7961	15.80	**Prob > F**
C. Total	2	1225.1267		0.0724

Parameter Estimates

Term	Estimate	Std Error	t Ratio	Prob>|t|
Intercept	1001.6886	6.036702	165.93	0.0038*
x	-32.57018	3.72239	-8.75	0.0724

Exhibit A1. Liquidus Temperature Determinations

Bivariate Fit of y By x Glass ID=SWPF-13, VSL ID=GAP-19, Regression=% crys fit to temp

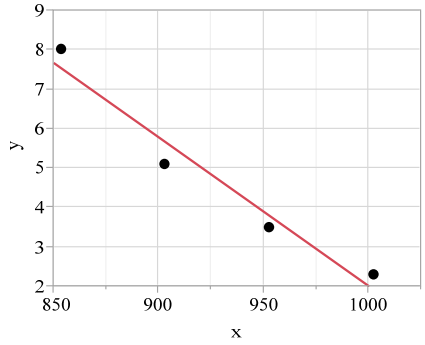

Linear Fit
y = 39.742896 - 0.0377328*x

Summary of Fit

RSquare	0.958223
RSquare Adj	0.937335
Root Mean Square Error	0.617383
Mean of Response	4.725
Observations (or Sum Wgts)	4

Analysis of Variance

Source	DF	Sum of Squares	Mean Square	F Ratio
Model	1	17.485176	17.4852	45.8734
Error	2	0.762324	0.3812	**Prob > F**
C. Total	3	18.247500		0.0211*

Parameter Estimates

Term	Estimate	Std Error	t Ratio	Prob>|t|
Intercept	39.742896	5.179436	7.67	0.0166*
x	-0.037733	0.005571	-6.77	0.0211*

Bivariate Fit of y By x Glass ID=SWPF-13, VSL ID=GAP-19, Regression=temps fit to % crys

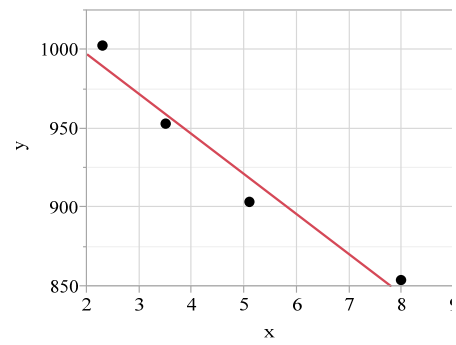

Linear Fit
y = 1048.0413 - 25.394986*x

Summary of Fit

RSquare	0.958223
RSquare Adj	0.937335
Root Mean Square Error	16.01656
Mean of Response	928.05
Observations (or Sum Wgts)	4

Analysis of Variance

Source	DF	Sum of Squares	Mean Square	F Ratio
Model	1	11767.909	11767.9	45.8734
Error	2	513.061	256.5	**Prob > F**
C. Total	3	12280.970		0.0211*

Parameter Estimates

Term	Estimate	Std Error	t Ratio	Prob>|t|
Intercept	1048.0413	19.44209	53.91	0.0003*
x	-25.39499	3.749451	-6.77	0.0211*

Bivariate Fit of y By x Glass ID=SWPF-15, VSL ID=GAP-14, Regression=% crys fit to temp

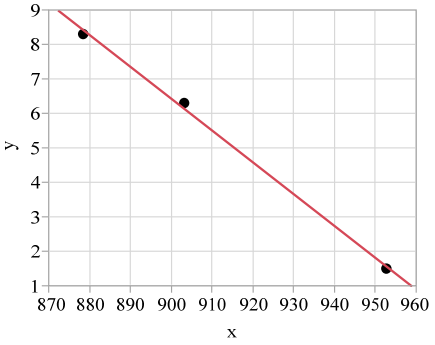

Linear Fit
y = 89.498274 - 0.0922968*x

Summary of Fit

RSquare	0.998085
RSquare Adj	0.99617
Root Mean Square Error	0.216276
Mean of Response	5.366667
Observations (or Sum Wgts)	3

Analysis of Variance

Source	DF	Sum of Squares	Mean Square	F Ratio
Model	1	24.379891	24.3799	521.2140
Error	1	0.046775	0.0468	**Prob > F**
C. Total	2	24.426667		0.0279*

Parameter Estimates

Term	Estimate	Std Error	t Ratio	Prob>|t|
Intercept	89.498274	3.687231	24.27	0.0262*
x	-0.092297	0.004043	-22.83	0.0279*

Bivariate Fit of y By x Glass ID=SWPF-15, VSL ID=GAP-14, Regression=temps fit to % crys

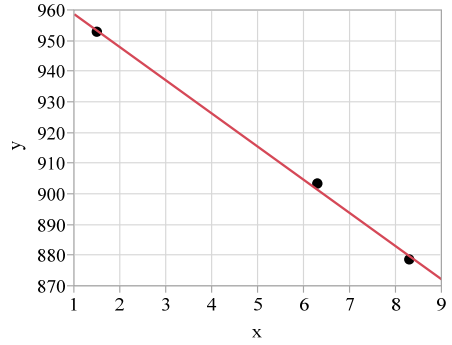

Linear Fit
y = 969.56774 - 10.813865*x

Summary of Fit

RSquare	0.998085
RSquare Adj	0.99617
Root Mean Square Error	2.341019
Mean of Response	911.5333
Observations (or Sum Wgts)	3

Analysis of Variance

Source	DF	Sum of Squares	Mean Square	F Ratio
Model	1	2856.4463	2856.45	521.2140
Error	1	5.4804	5.48	**Prob > F**
C. Total	2	2861.9267		0.0279*

Parameter Estimates

Term	Estimate	Std Error	t Ratio	Prob>|t|
Intercept	969.56774	2.878995	336.77	0.0019*
x	-10.81386	0.473667	-22.83	0.0279*

Exhibit A1. Liquidus Temperature Determinations

Bivariate Fit of y By x Glass ID=SWPF-16, VSL ID=GAP-26, Regression=% crys fit to temp

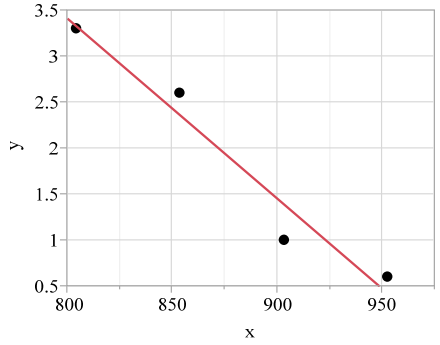

Linear Fit

Linear Fit
y = 19.077651 - 0.0195818*x

Summary of Fit

RSquare	0.95105
RSquare Adj	0.926576
Root Mean Square Error	0.347979
Mean of Response	1.875
Observations (or Sum Wgts)	4

Analysis of Variance

Source	DF	Sum of Squares	Mean Square	F Ratio
Model	1	4.7053216	4.70532	38.8583
Error	2	0.2421784	0.12109	**Prob > F**
C. Total	3	4.9475000		0.0248*

Parameter Estimates

Term	Estimate	Std Error	t Ratio	Prob>|t|
Intercept	19.077651	2.765126	6.90	0.0204*
x	-0.019582	0.003141	-6.23	0.0248*

Bivariate Fit of y By x Glass ID=SWPF-16, VSL ID=GAP-26, Regression=temps fit to % crys

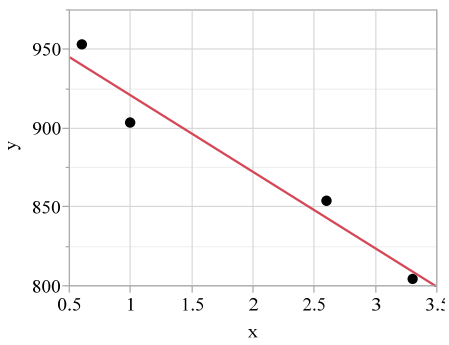

Linear Fit

Linear Fit
y = 969.56493 - 48.567964*x

Summary of Fit

RSquare	0.95105
RSquare Adj	0.926576
Root Mean Square Error	17.33009
Mean of Response	878.5
Observations (or Sum Wgts)	4

Analysis of Variance

Source	DF	Sum of Squares	Mean Square	F Ratio
Model	1	11670.396	11670.4	38.8583
Error	2	600.664	300.3	**Prob > F**
C. Total	3	12271.060		0.0248*

Parameter Estimates

Term	Estimate	Std Error	t Ratio	Prob>|t|
Intercept	969.56493	16.98513	57.08	0.0003*
x	-48.56796	7.791264	-6.23	0.0248*

Bivariate Fit of y By x Glass ID=SWPF-17, VSL ID=GAP-05, Regression=% crys fit to temp

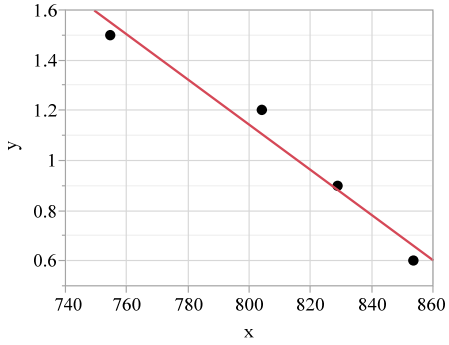

Linear Fit

Linear Fit
y = 8.3396953 - 0.0089957*x

Summary of Fit

RSquare	0.965542
RSquare Adj	0.948314
Root Mean Square Error	0.088051
Mean of Response	1.05
Observations (or Sum Wgts)	4

Analysis of Variance

Source	DF	Sum of Squares	Mean Square	F Ratio
Model	1	0.43449409	0.434494	56.0424
Error	2	0.01550591	0.007753	**Prob > F**
C. Total	3	0.45000000		0.0174*

Parameter Estimates

Term	Estimate	Std Error	t Ratio	Prob>|t|
Intercept	8.3396953	0.974753	8.56	0.0134*
x	-0.008996	0.001202	-7.49	0.0174*

Bivariate Fit of y By x Glass ID=SWPF-17, VSL ID=GAP-05, Regression=temps fit to % crys

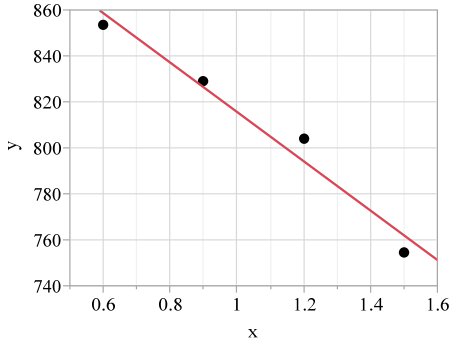

Linear Fit

Linear Fit
y = 923.05 - 107.33333*x

Summary of Fit

RSquare	0.965542
RSquare Adj	0.948314
Root Mean Square Error	9.617952
Mean of Response	810.35
Observations (or Sum Wgts)	4

Analysis of Variance

Source	DF	Sum of Squares	Mean Square	F Ratio
Model	1	5184.2000	5184.20	56.0424
Error	2	185.0100	92.50	**Prob > F**
C. Total	3	5369.2100		0.0174*

Parameter Estimates

Term	Estimate	Std Error	t Ratio	Prob>|t|
Intercept	923.05	15.80391	58.41	0.0003*
x	-107.3333	14.3376	-7.49	0.0174*

Exhibit A1. Liquidus Temperature Determinations

Bivariate Fit of y By x Glass ID=SWPF-18, VSL ID=GAP-29, Regression=% crys fit to temp

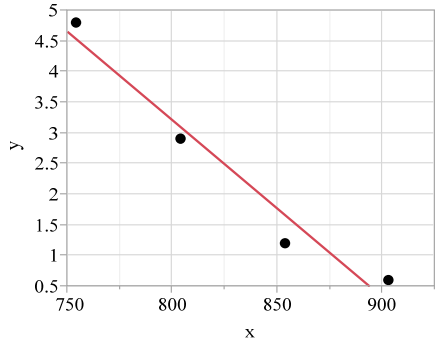

Linear Fit
y = 26.292841 - 0.0288532*x

Summary of Fit

RSquare	0.95663
RSquare Adj	0.934944
Root Mean Square Error	0.481415
Mean of Response	2.375
Observations (or Sum Wgts)	4

Analysis of Variance

Source	DF	Sum of Squares	Mean Square	F Ratio
Model	1	10.223979	10.2240	44.1144
Error	2	0.463521	0.2318	**Prob > F**
C. Total	3	10.687500		0.0219*

Parameter Estimates

Term	Estimate	Std Error	t Ratio	Prob>|t|
Intercept	26.292841	3.609107	7.29	0.0183*
x	-0.028853	0.004344	-6.64	0.0219*

Bivariate Fit of y By x Glass ID=SWPF-18, VSL ID=GAP-29, Regression=temps fit to % crys

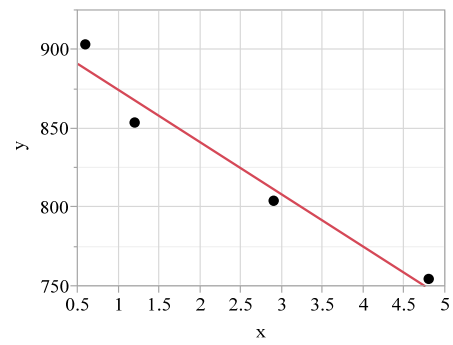

Linear Fit
y = 907.69333 - 33.155088*x

Summary of Fit

RSquare	0.95663
RSquare Adj	0.934944
Root Mean Square Error	16.31917
Mean of Response	828.95
Observations (or Sum Wgts)	4

Analysis of Variance

Source	DF	Sum of Squares	Mean Square	F Ratio
Model	1	11748.340	11748.3	44.1144
Error	2	532.630	266.3	**Prob > F**
C. Total	3	12280.970		0.0219*

Parameter Estimates

Term	Estimate	Std Error	t Ratio	Prob>|t|
Intercept	907.69333	14.39215	63.07	0.0003*
x	-33.15509	4.991832	-6.64	0.0219*

Bivariate Fit of y By x Glass ID=SWPF-19, VSL ID=GAP-35, Regression=% crys fit to temp

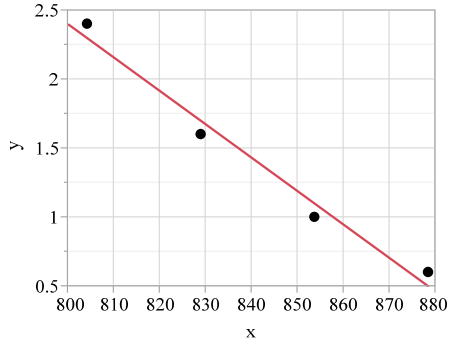

Linear Fit
y = 21.776527 - 0.0242196*x

Summary of Fit

RSquare	0.977997
RSquare Adj	0.966995
Root Mean Square Error	0.142278
Mean of Response	1.4
Observations (or Sum Wgts)	4

Analysis of Variance

Source	DF	Sum of Squares	Mean Square	F Ratio
Model	1	1.7995138	1.79951	88.8952
Error	2	0.0404862	0.02024	**Prob > F**
C. Total	3	1.8400000		0.0111*

Parameter Estimates

Term	Estimate	Std Error	t Ratio	Prob>|t|
Intercept	21.776527	2.162351	10.07	0.0097*
x	-0.02422	0.002569	-9.43	0.0111*

Bivariate Fit of y By x Glass ID=SWPF-19, VSL ID=GAP-35, Regression=temps fit to % crys

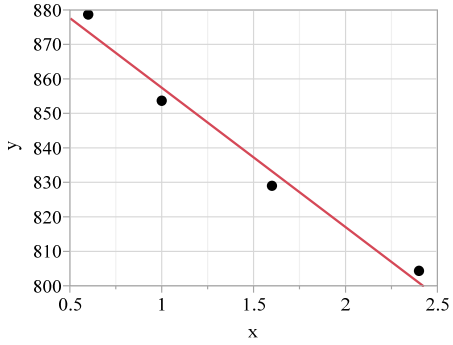

Linear Fit
y = 897.85761 - 40.380435*x

Summary of Fit

RSquare	0.977997
RSquare Adj	0.966995
Root Mean Square Error	5.809526
Mean of Response	841.325
Observations (or Sum Wgts)	4

Analysis of Variance

Source	DF	Sum of Squares	Mean Square	F Ratio
Model	1	3000.2663	3000.27	88.8952
Error	2	67.5012	33.75	**Prob > F**
C. Total	3	3067.7675		0.0111*

Parameter Estimates

Term	Estimate	Std Error	t Ratio	Prob>|t|
Intercept	897.85761	6.662535	134.76	<.0001*
x	-40.38043	4.28284	-9.43	0.0111*

Exhibit A1. Liquidus Temperature Determinations

Bivariate Fit of y By x Glass ID=SWPF-20, VSL ID=GAP-46, Regression=% crys fit to temp

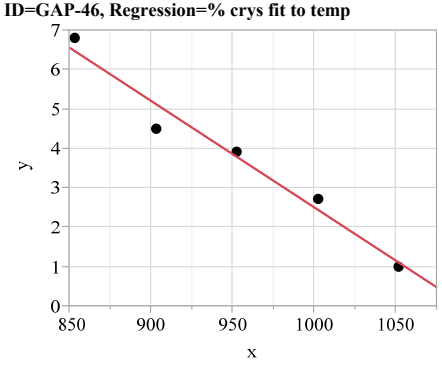

Linear Fit
y = 29.53871 - 0.0270336*x

Summary of Fit

RSquare	0.968164
RSquare Adj	0.957552
Root Mean Square Error	0.443655
Mean of Response	3.78
Observations (or Sum Wgts)	5

Analysis of Variance

Source	DF	Sum of Squares	Mean Square	F Ratio
Model	1	17.957512	17.9575	91.2339
Error	3	0.590488	0.1968	**Prob > F**
C. Total	4	18.548000		0.0024*

Parameter Estimates

Term	Estimate	Std Error	t Ratio	Prob>|t|
Intercept	29.53871	2.704072	10.92	0.0016*
x	-0.027034	0.00283	-9.55	0.0024*

Bivariate Fit of y By x Glass ID=SWPF-20, VSL ID=GAP-46, Regression=temps fit to % crys

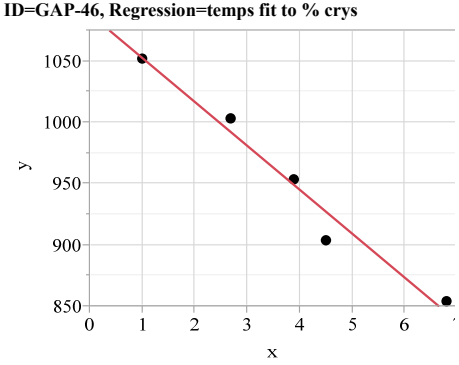

Linear Fit
y = 1088.2145 - 35.813349*x

Summary of Fit

RSquare	0.968164
RSquare Adj	0.957552
Root Mean Square Error	16.14788
Mean of Response	952.84
Observations (or Sum Wgts)	5

Analysis of Variance

Source	DF	Sum of Squares	Mean Square	F Ratio
Model	1	23789.590	23789.6	91.2339
Error	3	782.262	260.8	**Prob > F**
C. Total	4	24571.852		0.0024*

Parameter Estimates

Term	Estimate	Std Error	t Ratio	Prob>|t|
Intercept	1088.2145	15.90666	68.41	<.0001*
x	-35.81335	3.749444	-9.55	0.0024*

Bivariate Fit of y By x Glass ID=SWPF-21, VSL ID=GAP-41, Regression=% crys fit to temp

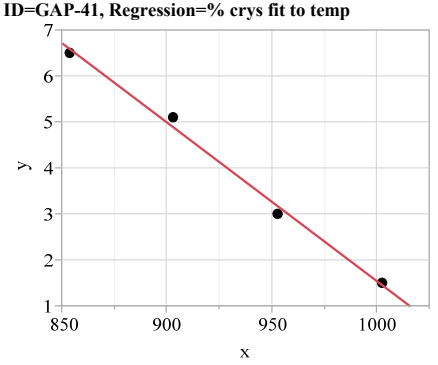

Linear Fit
y = 36.045108 - 0.0345026*x

Summary of Fit

RSquare	0.994023
RSquare Adj	0.991035
Root Mean Square Error	0.209642
Mean of Response	4.025
Observations (or Sum Wgts)	4

Analysis of Variance

Source	DF	Sum of Squares	Mean Square	F Ratio
Model	1	14.619601	14.6196	332.6437
Error	2	0.087899	0.0439	**Prob > F**
C. Total	3	14.707500		0.0030*

Parameter Estimates

Term	Estimate	Std Error	t Ratio	Prob>|t|
Intercept	36.045108	1.758757	20.49	0.0024*
x	-0.034503	0.001892	-18.24	0.0030*

Bivariate Fit of y By x Glass ID=SWPF-21, VSL ID=GAP-41, Regression=temps fit to % crys

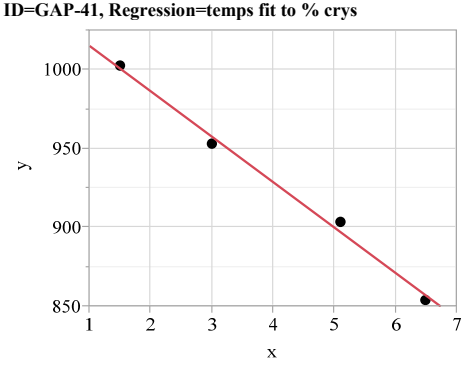

Linear Fit
y = 1044.0108 - 28.810131*x

Summary of Fit

RSquare	0.994023
RSquare Adj	0.991035
Root Mean Square Error	6.057941
Mean of Response	928.05
Observations (or Sum Wgts)	4

Analysis of Variance

Source	DF	Sum of Squares	Mean Square	F Ratio
Model	1	12207.573	12207.6	332.6437
Error	2	73.397	36.7	**Prob > F**
C. Total	3	12280.970		0.0030*

Parameter Estimates

Term	Estimate	Std Error	t Ratio	Prob>|t|
Intercept	1044.0108	7.042656	148.24	<.0001*
x	-28.81013	1.579631	-18.24	0.0030*

Exhibit A1. Liquidus Temperature Determinations

Bivariate Fit of y By x Glass ID=SWPF-22, VSL ID=GAP-20, Regression=% crys fit to temp

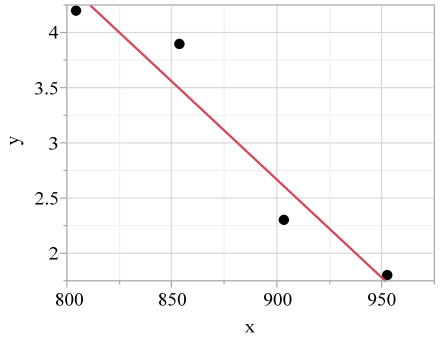

Linear Fit

Linear Fit
y = 18.656883 - 0.0177654*x

Summary of Fit

RSquare	0.928742
RSquare Adj	0.893112
Root Mean Square Error	0.385453
Mean of Response	3.05
Observations (or Sum Wgts)	4

Analysis of Variance

Source	DF	Sum of Squares	Mean Square	F Ratio
Model	1	3.8728521	3.87285	26.0668
Error	2	0.2971479	0.14857	**Prob > F**
C. Total	3	4.1700000		0.0363*

Parameter Estimates

Term	Estimate	Std Error	t Ratio	Prob>|t|
Intercept	18.656883	3.062905	6.09	0.0259*
x	-0.017765	0.00348	-5.11	0.0363*

Bivariate Fit of y By x Glass ID=SWPF-22, VSL ID=GAP-20, Regression=temps fit to % crys

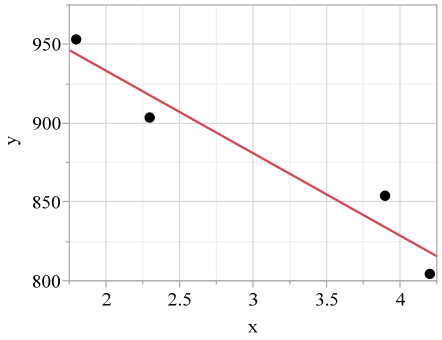

Linear Fit

Linear Fit
y = 1037.9484 - 52.278177*x

Summary of Fit

RSquare	0.928742
RSquare Adj	0.893112
Root Mean Square Error	20.90954
Mean of Response	878.5
Observations (or Sum Wgts)	4

Analysis of Variance

Source	DF	Sum of Squares	Mean Square	F Ratio
Model	1	11396.643	11396.6	26.0668
Error	2	874.417	437.2	**Prob > F**
C. Total	3	12271.060		0.0363*

Parameter Estimates

Term	Estimate	Std Error	t Ratio	Prob>|t|
Intercept	1037.9484	32.93378	31.52	0.0010*
x	-52.27818	10.23944	-5.11	0.0363*

Bivariate Fit of y By x Glass ID=SWPF-23, VSL ID=GAP-23, Regression=% crys fit to temp

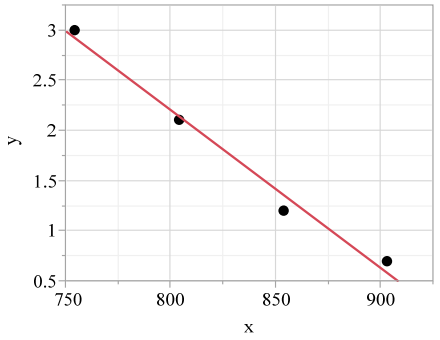

Linear Fit

Linear Fit
y = 14.796156 - 0.0157382*x

Summary of Fit

RSquare	0.984425
RSquare Adj	0.976638
Root Mean Square Error	0.155123
Mean of Response	1.75
Observations (or Sum Wgts)	4

Analysis of Variance

Source	DF	Sum of Squares	Mean Square	F Ratio
Model	1	3.0418736	3.04187	126.4118
Error	2	0.0481264	0.02406	**Prob > F**
C. Total	3	3.0900000		0.0078*

Parameter Estimates

Term	Estimate	Std Error	t Ratio	Prob>|t|
Intercept	14.796156	1.162939	12.72	0.0061*
x	-0.015738	0.0014	-11.24	0.0078*

Bivariate Fit of y By x Glass ID=SWPF-23, VSL ID=GAP-23, Regression=temps fit to % crys

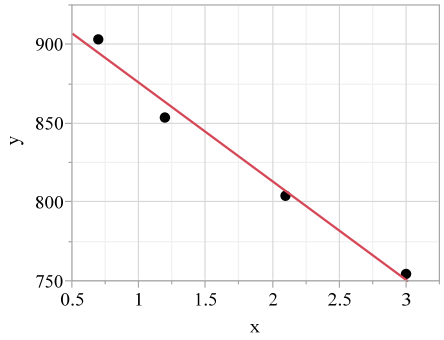

Linear Fit

Linear Fit
y = 938.41278 - 62.550162*x

Summary of Fit

RSquare	0.984425
RSquare Adj	0.976638
Root Mean Square Error	9.779436
Mean of Response	828.95
Observations (or Sum Wgts)	4

Analysis of Variance

Source	DF	Sum of Squares	Mean Square	F Ratio
Model	1	12089.695	12089.7	126.4118
Error	2	191.275	95.6	**Prob > F**
C. Total	3	12280.970		0.0078*

Parameter Estimates

Term	Estimate	Std Error	t Ratio	Prob>|t|
Intercept	938.41278	10.89475	86.13	0.0001*
x	-62.55016	5.563327	-11.24	0.0078*

Exhibit A1. Liquidus Temperature Determinations

Bivariate Fit of y By x Glass ID=SWPF-24, VSL ID=GAP-42, Regression=% crys fit to temp

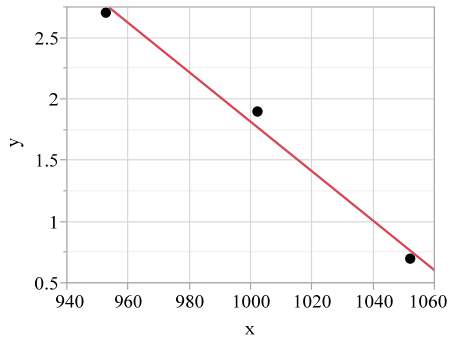

Linear Fit

Linear Fit
y = 21.976344 - 0.0201613*x

Summary of Fit

RSquare	0.986842
RSquare Adj	0.973684
Root Mean Square Error	0.163299
Mean of Response	1.766667
Observations (or Sum Wgts)	3

Analysis of Variance

Source	DF	Sum of Squares	Mean Square	F Ratio
Model	1	2.0000000	2.00000	75.0000
Error	1	0.0266667	0.02667	**Prob > F**
C. Total	2	2.0266667		0.0732

Parameter Estimates

Term	Estimate	Std Error	t Ratio	Prob>|t|
Intercept	21.976344	2.335516	9.41	0.0674
x	-0.020161	0.002328	-8.66	0.0732

Bivariate Fit of y By x Glass ID=SWPF-24, VSL ID=GAP-42, Regression=temps fit to % crys

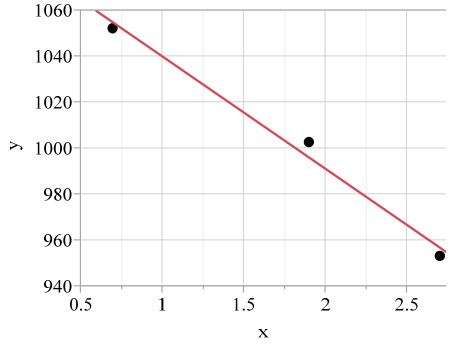

Linear Fit

Linear Fit
y = 1088.8737 - 48.947368*x

Summary of Fit

RSquare	0.986842
RSquare Adj	0.973684
Root Mean Square Error	8.046182
Mean of Response	1002.4
Observations (or Sum Wgts)	3

Analysis of Variance

Source	DF	Sum of Squares	Mean Square	F Ratio
Model	1	4855.5789	4855.58	75.0000
Error	1	64.7411	64.74	**Prob > F**
C. Total	2	4920.3200		0.0732

Parameter Estimates

Term	Estimate	Std Error	t Ratio	Prob>|t|
Intercept	1088.8737	11.01286	98.87	0.0064*
x	-48.94737	5.651955	-8.66	0.0732

Bivariate Fit of y By x Glass ID=SWPF-25, VSL ID=GAP-17, Regression=% crys fit to temp

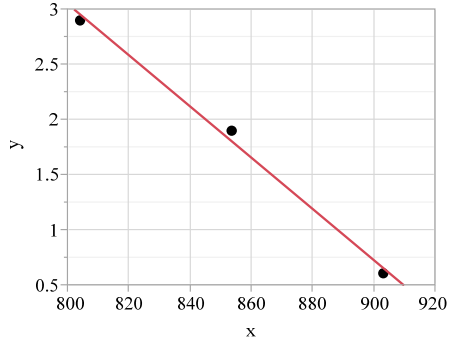

Linear Fit

Linear Fit
y = 21.615057 - 0.0232099*x

Summary of Fit

RSquare	0.994448
RSquare Adj	0.988896
Root Mean Square Error	0.121527
Mean of Response	1.8
Observations (or Sum Wgts)	3

Analysis of Variance

Source	DF	Sum of Squares	Mean Square	F Ratio
Model	1	2.6452312	2.64523	179.1094
Error	1	0.0147688	0.01477	**Prob > F**
C. Total	2	2.6600000		0.0475*

Parameter Estimates

Term	Estimate	Std Error	t Ratio	Prob>|t|
Intercept	21.615057	1.482256	14.58	0.0436*
x	-0.02321	0.001734	-13.38	0.0475*

Bivariate Fit of y By x Glass ID=SWPF-25, VSL ID=GAP-17, Regression=temps fit to % crys

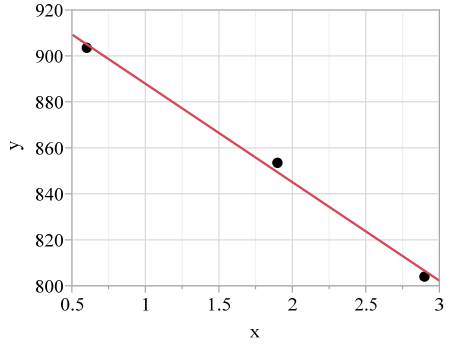

Linear Fit

Linear Fit
y = 930.85589 - 42.845865*x

Summary of Fit

RSquare	0.994448
RSquare Adj	0.988896
Root Mean Square Error	5.221443
Mean of Response	853.7333
Observations (or Sum Wgts)	3

Analysis of Variance

Source	DF	Sum of Squares	Mean Square	F Ratio
Model	1	4883.1432	4883.14	179.1094
Error	1	27.2635	27.26	**Prob > F**
C. Total	2	4910.4067		0.0475*

Parameter Estimates

Term	Estimate	Std Error	t Ratio	Prob>|t|
Intercept	930.85589	6.503535	143.13	0.0044*
x	-42.84586	3.201472	-13.38	0.0475*

Exhibit A1. Liquidus Temperature Determinations

Bivariate Fit of y By x Glass ID=SWPF-26, VSL ID=GAP-06, Regression=% crys fit to temp

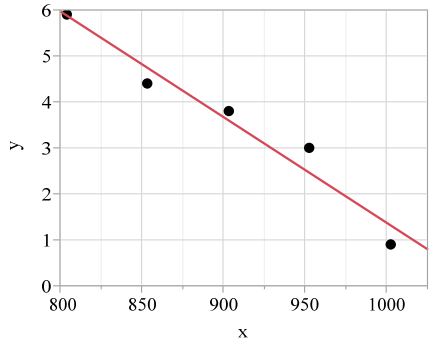

Linear Fit
y = 24.382186 - 0.0230075*x

Summary of Fit

RSquare	0.954219
RSquare Adj	0.938958
Root Mean Square Error	0.455903
Mean of Response	3.6
Observations (or Sum Wgts)	5

Analysis of Variance

Source	DF	Sum of Squares	Mean Square	F Ratio
Model	1	12.996459	12.9965	62.5289
Error	3	0.623541	0.2078	**Prob > F**
C. Total	4	13.620000		0.0042*

Parameter Estimates

Term	Estimate	Std Error	t Ratio	Prob>|t|
Intercept	24.382186	2.63605	9.25	0.0027*
x	-0.023007	0.00291	-7.91	0.0042*

Bivariate Fit of y By x Glass ID=SWPF-26, VSL ID=GAP-06, Regression=temps fit to % crys

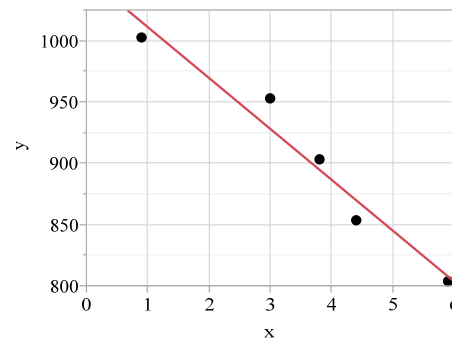

Linear Fit
y = 1052.5875 - 41.474302*x

Summary of Fit

RSquare	0.954219
RSquare Adj	0.938958
Root Mean Square Error	19.35651
Mean of Response	903.28
Observations (or Sum Wgts)	5

Analysis of Variance

Source	DF	Sum of Squares	Mean Square	F Ratio
Model	1	23428.004	23428.0	62.5289
Error	3	1124.024	374.7	**Prob > F**
C. Total	4	24552.028		0.0042*

Parameter Estimates

Term	Estimate	Std Error	t Ratio	Prob>|t|
Intercept	1052.5875	20.77146	50.67	<.0001*
x	-41.4743	5.244917	-7.91	0.0042*

Bivariate Fit of y By x Glass ID=SWPF-27, VSL ID=GAP-24, Regression=% crys fit to temp

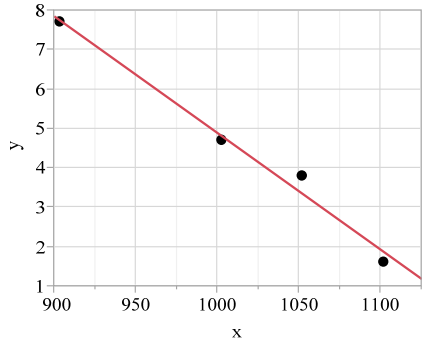

Linear Fit
y = 34.523147 - 0.0296346*x

Summary of Fit

RSquare	0.98434
RSquare Adj	0.97651
Root Mean Square Error	0.387425
Mean of Response	4.45
Observations (or Sum Wgts)	4

Analysis of Variance

Source	DF	Sum of Squares	Mean Square	F Ratio
Model	1	18.869804	18.8698	125.7164
Error	2	0.300196	0.1501	**Prob > F**
C. Total	3	19.170000		0.0079*

Parameter Estimates

Term	Estimate	Std Error	t Ratio	Prob>|t|
Intercept	34.523147	2.689136	12.84	0.0060*
x	-0.029635	0.002643	-11.21	0.0079*

Bivariate Fit of y By x Glass ID=SWPF-27, VSL ID=GAP-24, Regression=temps fit to % crys

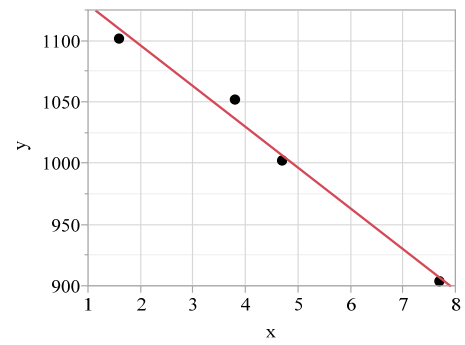

Linear Fit
y = 1162.611 - 33.215962*x

Summary of Fit

RSquare	0.98434
RSquare Adj	0.97651
Root Mean Square Error	12.97066
Mean of Response	1014.8
Observations (or Sum Wgts)	4

Analysis of Variance

Source	DF	Sum of Squares	Mean Square	F Ratio
Model	1	21150.264	21150.3	125.7164
Error	2	336.476	168.2	**Prob > F**
C. Total	3	21486.740		0.0079*

Parameter Estimates

Term	Estimate	Std Error	t Ratio	Prob>|t|
Intercept	1162.611	14.69178	79.13	0.0002*
x	-33.21596	2.962449	-11.21	0.0079*

Exhibit A1. Liquidus Temperature Determinations

Bivariate Fit of y By x Glass ID=SWPF-28, VSL ID=GAP-50, Regression=% crys fit to temp

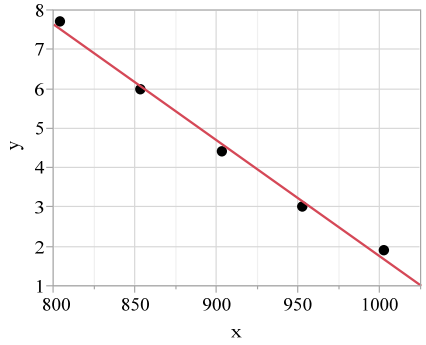

Linear Fit

Linear Fit
y = 31.214943 - 0.0294648*x

Summary of Fit

RSquare	0.993262
RSquare Adj	0.991016
Root Mean Square Error	0.219539
Mean of Response	4.6
Observations (or Sum Wgts)	5

Analysis of Variance

Source	DF	Sum of Squares	Mean Square	F Ratio
Model	1	21.315408	21.3154	442.2531
Error	3	0.144592	0.0482	**Prob > F**
C. Total	4	21.460000		0.0002*

Parameter Estimates

Term	Estimate	Std Error	t Ratio	Prob>|t|
Intercept	31.214943	1.269384	24.59	0.0001*
x	-0.029465	0.001401	-21.03	0.0002*

Bivariate Fit of y By x Glass ID=SWPF-28, VSL ID=GAP-50, Regression=temps fit to % crys

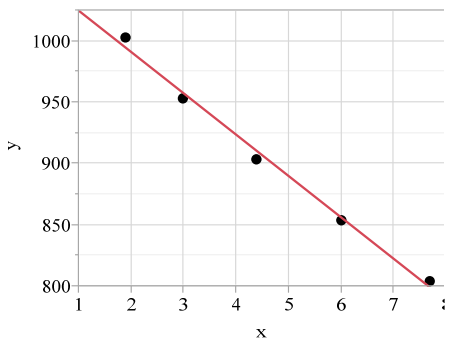

Linear Fit

Linear Fit
y = 1058.3467 - 33.710158*x

Summary of Fit

RSquare	0.993262
RSquare Adj	0.991016
Root Mean Square Error	7.425748
Mean of Response	903.28
Observations (or Sum Wgts)	5

Analysis of Variance

Source	DF	Sum of Squares	Mean Square	F Ratio
Model	1	24386.603	24386.6	442.2531
Error	3	165.425	55.1	**Prob > F**
C. Total	4	24552.028		0.0002*

Parameter Estimates

Term	Estimate	Std Error	t Ratio	Prob>|t|
Intercept	1058.3467	8.086978	130.87	<.0001*
x	-33.71016	1.60297	-21.03	0.0002*

Bivariate Fit of y By x Glass ID=SWPF-29, VSL ID=GAP-32, Regression=% crys fit to temp

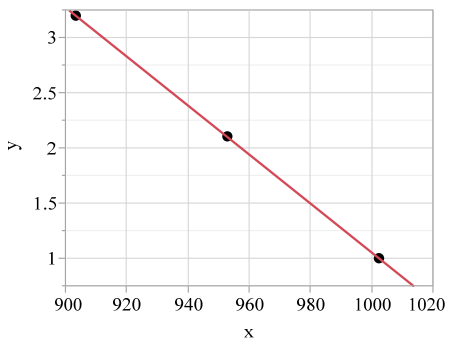

Linear Fit

Linear Fit
y = 23.252701 - 0.0221998*x

Summary of Fit

RSquare	1
RSquare Adj	0.999999
Root Mean Square Error	0.000906
Mean of Response	2.1
Observations (or Sum Wgts)	3

Analysis of Variance

Source	DF	Sum of Squares	Mean Square	F Ratio
Model	1	2.4199992	2.42000	2946242
Error	1	8.21385e-7	8.214e-7	**Prob > F**
C. Total	2	2.4200000		0.0004*

Parameter Estimates

Term	Estimate	Std Error	t Ratio	Prob>|t|
Intercept	23.252701	0.012335	1885.2	0.0003*
x	-0.0222	0.000013	-1716	0.0004*

Bivariate Fit of y By x Glass ID=SWPF-29, VSL ID=GAP-32, Regression=temps fit to % crys

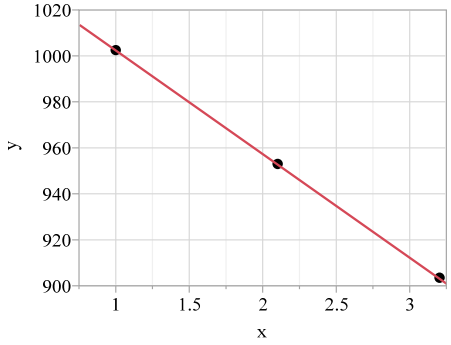

Linear Fit

Linear Fit
y = 1047.4288 - 45.045455*x

Summary of Fit

RSquare	1
RSquare Adj	0.999999
Root Mean Square Error	0.040825
Mean of Response	952.8333
Observations (or Sum Wgts)	3

Analysis of Variance

Source	DF	Sum of Squares	Mean Square	F Ratio
Model	1	4910.4050	4910.40	2946242
Error	1	0.0017	0.001667	**Prob > F**
C. Total	2	4910.4067		0.0004*

Parameter Estimates

Term	Estimate	Std Error	t Ratio	Prob>|t|
Intercept	1047.4288	0.05994	17475	<.0001*
x	-45.04545	0.026243	-1716	0.0004*

Exhibit A1. Liquidus Temperature Determinations

Bivariate Fit of y By x Glass ID=SWPF-30, VSL ID=GAP-16, Regression=% crys fit to temp

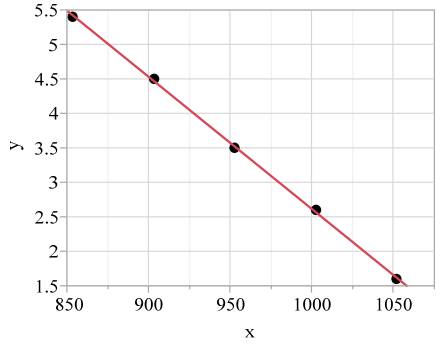

Linear Fit
y = 21.780964 - 0.0191648*x

Summary of Fit

RSquare	0.999663
RSquare Adj	0.999551
Root Mean Square Error	0.03183
Mean of Response	3.52
Observations (or Sum Wgts)	5

Analysis of Variance

Source	DF	Sum of Squares	Mean Square	F Ratio
Model	1	9.0249606	9.02496	8907.877
Error	3	0.0030394	0.00101	**Prob > F**
C. Total	4	9.0280000		<.0001*

Parameter Estimates

Term	Estimate	Std Error	t Ratio	Prob>|t|
Intercept	21.780964	0.194003	112.27	<.0001*
x	-0.019165	0.000203	-94.38	<.0001*

Bivariate Fit of y By x Glass ID=SWPF-30, VSL ID=GAP-16, Regression=temps fit to % crys

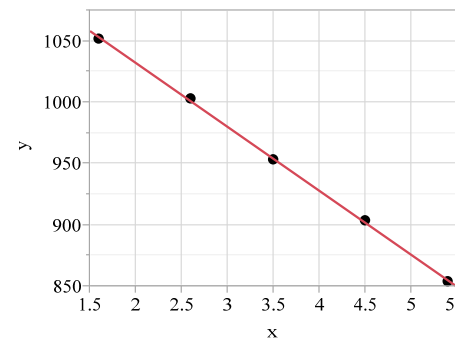

Linear Fit
y = 1136.4485 - 52.161498*x

Summary of Fit

RSquare	0.999663
RSquare Adj	0.999551
Root Mean Square Error	1.660576
Mean of Response	952.84
Observations (or Sum Wgts)	5

Analysis of Variance

Source	DF	Sum of Squares	Mean Square	F Ratio
Model	1	24563.579	24563.6	8907.877
Error	3	8.273	2.8	**Prob > F**
C. Total	4	24571.852		<.0001*

Parameter Estimates

Term	Estimate	Std Error	t Ratio	Prob>|t|
Intercept	1136.4485	2.082313	545.76	<.0001*
x	-52.1615	0.552666	-94.38	<.0001*

Bivariate Fit of y By x Glass ID=SWPF-31, VSL ID=GAP-30, Regression=% crys fit to temp

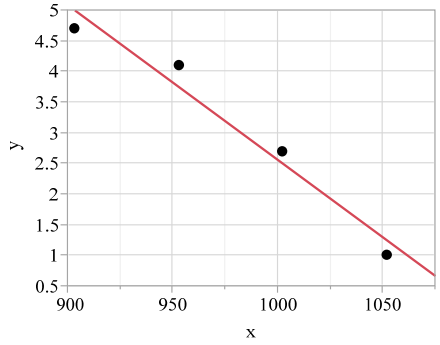

Linear Fit
y = 27.780019 - 0.0252193*x

Summary of Fit

RSquare	0.961429
RSquare Adj	0.942143
Root Mean Square Error	0.39591
Mean of Response	3.125
Observations (or Sum Wgts)	4

Analysis of Variance

Source	DF	Sum of Squares	Mean Square	F Ratio
Model	1	7.8140112	7.81401	49.8519
Error	2	0.3134888	0.15674	**Prob > F**
C. Total	3	8.1275000		0.0195*

Parameter Estimates

Term	Estimate	Std Error	t Ratio	Prob>|t|
Intercept	27.780019	3.497527	7.94	0.0155*
x	-0.025219	0.003572	-7.06	0.0195*

Bivariate Fit of y By x Glass ID=SWPF-31, VSL ID=GAP-30, Regression=temps fit to % crys

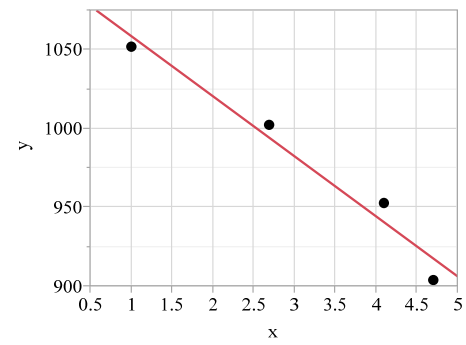

Linear Fit
y = 1096.7585 - 38.122731*x

Summary of Fit

RSquare	0.961429
RSquare Adj	0.942143
Root Mean Square Error	15.39294
Mean of Response	977.625
Observations (or Sum Wgts)	4

Analysis of Variance

Source	DF	Sum of Squares	Mean Square	F Ratio
Model	1	11812.042	11812.0	49.8519
Error	2	473.885	236.9	**Prob > F**
C. Total	3	12285.928		0.0195*

Parameter Estimates

Term	Estimate	Std Error	t Ratio	Prob>|t|
Intercept	1096.7585	18.54548	59.14	0.0003*
x	-38.12273	5.399369	-7.06	0.0195*

Exhibit A1. Liquidus Temperature Determinations

Bivariate Fit of y By x Glass ID=SWPF-32, VSL ID=GAP-09, Regression=% crys fit to temp

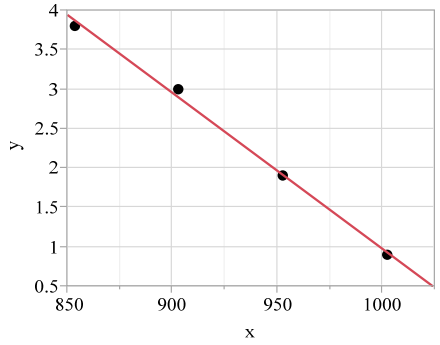

Linear Fit
y = 20.750966 - 0.0197737*x

Summary of Fit

RSquare	0.996233
RSquare Adj	0.994349
Root Mean Square Error	0.095286
Mean of Response	2.4
Observations (or Sum Wgts)	4

Analysis of Variance

Source	DF	Sum of Squares	Mean Square	F Ratio
Model	1	4.8018410	4.80184	528.8670
Error	2	0.0181590	0.00908	**Prob > F**
C. Total	3	4.8200000		0.0019*

Parameter Estimates

Term	Estimate	Std Error	t Ratio	Prob>|t|
Intercept	20.750966	0.799389	25.96	0.0015*
x	-0.019774	0.00086	-23.00	0.0019*

Bivariate Fit of y By x Glass ID=SWPF-32, VSL ID=GAP-09, Regression=temps fit to % crys

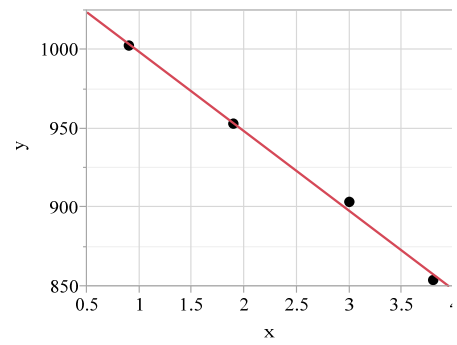

Linear Fit
y = 1048.9662 - 50.381743*x

Summary of Fit

RSquare	0.996233
RSquare Adj	0.994349
Root Mean Square Error	4.809761
Mean of Response	928.05
Observations (or Sum Wgts)	4

Analysis of Variance

Source	DF	Sum of Squares	Mean Square	F Ratio
Model	1	12234.702	12234.7	528.8670
Error	2	46.268	23.1	**Prob > F**
C. Total	3	12280.970		0.0019*

Parameter Estimates

Term	Estimate	Std Error	t Ratio	Prob>|t|
Intercept	1048.9662	5.781766	181.43	<.0001*
x	-50.38174	2.190786	-23.00	0.0019*

Bivariate Fit of y By x Glass ID=SWPF-33, VSL ID=GAP-40, Regression=% crys fit to temp

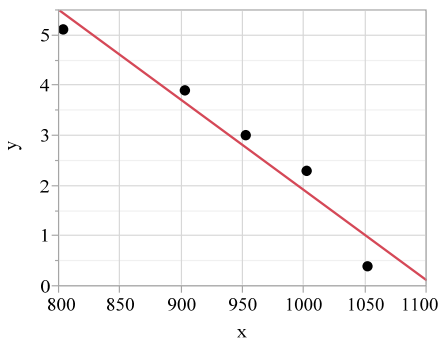

Linear Fit
y = 19.86009 - 0.017944*x

Summary of Fit

RSquare	0.939865
RSquare Adj	0.91982
Root Mean Square Error	0.499599
Mean of Response	2.94
Observations (or Sum Wgts)	5

Analysis of Variance

Source	DF	Sum of Squares	Mean Square	F Ratio
Model	1	11.703203	11.7032	46.8880
Error	3	0.748797	0.2496	**Prob > F**
C. Total	4	12.452000		0.0064*

Parameter Estimates

Term	Estimate	Std Error	t Ratio	Prob>|t|
Intercept	19.86009	2.481075	8.00	0.0041*
x	-0.017944	0.002621	-6.85	0.0064*

Bivariate Fit of y By x Glass ID=SWPF-33, VSL ID=GAP-40, Regression=temps fit to % crys

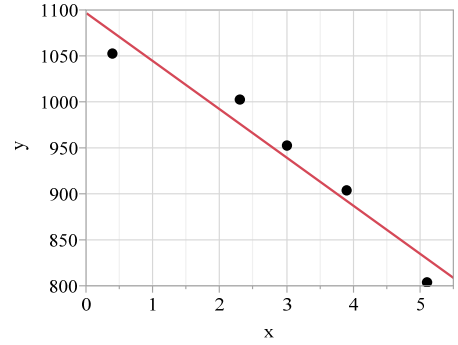

Linear Fit
y = 1096.9306 - 52.377771*x

Summary of Fit

RSquare	0.939865
RSquare Adj	0.91982
Root Mean Square Error	26.99204
Mean of Response	942.94
Observations (or Sum Wgts)	5

Analysis of Variance

Source	DF	Sum of Squares	Mean Square	F Ratio
Model	1	34161.201	34161.2	46.8880
Error	3	2185.711	728.6	**Prob > F**
C. Total	4	36346.912		0.0064*

Parameter Estimates

Term	Estimate	Std Error	t Ratio	Prob>|t|
Intercept	1096.9306	25.52359	42.98	<.0001*
x	-52.37777	7.649203	-6.85	0.0064*

Exhibit A1. Liquidus Temperature Determinations

Bivariate Fit of y By x Glass ID=SWPF-34, VSL ID=GAP-36, Regression=% crys fit to temp

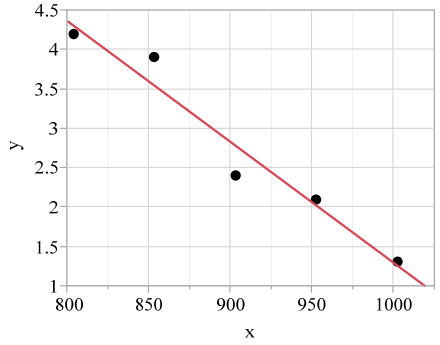

Linear Fit
y = 16.635355 - 0.0153389*x

Summary of Fit

RSquare	0.95199
RSquare Adj	0.935986
Root Mean Square Error	0.311623
Mean of Response	2.78
Observations (or Sum Wgts)	5

Analysis of Variance

Source	DF	Sum of Squares	Mean Square	F Ratio
Model	1	5.7766742	5.77667	59.4867
Error	3	0.2913258	0.09711	**Prob > F**
C. Total	4	6.0680000		0.0045*

Parameter Estimates

Term	Estimate	Std Error	t Ratio	Prob>|t|
Intercept	16.635355	1.801816	9.23	0.0027*
x	-0.015339	0.001989	-7.71	0.0045*

Bivariate Fit of y By x Glass ID=SWPF-34, VSL ID=GAP-36, Regression=temps fit to % crys

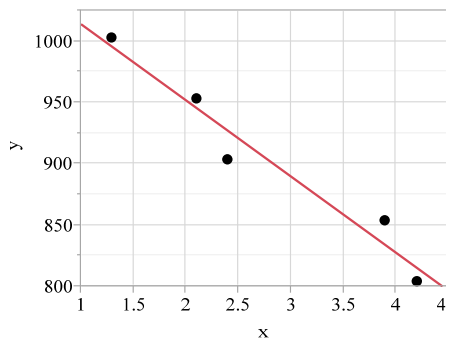

Linear Fit
y = 1075.8168 - 62.063612*x

Summary of Fit

RSquare	0.95199
RSquare Adj	0.935986
Root Mean Square Error	19.8221
Mean of Response	903.28
Observations (or Sum Wgts)	5

Analysis of Variance

Source	DF	Sum of Squares	Mean Square	F Ratio
Model	1	23373.281	23373.3	59.4867
Error	3	1178.747	392.9	**Prob > F**
C. Total	4	24552.028		0.0045*

Parameter Estimates

Term	Estimate	Std Error	t Ratio	Prob>|t|
Intercept	1075.8168	24.0627	44.71	<.0001*
x	-62.06361	8.04687	-7.71	0.0045*

Bivariate Fit of y By x Glass ID=SWPF-35, VSL ID=GAP-03, Regression=% crys fit to temp

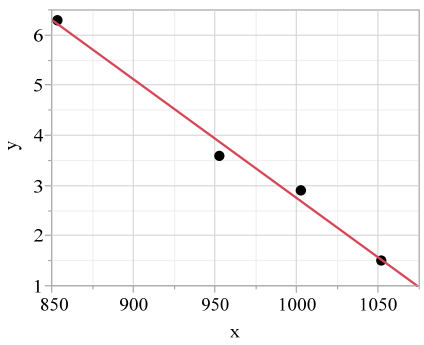

Linear Fit
y = 26.438293 - 0.023687*x

Summary of Fit

RSquare	0.989981
RSquare Adj	0.984971
Root Mean Square Error	0.247091
Mean of Response	3.575
Observations (or Sum Wgts)	4

Analysis of Variance

Source	DF	Sum of Squares	Mean Square	F Ratio
Model	1	12.065392	12.0654	197.6187
Error	2	0.122108	0.0611	**Prob > F**
C. Total	3	12.187500		0.0050*

Parameter Estimates

Term	Estimate	Std Error	t Ratio	Prob>|t|
Intercept	26.438293	1.631076	16.21	0.0038*
x	-0.023687	0.001685	-14.06	0.0050*

Bivariate Fit of y By x Glass ID=SWPF-35, VSL ID=GAP-03, Regression=temps fit to % crys

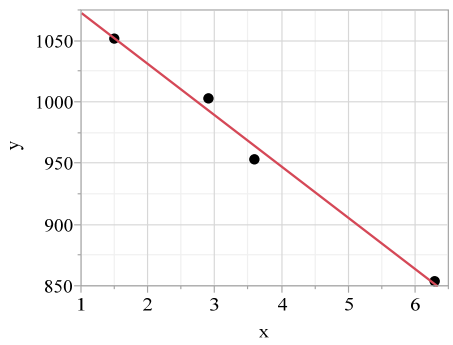

Linear Fit
y = 1114.6395 - 41.794256*x

Summary of Fit

RSquare	0.989981
RSquare Adj	0.984971
Root Mean Square Error	10.3791
Mean of Response	965.225
Observations (or Sum Wgts)	4

Analysis of Variance

Source	DF	Sum of Squares	Mean Square	F Ratio
Model	1	21288.636	21288.6	197.6187
Error	2	215.452	107.7	**Prob > F**
C. Total	3	21504.087		0.0050*

Parameter Estimates

Term	Estimate	Std Error	t Ratio	Prob>|t|
Intercept	1114.6395	11.82793	94.24	0.0001*
x	-41.79426	2.973052	-14.06	0.0050*

Exhibit A1. Liquidus Temperature Determinations

Bivariate Fit of y By x Glass ID=SWPF-36, VSL ID=GAP-11, Regression=% crys fit to temp

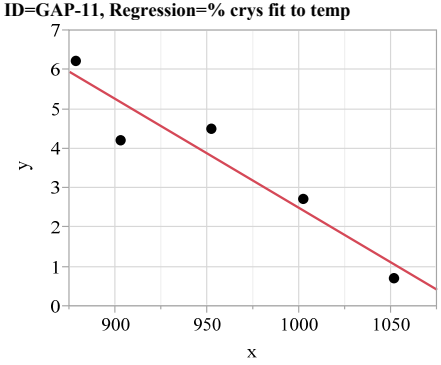

Linear Fit
y = 30.126443 - 0.0276325*x

Summary of Fit

RSquare	0.897912
RSquare Adj	0.863883
Root Mean Square Error	0.763537
Mean of Response	3.66
Observations (or Sum Wgts)	5

Analysis of Variance

Source	DF	Sum of Squares	Mean Square	F Ratio
Model	1	15.383033	15.3830	26.3865
Error	3	1.748967	0.5830	**Prob > F**
C. Total	4	17.132000		0.0143*

Parameter Estimates

Term	Estimate	Std Error	t Ratio	Prob>|t|
Intercept	30.126443	5.163646	5.83	0.0100*
x	-0.027633	0.005379	-5.14	0.0143*

Bivariate Fit of y By x Glass ID=SWPF-36, VSL ID=GAP-11, Regression=temps fit to % crys

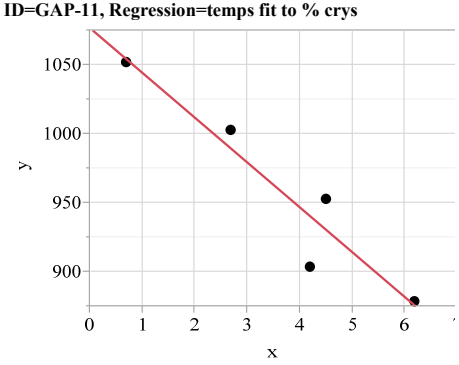

Linear Fit
y = 1076.7308 - 32.494747*x

Summary of Fit

RSquare	0.897912
RSquare Adj	0.863883
Root Mean Square Error	26.18342
Mean of Response	957.8
Observations (or Sum Wgts)	5

Analysis of Variance

Source	DF	Sum of Squares	Mean Square	F Ratio
Model	1	18089.825	18089.8	26.3865
Error	3	2056.715	685.6	**Prob > F**
C. Total	4	20146.540		0.0143*

Parameter Estimates

Term	Estimate	Std Error	t Ratio	Prob>|t|
Intercept	1076.7308	25.94545	41.50	<.0001*
x	-32.49475	6.3259	-5.14	0.0143*

Bivariate Fit of y By x Glass ID=SWPF-37, VSL ID=GAP-07, Regression=% crys fit to temp

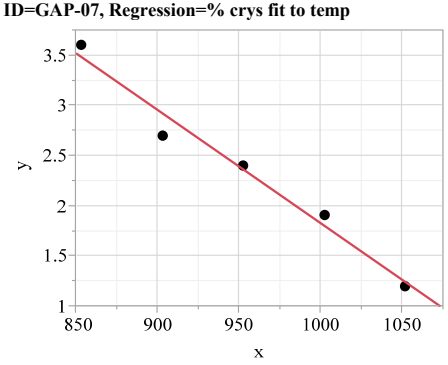

Linear Fit
y = 13.124768 - 0.0112976*x

Summary of Fit

RSquare	0.976409
RSquare Adj	0.968545
Root Mean Square Error	0.158928
Mean of Response	2.36
Observations (or Sum Wgts)	5

Analysis of Variance

Source	DF	Sum of Squares	Mean Square	F Ratio
Model	1	3.1362256	3.13623	124.1669
Error	3	0.0757744	0.02526	**Prob > F**
C. Total	4	3.2120000		0.0015*

Parameter Estimates

Term	Estimate	Std Error	t Ratio	Prob>|t|
Intercept	13.124768	0.968666	13.55	0.0009*
x	-0.011298	0.001014	-11.14	0.0015*

Bivariate Fit of y By x Glass ID=SWPF-37, VSL ID=GAP-07, Regression=temps fit to % crys

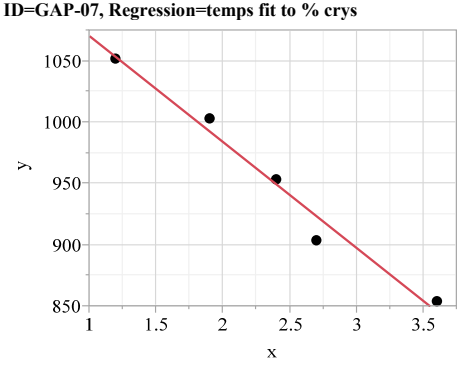

Linear Fit
y = 1156.8066 - 86.426526*x

Summary of Fit

RSquare	0.976409
RSquare Adj	0.968545
Root Mean Square Error	13.90055
Mean of Response	952.84
Observations (or Sum Wgts)	5

Analysis of Variance

Source	DF	Sum of Squares	Mean Square	F Ratio
Model	1	23992.176	23992.2	124.1669
Error	3	579.676	193.2	**Prob > F**
C. Total	4	24571.852		0.0015*

Parameter Estimates

Term	Estimate	Std Error	t Ratio	Prob>|t|
Intercept	1156.8066	19.33125	59.84	<.0001*
x	-86.42653	7.756113	-11.14	0.0015*

Exhibit A1. Liquidus Temperature Determinations

Bivariate Fit of y By x Glass ID=SWPF-38, VSL ID=GAP-13, Regression=% crys fit to temp

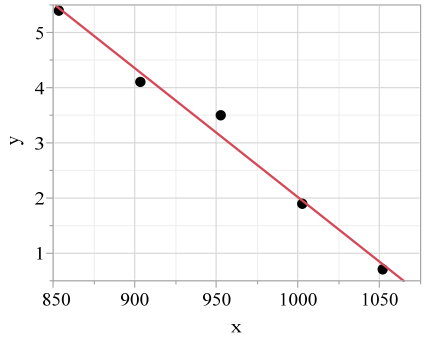

Linear Fit
y = 25.418498 - 0.0234021*x

Summary of Fit

RSquare	0.986007
RSquare Adj	0.981343
Root Mean Square Error	0.252304
Mean of Response	3.12
Observations (or Sum Wgts)	5

Analysis of Variance

Source	DF	Sum of Squares	Mean Square	F Ratio
Model	1	13.457028	13.4570	211.3980
Error	3	0.190972	0.0637	**Prob > F**
C. Total	4	13.648000		0.0007*

Parameter Estimates

Term	Estimate	Std Error	t Ratio	Prob>|t|
Intercept	25.418498	1.537791	16.53	0.0005*
x	-0.023402	0.00161	-14.54	0.0007*

Bivariate Fit of y By x Glass ID=SWPF-38, VSL ID=GAP-13, Regression=temps fit to % crys

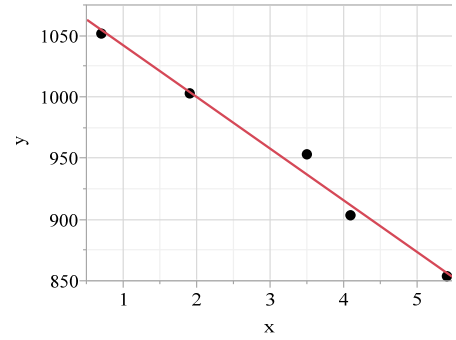

Linear Fit
y = 1084.2956 - 42.133206*x

Summary of Fit

RSquare	0.986007
RSquare Adj	0.981343
Root Mean Square Error	10.70554
Mean of Response	952.84
Observations (or Sum Wgts)	5

Analysis of Variance

Source	DF	Sum of Squares	Mean Square	F Ratio
Model	1	24228.026	24228.0	211.3980
Error	3	343.826	114.6	**Prob > F**
C. Total	4	24571.852		0.0007*

Parameter Estimates

Term	Estimate	Std Error	t Ratio	Prob>|t|
Intercept	1084.2956	10.23064	105.99	<.0001*
x	-42.13321	2.897838	-14.54	0.0007*

Bivariate Fit of y By x Glass ID=SWPF-39, VSL ID=GAP-49, Regression=% crys fit to temp

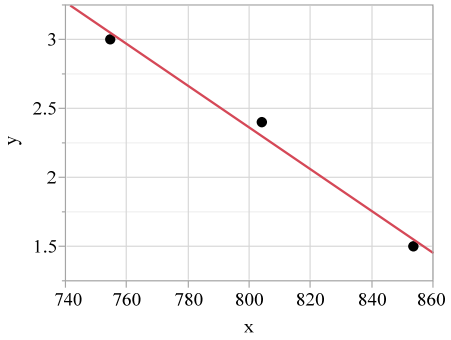

Linear Fit
y = 14.471225 - 0.0151352*x

Summary of Fit

RSquare	0.986709
RSquare Adj	0.973418
Root Mean Square Error	0.123092
Mean of Response	2.3
Observations (or Sum Wgts)	3

Analysis of Variance

Source	DF	Sum of Squares	Mean Square	F Ratio
Model	1	1.1248483	1.12485	74.2389
Error	1	0.0151517	0.01515	**Prob > F**
C. Total	2	1.1400000		0.0736

Parameter Estimates

Term	Estimate	Std Error	t Ratio	Prob>|t|
Intercept	14.471225	1.414385	10.23	0.0620
x	-0.015135	0.001757	-8.62	0.0736

Bivariate Fit of y By x Glass ID=SWPF-39, VSL ID=GAP-49, Regression=temps fit to % crys

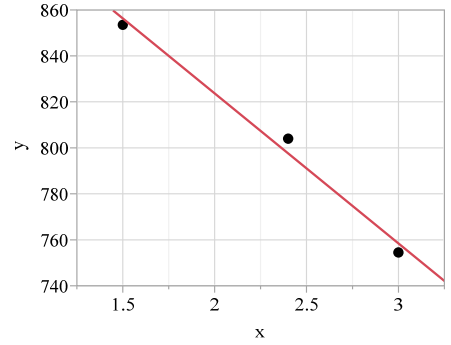

Linear Fit
y = 954.11053 - 65.192982*x

Summary of Fit

RSquare	0.986709
RSquare Adj	0.973418
Root Mean Square Error	8.078627
Mean of Response	804.1667
Observations (or Sum Wgts)	3

Analysis of Variance

Source	DF	Sum of Squares	Mean Square	F Ratio
Model	1	4845.1425	4845.14	74.2389
Error	1	65.2642	65.26	**Prob > F**
C. Total	2	4910.4067		0.0736

Parameter Estimates

Term	Estimate	Std Error	t Ratio	Prob>|t|
Intercept	954.11053	18.01676	52.96	0.0120*
x	-65.19298	7.566327	-8.62	0.0736

Exhibit A1. Liquidus Temperature Determinations

Bivariate Fit of y By x Glass ID=SWPF-40, VSL ID=GAP-48, Regression=% crys fit to temp

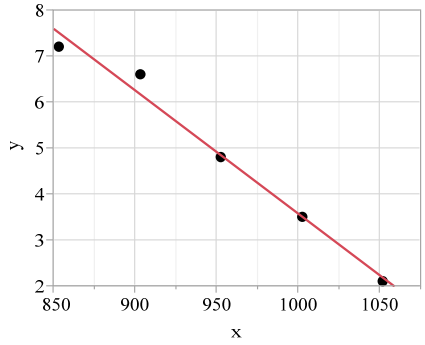

Linear Fit
y = 30.404899 - 0.0268302*x

Summary of Fit

RSquare	0.984214
RSquare Adj	0.978952
Root Mean Square Error	0.307517
Mean of Response	4.84
Observations (or Sum Wgts)	5

Analysis of Variance

Source	DF	Sum of Squares	Mean Square	F Ratio
Model	1	17.688300	17.6883	187.0460
Error	3	0.283700	0.0946	**Prob > F**
C. Total	4	17.972000		0.0008*

Parameter Estimates

Term	Estimate	Std Error	t Ratio	Prob>|t|
Intercept	30.404899	1.874313	16.22	0.0005*
x	-0.02683	0.001962	-13.68	0.0008*

Bivariate Fit of y By x Glass ID=SWPF-40, VSL ID=GAP-48, Regression=temps fit to % crys

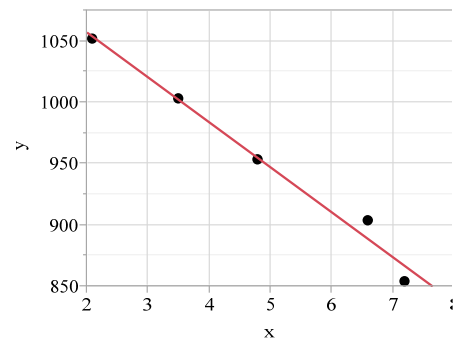

Linear Fit
y = 1130.386 - 36.683063*x

Summary of Fit

RSquare	0.984214
RSquare Adj	0.978952
Root Mean Square Error	11.37076
Mean of Response	952.84
Observations (or Sum Wgts)	5

Analysis of Variance

Source	DF	Sum of Squares	Mean Square	F Ratio
Model	1	24183.969	24184.0	187.0460
Error	3	387.883	129.3	**Prob > F**
C. Total	4	24571.852		0.0008*

Parameter Estimates

Term	Estimate	Std Error	t Ratio	Prob>|t|
Intercept	1130.386	13.94229	81.08	<.0001*
x	-36.68306	2.682201	-13.68	0.0008*

Bivariate Fit of y By x Glass ID=SWPF-41, VSL ID=GAP-04, Regression=% crys fit to temp

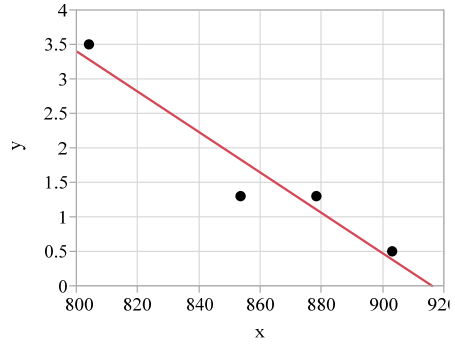

Linear Fit
y = 26.836337 - 0.029289*x

Summary of Fit

RSquare	0.923249
RSquare Adj	0.884873
Root Mean Square Error	0.4376
Mean of Response	1.65
Observations (or Sum Wgts)	4

Analysis of Variance

Source	DF	Sum of Squares	Mean Square	F Ratio
Model	1	4.6070122	4.60701	24.0583
Error	2	0.3829878	0.19149	**Prob > F**
C. Total	3	4.9900000		0.0391*

Parameter Estimates

Term	Estimate	Std Error	t Ratio	Prob>|t|
Intercept	26.836337	5.139569	5.22	0.0348*
x	-0.029289	0.005971	-4.90	0.0391*

Bivariate Fit of y By x Glass ID=SWPF-41, VSL ID=GAP-04, Regression=temps fit to % crys

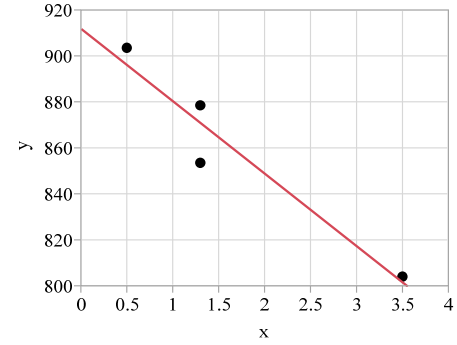

Linear Fit
y = 911.93637 - 31.522044*x

Summary of Fit

RSquare	0.923249
RSquare Adj	0.884873
Root Mean Square Error	14.35597
Mean of Response	859.925
Observations (or Sum Wgts)	4

Analysis of Variance

Source	DF	Sum of Squares	Mean Square	F Ratio
Model	1	4958.2599	4958.26	24.0583
Error	2	412.1876	206.09	**Prob > F**
C. Total	3	5370.4475		0.0391*

Parameter Estimates

Term	Estimate	Std Error	t Ratio	Prob>|t|
Intercept	911.93637	12.80494	71.22	0.0002*
x	-31.52204	6.426613	-4.90	0.0391*

Exhibit A1. Liquidus Temperature Determinations

Bivariate Fit of y By x Glass ID=SWPF-42, VSL ID=GAP-27, Regression=% crys fit to temp

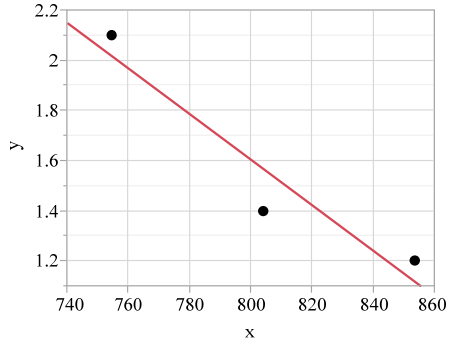

Linear Fit

Linear Fit
y = 8.871258 - 0.0090834*x

Summary of Fit

RSquare	0.907055
RSquare Adj	0.81411
Root Mean Square Error	0.203753
Mean of Response	1.566667
Observations (or Sum Wgts)	3

Analysis of Variance

Source	DF	Sum of Squares	Mean Square	F Ratio
Model	1	0.40515124	0.405151	9.7591
Error	1	0.04151543	0.041515	**Prob > F**
C. Total	2	0.44666667		0.1972

Parameter Estimates

Term	Estimate	Std Error	t Ratio	Prob>|t|
Intercept	8.871258	2.341213	3.79	0.1643
x	-0.009083	0.002908	-3.12	0.1972

Bivariate Fit of y By x Glass ID=SWPF-42, VSL ID=GAP-27, Regression=temps fit to % crys

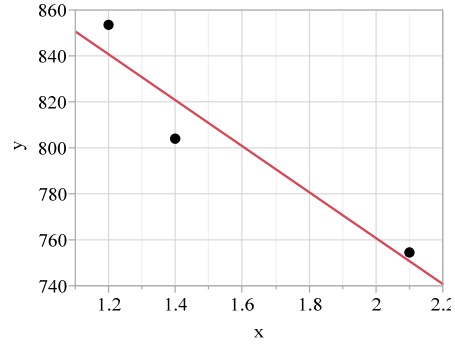

Linear Fit

Linear Fit
y = 960.61119 - 99.858209*x

Summary of Fit

RSquare	0.907055
RSquare Adj	0.81411
Root Mean Square Error	21.36347
Mean of Response	804.1667
Observations (or Sum Wgts)	3

Analysis of Variance

Source	DF	Sum of Squares	Mean Square	F Ratio
Model	1	4454.0090	4454.01	9.7591
Error	1	456.3977	456.40	**Prob > F**
C. Total	2	4910.4067		0.1972

Parameter Estimates

Term	Estimate	Std Error	t Ratio	Prob>|t|
Intercept	960.61119	51.57566	18.63	0.0341*
x	-99.85821	31.96539	-3.12	0.1972

Bivariate Fit of y By x Glass ID=SWPF-43, VSL ID=GAP-28, Regression=% crys fit to temp

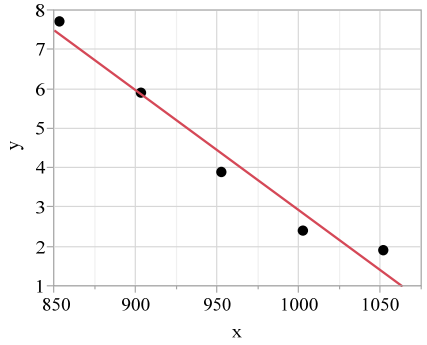

Linear Fit

Linear Fit
y = 33.384026 - 0.0304605*x

Summary of Fit

RSquare	0.964745
RSquare Adj	0.952994
Root Mean Square Error	0.526984
Mean of Response	4.36
Observations (or Sum Wgts)	5

Analysis of Variance

Source	DF	Sum of Squares	Mean Square	F Ratio
Model	1	22.798865	22.7989	82.0954
Error	3	0.833135	0.2777	**Prob > F**
C. Total	4	23.632000		0.0028*

Parameter Estimates

Term	Estimate	Std Error	t Ratio	Prob>|t|
Intercept	33.384026	3.211962	10.39	0.0019*
x	-0.030461	0.003362	-9.06	0.0028*

Bivariate Fit of y By x Glass ID=SWPF-43, VSL ID=GAP-28, Regression=temps fit to % crys

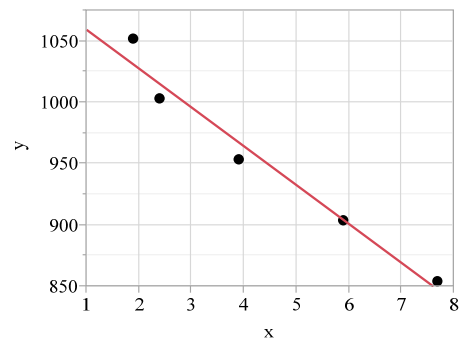

Linear Fit

Linear Fit
y = 1090.9298 - 31.67197*x

Summary of Fit

RSquare	0.964745
RSquare Adj	0.952994
Root Mean Square Error	16.99283
Mean of Response	952.84
Observations (or Sum Wgts)	5

Analysis of Variance

Source	DF	Sum of Squares	Mean Square	F Ratio
Model	1	23705.583	23705.6	82.0954
Error	3	866.269	288.8	**Prob > F**
C. Total	4	24571.852		0.0028*

Parameter Estimates

Term	Estimate	Std Error	t Ratio	Prob>|t|
Intercept	1090.9298	17.03018	64.06	<.0001*
x	-31.67197	3.49555	-9.06	0.0028*

Exhibit A1. Liquidus Temperature Determinations

Bivariate Fit of y By x Glass ID=SWPF-44, VSL ID=GAP-01, Regression=% crys fit to temp

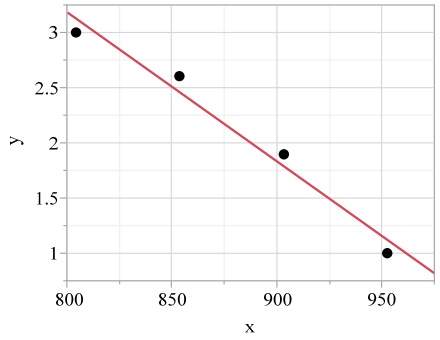

Linear Fit
y = 14.006277 - 0.0135245*x

Summary of Fit

RSquare	0.972709
RSquare Adj	0.959064
Root Mean Square Error	0.177445
Mean of Response	2.125
Observations (or Sum Wgts)	4

Analysis of Variance

Source	DF	Sum of Squares	Mean Square	F Ratio
Model	1	2.2445267	2.24453	71.2850
Error	2	0.0629733	0.03149	**Prob > F**
C. Total	3	2.3075000		0.0137*

Parameter Estimates

Term	Estimate	Std Error	t Ratio	Prob>|t|
Intercept	14.006277	1.410021	9.93	0.0100*
x	-0.013525	0.001602	-8.44	0.0137*

Bivariate Fit of y By x Glass ID=SWPF-44, VSL ID=GAP-01, Regression=temps fit to % crys

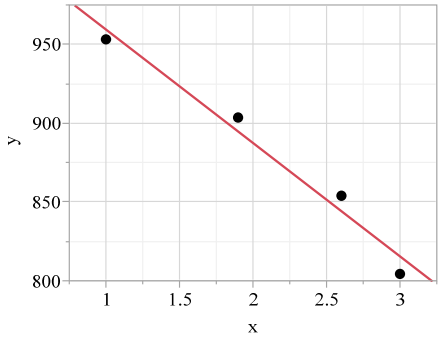

Linear Fit
y = 1031.3342 - 71.921993*x

Summary of Fit

RSquare	0.972709
RSquare Adj	0.959064
Root Mean Square Error	12.93998
Mean of Response	878.5
Observations (or Sum Wgts)	4

Analysis of Variance

Source	DF	Sum of Squares	Mean Square	F Ratio
Model	1	11936.174	11936.2	71.2850
Error	2	334.886	167.4	**Prob > F**
C. Total	3	12271.060		0.0137*

Parameter Estimates

Term	Estimate	Std Error	t Ratio	Prob>|t|
Intercept	1031.3342	19.22331	53.65	0.0003*
x	-71.92199	8.51849	-8.44	0.0137*

Bivariate Fit of y By x Glass ID=SWPF-45, VSL ID=GAP-08, Regression=% crys fit to temp

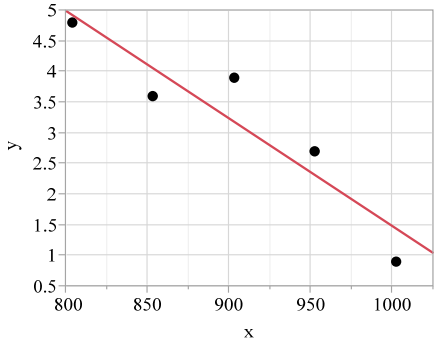

Linear Fit
y = 19.039698 - 0.0175579*x

Summary of Fit

RSquare	0.865214
RSquare Adj	0.820286
Root Mean Square Error	0.626925
Mean of Response	3.18
Observations (or Sum Wgts)	5

Analysis of Variance

Source	DF	Sum of Squares	Mean Square	F Ratio
Model	1	7.5688937	7.56889	19.2575
Error	3	1.1791063	0.39304	**Prob > F**
C. Total	4	8.7480000		0.0219*

Parameter Estimates

Term	Estimate	Std Error	t Ratio	Prob>|t|
Intercept	19.039698	3.624912	5.25	0.0134*
x	-0.017558	0.004001	-4.39	0.0219*

Bivariate Fit of y By x Glass ID=SWPF-45, VSL ID=GAP-08, Regression=temps fit to % crys

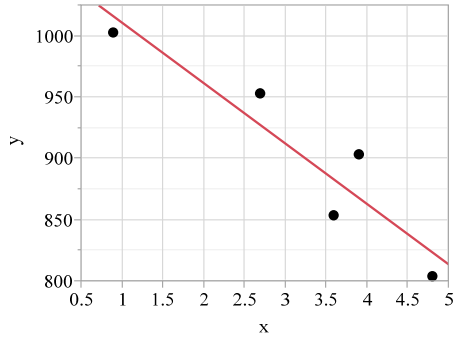

Linear Fit
y = 1059.9833 - 49.277778*x

Summary of Fit

RSquare	0.865214
RSquare Adj	0.820286
Root Mean Square Error	33.21277
Mean of Response	903.28
Observations (or Sum Wgts)	5

Analysis of Variance

Source	DF	Sum of Squares	Mean Square	F Ratio
Model	1	21242.763	21242.8	19.2575
Error	3	3309.265	1103.1	**Prob > F**
C. Total	4	24552.028		0.0219*

Parameter Estimates

Term	Estimate	Std Error	t Ratio	Prob>|t|
Intercept	1059.9833	38.67495	27.41	0.0001*
x	-49.27778	11.22925	-4.39	0.0219*

Exhibit A1. Liquidus Temperature Determinations

Bivariate Fit of y By x Glass ID=SWPF-46, VSL ID=GAP-39, Regression=% crys fit to temp

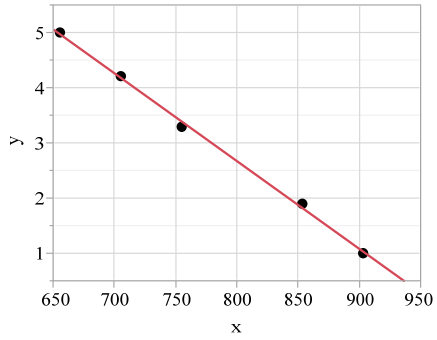

Linear Fit
y = 15.398667 - 0.015907*x

Summary of Fit

RSquare	0.998356
RSquare Adj	0.997808
Root Mean Square Error	0.076597
Mean of Response	3.08
Observations (or Sum Wgts)	5

Analysis of Variance

Source	DF	Sum of Squares	Mean Square	F Ratio
Model	1	10.690399	10.6904	1822.112
Error	3	0.017601	0.0059	**Prob > F**
C. Total	4	10.708000		<.0001*

Parameter Estimates

Term	Estimate	Std Error	t Ratio	Prob>|t|
Intercept	15.398667	0.290613	52.99	<.0001*
x	-0.015907	0.000373	-42.69	<.0001*

Bivariate Fit of y By x Glass ID=SWPF-46, VSL ID=GAP-39, Regression=temps fit to % crys

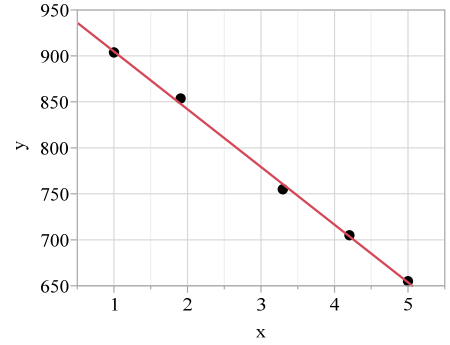

Linear Fit
y = 967.72768 - 62.762234*x

Summary of Fit

RSquare	0.998356
RSquare Adj	0.997808
Root Mean Square Error	4.811329
Mean of Response	774.42
Observations (or Sum Wgts)	5

Analysis of Variance

Source	DF	Sum of Squares	Mean Square	F Ratio
Model	1	42179.861	42179.9	1822.112
Error	3	69.447	23.1	**Prob > F**
C. Total	4	42249.308		<.0001*

Parameter Estimates

Term	Estimate	Std Error	t Ratio	Prob>|t|
Intercept	967.72768	5.013758	193.01	<.0001*
x	-62.76223	1.470317	-42.69	<.0001*

Bivariate Fit of y By x Glass ID=SWPF-47, VSL ID=GAP-45, Regression=% crys fit to temp

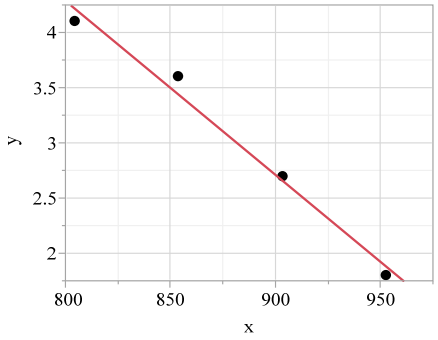

Linear Fit
y = 16.882137 - 0.0157452*x

Summary of Fit

RSquare	0.984507
RSquare Adj	0.97676
Root Mean Square Error	0.154717
Mean of Response	3.05
Observations (or Sum Wgts)	4

Analysis of Variance

Source	DF	Sum of Squares	Mean Square	F Ratio
Model	1	3.0421255	3.04213	127.0874
Error	2	0.0478745	0.02394	**Prob > F**
C. Total	3	3.0900000		0.0078*

Parameter Estimates

Term	Estimate	Std Error	t Ratio	Prob>|t|
Intercept	16.882137	1.229418	13.73	0.0053*
x	-0.015745	0.001397	-11.27	0.0078*

Bivariate Fit of y By x Glass ID=SWPF-47, VSL ID=GAP-45, Regression=temps fit to % crys

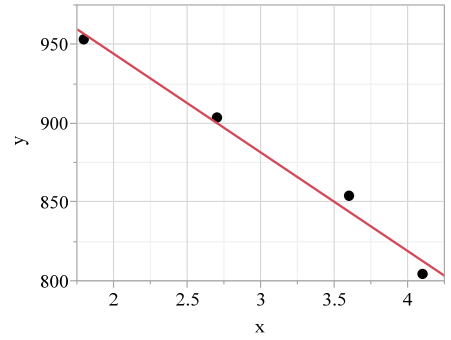

Linear Fit
y = 1069.2089 - 62.527508*x

Summary of Fit

RSquare	0.984507
RSquare Adj	0.97676
Root Mean Square Error	9.749876
Mean of Response	878.5
Observations (or Sum Wgts)	4

Analysis of Variance

Source	DF	Sum of Squares	Mean Square	F Ratio
Model	1	12080.940	12080.9	127.0874
Error	2	190.120	95.1	**Prob > F**
C. Total	3	12271.060		0.0078*

Parameter Estimates

Term	Estimate	Std Error	t Ratio	Prob>|t|
Intercept	1069.2089	17.60526	60.73	0.0003*
x	-62.52751	5.546511	-11.27	0.0078*

Exhibit A1. Liquidus Temperature Determinations

Bivariate Fit of y By x Glass ID=SWPF-48, VSL ID=GAP-25, Regression=% crys fit to temp

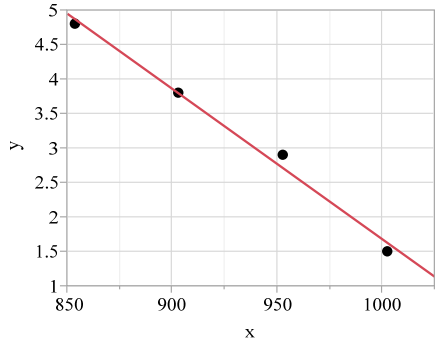

Linear Fit
y = 23.4743 - 0.0217923*x

Summary of Fit

RSquare	0.990197
RSquare Adj	0.985296
Root Mean Square Error	0.169911
Mean of Response	3.25
Observations (or Sum Wgts)	4

Analysis of Variance

Source	DF	Sum of Squares	Mean Square	F Ratio
Model	1	5.8322606	5.83226	202.0200
Error	2	0.0577394	0.02887	**Prob > F**
C. Total	3	5.8900000		0.0049*

Parameter Estimates

Term	Estimate	Std Error	t Ratio	Prob>|t|
Intercept	23.4743	1.42544	16.47	0.0037*
x	-0.021792	0.001533	-14.21	0.0049*

Bivariate Fit of y By x Glass ID=SWPF-48, VSL ID=GAP-25, Regression=temps fit to % crys

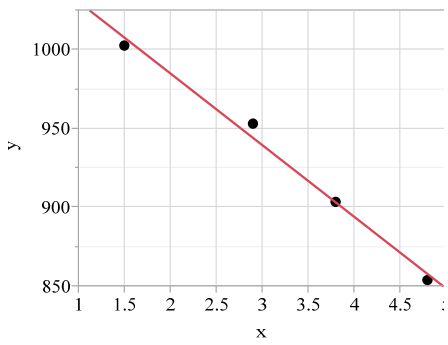

Linear Fit
y = 1075.7236 - 45.438031*x

Summary of Fit

RSquare	0.990197
RSquare Adj	0.985296
Root Mean Square Error	7.75854
Mean of Response	928.05
Observations (or Sum Wgts)	4

Analysis of Variance

Source	DF	Sum of Squares	Mean Square	F Ratio
Model	1	12160.580	12160.6	202.0200
Error	2	120.390	60.2	**Prob > F**
C. Total	3	12280.970		0.0049*

Parameter Estimates

Term	Estimate	Std Error	t Ratio	Prob>|t|
Intercept	1075.7236	11.09035	97.00	0.0001*
x	-45.43803	3.196851	-14.21	0.0049*

Bivariate Fit of y By x Glass ID=SWPF-49, VSL ID=GAP-02, Regression=% crys fit to temp

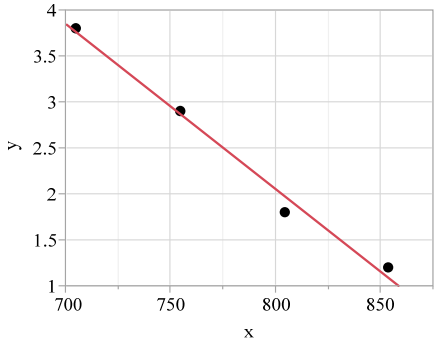

Linear Fit
y = 16.418911 - 0.0179553*x

Summary of Fit

RSquare	0.98837
RSquare Adj	0.982555
Root Mean Square Error	0.152653
Mean of Response	2.425
Observations (or Sum Wgts)	4

Analysis of Variance

Source	DF	Sum of Squares	Mean Square	F Ratio
Model	1	3.9608940	3.96089	169.9737
Error	2	0.0466060	0.02330	**Prob > F**
C. Total	3	4.0075000		0.0058*

Parameter Estimates

Term	Estimate	Std Error	t Ratio	Prob>|t|
Intercept	16.418911	1.076077	15.26	0.0043*
x	-0.017955	0.001377	-13.04	0.0058*

Bivariate Fit of y By x Glass ID=SWPF-49, VSL ID=GAP-02, Regression=temps fit to % crys

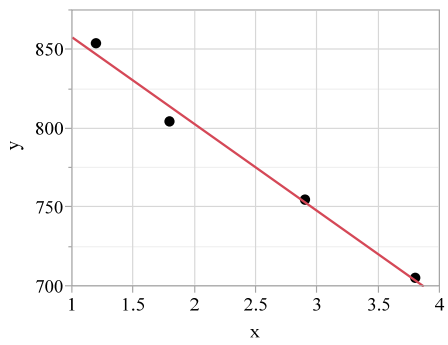

Linear Fit
y = 912.86195 - 55.046163*x

Summary of Fit

RSquare	0.98837
RSquare Adj	0.982555
Root Mean Square Error	8.452262
Mean of Response	779.375
Observations (or Sum Wgts)	4

Analysis of Variance

Source	DF	Sum of Squares	Mean Square	F Ratio
Model	1	12143.046	12143.0	169.9737
Error	2	142.881	71.4	**Prob > F**
C. Total	3	12285.928		0.0058*

Parameter Estimates

Term	Estimate	Std Error	t Ratio	Prob>|t|
Intercept	912.86195	11.07667	82.41	0.0001*
x	-55.04616	4.222174	-13.04	0.0058*

Exhibit A1. Liquidus Temperature Determinations

Bivariate Fit of y By x Glass ID=SWPF-50, VSL ID=GAP-18, Regression=% crys fit to temp

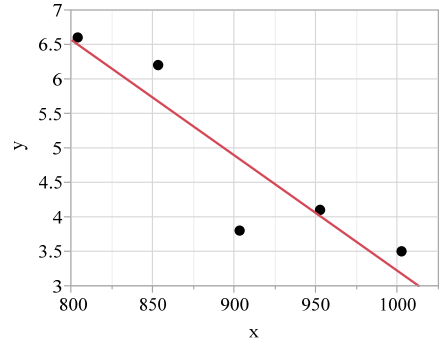

Linear Fit
y = 19.971762 - 0.016752*x

Summary of Fit

RSquare	0.822986
RSquare Adj	0.763981
Root Mean Square Error	0.702842
Mean of Response	4.84
Observations (or Sum Wgts)	5

Analysis of Variance

Source	DF	Sum of Squares	Mean Square	F Ratio
Model	1	6.8900377	6.89004	13.9478
Error	3	1.4819623	0.49399	**Prob > F**
C. Total	4	8.3720000		0.0335*

Parameter Estimates

Term	Estimate	Std Error	t Ratio	Prob>|t|
Intercept	19.971762	4.063868	4.91	0.0161*
x	-0.016752	0.004486	-3.73	0.0335*

Bivariate Fit of y By x Glass ID=SWPF-50, VSL ID=GAP-18, Regression=temps fit to % crys

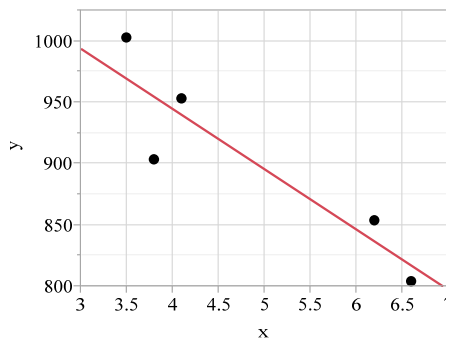

Linear Fit
y = 1141.0574 - 49.127568*x

Summary of Fit

RSquare	0.822986
RSquare Adj	0.763981
Root Mean Square Error	38.0616
Mean of Response	903.28
Observations (or Sum Wgts)	5

Analysis of Variance

Source	DF	Sum of Squares	Mean Square	F Ratio
Model	1	20205.972	20206.0	13.9478
Error	3	4346.056	1448.7	**Prob > F**
C. Total	4	24552.028		0.0335*

Parameter Estimates

Term	Estimate	Std Error	t Ratio	Prob>|t|
Intercept	1141.0574	65.90362	17.31	0.0004*
x	-49.12757	13.15444	-3.73	0.0335*

Appendix B. Property Acceptance Region (PAR) Determination

The determination of the T_L PAR is accomplished by accounting for the property model uncertainty for the revised T_L model and the approach is identical to that used for the current T_L model [6, 105]: a one-sided, 100(1−α)% Scheffé simultaneous lower confidence band on the inverse of liquidus temperature (or $1/T_L$) as given by:

Equation B1

$$\text{Prediction} - s_r\sqrt{pF_{2\alpha}(p,n-p)}\sqrt{\underline{c}_0\left(\mathbf{X}^T\mathbf{X}\right)^{-1}\underline{c}_0{}^T}$$

where s_r is the root mean square error (RMSE) of the revised model, $F_{2\alpha}(p,n-p)$, is the 100(1−2α)% percentile of the F-distribution with p and n-p degrees of freedom in numerator and denominator, respectively, $\underline{c}_0$ is the vector of independent variables for which the prediction is to be made, and $(\mathbf{X}^T\mathbf{X})$ is the product moment matrix representing the independent variables used in fitting the revised model.

Because the inverse of liquidus temperature (or $1/T_L$) is predicted, the T_L constraint translates into a lower limit on $(1/T_L)$ of approximately $7.56\text{x}10^{-4}\text{K}^{-1}$ (i.e., TL ≤ 1050°C). Therefore, the test for liquidus temperature should be one-sided based upon the one-sided lower bound on the $(1/T_L)$ prediction, or:

Equation B2

$$\frac{1}{T_L(K)} - s_r\sqrt{pF_{2\alpha}(p,n-p)}\sqrt{\underline{c}_0\left(\mathbf{X}^T\mathbf{X}\right)^{-1}\underline{c}_0{}^T} \geq 7.56x10^{-4}K^{-1}$$

where the predicted $(1/T_L)$ is obtained using the revised model above. Re-stating this constraint using information generated during the fitting of the revised model leads to

Equation B3

$$\ln\left\{(M_2)^{-0.000353617}(M_1)^{-0.000691213}(M_T)^{-0.000389016}\right\} - 0.002023544$$
$$-\left(2.41717x10^{-5}\right)\sqrt{pF_{2\alpha}(p,N-p)}\sqrt{\xi\begin{bmatrix} 142 & -188.873614 & -388.925653 & -157.601204 \\ -188.873614 & 254.982966 & 515.389786 & 208.284252 \\ -388.925653 & 515.389786 & 1069.743318 & 428.191038 \\ -157.601204 & 208.284252 & 428.191038 & 181.683573 \end{bmatrix}^{-1}\xi^T}$$
$$\geq 7.56x10^{-4}K^{-1}$$

where ξ is defined to be the vector (i.e., [1 $\ln(M_2)$ $\ln(M_1)$ $\ln(M_T)$]) of values at which to predict $(1/T_L)$, p=4, and n=142, α=0.05 (or 5%), and thus, $F_{0.10}(4,138)=1.986045$. Thus, for a given SME composition, compute the values of $\ln(M_2)$, $\ln(M_1)$, and $\ln(M_T)$ and see if this inequality is satisfied. If so, the composition is in the T_L PAR.

Another way of looking at the PAR for this constraint is to invert the PAR limit (after converting from Kelvin to the Celsius scale) for $1/T_L$ determined above, subtract away the predicted T_L derived from the model, and use this difference to represent the property prediction uncertainty. This amount can then be subtracted from the 1050 °C expected property acceptability region (EPAR) limit to obtain the PAR limit in °C against which the T_L prediction can be directly compared. That is, the predicted T_L has to be below this PAR limit expressed in degrees Celsius for the SME composition to be within the liquidus temperature PAR (with 95% confidence).

Appendix C. Measurement Acceptance Region (MAR) Determination

Apart from the prediction errors (as addressed in Appendix B for the model data), any errors associated with measuring the composition from which the liquidus temperature must be predicted must be introduced to assure that the glass in question will not crystallize in the DWPF melter. The relationship between liquidus temperature and composition is related via:

Equation C1

$$\left(\frac{1}{T_L}\right)_{pred} \approx \ln\left\{(M_2)^{a'}(M_1)^{b'}(M_T)^{c'}\right\} + d$$

where the terms representing the melt phase complexes are given by:

$$M_2 \equiv \frac{\Sigma_{M2}}{\Sigma}, \quad M_1 \equiv \frac{\Sigma_{M1}}{\Sigma}, \text{ and } \quad M_T \equiv \frac{\Sigma_{MT}}{\Sigma}$$

with

$$\Sigma \equiv \Sigma_{M2} + \Sigma_{M1} + \Sigma_{MT} + \Sigma_{N1} + \Sigma_{T1}$$

and

$$\Sigma_{M2} \equiv \phi_{M2,NiO} z_{NiO} + \phi_{M2,MgO} z_{MgO} + \phi_{M2,MnO} z_{MnO} + \phi_{M2,CaO} z_{CaO} + \phi_{M2,K_2O} z_{K_2O} + \phi_{M2,Li_2O} z_{Li_2O} + \phi_{M2,Na_2O} z_{Na_2O}$$

$$\Sigma_{M1} \equiv \phi_{M1,Al_2O_3} z_{Al_2O_3} + \phi_{M1,Fe_2O_3} z_{Fe_2O_3} + \phi_{M1,TiO_2} z_{TiO_2} + \phi_{M1,Cr_2O_3} z_{Cr_2O_3} + \phi_{M1,ZrO_2} z_{ZrO_2} + \phi_{M1,NiO} z_{NiO} + \phi_{M1,MgO} z_{MgO} + \phi_{M1,MnO} z_{MnO}$$

$$\Sigma_{MT} \equiv \phi_{T,SiO_2} z_{SiO_2} + \phi_{T,Al_2O_3} z_{Al_2O_3} + \phi_{T,Fe_2O_3} z_{Fe_2O_3}$$

$$\Sigma_{N1} \equiv \phi_{N1,K_2O} z_{K_2O} + \phi_{N1,Li_2O} z_{Li_2O} + \phi_{N1,Na_2O} z_{Na_2O}$$

$$\Sigma_{T1} \equiv \phi_{T1,SiO_2} z_{SiO_2} + \phi_{T1,Al_2O_3} z_{Al_2O_3} + \phi_{T1,Fe_2O_3} z_{Fe_2O_3} + \phi_{T1,TiO_2} z_{TiO_2}$$

To estimate the relevant measurement uncertainties, the error for each measured concentration can be first propagated through the model and the resulting pair-wise covariances summed to provide an estimate of the measurement variance. For the model in Equation C1, the variance, V(•), would be

Equation C2

$$V\left(\frac{1}{T_L}\right) \approx \sum_i \sum_j \left\{\left[\frac{\partial}{\partial[i]}\left(\frac{1}{T_L}\right)_{pred}\right](r_i[i])\left[\frac{\partial}{\partial[j]}\left(\frac{1}{T_L}\right)_{pred}\right](r_j[j])\rho_{i,j}\right\}$$

for i and j from Al_2O_3, CaO, Cr_2O, Fe_2O_3, K_2O, Li_2O, Na_2O, MgO, MnO, NiO, SiO_2, TiO_2, and ZrO_2; and where r_i, [i], and $\rho_{i,j}$ are the relative standard deviation, molar concentration (on a 100g glass basis), and correlation coefficient, respectively.

Then the partial derivatives of the expression can be computed and used to estimate the effect of measurement error on the liquidus temperature prediction for the revised model as it was for the prediction from the current model. For the current model, these calculations were presented in the "Measurement Variance Estimation" Appendix of [6]. For completeness, these results are repeated as part of this appendix.

Appendix C. Measurement Acceptance Region (MAR) Determination

$$rTL_{pred}(z) = \ln\left[(M2(z))^{a}\cdot(M1(z))^{b}\cdot(MT(z))^{c}\right] + d$$

$$\Sigma M2(z) = A\cdot NiO + B\cdot MgO + C\cdot MnO + D\cdot CaO + E\cdot K2O + F\cdot Li2O + G\cdot Na2O$$

$$\Sigma M1(z) = H\cdot Al2O3 + I\cdot Fe2O3 + J\cdot TiO2 + K\cdot Cr2O3 + L\cdot ZrO2 + M\cdot NiO + N\cdot MgO + O\cdot MnO$$

$$\Sigma MT(z) = P\cdot SiO2 + Q\cdot Al2O3 + R\cdot Fe2O3$$

$$\Sigma N1(z) = S\cdot K2O + T\cdot Li2O + U\cdot Na2O$$

$$\Sigma T1(z) = V\cdot SiO2 + W\cdot Al2O3 + X\cdot Fe2O3 + Y\cdot TiO2$$

$$\Sigma(z) = \Sigma M2(z) + \Sigma M1(z) + \Sigma MT(z) + \Sigma T1(z) + \Sigma N1(z)$$

$$M2(z) = \frac{\Sigma M2(z)}{\Sigma(z)} \qquad M1(z) = \frac{\Sigma M1(z)}{\Sigma(z)} \qquad T(z) = \frac{\Sigma MT(z)}{\Sigma(z)}$$

$$\begin{aligned}\Sigma = {} & (A\cdot NiO + B\cdot MgO + C\cdot MnO + D\cdot CaO + E\cdot K2O + F\cdot Li2O + G\cdot Na2O) \ldots \\ & + (H\cdot Al2O3 + I\cdot Fe2O3 + J\cdot TiO2 + K\cdot Cr2O3 + L\cdot ZrO2 + M\cdot NiO + N\cdot MgO + O\cdot MnO) \ldots \\ & + (P\cdot SiO2 + Q\cdot Al2O3 + R\cdot Fe2O3) + (S\cdot K2O + T\cdot Li2O + U\cdot Na2O) \ldots \\ & + (V\cdot SiO2 + W\cdot Al2O3 + X\cdot Fe2O3 + Y\cdot TiO2)\end{aligned}$$

$$\begin{aligned}\Sigma = {} & (W + H + Q)\cdot Al2O3 + D\cdot CaO + K\cdot Cr2O3 + (X + I + R)\cdot Fe2O3 + (S + E)\cdot K2O + (F + T)\cdot Li2O \ldots \\ & + (N + B)\cdot MgO + (C + O)\cdot MnO + (U + G)\cdot Na2O + (A + M)\cdot NiO + (P + V)\cdot SiO2 \ldots \\ & + (Y + J)\cdot TiO2 + L\cdot ZrO2\end{aligned}$$

$$\begin{aligned}\Sigma = {} & AA\cdot Al2O3 + D\cdot CaO + K\cdot Cr2O3 + BB\cdot Fe2O3 + CC\cdot K2O + DD\cdot Li2O + EE\cdot MgO + FF\cdot MnO \ldots \\ & + GG\cdot Na2O + HH\cdot NiO + II\cdot SiO2 + JJ\cdot TiO2 + L\cdot ZrO2\end{aligned}$$

$$M2 = \frac{A\cdot NiO + B\cdot MgO + C\cdot MnO + D\cdot CaO + E\cdot K2O + F\cdot Li2O + G\cdot Na2O}{\begin{aligned}& AA\cdot Al2O3 + D\cdot CaO + K\cdot Cr2O3 + BB\cdot Fe2O3 + CC\cdot K2O + DD\cdot Li2O + EE\cdot MgO + FF\cdot MnO \ldots \\ & + GG\cdot Na2O + HH\cdot NiO + II\cdot SiO2 + JJ\cdot TiO2 + L\cdot ZrO2\end{aligned}}$$

$$M1 = \frac{H\cdot Al2O3 + I\cdot Fe2O3 + J\cdot TiO2 + K\cdot Cr2O3 + L\cdot ZrO2 + M\cdot NiO + N\cdot MgO + O\cdot MnO}{\begin{aligned}& AA\cdot Al2O3 + D\cdot CaO + K\cdot Cr2O3 + BB\cdot Fe2O3 + CC\cdot K2O + DD\cdot Li2O + EE\cdot MgO + FF\cdot MnO \ldots \\ & + GG\cdot Na2O + HH\cdot NiO + II\cdot SiO2 + JJ\cdot TiO2 + L\cdot ZrO2\end{aligned}}$$

$$MT = \frac{P\cdot SiO2 + Q\cdot Al2O3 + R\cdot Fe2O3}{\begin{aligned}& AA\cdot Al2O3 + D\cdot CaO + K\cdot Cr2O3 + BB\cdot Fe2O3 + CC\cdot K2O + DD\cdot Li2O + EE\cdot MgO + FF\cdot MnO \ldots \\ & + GG\cdot Na2O + HH\cdot NiO + II\cdot SiO2 + JJ\cdot TiO2 + L\cdot ZrO2\end{aligned}}$$

Separate the expression for T_L into linear terms:

$$rTL_{pred}(z) = \ln\left[(M2(z))^{a}\cdot(M1(z))^{b}\cdot(MT(z))^{c}\right] + d = a\cdot\ln(M2) + b\cdot\ln(M1) + c\cdot\ln(MT) + d$$

and take the partial derivatives on each term.

Appendix C. Measurement Acceptance Region (MAR) Determination

$$\frac{d}{dAl2O3}\left(a\cdot\ln\left(\frac{A\cdot NiO+B\cdot MgO+C\cdot MnO+D\cdot CaO+E\cdot K2O+F\cdot Li2O+G\cdot Na2O}{\begin{array}{l}AA\cdot Al2O3+D\cdot CaO+K\cdot Cr2O3+BB\cdot Fe2O3+CC\cdot K2O+DD\cdot Li2O+EE\cdot MgO\ \ldots\\+FF\cdot MnO+GG\cdot Na2O+HH\cdot NiO+II\cdot SiO2+JJ\cdot TiO2+L\cdot ZrO2\end{array}}\right)\right)$$

$$\frac{d}{dAl2O3}(a\cdot\ln(M2))=\frac{-a}{\Sigma}\cdot AA \qquad \frac{d}{dCaO}(a\cdot\ln(M2))=a\cdot D\cdot\left(\frac{1}{\Sigma M2}-\frac{1}{\Sigma}\right)$$

$$\frac{d}{dCr2O3}(a\cdot\ln(M2))=-\left(\frac{a}{\Sigma}\right)\cdot K \qquad \frac{d}{dFe2O3}(a\cdot\ln(M2))=-\left(\frac{a}{\Sigma}\right)\cdot BB$$

$$\frac{d}{dK2O}(a\cdot\ln(M2))=a\cdot\left(\frac{E}{\Sigma M2}-\frac{CC}{\Sigma}\right) \qquad \frac{d}{dLi2O}(a\cdot\ln(M2))=a\cdot\left(\frac{F}{\Sigma M2}-\frac{DD}{\Sigma}\right)$$

$$\frac{d}{dMgO}(a\cdot\ln(M2))=a\cdot\left(\frac{B}{\Sigma M2}-\frac{EE}{\Sigma}\right) \qquad \frac{d}{dMnO}(a\cdot\ln(M2))=a\cdot\left(\frac{C}{\Sigma M2}-\frac{FF}{\Sigma}\right)$$

$$\frac{d}{dNa2O}(a\cdot\ln(M2))=a\cdot\left(\frac{G}{\Sigma M2}-\frac{GG}{\Sigma}\right) \qquad \frac{d}{dNiO}(a\cdot\ln(M2))=a\cdot\left(\frac{A}{\Sigma M2}-\frac{HH}{\Sigma}\right)$$

$$\frac{d}{dSiO2}(a\cdot\ln(M2))=-\left(\frac{a}{\Sigma}\right)\cdot II \qquad \frac{d}{dTiO2}(a\cdot\ln(M2))=-\left(\frac{a}{\Sigma}\right)\cdot JJ$$

$$\frac{d}{dZrO2}(a\cdot\ln(M2))=-\left(\frac{a}{\Sigma}\right)\cdot L$$

$$\frac{d}{dAl2O3}\left(b\cdot\ln\left(\frac{H\cdot Al2O3+I\cdot Fe2O3+J\cdot TiO2+K\cdot Cr2O3+L\cdot ZrO2+M\cdot NiO+N\cdot MgO+O\cdot MnO}{\begin{array}{l}AA\cdot Al2O3+D\cdot CaO+K\cdot Cr2O3+BB\cdot Fe2O3+CC\cdot K2O+DD\cdot Li2O+EE\cdot MgO\ \ldots\\+FF\cdot MnO+GG\cdot Na2O+HH\cdot NiO+II\cdot SiO2+JJ\cdot TiO2+L\cdot ZrO2\end{array}}\right)\right)$$

$$\frac{d}{dAl2O3}(b\cdot\ln(M1))=b\cdot\left(\frac{H}{\Sigma M1}-\frac{AA}{\Sigma}\right) \qquad \frac{d}{dCaO}(b\cdot\ln(M1))=-\left(\frac{b}{\Sigma}\right)\cdot D$$

$$\frac{d}{dCr2O3}(b\cdot\ln(M1))=b\cdot\left(\frac{K}{\Sigma M1}-\frac{K}{\Sigma}\right) \qquad \frac{d}{dFe2O3}(b\cdot\ln(M1))=b\cdot\left(\frac{I}{\Sigma M1}-\frac{BB}{\Sigma}\right)$$

$$\frac{d}{dK2O}(b\cdot\ln(M1))=-\left(\frac{b}{\Sigma}\right)\cdot CC \qquad \frac{d}{dLi2O}(b\cdot\ln(M1))=-\left(\frac{b}{\Sigma}\right)\cdot DD$$

$$\frac{d}{dMgO}(b\cdot\ln(M1))=b\cdot\left(\frac{N}{\Sigma M1}-\frac{EE}{\Sigma}\right) \qquad \frac{d}{dMnO}(b\cdot\ln(M1))=b\cdot\left(\frac{O}{\Sigma M1}-\frac{FF}{\Sigma}\right)$$

$$\frac{d}{dNa2O}(b\cdot\ln(M1))=-\left(\frac{b}{\Sigma}\right)\cdot GG \qquad \frac{d}{dNiO}(b\cdot\ln(M1))=b\cdot\left(\frac{M}{\Sigma M1}-\frac{HH}{\Sigma}\right)$$

$$\frac{d}{dSiO2}(b\cdot\ln(M1))=-\left(\frac{b}{\Sigma}\right)\cdot II \qquad \frac{d}{dTiO2}(b\cdot\ln(M1))=b\cdot\left(\frac{J}{\Sigma M1}-\frac{JJ}{\Sigma}\right)$$

$$\frac{d}{dZrO2}(b\cdot\ln(M1))=b\cdot\left(\frac{L}{\Sigma M1}-\frac{L}{\Sigma}\right)$$

Appendix C. Measurement Acceptance Region (MAR) Determination

$$\frac{d}{dAl2O3}\left(c\cdot\ln\left(\frac{P\cdot SiO2+Q\cdot Al2O3+R\cdot Fe2O3}{\begin{matrix}AA\cdot Al2O3+D\cdot CaO+K\cdot Cr2O3+BB\cdot Fe2O3+CC\cdot K2O+DD\cdot Li2O+EE\cdot MgO\ ...\\+FF\cdot MnO+GG\cdot Na2O+HH\cdot NiO+II\cdot SiO2+JJ\cdot TiO2+L\cdot ZrO2\end{matrix}}\right)\right)$$

$$\frac{d}{dAl2O3}(c\cdot\ln(MT))=c\cdot\left(\frac{Q}{\Sigma MT}-\frac{AA}{\Sigma}\right)\qquad \frac{d}{dCaO}(c\cdot\ln(MT))=-\left(\frac{c}{\Sigma}\right)\cdot D$$

$$\frac{d}{dCr2O3}(c\cdot\ln(MT))=-\left(\frac{c}{\Sigma}\right)\cdot K\qquad \frac{d}{dFe2O3}(c\cdot\ln(MT))=c\cdot\left(\frac{R}{\Sigma MT}-\frac{BB}{\Sigma}\right)$$

$$\frac{d}{dK2O}(c\cdot\ln(MT))=-\left(\frac{c}{\Sigma}\right)\cdot CC\qquad \frac{d}{dLi2O}(c\cdot\ln(MT))=-\left(\frac{c}{\Sigma}\right)\cdot DD$$

$$\frac{d}{dMgO}(c\cdot\ln(MT))=-\left(\frac{c}{\Sigma}\right)\cdot EE\qquad \frac{d}{dMnO}(c\cdot\ln(MT))=-\left(\frac{c}{\Sigma}\right)\cdot FF$$

$$\frac{d}{dNa2O}(c\cdot\ln(MT))=-\left(\frac{c}{\Sigma}\right)\cdot GG\qquad \frac{d}{dNiO}(c\cdot\ln(MT))=-\left(\frac{c}{\Sigma}\right)\cdot HH$$

$$\frac{d}{dSiO2}(c\cdot\ln(MT))=c\cdot\left(\frac{P}{\Sigma MT}-\frac{II}{\Sigma}\right)\qquad \frac{d}{dTiO2}(c\cdot\ln(MT))=-\left(\frac{c}{\Sigma}\right)\cdot JJ$$

$$\frac{d}{dZrO2}(c\cdot\ln(MT))=-\left(\frac{c}{\Sigma}\right)\cdot L$$

Also define the following for each:

$\Sigma Al2O3 = W + H + Q = AA$ $\quad \Sigma CaO = D$

$\Sigma Cr2O3 = K$ $\quad \Sigma Fe2O3 = X + I + R = BB$ $\quad \Sigma K2O = S + E = CC$

$\Sigma Li2O = F + T = DD$ $\quad \Sigma MgO = N + B = EE$ $\quad \Sigma MnO = C + O = FF$

$\Sigma Na2O = U + G = GG$ $\quad \Sigma NiO = A + M = HH$ $\quad \Sigma SiO2 = P + V = II$

$\Sigma TiO2 = Y + J = JJ$ $\quad \Sigma ZrO2 = L$

which can easily be implemented in code. The following partial derivatives follow from above:

$$\frac{d}{dAl2O3}\left(rTL_{pred}\right)=\frac{-a}{\Sigma}\cdot AA+b\cdot\left(\frac{H}{\Sigma M1}-\frac{AA}{\Sigma}\right)+c\cdot\left(\frac{Q}{\Sigma MT}-\frac{AA}{\Sigma}\right)$$

$$\frac{d}{dAl2O3}\left(rTL_{pred}\right)=\frac{-(a+b+c)}{\Sigma}\cdot\Sigma Al2O3+\left(H\cdot\frac{b}{\Sigma M1}+Q\cdot\frac{c}{\Sigma MT}\right)$$

$$\frac{d}{dCaO}\left(rTL_{pred}\right)=a\cdot D\cdot\left(\frac{1}{\Sigma M2}-\frac{1}{\Sigma}\right)+-\left(\frac{b}{\Sigma}\right)\cdot D+-\left(\frac{c}{\Sigma}\right)\cdot D=\frac{-(a+b+c)}{\Sigma}\cdot\Sigma CaO+\left(D\cdot\frac{a}{\Sigma M2}\right)$$

$$\frac{d}{dCr2O3}\left(rTL_{pred}\right)=-\left(\frac{a}{\Sigma}\right)\cdot K+b\cdot\left(\frac{K}{\Sigma M1}-\frac{K}{\Sigma}\right)+-\left(\frac{c}{\Sigma}\right)\cdot K=\frac{-(a+b+c)}{\Sigma}\cdot\Sigma Cr2O3+\left(K\cdot\frac{b}{\Sigma M1}\right)$$

$$\frac{d}{dFe2O3}rTL_{pred}=\frac{-(a+b+c)}{\Sigma}\cdot\Sigma Fe2O3+\left(I\cdot\frac{b}{\Sigma M1}+R\cdot\frac{c}{\Sigma MT}\right)$$

$$\frac{d}{dK2O}\left(rTL_{pred}\right)=a\cdot\left(\frac{E}{\Sigma M2}-\frac{CC}{\Sigma}\right)+-\left(\frac{b}{\Sigma}\right)\cdot CC+-\left(\frac{c}{\Sigma}\right)\cdot CC=\frac{-(a+b+c)}{\Sigma}\cdot\Sigma K2O+\left(E\cdot\frac{a}{\Sigma M2}\right)$$

Appendix C. Measurement Acceptance Region (MAR) Determination

$$\frac{d}{dLi2O}\left(rTL_{pred}\right) = a\cdot\left(\frac{F}{\Sigma M2} - \frac{DD}{\Sigma}\right) + -\left(\frac{b}{\Sigma}\right)\cdot DD + -\left(\frac{c}{\Sigma}\right)\cdot DD = \frac{-(a+b+c)}{\Sigma}\cdot \Sigma Li2O + \left(F\cdot\frac{a}{\Sigma M2}\right)$$

$$\frac{d}{dMgO}\left(rTL_{pred}\right) = \frac{-(a+b+c)}{\Sigma}\cdot \Sigma MgO + \left(B\cdot\frac{a}{\Sigma M2} + N\cdot\frac{b}{\Sigma M1}\right)$$

$$\frac{d}{dMnO}\left(rTL_{pred}\right) = \frac{-(a+b+c)}{\Sigma}\cdot \Sigma MnO + \left(C\cdot\frac{a}{\Sigma M2} + O\cdot\frac{b}{\Sigma M1}\right)$$

$$\frac{d}{dNa2O}\left(rTL_{pred}\right) = a\cdot\left(\frac{G}{\Sigma M2} - \frac{GG}{\Sigma}\right) + -\left(\frac{b}{\Sigma}\right)\cdot GG + -\left(\frac{c}{\Sigma}\right)\cdot GG = \frac{-(a+b+c)}{\Sigma}\cdot \Sigma Na2O + \left(G\cdot\frac{a}{\Sigma M2}\right)$$

$$\frac{d}{dNiO}\left(rTL_{pred}\right) = \frac{-(a+b+c)}{\Sigma}\cdot \Sigma NiO + \left(A\cdot\frac{a}{\Sigma M2} + M\cdot\frac{b}{\Sigma M1}\right)$$

$$\frac{d}{dSiO2}\left(rTL_{pred}\right) = -\left(\frac{a}{\Sigma}\right)\cdot II + -\left(\frac{b}{\Sigma}\right)\cdot II + c\cdot\left(\frac{P}{\Sigma MT} - \frac{II}{\Sigma}\right) = \frac{-(a+b+c)}{\Sigma}\cdot \Sigma SiO2 + \left(P\cdot\frac{c}{\Sigma MT}\right)$$

$$\frac{d}{dTiO2}\left(rTL_{pred}\right) = -\left(\frac{a}{\Sigma}\right)\cdot JJ + b\cdot\left(\frac{J}{\Sigma M1} - \frac{JJ}{\Sigma}\right) + -\left(\frac{c}{\Sigma}\right)\cdot JJ = \frac{-(a+b+c)}{\Sigma}\cdot \Sigma TiO2 + \left(J\cdot\frac{b}{\Sigma M1}\right)$$

$$\frac{d}{dZrO2}\left(rTL_{pred}\right) = -\left(\frac{a}{\Sigma}\right)\cdot L + b\cdot\left(\frac{L}{\Sigma M1} - \frac{L}{\Sigma}\right) + -\left(\frac{c}{\Sigma}\right)\cdot L = \frac{-(a+b+c)}{\Sigma}\cdot \Sigma ZrO2 + \left(L\cdot\frac{b}{\Sigma M1}\right)$$

Table C1 summarizes the critical information needed in evaluating the partial derivatives for each molar oxide of interest. In this table, the vector of partial derivatives (evaluated at the SME average composition, $\underline{z}_n$) is represented by $\underline{p}$. These partial derivatives are provided as expressions of the model terms (sum, sm1, sm2, and smt), the model coefficients (a, b, c, and d), and the speciation values (labeled A through Y) for the model terms.

Appendix C. Measurement Acceptance Region (MAR) Determination

Table C1. Evaluation of Partial Derivatives at SME Average Molar Composition

	Evaluation of Partial Derivatives of Model				
	with respect to Individual Oxides				
Oxide	— Vector of partials represented by $\underline{p}^T$ —	where			
Al_2O_3	-((a+b+c)/sum)*AA+((H*b/sm1)+Q*c/smt)	sum	=	Σ	in T_L model
B_2O_3	0	sm1	=	M_1	in T_L model
BaO	0	sm2	=	M_2	in T_L model
HCOO	0	smt	=	M_T	in T_L model
CaO	-((a+b+c)/sum)*D+(D*a/sm2)	a	=	-0.000353617	in T_L model
Ce_2O_3	0	b	=	-0.000691213	in T_L model
NaCl	0	c	=	-0.000389016	in T_L model
Cr_2O_3	-((a+b+c)/sum)*K+(K*b/sm1)	d	=	-0.002023544	in T_L model
Cs_2O	0	A	=	0	NiO in ΣM2
CuO	0	B	=	0.0167	MgO in ΣM2
NaF	0	C	=	0.994	MnO in ΣM2
Fe_2O_3	-((a+b+c)/sum)*BB+((I*b/sm1)+R*c/smt)	D	=	0.029	CaO in ΣM2
K_2O	-((a+b+c)/sum)*CC+(E*a/sm2)	E	=	0.3041	K_2O in ΣM2
La_2O_3	0	F	=	0.140267	Li_2O in ΣM2
Li_2O	-((a+b+c)/sum)*DD+(F*a/sm2)	G	=	0.077275	Na_2O in ΣM2
MgO	-((a+b+c)/sum)*EE+(B*a/sm2)+(N*b/sm1)	H	=	0.0607	Al_2O_3 in ΣM1
MnO	-((a+b+c)/sum)*FF+(C*a/sm2)+(O*b/sm1)	I	=	0.127347	Fe_2O_3 in ΣM1
MoO_3	0	J	=	0.047186	TiO_2 in ΣM1
NO_2	0	K	=	0.9202	Cr_2O_3 in ΣM1
NO_3	0	L	=	0.0458	ZrO_2 in ΣM1
Na_2O	-((a+b+c)/sum)*GG+(G*a/sm2)	M	=	0.1079	NiO in ΣM1
Na_2SO_4	0	N	=	0.0223	MgO in ΣM1
Nd_2O3	0	O	=	0.006	MnO in ΣM1
NiO	-((a+b+c)/sum)*HH+(A*a/sm2)+(M*b/sm1)	P	=	0.0193	SiO_2 in ΣMT
P_2O_5	0	Q	=	0.9393	Al_2O_3 in ΣMT
PbO	0	R	=	0.223553	Fe_2O_3 in ΣMT
SiO_2	-((a+b+c)/sum)*II+(P*c/smt)	S	=	0.1049	K_2O in ΣN1
ThO_2	0	T	=	0.064189	Li_2O in ΣN1
TiO_2	-((a+b+c)/sum)*JJ+(J*b/sm1)	U	=	0.136697	Na_2O in ΣN1
U_3O_8	0	V	=	0.0133	SiO_2 in ΣT1
Y_2O_3	0	W	=	0	Al_2O_3 in ΣT1
ZnO	0	X	=	0.503634	Fe_2O_3 in ΣT1
ZrO_2	-((a+b+c)/sum)*L+(L*b/sm1)	Y	=	0.148511	TiO_2 in ΣT1
		AA	=	W+H+Q	
		BB	=	X+I+R	
		CC	=	S+E	
		DD	=	F+T	
		EE	=	N+B	
		FF	=	C+O	
		GG	=	U+G	
		HH	=	A+M	
		II		P+V	
		JJ		Y+J	

Based upon the discussion in [105], the measurement uncertainty is to be computed using both the historical and current SME compositions. These calculations are made relative to the PAR limit computed in the Appendix B. First, consider the measurement uncertainty derived using the current SME composition. Let the vector $\underline{p}$ represent the partial derivatives of Table C1, the vector $\underline{r}$ represent the historical, relative standard deviations (these values are provided in Table B3 of reference [105]) and $\underline{C}_m$

represents the correlation matrix (these values are provided in Table B1 of reference [105]), then compute the vector $\underline{s}_m$ by

Equation C3

$$\underline{\mathbf{s}}_m = (\underline{\mathbf{z}} \# \underline{\mathbf{r}} \# \underline{\mathbf{p}})$$

where the operator # implies element by element multiplication between two vectors, and compute S_m as

Equation C4

$$\mathbf{S}_m = \underline{\mathbf{s}}_m * \underline{\mathbf{C}}_m * \underline{\mathbf{s}}_m'$$

The final step in assessing the impact of measurement uncertainty using the current SME composition is to compute:

Equation C5

$$MAR_{current} = PAR_{1/T_L} + t_\alpha (m-1) \cdot \sqrt{S_m / 4}$$

where PAR_{1/T_L} represents the PAR limit as $1/T_L$ (i.e., for the original model) and $t_\alpha(m\text{-}1)$ is the upper 100α % tail of the Student's t distribution with m-1 degrees of freedom.

A similar approach is used to estimate the measurement uncertainty derived using the historical composition. Let the vectors $\underline{g}$ and $\underline{M}$ represent the gravimetric factors and molecular weights, respectively, (these values are provided Table A2 of reference [105]), and the vector $\underline{h}$ represent the historical elemental compositions (these values are provided in Table B2 of reference [105]), then compute the vector $\underline{s}_n$ by

Equation C6

$$\underline{\mathbf{s}}_n = (\underline{\mathbf{g}} \# \underline{\mathbf{h}} \# \underline{\mathbf{r}} \# \underline{\mathbf{p}})/\underline{\mathbf{M}}$$

where once again, the operator # implies element by element multiplication between two vectors, and the division represented by "/" is also element by element.

Next, compute S_n as

Equation C7

$$\mathbf{S}_n = \underline{\mathbf{s}}_n * \underline{\mathbf{C}}_m * \underline{\mathbf{s}}_n'$$

The final step in assessing the impact of measurement uncertainty using the historical composition is to compute:

Equation C8

$$MAR_{historical} = PAR_{1/T_L} + t_\alpha (m-1) \cdot \sqrt{S_n / 4}$$

where PAR_{1/T_L} represents the PAR limit as $1/T_L$ (i.e., for the original model) and $t_\alpha(m\text{-}1)$ is the upper 100α % tail of the Student's t distribution with m-1 degrees of freedom.

Appendix C. Measurement Acceptance Region (MAR) Determination

As the final step in assessing the measurement uncertainty for the liquidus temperature model, find the larger of $MAR_{historical}$ and $MAR_{current}$; call this value, MAR_{1/T_L}, since it is still in terms of $1/T_L$. This MAR limit may be expressed in degrees Celsius as

Equation C9

$$MAR_{T_L} = \left(1 / MAR_{1/T_L} \right) - 273$$

A SME composition with a predicted T_L value less than MAR_{T_L} would satisfy the liquidus temperature MAR with 95% confidence. Note that the nominal 95% confidence level (equal to $100[1-\alpha]\%$) for the T_L constraint can be adjusted based upon management discretion.

DISTRIBUTION

S.L. Marra
A.P. Fellinger
T.L. Fellinger
C.C. Herman
J.W. Amoroso
K.M. Brotherton
A.D. Cozzi
C.L. Crawford
D.E. Dooley
R.E. Edwards
T.B. Edwards
T.L. Fellinger
S.D. Fink
K.M. Fox
E.J. Freed
V. Jain
C.M. Jantzen
F.C. Johnson
B.T. Geyer
J.M. Gillam
B.A. Hamm
E.W. Holtzscheiter
J.F. Iaukea
V.M. Kmiec
C.J. Martino
D.L. McClane
J.M. Pareizs
J.W. Ray
H.B. Shah
A.V. Staub
M.E. Stone
C.L. Trivelpiece

7.0 References

1 R.L. Postles and K.G. Brown, **"The DWPF Product Composition Control System at Savannah River: Statistical Process Control Algorithm,"** Ceramic Transactions, V.23, American Ceramic Society, Westerville, OH, 559-568 (1991).

2 C.M. Jantzen, **"Method for Melting Glass by Measurement of Non-Bridging Oxygen."** U.S. Patent #5,102,439, (1992).

3 C.M. Jantzen, **"The Impacts of Uranium and Thorium on the Defense Waste Processing Facility (DWPF) Viscosity Model,"** U.S. DOE Report WSRC-TR-2004-00311, Rev. 0, Westinghouse Savannah River Co., Savannah River Technology Center, Aiken, SC (2005).

4 C.M. Jantzen, K.G. Brown, T.B. Edwards, and J.B. Pickett, **"Method of Determining Glass Durability."** U.S. Patent #5,846,278, (1998).

5 C.M. Jantzen, J.B. Pickett, K.G. Brown, T.B. Edwards, and D.C. Beam, **"Process/Product Models for the Defense Waste Processing Facility (DWPF): Part I. Predicting Glass Durability from Composition Using a Thermodynamic Hydration Energy Reaction MOdel (THERMO™)**," U.S. DOE Report WSRC-TR-93-0672, Rev. 0, Westinghouse Savannah River Co., Savannah River Technology Center, Aiken, SC (1995).

6 K.G. Brown, C.M. Jantzen, and G. Ritzhaupt, **"Relating Liquidus Temperature to Composition for Defense Waste Processing Facility (DWPF) Process Control,"** U.S. DOE Report WSRC-TR-2001-00520, Rev. 0, Westinghouse Savannah River Company, Aiken, SC (2001).

7 C.M. Jantzen and K.G. Brown, **"Predicting the Spinel-Nepheline Liquidus for Application to Nuclear Waste Glass Processing. Part I: Primary Phase Analysis, Liquidus Measurement, and Quasicrystalline Approach,"** Journal of the American Ceramic Society, 90 [6], 1866-1879 (2007).

8 C.M. Jantzen and K.G. Brown, **"Predicting the Spinel-Nepheline Liquidus for Application to Nuclear Waste Glass Processing. Part II: Quasicrystalline Freezing Point Depression Model,"** Journal of the American Ceramic Society, 90 [6], 1880-1891 (2007).

9 T.H. Lorier and C.M. Jantzen, **"Evaluation of the TiO_2 Limit for DWPF Glass,"** U.S. DOE Report WSRC-TR-2003-00396, Westinghouse Savannah River Company, Savannah River Technology Center, Aiken, SC (2003).

10 D.K. Peeler and T.B. Edwards, **"Integration of SWPF into DWPF Flowsheet: Gap Analysis and Test Matrix Development,"** U.S. DOE Report SRNL-STI-2014-00578, Savannah River Nuclear Solutions, Savannah River National Laboratory, Aiken, SC (2014).

11 D.K. Peeler and T.B. Edwards, **"SWPF Integration into the DWPF Flowsheet: Definition of Oxide Concentrations to Define the Future Glass Operating Region,"** U.S. DOE Memorandum SRNL-L3100-2014-00189, Savannah River Nuclear Solutions, Savannah River National Laboratory, Aiken, SC (2014).

12 W.K. Kot and I.L. Pegg, **"Letter Report Measurements of Glass Density and Melt Viscosity to Support Salt Waste Processing Facility (SWPF) Gap Analysis Study,"** VSL-15L3500-2 (2015).

13 W.K. Kot and I.L. Pegg**, "Chemical Compositions and Durability Study of Salt Waste Processing Facility (SWFP) Gap Glasses,"** VSL-16L3500-1, Vitreous State Laboratory, The Catholic University of America Washington, DC (2016).

14 W.K. Kot, B. Bennett, and I.L. Pegg, **"Final Report Liquidus Temperature Measurements of Vitreous State Laboratory Salt Waste Processing Facility (SWPF) Gap Glasses,"** VSL-16R4080-1, Revision 0 (2016).

15 D.F. Bickford, A. Applewhite-Ramsey, C.M. Jantzen and K.G. Brown, **"Control of Radioactive Waste Glass Melters: I, Preliminary General Limits at Savannah River,"** Journal of the American Ceramic Society, 73 [10] 2896-2902 (1990).

16 M.J. Plodinec, **"Long-Term Waste Management Progress Report Small-Scale Electric Melter,"** II. Slag Formation, U.S. DOE Report DPST-78-453, E.I. duPont deNemours & Co., Savannah River Laboratory, Aiken, SC (1978).

17 M.J. Plodinec and J.R. Wiley, **"Viscosity and Electrical Conductivity of Glass Melts as a Function of Waste Composition,"** Proceedings International Symposium on Ceramics in Nuclear Waste Management," CONF-790420, U.S. DOE, Cincinnati, OH, 210-212 (1979).

18 "**Defense Waste Processing Facility System Design Description (U), Melter and Associated Equipment, GP-02**" U.S. DOE Report G-SYD-S-00060, Rev. 5, Savannah River Remediation, Aiken, SC (2016).

19 C. M. Jantzen, K.G. Brown, K.J. Imrich, and J.B. Pickett. **"High Chrome Refractory Characterization: Part I. Impact of Melt REDuction/Oxidation (REDOX) on the Corrosion Mechanism,"** International Journal of Applied Glass Science, 6[2], 137-157 (2015).

20 C. M. Jantzen, K.G. Brown, K.J. Imrich, and J.B. Pickett. **"High Chrome Refractory Characterization: Part II. Accumulation of Spinel Corrosion Deposits in Radioactive Waste Glass Melters,"** International Journal of Applied Glass Science, 6[2], 158-171 (2015).

21 C.M. Jantzen, **"Relationship of Glass Composition to Glass Viscosity, Resistivity, Liquidus Temperature, and Durability: First Principles Process-Product Models for Vitrification of Nuclear Waste,"** Proceedings of the 5th International Symposium on Ceramics in Nuclear Waste Management, G.G. Wicks, D.F. Bickford, and R. Bunnell (Eds.), American Ceramic Society, Westerville, OH, 37-51 (1991).

22 N.L. Bowen and J.F. Schairer, **"The Fusion Relations of Acmite,"** American Journal of Science, 18, 365-374 (1929).

23 N.L. Bowen, J.F. Schairer, and H.W. V. Willems, **"The Ternary System: Na_2SiO_3-Fe_2O_3-SiO_2,"** American Journal of Science, 20, 405-455 (1930).

24 J. Nolan, **"Melting Relations in the System $NaAlSi_3O_8$-$NaAlSiO_4$-$NaFeSi_2O_6$-$CaMgSi_2O_6$-H_2O, and their Bearing on the Genesis of Alkaline Undersaturated Rocks,"** Quarterly Journal of the Geological Society of London, 122, 119-157 (1966).

25 I. Kushiro, **"On the Nature of Silicate Melt and its Significance in Magma Genesis: Regularities in the Shift of Liquidus Boundaries Involving Olivine Pyroxene, and Silica Materials,"** American Journal of Science, 275, 411-431 (1975).

26 B.O. Mysen, **"The Structure and Properties of Silicate Melts,"** Developments in Geochemistry, 4, Elsevier, New York 354pp (1988).

27 F.J. Ryerson, **"Oxide Solid Solution Mechanisms in Silicate Melts: Systematic Variations in Activity Coefficient of SiO_2,"** Geochimica Cosmochimica Acta, 49, 637-651 (1985).

28 C.W. Burnham, **"The Nature of Multicomponent Aluminosilicate Melts,"** Physics and Chemistry of the Earth, 13 & 14, 191-227 (1981).

29 G.E. Brown, Jr., F. Farges, and G. Calas, **"X-Ray Scattering and X-Ray Spectroscopy Studies of Silicate Melts,"** Structure, Dynamics and Properties of Silicate Melts, J.F. Stebbins, P.F. McMillan, and D.B. Dingwell (Eds.), Reviews in Mineralogy, V.32, 317-410 (1995).

30 R.J.P. Williams, **"Deposition of Trace elements in Basic Magmas,"** Nature, v.184, 144 (1959).

31 P.L. Roeder, **"Activity of Iron and Olivine Solubility in Basaltic Liquids,"** Earth and Planetary Science Letters, 23, 397-410 (1974).

32 E. Takahashi, "**Partitioning of Ni^{2+}, Co^{2+}, Fe^{2+}, Mn^{2+}, and Mg^{2+} Between Olivine and Silicate Melts: Compositional Dependence of Partition Coefficients,"** Geochimica et. Cosmochimica Acta 42 [12], 1829-1844 (1978).

33 J.D. Vienna, P. Hrma, J.V. Crum, and M. Mika, **"Liquidus Temperature-Composition Model for Multi-Component Glasses in the Fe, Cr, Ni, and Mn Spinel Primary Phase Field,"** Journal of Non-crystalline Solids, 292 [1-3], 1-24 (2001).

34 M. Taylor and G.E. Brown, Jr. **"Structure of Mineral Glasses-II. The SiO_2-$NaAlSiO_4$ Join,"** Geochimica et. Cosmochimica Acta, 43 [9], p.1467-1479 (1979).

35 E.D. Lacy, **"A Statistical Model of Polymerisation/depolymerisation Relationships in Silicate Melts and Glasses,"** Phys. Chem. Glasses, 6[5], 171-180 (1965).

36 R.M. Smart and F.P. Glasser**, "Silicate Anion Constitution of Lead Silicate Glasses and Crystals,"** Physics and Chemistry of Glasses, 19[5], 95-102 (1978).

37 K.D. Keefer, **"Phase Separation and Crystallization Phenomena in Silicate Systems,"** Unpublished PhD Thesis, Stanford University, 159p.(November, 1980).

38 P.C. Hess, **"Thermodynamic Mixing Properties and the Structure of Silicate Melts,"** in Thermodynamic Modeling of Geological Materials: Minerals, Fluids, and Melts Reviews in Mineralogy, v.32, Mineralogic Society of America, Washington, DC, 145-189 (1995).

39 L. Bragg and G.F. Claringbull, **"Crystal Structure of Minerals,"** The Crystalline State, Vol. IV, G. Bell and Sons, Ltd., London, 409pp. (1965).

40 A.J.G. Ellison and A. Navrotsky, **"Thermochemistry and Structure of Model Waste Glass Compositions,"** Scientific Basis for Nuclear Waste Management, **XIII**, V.M. Oversby and P.W. Brown (Eds.) Materials Research Society, Pittsburgh, PA, 193-207 (1990).

41 P. Izak, P. Hrma, and M.J. Schweiger, "**Kinetics of Conversion of High-Level Waste to Glass,"** in Nuclear Site Remediation, P.G. Eller and W.R. Heineman (Eds.), ACS Symposium Series, v. 778, American Chemical Society, Washington, DC, 314-328 (2001).

42 P. Izak, P. Hrma, J.S. Young, J. Klouzek, **"Evolution of Crystalline Phases During High Level Waste Feed-to-Glass Conversion,"** Ceramic Transactions, 119, Amer. Ceramic Soc., Westerville, OH, 509-515 (2001).

43 J.W. Hastie, E.R. Plante, and D.W. Bonnell**, "Vaporization of Simulated Nuclear Waste Glass,"** NBSIR 83-2731, National Bureau of Standards, Washington, DC (1983).

44 D.W. Bonnell, E.R. Plante, and J.W. Hastie**, "Vaporization of Simulated Nuclear Waste Glass,"** Journal of Non-Crystalline Solids, 84, 268-275 (1986).

45 R.G.C. Beerkens, **"Modeling the Kinetics of Volatilization from Glass Melts,"** Journal of the American Ceramic Society, 84 [9], 1952-1960 (2001).

46 H. Li, Y. Su, J.D. Vienna, and P. Hrma**, "Raman Spectroscopic Study - Effects of B_2O_3, Na_2O, and SiO_2 on Nepheline ($NaAlSiO_4$) Crystallization in Simulated High Level Waste Glasses,"** Environmental Issues and Waste Management Technologies, V, G.T. Chandler and X. Feng (Eds.), Ceramic Trans. 107, American Ceramic Society, Westerville, OH, 469-477 (2000).

47 H. Li, B. Jones, P. Hrma, J.D. Vienna, **"Compositional Effects on Liquidus Temperature of Hanford Simulated High-Level Waste Glasses Precipitating Nepheline ($NaAlSiO_4$),"** Environmental Issues and Waste Management Technologies in the Ceramic and Nuclear Industries, III, D.K. Peeler and J.C. Marra (Eds.), American Ceramic Society, Westerville, OH, 279-288 (1998).

48 D. J. Stein and F.J. Spera, **"Molecular Dynamics Simulations of Liquids and Glasses in the System $NaAlSiO_4$-SiO_2: Methodology and Melt Structures,"** American Mineralogist, 80, 417-431 (1995).

49 C. Nelson, T. Furukawa, and W.B. White, **"Transition Metal Ions in Glasses: Network Modifiers or Quasi-Molecular Complexes?"** Materials Research Bulletin, 18, 959-966 (1983).

50 C.M. Jantzen, D.F. Bickford, and D.G. Karraker**, "Time-Temperature-Transformation Kinetics in SRL Waste Glass,"** Advances in Ceramics, 8, American Ceramic Society, Westerville, OH, 30-38 (1984).

51 C.M. Jantzen and D.F. Bickford, **"Leaching of Devitrified Glass Containing Simulated SRP Nuclear Waste,"** Sci. Basis for Nuclear Waste Management, VIII, C.M. Jantzen, J.A. Stone and R.C. Ewing (eds.), Materials Research Society, Pittsburgh, PA 135-146 (1985).

52 S.L. Marra, M.K. Andrews and C.A. Cicero, **"Phase Stability Determinations of DWPF Waste Glasses,"** US DOE Report WSRC-TR-93-00227, Rev. 0 (1993).

53 M. Mika, M.J. Schweiger, J.D. Vienna, and P. Hrma**, "Liquidus Temperature of Spinel Precipitating High-Level Waste Glasses,"** Scientific Basis for Nuclear Waste Management, XX, W.J. Gray and I.R. Triay (Eds.), Materials Research Society, Pittsburgh, PA 71-78 (1997).

54 H. Li, P. Hrma, J.D. Vienna, M. Qian, Y. Su, D.E. Smith, **"Effects of Al_2O_3, B_2O_3, Na_2O, and SiO_2 on Nepheline Formation in Borosilicate Glasses: Chemical and Physical Correlations,"** Journal of Non-Crystalline Solids, 331 [1-3], 202-216 (2003).

55 M.J. Plodinec, **"Improved Glass Compositions for Immobilization of SRP Waste*,"** Scientific Basis for Nuclear Waste Management, 2, J.M. Clyde Northrup, Jr., Plenum Press, New York, 223-229 (1980).

56 D.A. Duke, J.F. McDowell, and B.R. Karstetter**, "Crystallization and Chemical Strengthening of Nepheline Glass-Ceramics,"** Journal of the American Ceramic Society, 50 [2], 67-75 (1967).

57 W.A. Deer, R.A. Howie, and J. Zussman, **"Rock-Forming Minerals, V.4 Framework Silicates,"** John Wiley & Sons, New York, 435 pp., (1963).

58 P.R. Hrma, G.F. Peipel, M.J. Schweiger, D.E. Smith, D.S. Kim, P.E. Redgate, J.D. Vienna, C.A. LoPresti, D.B. Simpson, D.K. Peeler, M.H. Langowski, **"Property/Composition Relationships for Hanford High-Level Waste Glasses Melting at 1150°C,"** U.S. DOE Report PNL-10359-Vol 1 and PNL-10359-Vol 2, Battelle Memorial Institute, Pacific Northwest Laboratory, Richland, WA (1994).

59 P. Hrma, J.D. Vienna, M. Mika, J.V. Crum, G.F. Piepel**, "Liquidus Temperature Data for DWPF Glass,"** U.S. DOE Report PNNL-11790, Battelle Memorial Institute, Pacific Northwest National Laboratory, Richland, WA (May, 1999).

60 W.A. Deer, R.A. Howie, and J. Zussman**, "Rock-Forming Minerals, V.5 Non-Silicates,"** John Wiley & Sons, New York, 363pp., (1962).

61 A. Navrotsky and O.J. Kleppa**, "The Thermodynamics of Cation Distributions in Simple Spinels,"** Journal of Inorganic and Nuclear Chemistry, 29 [11], 2701-2714 (1967).

62 J.G. Reynolds, **"Spinel Structure and Liquidus Temperature Relationships in Nuclear Waste Glass,"** Journal of Materials Science, 40 [15], 3987-3991 (2005).

63 W.A. Deer, R.A. Howie, and J. Zussman, **"Rock-Forming Minerals, V.2 Chain Silicates,"** John Wiley & Sons, New York, 379pp., (1963).

64 M.F.J. Flower, **"Phase Relations of Titan-Acmite in the System Na_2O-Fe_2O_3-Al_2O_3-TiO_2-SiO_2 at 1000 Bars Total Water Pressure,"** American Mineralogist, 59, 536-548 (1974).

65 A.C. Buechele, X. Feng, H. Gu, and I.L. Pegg**, "Alteration of Microstructure of West Valley Glass by Heat Treatment,"** Scientific Basis for Nuclear Waste Management, XIII, V.M. Oversby and P.W. Brown (Eds.), Materials Research Society, Pittsburgh, PA, 393-402 (1990).

66 I. Joseph, T.V. Palmiter and L.D. Pye, "**Phase Stability of Simulated Nuclear Waste Glass,"** Proceedings of Third International Conference on High Level Waste Management, Vol. 1, American Nuclear Society, La Grange Park, IL, 911-916 (1992).

67 J.V. Crum, M.J. Schweiger, P. Hrma, and J.D. Vienna, **"Liquidus Temperature Model for Hanford High-Level Waste Glasses with High Concentrations of Zirconia,"** Scientific Basis for Nuclear Waste Managment, XX, W.J. Gray and I.R. Triay (Eds.), Materials Research Society, Pittsburgh, PA 79-85 (1997).

68 D.F. Bickford and C.M. Jantzen, **"Devitrification of Defense Nuclear Waste Glasses: Role of Melt Insolubles,"** Journal of Non-Crystalline Solids ,84 [1-3] ,299-307 (1986).

69 G. Donnay, J.F. Schairer, and J.D.H. Donnay, **"Nepheline Solid Solutions,"** Mineralogic Magazine, 32 [245], 93-109 (1959).

70 A. Navrotsky, **"Models of Crystalline Solution,"** in Thermodynamic Modeling of Geological Materials: Minerals, Fluids, and Melts, Reviews in Mineralogy, V. 17, Mineralogic Society of America., Washington, D.C., 35-69 (1987).

71 SAS Institute, Inc., JMP Pro Version 11.2.1, SAS Institute, Inc., Cary, NC (2014).

72 K.M. Fox, T.B. Edwards, and C.M. Jantzen, **"Task Technical and Quality Assurance Plan for SWPF Integration into the DWPF-Glass Property/Model Impacts,"** U.S. DOE Report SRNL-RP-2014-00348, Rev. 1, Savannah River Nuclear Solutions, Savannah River National Laboratory, Aiken, SC (2017).

73 C.M. Jantzen, **"Verification of Glass Composition and Strategy for SGM and DWPF Glass Composition Determination,"** U.S. DOE Report DPST-86-708, E.I. DuPont deNemours & Co., Savannah River Laboratory, Aiken, SC (1986).

74 D.K. Peeler and T.B. Edwards, **"Impact of Redox on Glass Durability: The Glass Selection Process,"** U.S. DOE Report WSRC-TR-2004-00135, Rev.0, Westinghouse Savannah River Co., Savannah River Technology Center, Aiken, SC (2004).

75 D.K. Peeler and T.B. Edwards, **"Impact of Redox on Glass Durability: Experimental Results,"** U.S. DOE Report WSRC-TR-2004-00313, Rev. 0, Westinghouse Savannah River Co., Savannah River Technology Center, Aiken, SC (2004).

76 A.D. Cozzi, T.B. Edwards, D.K. Peeler, and D.R. Best, **"The Impact of REDOX on Durability for Sludge Batch 2, Part II: Experimental Results and Recommendations"** U.S. DOE Report WSRC-TR-2003-00246, Rev. 0, Westinghouse Savannah River Co., Savannah River Technology Center, Aiken, SC (May 2003).

77 C.M. Jantzen, T.B. Edwards, and C.L. Trivelpiece, **"Defense Waste Processing Facility (DWPF) Durability-Composition Models and the Applicability of the Associated Reduction of Constraints (ROC) Criteria for High TiO_2 Containing Glasses,"** U.S. DOE Report SRNL-STI-2016-00372, Rev. 0, Savannah River Nuclear Solutions, Savannah River National Laboratory, Aiken, SC (2016).

78 I. Tovena, T. Advocat, D. Ghaleb, E. Vernaz and F. Larche, **"Thermodynamic and Structural Models Compared with the Initial Dissolution Rates of "SON" Glass Samples,"** Scientific Basis for Nuclear Waste Management, XVII, A. Barkatt and R.A. Van Konynenburg (Eds.), Mat. Res. Soc., Pittsburgh, PA, 595-602 (1994).

79 B.C. Bunker, G.W. Arnold, D.E. Day and P.J. Bray, **"The Effect of Molecular Structure on Borosilicate Glass Leaching,"** Journal of Non-Crystalline Solids, 87 [1-2], 226-253 (1986).

80 C.M. Jantzen, K.G. Brown, and J.B. Pickett, **"Durable Glass for Thousands of Years,"** International Journal of Applied Glass Science, 1 [1], 38-62 (2010).

81 M. Tomozawa and S. Sridharan, **"Viscosity Increase of Phase-Separated Borosilicate Glasses,"** Journal of the American Ceramic Society, 75 [11], 3103-10 (1992).

82 W. Zheng, M. Lin, J. Cheng, **"Effect of Phase Separation on the Crystallization and Properties of Lithium Aluminosilicate Glass-ceramics,"** Glass Physics and Chemistry, 39 [2], 142-149 (2013).

83 ASTM C829-81 (2015). Annual Book of ASTM Standards, Vol. 15.02: **Standard Practices for Measurement of Liquidus Temperature of Glass by the Gradient Furnace Method**

84 ASTM C1720-11. Annual Book of ASTM Standards, Vol. 12.01: **Standard Test Methods for Determining the Liquidus Temperature (TL) of Waste Glasses and Simulated Waste Glasses**

85 R.F. Crow and J.D. Connolly, **"Atomic Absorption Analysis of Portland Cement and Raw Mix Using Lithium Metaborate Fusion,"** Journal of Testing and Evaluation, 1 [5], 382, (1973).

86 W.G. Ramsey and R.F. Schumacher, **"Effects of Formate and Nitrate on Waste Glass Redox at High Copper Concentration,"** U.S. DOE Report WSRC-TR-92-484, Westinghouse Savannah River Company, Savannah River Technology Center, Aiken, SC (1992).

87 C.M. Jantzen, N.E. Bibler, D.C. Beam, and M.A. Pickett, **"Characterization of the Defense Waste Processing Facility (DWPF) Environmental Assessment (EA) Glass Standard Reference Material,"** U.S. DOE Report WSRC-TR-92-346, Rev. 1, Westinghouse Savannah River Company, Savannah River Technology Center, Aiken, SC (1993).

88 C.M. Jantzen, N.E. Bibler, D.C. Beam, and M.A. Pickett , **"Development and Characterization of the Defense Waste Processing Facility (DWPF) Environmental Assessment (EA) Glass Standard Reference Material,"** Environmental and Waste Management Issues in the Ceramic Industry, Ceramic Transactions, 39, American Ceramic Society, Westerville, OH, 313-322 (1994).

89 T.B. Edwards and K.M. Fox, **"Evaluations of the Measurements of Chemical Composition, Viscosity, and Density of the SWPF Study Glasses with High Concentrations of Titanium,"** U.S. DOE Report SRNL-TR-2016-00094, Rev.0 Savannah River Nuclear Solutions, Savannah River National Laboratory, Aiken, SC (2016).

90 F.C. Raszewski, T.B. Edwards, and D.K. Peeler, **"Matrix 2 Results of the FY07 Enhanced DOE High-Level Waste Melter Throughput Studies at SRNL,"** U.S. DOE Report SRNS-STI-2008-00055, Rev. 0, Savannah River Nuclear Solutions, Savannah River National Laboratory, Aiken, SC (2008).

91 F.C. Raszewski and T.B. Edwards, **"Results of the FY09 Enhanced DOE High-Level Waste Melter Throughput Studies at SRNL,"** U.S. DOE Report, SRNL-STI-2009-00778, Rev. 0, Savannah River Nuclear Solutions, Savannah River National Laboratory, Aiken, SC (2010).

92 ASTM C1463-13. Annual Book of ASTM Standards, Vol. 12.01: **Standard Practice for Dissolving Glass Containing Radioactive and Mixed Waste for Chemical and Radiochemical Analysis.**

93 C.M. Jantzen and T.B. Edwards, **"Defense Waste Processing Facility (DWPF) Viscosity Model: Revisions for Processing High TiO_2 Glasses,"** U.S. DOE Report SRNL-STI-2016-00115, Rev.0 Savannah River Nuclear Solutions, Savannah River National Laboratory, Aiken, SC (2016).

94 J.F.W. Bowles, R.A. Howie, D.J. Vaughan and J. Zussman, **"Rock-Forming Minerals. Vol. 5A, Non-Silicates (Oxides, Hydroxides and Sulphides),"** The Geological Society, London, U.K., 920pp. (2011).

95 M.B. Volf, **"Chemical Approach to Glass,"** Glass Science and Technology, V. 7, Elsevier Science Publishing Co., Inc., New York, 594 pp (1984).

96 G. Ottonello, **"Principles of Geochemistry,"** Columbia University Press, New York, 894pp. (1997).

97 R.G. Burns, **"Mineralogical Applications of Crystal Field Theory,"** Cambridge University Press, London, U.K., 224pp. (1993).

98 F. Farges, G.E. Brown Jr., A. Navrotsky, H. Gan, and J.J. Rehr, **"Coordination Chemistry of Ti(IV) in Silicate Glasses and Melts: II. Glasses at Ambient Temperature and Pressure,"** Geochemica Cosmochimica Acta, 60[16], 3039-3053 (1996).

99 B.O. Mysen and P. Richet, **"Silicate Glasses and Melts, Properties and Structures,"** Developments in Geochemistry V. 10, Elsevier Science, New York, 544pp. (2005).

100 F. Marumo, Y. TTabira, T. Mabuckhi, and H. Morikawa, **"Coordination of Transition Metals in Amorphous Silicates,"** in Dynamic Processes of Material Transport and Transformation in the Earth's Interior, F. Marumo (Ed.) 53-65, Terra Scientific, Tokyo (1990).

101 V.A. Silva, M.L.F. Nascimento, P.C. Morais, and N.O. Dantas, **"The Structural Role of Ti in a Thermally-treated Li_2O-B_2O_3-Al_2O_3 Glass System,"** Journal of Non-Crystalline Solids, 404, 104-108 (2014).

102 C. Romano, E. Paris, B.T. Poe, G. Giuli, D.B. Dingwell, and A. Montana, **"Effect of Aluminum on Ti-Coordination in Silicate Glasses: A XANES Study,"** Am. Mineralogist, 85, 108-117 (2000).

103 P.A. Sabine, **"The Optical Properties and Composition of Acmitic Pyroxenes,"** Mineralogic Magazine, 29, 113-125 (1950).

104 W.A. Deer, R.A. Howie, and J. Zussman, **"Rock Forming Minerals: V.2A. Single-Chain Silicates,"** The Geological Society, London, U.K., 668pp. (1997).

105 K.G. Brown, R.L. Postles, and T.B. Edwards**. "SME Acceptability Determination for DWPF Process Control (U),"** U.S. DOE Report WSRC-TR-95-00364, Rev. 5, Savannah River Nuclear Solutions, Savannah River National Laboratory, Aiken, SC, (2006).